The Role of Film and Subphase Complexity: Understanding Hydration, Hydrogen Bond Order, Co-adsorption, and Binding at the Air-Water Interface

Dissertation

Presented in Partial Fulfillment of the Requirements for the Degree Doctor of Philosophy

in the Graduate School of The Ohio State University

By

Maria Guadalupe Vazquez de Vasquez

Graduate Program in Chemistry

The Ohio State University

2022

Dissertation Committee

Prof. Heather C. Allen, Advisor

Prof. James Coe

Assoc. Prof. Zachary Schultz

Abstract

Ocean aqueous interfaces comprise one of the major biological and chemical networks in Earth's biosphere and atmosphere, thus understanding the various chemical processes at these interfaces is crucial for advising climate models. Upon wind breaking on the ocean surface, sea spray aerosol (SSA) is generated and released into the atmosphere. SSA is enriched in the organics and ions present in the sea surface microlayer (SSML), due to the transfer of these species to the aerosol phase and can ultimately impact the climate through various mechanisms. SSA organic coatings contain a diverse array of surface-active molecules such as fatty acid and alcohols. Because of the impact of these organic films on SSA's climate-relevant properties, an understanding of fundamental chemistry of lipids and ions in these interfaces is important. In this dissertation, surface sensitive techniques are used to probe the structure and properties of fatty acid model systems with a range of salts and under varying temperature conditions.

First, the binding of group II metal cations, such as Ca^{2+} and Mg^{2+}, to a fatty acid carboxylate headgroup was investigated. These cations are known to be enriched at the ocean surface; therefore, it is imperative that a deeper understanding be sought to include hydration effects. Here, infrared reflection–absorption (IRRAS) and Raman spectroscopy were used to obtain surface and solution carboxylate binding information.

Results show that Ca^{2+} directly binds to the carboxylate headgroup in contact ion pairs where Mg^{2+} rarely does, revealing the dominance of the solvent-shared ion pair of Mg^{2+} with carboxylate at the air–water interface.

Next, the temperature-dependent hydration structure of long-chain fatty acids and alcohols at the air–water interface, which has great underlying significance in fundamental ice nucleation interactions in the atmosphere, were investigated. This study presents an experimental approach by providing insight into the temperature-dependent vibrational structure and electric field character of the immediate hydration shells of fatty alcohols and acid headgroups. The IRRAS spectral features reveal that intra- and intermolecular vibrational couplings strongly impact the OH stretching region at fatty acid and alcohol water interfaces. Overall, results are consistent with ice templating behavior for both the fatty acid and the alcohol, yet the surface potential is stronger for the fatty alcohol. These findings develop a better understanding of the complex surface potential and spectral signatures involved in ice templating.

The following chapters focus on adding complexity within the monolayer and the underlying solution. Fatty alcohols present in aerosol particles are an important source of ice nucleation activity in SSA, yet their interactions with other aerosol components and the influence on freezing are largely unknown. This study reports quantitative measurements of fatty alcohols in model SSA and examines the relationship between composition and structure of surfactants and subphases. Results show that the deposited mixtures of surfactants retain the ability to nucleate ice, even in fatty acid-dominant compositions. Moreover, strong refreezing effects are observed, where previously frozen water-surfactant samples nucleate more efficiently. Such structural sources of refreezing behavior were identified as kinetically trapped film states.

Metal binding within a single substance monolayer on aqueous solutions has been previously studied. However, such binding events within mixed monolayers, particularly those of ocean-relevant ratios, are not well explored. In this study, monolayer ratios of stearic acid (octadecanoic acid) and stearyl alcohol (octadecanol) on aqueous solutions with varying $ZnCl_2$ concentrations and an ocean relevant NaCl concentration were explored. Langmuir surface pressure–area (Π–A) isotherms and IRRAS were used to quantify the Zn^{2+}–carboxylate surface binding affinities for each monolayer composition. Results show that Zn^{2+}–carboxylate surface binding is enhanced by ~300 times when compared to the bulk solution. The addition of 10% stearyl alcohol reduces the apparent surface binding affinity by over 50%; this is significantly more than predicted from the slight reduction in viable 1:1 binding sites.

Lastly, saccharide co-adsorption to deprotonated monolayers was investigated. This study expands upon previously defined co-adsorption mechanisms by investigating the alginate and monomeric form, glucuronate, co-adsorption to a stearic acid monolayer as a function of saccharide concentration on an ocean proxy solution. Langmuir (Π–A) isotherms, surface-sensitive IRRAS, and Brewster angle microscopy results demonstrate that the mechanism of co-adsorption significantly differs between glucuronate and alginate. Film thickness calculations show an increase from ~ 4 nm to 5.5 nm and from ~ 4 nm to ~4.2 nm upon co-adsorption of alginate and glucuronate to stearic-d_{35} acid monolayers, respectively, indicating that alginate forms multilayers underneath the monolayer. Glucuronate does not co-adsorb, whereas it likely intercalates and induces significant reorganization within the monolayer. To improve Earth system model parameterization of saccharide enrichment in SSA, the Langmuir adsorption coefficients and half-saturation concentrations of both alginate and glucuronate co-adsorption to stearic-d_{35} acid were quantified. This study demonstrates that the use of monosaccharides alone as a proxy for saccharide enrichment is insufficient and provides important parameters for better representation of saccharides in marine aerosol climate models.

Dedication

To Brian, my parents Dolores and Francisco, and Rat Boy.

In loving memory of Pantera.

Acknowledgments

Growing up in Aguascalientes, Ags. Mexico, I dreamed of having an academic degree, but due to various life events this dream was put on hold. Years later, I moved to Los Angeles, California where I had the opportunity to return to school. My academic journey has not been an easy one, particularly graduate school, but thanks to my spouse Brian Vasquez who has been my biggest support I am here now writing my dissertation. Brian accepted the challenge to move to a different state, took over all household responsibilities during my first year of graduate school, and has been and unending source of encouragement and support throughout my graduate school. Also, I would like to thank my family for supporting me and my education, by answering my phone calls, listening to my complaints, and making this journey more joyful. Lastly, I would like to thank my family in law for always celebrating my academic accomplishments and always providing extra support.

In the Allen Lab, I would like to thank my advisor, Dr. Heather Allen, for her mentorship and guidance through my graduate career at The Ohio State University. I would also like to thank my mentors, Dr. James Coe, and Dr. Zachary Schultz who helped me to grow as a scientist over the course of my graduate career. Moreover, I want to thank my external collaborators, Russell Perkins, Marcel Baer, Laura McCaslin, and Bethany Wellen Rudd, for their help communicating our science. I also would like to

acknowledge past and present colleagues in the Allen Lab, Kimberly Carter-Fenk, Mickey Rogers, Jennifer Neal, Tehseen Adel, and Jessica Clark, for their collaboration and assistance. Moreover, I am also incredibly grateful to my undergraduate researchers Emma Beasley and Nicole Auvil, who assisted me in data collection for the various projects in this dissertation. Finally, I would also like to extend my endless appreciation to the amazing people and friends that helped me through graduate school, Mickey Rogers and Kimberly Carter-Fenk.

Vita

2012……………………………………………A. A. in Natural Sciences East Los Angeles College Monterey Park, CA

2012……………………………………………A. A., Eat Los Angeles College Monterey Park, CA

2015……………………………………………B. S. Chemistry, California State University Los Angeles, CA

2017……………………………………………M. S. Chemistry, California State University Los Angeles, CA

2018-present……………………………….....Graduate Teaching Assistant, Department of Chemistry and Biochemistry, The Ohio State University, Columbus, OH

2019-present……………………………….....Graduate Research Assistant, Department of Chemistry and Biochemistry, The Ohio State University, Columbus, OH

Publications

- Maria G. Vazquez de Vasquez, Mickey M. Rogers, Kimberly A. Carter-Fenk, and Heather C. Allen. Discerning Poly-and Monosaccharide Enrichment Mechanisms:

Alginate and Glucuronate Co-Adsorption to a Stearic Acid Sea Surface Microlayer. *ACS Earth Space Chem*. **2022** (Submitted)

- Mickey M. Rogers, Maria G. Vazquez de Vasquez, Jennifer F. Neal, Mia M. Zerkle, Brittany M. Shook, and Heather C. Allen. Phase State and Thermodynamic Properties of Proxy Sea Spray Aerosol Interfaces Derived from Temperature-Dependent Equilibrium Surface Pressure. *ACS Earth Space Chem*. **2022** (Submitted)
- Maria G. Vazquez de Vasquez†, Kimberly A. Carter-Fenk†, Laura M. McCaslin, Emma E. Beasley, Jessica B. Clark, and Heather C. Allen. Hydration and Hydrogen Bond Disorder of Octadecanoic Acid and Octadecanol Films on Water at 21 °C and 1 °C. *J. Phys. Chem A.*, **2021**,*125*, 10065–10078.
- Maria G. Vazquez de Vasquez†, Bethany A. Wellen Rudd†, Marcel D. Baer, Emma E. Beasley, and Heather C. Allen. Role of Hydration in Magnesium versus Calcium Ion Pairing with Carboxylate: Solution and Aqueous Interface. *J. Phys. Chem B.*, **2021**, *125*, 11308–11319.
- Nicole C. Auvil†, Maria G. Vazquez de Vasquez†, and Heather C. Allen. Zinc–Carboxylate Binding in Mixed Octadecanoic Acid and Octadecanol Monolayer on Proxy Seawater Solution Surfaces. *ACS Earth Space Chem*. **2021**, *5*, 2947–2956.
- Tehseen Adel, Ka Chon Ng, Maria G. Vazquez de Vasquez, Juan Velez-Alvarez, and Heather C. Allen. Insight into the Ionizing Potential Method and Aqueous Sodium Surfaces. *Langmuir*. **2021**,37,7863-7874.

- Russell J. Perkins, Maria G. Vazquez de Vasquez, Emma E. Beasley, Thomas C. J. Hill, Elizabeth A. Stone, Heather C. Allen, and Paul J. DeMott. Relating Structure and Ice Nucleation Surfactant Systems Relevant to Sea Spray Aerosol. *J. Phys. Chem A.*, **2020**, *124*, 8806-8821.
- Herbe Pech, Maria G. Vazquez, Jean Van Buren, Michelle M. Ivey, Tina M. Salmassi, Matthew A. Pasek, and Krishna L. Foster. Elucidating the Redox Cycle of Environmental Phosphorus Using Ion Chromatography. *J. Chromatogr. Sci.*, **2011**, 49, 573-581.

Fields of Study

Major Field: Chemistry

Table of Contents

List of Tables

List of Figures

List of Abbreviations

SSA	Sea Spray Aerosol
SSML	Sea Surface Microlayer
CAICE	Center for Aerosol Impacts on Chemistry of the Environment
CCN	Cloud Condensation nuclei
IN	Ice Nuclei/ Ice Nucleation
INPs	Ice Nucleating Particles
INEs	Ice Nucleating Entities
BAM	Brewster Angle Microscopy
IRRAS	Infrared Reflection–Absorption Spectroscopy
AIMD	*ab inito* Molecular Dynamics
OA	Octadecanoic Acid
OL	Octadecanol
SPOT	Surface Potentiometry
Π–A	Surface Pressure Area
Π	Surface Pressure
MMA	Mean Molecular Area
G-TC	Gas-Tilted Condensed
TC	Tilted Condensed
UC	Untilted Condensed
EDL	Electrical Double Layer
ΔV	Surface Potential
θ_B	Brewster Angle
R	Reflectance
RA	Reflectance–Absorbance
MCT	HgCdTe
V	Parallel Polarized
H	Perpendicular Polarized
FTIR	Fourier Transform Infrared
IR	Infrared
DFT	Density Functional Theory
WHAM	Weighted Histogram Analysis Method
PMF	Potential Mean Force
M	Monodentate
B	Bidentate
SS	Solvent-shared
MD	Molecular Dynamics

3D	3-Dimensional
2D	2-Dimensional
FWHM	Full Width at Half Max
L_1	Liquid Expanded
L_2	Liquid Condensed
S	Solid
CS	Crystalline Solid
ESP	Equilibrium Spreading Pressure
MDS	Measure Distance

Chapter 1. Introduction

1.1 Motivation

The studies in this dissertation were conducted to inform on the fundamental physical chemistry of atmospherically-relevant interfaces. Sea spray aerosol (SSA) and the sea surface microlayer (SSML) are the focal interfaces of interest in this study where lipids and ions are prevalent at high concentrations. A major outcome of these efforts is the key information gained on the interfacial solvation structure of polar headgroups, ion carboxylate binding interactions, and the adsorption process for organic enrichment, particularly saccharides, in the SSML and in SSA.

This work is supported by the Center for Aerosol Impacts on Chemistry of the Environment (CAICE). The main goal of this collaborative center is to be able to understand and interpret SSA chemistry, from aerosol production, to reactivity in the atmosphere, to the formation of clouds and ice via aerosol particles nucleation. Through analysis of SSA production, the molecules and ions transferred from bulk sea water and SSML to the aerosol can be quantified. Then, fundamental chemistry can be investigated from the analysis of SSA model proxy systems. This work combines surface science, spectroscopy, and computational chemistry to describe interfacial surfactant film organization at model marine aqueous interfaces. I aim to investigate interfacial organization, particularly the role of hydration, hydrogen bond order, ion–carboxylate binding interactions, and adsorption processes which can be responsible for the organic and ion enrichment in the SSML and SSA. Ultimately, the goal of these fundamental measurements of proxy marine surfaces is to inform Earth system model parameterization.

1.2 Environmental Impact Production and Composition of SSA

The oceans cover about 70% of the Earth's surface, making the oceans one of the most significant sources of natural aerosol emissions in the planet.[1,2] On all of these water surfaces exist the sea surface microlayer (SSML). The SSML, which is 1–1000 μm in thickness, is the boundary interface between the oceans and the atmosphere. Because of its unique position at the air–sea interface, the SSML is the key region for several global biogeochemical and climate-related processes.[3] About three decades ago, Seiburth hypothesized that the SSML consisted of a hydrated gel-like complex mixture of lipids, carbohydrates, and proteins.[4] This hypothesis has been confirmed in recent years. The SSML is an enriched biofilm with a high exposure to solar radiation acting as a highly efficient microreactor.[3,5] It acts as an efficient microreactor where different processes,[4] and unique arrangements of chemical compounds are found.[5,6]

SSA is formed via wave breaking at the air-seawater interface. The bubble-bursting process produces two distinct types of aerosols, film drops and jet drops. Film drops are produced from the bursting of the thin water film at the bubble–air interface, such drops are smaller and contain a larger organic fraction than jet drops. Jet drops are generated from the collapse of the bubble cavity after the bubble burst. SSA composition determines how effectively cloud droplets and ice crystals can form.[7,8] SSA influences

Earths' climate by changing the atmospheric optical properties and albedo by acting as cloud condensation nuclei (CCN) and ice nuclei (IN) in the atmosphere.[9] Interfacial composition of SSA plays a direct and indirect role in affecting climate, and the interfacial composition at the air–sea interface controls the composition of SSA. Consequently, studying the processes driving SSA interfacial composition is essentially important for developing a better understanding of marine influences on climate.

Organic coatings on SSA are largely comprised of fatty acids in addition to a vast array of other organic molecules including fatty alcohols. The presence of these molecules at the interface can also affect the ability of an aerosol to acts as an efficient ice nucleating particle (INP), which strongly depends on the identity and packing structure of the interfacial species. Ocean-sourced ice nucleating particles (INPs), released in SSA, can be important in regions with little terrestrial influence.[10–12] The exact identities of ocean-sourced ice nucleating entities (INEs) are not certain, although there are several promising candidates. Cultures of several phytoplankton species have been shown to promote freezing, although the ice nucleation (IN) active components are not known.[13] Analysis of residual components of frozen particles suggests that 15 to 75% of INPs active at −30 °C are predominately composed of fatty acid particles, depending on the time period examined.[14] Simple surfactants such as fatty acids and fatty alcohols are produced biogenically from the breakdown of cell membranes. Previously, monolayers of fatty alcohols have been shown to be good ice nucleators.[15–18] However, different surfactant headgroups can produce vastly different behavior. Experimental investigation of fatty acid freezing has found that these monolayers are, by contrast, poor ice nucleators, although solid fatty acid particles are more promising as INEs.[19] Fatty alcohols have drawn a great deal of interest because they are one of the few unambiguously identified compounds with the ability to nucleate ice, that are also found in the environment. Studies have examined the ability of fatty alcohols to "template" ice and promote freezing.[20]

Salts also form a major component in seawater. Some of the major cations in seawater are Na^+, Mg^{2+}, Ca^{2+}, K^+ which are also enriched in fine SSA. Studies have shown that the binding of divalent cations, Ca^{2+} and Mg^{2+}, to negatively charged functional groups, such as carboxylate, has significant consequences in the structure and function of many systems of atmospheric interest.[21–29] The role of Ca^{2+} and Mg^{2+} in atmospheric aerosol chemistry is an important area of research. Despite its lesser concentration in bulk seawater (10 mM compared to 50 mM),[30,31] studies have shown that Ca^{2+} enrichment in sea spray aerosols is much higher than that of Mg^{2+}.[24,25] This likely indicates a preferential binding of Ca^{2+} ions to negatively charged surfactant headgroups at the air-sea interface,[32] thus leading to increased transfer of Ca^{2+} to the aerosol phase. The binding of Ca^{2+} and Mg^{2+} to the carboxylate headgroups of marine prevalent fatty acids such as palmitic acid and stearic acid has significant effects on the organization and structure of organic films on SSA, thus impacting the climate properties of these particles.[22,24,25,29,33,34]

Saccharides also comprise a significant fraction of organic carbon in sea spray aerosol (SSA).[35] Estimates have shown that up to 61% of SSA content by mass comes from saccharides with submicron SSA being the most enriched.[24,36,37] The exact transport of saccharides from ocean bulk to the sea surface microlayer (SSML) remains understudied,[38] causing an underestimation of saccharide presence in SSA.[21,39,40] Atmospheric processes are dependent on SSA composition.[41–45] SSA compounds, especially saccharides, serve as important sites for cold cloud and ice formation.[46–57] Clouds and ice are important regulators of the overall radiative budget on earth, scattering and absorbing solar radiation. Changes in SSA composition alter the abundance of cloud condensation nuclei and ice nucleating particles which ultimately drive climate processes, like temperature and weather, in the marine boundary layer.[24,58–60] Without accurate measures of saccharide content within SSA, climate models will be based on underestimated inputs, limiting our accurate understanding of global climate trends.

1.3 Dissertation Highlights

This section highlights key parts of the dissertation. Chapter 2 provides a summary of the techniques and instrumentation utilized throughout these studies. These techniques and instrumentation were used to conduct surface-sensitive measurements including surface tensiometry and surface potentiometry methods, Brewster angle microscopy (BAM), infrared reflection–absorption spectroscopy (IRRAS), and Raman spectroscopy.

Chapter 3 provides insight into the binding of group II metal cations such as Ca^{2+} and Mg^{2+}. Here, IRRAS and Raman spectra was utilized to obtain surface and solution phase carboxylate binding information, respectively. Spectral non-coincidence effect analysis, temperature studies, result in a concise interpretation of binding motifs that include the role of mediating water molecules, that is, contact and solvent-shared ion pairs. Results show that Ca^{2+} directly binds to the carboxylate group in contact ion pairs where magnesium rarely does. Moreover, this study reveals the dominance of the solvent-shared ion pair of magnesium with carboxylate at the air–water interface and in solution.

Chapter 4 shows that the temperature-dependent hydration structure of long-chain fatty acids and alcohols at air-water interfaces is important in the fundamental interactions underlying ice nucleation in the atmosphere. This study used a combination of surface-sensitive IRRAS and surface potentiometry to elucidate detailed molecular structures of the octadecanoic acid and octadecanol (stearic acid and stearyl alcohol, respectively) headgroup hydration shells at room temperature and near freezing. The findings suggest that intra- and intermolecular vibrational couplings strongly impact the OH stretching region at fatty acid and fatty alcohol water interfaces. These findings develop a better understanding of the complex surface potential and spectral signatures involved in ice templating.

Chapter 5 describes the interaction of fatty alcohols with other aerosol components, such as fatty acids, and their influence on freezing. Here, quantitative measurements of fatty alcohols in model SSA were reported and the relationship between composition and structure of surfactants and subphases were examined. It was found that deposited mixtures of surfactants retain the ability to nucleate ice, even in fatty-acid-dominant compositions. Strong refreezing effects are also observed, where previously frozen water-surfactant samples nucleate more efficiently. Structural sources of refreezing behavior are identified as either kinetically trapped film states or 3-Dimentional (3D) solid surfactant particles.

Chapter 6 primary goal was to probe the effect of mixed monolayer composition on trace metal binding with monolayers composed of fatty acid and fatty alcohol molecules, typical components in SSML and SSA. Mixed monolayers of stearic acid (octadecanoic acid), and stearyl alcohol (octadecanol) were thus systematically evaluated at four different ratios, and each ratio was studied on eight aqueous solutions of differing concentrations of $ZnCl_2$ while maintaining a constant seawater NaCl concentration. IRRAS was used to probe these surface films and to quantify the Zn^{2+}–carboxylate surface binding affinities. All 1:1 Zn^{2+}–carboxylate surface binding affinities are found to be on the order of 10^3, which is about 300 times stronger than the analogous bulk binding process, indicating enhanced binding at the interface. Results reveal that ratios similar to those found in the SSML and in SSA films of octadecanoic acid and octadecanol impact surface binding affinity of Zn^{2+}, an oceanic trace metal.

Chapter 7 shows the importance of saccharides studies to elucidate important inputs for climate models. Here, saccharide co-adsorption to deprotonated monolayers was expanded by studying alginate and glucuronate. Langmuir (Π–A) isotherms, surface-sensitive IRRAS, and BAM results demonstrated that the mechanism of co-adsorption of anionic alginate and glucuronate are not the same. Thus, the use of a monosaccharides as a proxy for larger saccharide entities would not sustain polysaccharide complexity. This study quantified the Langmuir adsorption coefficient and half-saturation concentration of both alginate and glucuronate to stearic-d_{35} acid (octadecanoic-d_{35} acid) monolayers. These parameters present important inputs for producing accurate climate models. Moreover, monolayer thickness was also calculated. The differences in monolayer thickness demonstrate the complexity of saccharide co-adsorption to the interface, suggesting that the role of monosaccharides as a proxy for a more complex system cannot provide a full picture of the monolayer complexity.

Chapter 2. Theoretical Background and Instrumentation

This chapter provides a brief overview of the theory of Langmuir trough compression, surface potentiometry (SPOT), infrared reflection–adsorption spectroscopy (IRRAS), Brewster angle microscopy (BAM), and Raman spectroscopy as well as instrumental details. Experimental details relating to each experiment are provided in specific chapters.

2.1 Theoretical Background

2.1.1 Surface Tensiometry Theory

Complete derivations of the equations relating to surface tension have been presented in other works, thus only a brief introduction will be presented in this dissertation.[61,62] Commonly, the air–water interface can be expressed as a three-phase system consisting of two bulk phases, vapor (*v*) and liquid(*l*), and a surface phase. The changes in the internal energy (*U*) of a two-phase system, ignoring non-expansion work, can be expressed as follows:

$$dU = TdS - PdV + \sum \mu_i dN_i + \gamma dA \qquad (2.1)$$

It is known that the Gibbs free energy is defined as $G = U + PV - TS$, this can also be expressed as the change in the total interfacial Gibbs free energy shown by the following equation:

$$dG = SdT + V^v dP^v + V^l dP^l + \sum \mu_i dN_i + \gamma dA \qquad (2.2)$$

In the case of a planal interface, the surface tension (γ) is described as

$$\gamma \equiv \frac{\partial G}{\partial A}\bigg|_{T,P,N_i} \tag{2.3}$$

2.2 Surface Tensiometry Instrumentation

These following sections describe the surface tension instrumentation and techniques utilized throughout the different projects composing this dissertation. For all surface-sensitive methods, the Wilhelmy plate technique was employed to measure surface pressure.

2.2.1 Wilhelmy Plate Method

In the Wilhelmy plate method, a measurement is made to determine the force due to γ on a suspended plate that it is partially immersed into the subphase with the help of the dimensions of a thin plate. Typically, the materials used for these plates are platinum or filter paper.[63] In this method the filter papers are disposed after each individual use, and the platinum plate is cleaned by using a Bunsen burner flamed until glowing red to completely remove organic contaminants from the surface of the plate. Regardless of what material the plate is made of, one must ensure complete wetting of the plate so that the contact angle between the liquid and the plate is 0°.[64] In order to calculate the surface tension, the forces acting on the plate need to be considered by using the following equation.[62,65]

$$\gamma = \frac{F}{2(L+d)cos\theta} \tag{2.4}$$

where F is the total force, L is the length of the Wilhelmy plate , d is the plate thickness, and θ is the contact angle. If the following assumptions are made a) $\theta = 0$, the plate is completely wetted, and b) the plate is assumed to be infinitely thin ($d \rightarrow 0$), this expression can be simplified to the following expression.

$$\gamma = \frac{F}{2L} = \frac{g(m_s - m_p)}{2L} \tag{2.5}$$

where g is gravity, m_p is the mass of the plate, and m_s is the mass related to the surface force.

2.2.2 Langmuir Trough Compression, Non–Equilibrium Monolayer Relaxation

Insoluble monolayer surface tension-related properties are normally studied with Langmuir trough (**Figure 1**) using movable barriers to change the surface-area. Langmuir troughs are utilized in surface pressure–area (Π–A) isotherms, where the surface pressure (Π) is defined as the difference in surface tension between the bare aqueous interface (γ_0) and the surface covered with a surfactant monolayer (γ_m) see equation below.

$$\Pi = \gamma_0 - \gamma_m \tag{2.6}$$

the changes in surface pressure are assessed from a decrease in mean molecular area (MMA) by the amphiphiles molecules on the surface. It is crucial to note that in a compression isotherm, the measured surface pressure is actually the sum of two parts. One being the surface tension difference between the clean and the monolayer-covered surfaces (equation (2.6)), and the other being the contribution from a 2-Dimensional (2D) compression force acting on the molecules on the surface.[66]

$$\Pi = (\gamma_0 - \gamma_m) + F_{2Dcomp} \tag{2.7}$$

Due to this forcing, a metastable state is the result of a compression isotherm, this happens above the monolayer stability limit.

The work presented here uses the Langmuir trough compression isotherms (KSV NIMA) to evaluate monolayer stability. The barriers are quickly compressed to check for contaminants prior to surfactant addition, making sure that the Π is not greater than 0.20 mN/m. After checking that the surface is clean an amphiphile solution is spread dropwise using a Hamilton syringe. The monolayer is then compressed at a constant rate of 5mm/min/barrier. Different monolayer phases are observed as the amphiphile monolayer is compressed. These different phases are as follows gas-tilted condensed phase (G-TC), tilted condensed (TC), untilted condensed (UC), and Collapse.

In the mechanically-control, non-equilibrium relaxation (NER) experiments, the monolayer is compressed to a target surface pressure at a constant rate of 5mm/min/barrier. Once the surface pressure is achieved, it is maintained by motion of the barriers at a maximum rate forward/backward of 1mm/min/barrier. Analysis of the change in MMA under these conditions allows to determine the relaxation mechanism of the monolayer.

2.3 Surface Potentiometry Theory

This method is based on the *Kelvin* probe, where the electrode in air is moved with respect to the water surface. At the air–water interface, the change in capacity of the gap between the air and water leads to a current flow in the external circuit. The difference in these null potentials, with and without a monolayer, is given as ΔV where:

$$\Delta V = \Delta V_0 + \Delta V_m + \Psi_0 \tag{2.8}$$

where ΔV_0 is the surface potential of the clean air–water interface, ΔV_m is the monolayer dipolar contribution and Ψ_0 is the electrical double layer (EDL) potential.

Based on equation 2.8 the term ΔV_m can be defined by the Demchak-Forth model illustrated by equation 2.9 which can be described as a three-layer capacitor with three distinct regions, the headgroup, the tail, and the oriented water near the headgroup.[67–69]

$$\Delta V_m = \frac{1}{A\varepsilon_0}\left(\frac{\mu_{water}}{\varepsilon_{water}} + \frac{\mu_{head}}{\varepsilon_{head}} + \frac{\mu_{tail}}{\varepsilon_{tail}}\right) \tag{2.9}$$

where A is the average area per molecule, ε_0 is the vacuum permittivity, μ_i represents each region dipole moment normal to the interface and ε_i represents the dielectric constant in each region. Because the surface potential measurement cannot distinguish between the effect of the headgroup and interfacial water molecules, in equation 2.9 the second and third terms are summed up into one contribution. According to the classical Gouy-Chapman model of the electrical double layer (EDL) stating that a diffused layer of ions below the monolayer, the EDL contribution to the measured surface potential can be estimated by using the Grahame equation, equation 2.10:[67,68]

$$\Psi_0 = \frac{2RT}{F}\sinh^{-1}\left(\frac{\sigma}{\sqrt{8\varepsilon_0\varepsilon_r RTC_b}}\right) \tag{2.10}$$

where $\sigma = e\alpha/A$ is the surface charge density of the monolayer, where e is the electric unit charge and α the degree of dissociation of headgroup, R is the ideal gas constant, F the Faraday's constant. T is the temperature, ε_r the dielectric constant of the solvent and C_b is the concentration of the salt solution in the bulk.

2.3.1 Surface Potential Instrument

In these studies, a surface potential sensor (SPOT I, Biolin Scientific, USA, Linthicum Heights, MD) is used to obtain electric field data. This surface potential sensor is based on the vibrating plate (*Kelvin*) method, where the potential difference above and below the film is measured and is sensitive to all the individual dipole moments. Surface potential (ΔV) changes are measured by detecting the potential difference between the vibrating plate, and the counter electrode, illustrated in **Figure 2**. The SPOT sensor is utilized with the Langmuir trough by placing the sensor in the middle of the trough within enough distance from edges. The counter electrode is placed in the trough such that the subphase completely covered it, then the vibrating plate is placed about 1–2 mm above the subphase surface directly above the counter electrode. As recommended in the instrument manual, the SPOT head is turned on to equilibrate least 10 minutes before starting the experiment. The surface pressure is measured using the Wilhelmy plate method using a filter-paper plate (Ashless Grade 41, Whatman, GE Healthcare, Chicago, IL, USA). The trough is then filled with the subphase of interest. Surface cleanliness (≤ 0.20 mN/m) is checked then the surfactant is spread onto the subphase. Before the surfactant solution is spread both the surface pressure and surface potential are zeroed. Ten minutes are allowed for solvent evaporation, then symmetrical compression of the monolayer started at a rate of 10 mm/minute (5 mm/min/barrier).

2.4 Brewster Angle Microscopy Theory

BAM is a non-invasive imaging technique used to determined morphology and optical properties of an insoluble Langmuir monolayer at the air–water interface. This microscopy technique depends on the minimal reflectance on a *p*-polarized light at the Brewster angle (θ_B) of a clean surface. In the case of water, for instance, has a Brewster angle of approximately 53.1°, relative to the surface normal. The θ_B can be calculated by using the equations of reflectance. In a system only consisting of two media, reflectance (*R*) is defined as the ratio of the reflected and incident beam intensities (I_r and I_i respectively) which can be calculated using the Fresnel reflection coefficient a function of incidence angle (θ_i) and refracted angle (θ_t), shown below:[65,70,71]

$$R = \frac{I_r}{I_i} = |r|^2 \tag{2.11}$$

$$r_s = \frac{sin(\theta_i - \theta_t)}{sin(\theta_i + \theta_t)} \tag{2.12}$$

$$r_p = \frac{tan(\theta_i - \theta_t)}{tan(\theta_i + \theta_t)} \tag{2.13}$$

Based on equation (2.13), r_p approaches zero when the denominator approaches infinity. This occurs when $\theta i + \theta t = \frac{\pi}{2}$. Using Snell's law, shown below:

$$\mathrm{n}_1 sin\ \theta_i = n_2 sin\ \theta_t \tag{2.14}$$

Both the incident and refracted angles are associated to the refractive indices of the media, where n_1 is the refractive index of the air and n_2 is the refractive index of the subphase. When there is no reflection then $\theta_i = \theta_B$, and $\theta_t = \frac{\pi}{2} - \theta_B$, and based on these the Brewster angel can be calculated by

$$\theta_B = \tan^{-1}\left(\frac{n_2}{n_1}\right) \tag{2.15}$$

If a Langmuir film is present on the surface of and aqueous solution the refractive index is different, and the *p*-polarized light is reflected from the surface[63] (**Figure 3**). Thus, creating a contrast among the surfactant-rich (bright regions) and surfactant-poor regions (dark regions) in the captured image of the surface. In an ideal world, r_p from the interface vanishes at the θ_B, but for a real interface r_p has a minimal but non-zero value. A few reasons for this remaining reflectance are the finite thickness of the interface, surface roughness and the optical anisotropy of the interface.[70]

2.4.1 Brewster Angle Microscopy Instrument

BAM images are collected utilizing a custom-built setup (**Figure 3**). This setup has been previously described elsewhere. A brief description of the component of the instrument will be outlined here.[32,67,72,73] The BAM set up is mounted on a goniometer and positioned along the Brewster angle of the air–water interface at 53.1°. It utilizes a 1.5 mW HeNe laser source (Research Electro-Optics) to produce 543 nm *p*-polarized light with linear 500:1 polarization, and the polarized light is further filtered by a Glan-laser calcite polarizer (Ekspla). Reflected light from the surface is sent through a 10× infinity-corrected super long working distance objective lens(CF160 TU Plan EPI, Nikon), and the magnified light is collimated and focused by a tube lens (MXA22018, Nikon). Finally, the images are captured on a back-illuminated CCD camera ((DV887-BV, 512 × 512 active pixels, 16 × 16 μm pixel size, Andor). The images here were cropped form their original size of 8.2 × 8.2 mm to show only the most resolved portion.

2.5 Infrared Reflection–Absorption Spectroscopy Theory

IRRAS is a surface-sensitive spectroscopy technique used to determine the molecular organization and interaction of and within Langmuir films. This technique produces a vibrational spectrum of the interface.[71,74,75] In the work presented here, IRRAS is utilized to investigate ion binding to carboxylate headgroups as well as molecular vibrations which can provide insight into ice nucleation.

Usually, the spectra obtained from IRRAS are plotted in terms of reflectance–absorbance (*RA*), defined as

$$RA \; = \; -log \left(\frac{R}{R_0}\right) \tag{2.16}$$

where *R* is the reflectance of the surface with a spread monolayer and R_0 if the reflectance of a bare aqueous solution. Reflectance-absorbance is negative when the film reflectance is greater than the subphase reflectance ($R/R_0>1$) and is positive when the film reflectance is less than the subphase ($R/R_0<1$)

The reflectance observed in the spectra partially depends on the experimental geometry and properties of the media and can be approximated using a three-layer system, air, aqueous subphase and the thin layer of the deposited surfactant. For a three-layer model the Fresnel reflection coefficients for the *s* and *p*-polarizations can be describe as follows:[71,76]

$$r_s \; = \; -\frac{\sin(\theta_i - \theta_t) - i\frac{2\pi}{\lambda}\tilde{n}_2^{-1}\sin\theta_i \tilde{I}_1}{\sin(\theta_i + \theta_t) - i\frac{2\pi}{\lambda}\tilde{n}_2^{-1}\sin\theta_i \tilde{I}_1} \tag{2.17}$$

$$r_p = \frac{\sin(\theta_i - \theta_t)\cos(\theta_i + \theta_t) - i\frac{2\pi}{\lambda}\tilde{n}_2^{-1}\sin\theta_i(\tilde{I}_1\cos\theta_i\cos\theta_t - \tilde{I}_2\sin\theta_i\sin\theta_t)}{\sin(\theta_i + \theta_t)\cos(\theta_i - \theta_t) - i\frac{2\pi}{\lambda}\tilde{n}_2^{-1}\sin\theta_i(\tilde{I}_1\cos\theta_i\cos\theta_t - \tilde{I}_2\sin\theta_i\sin\theta_t)} \tag{2.18}$$

where:

$$\tilde{I}_1 \; = \; \int\left(\tilde{n}_x^2(z)\right) - \tilde{n}_2^2)d_z \tag{2.19}$$

$$\tilde{I}_2 \; = \; \int\frac{\left(\tilde{n}_z^2(z)\right) - \tilde{n}_2^2)}{\tilde{n}_z^2(z)}d_z \tag{2.20}$$

where ñ is the complex refractive index for the subphase ($\tilde{n}_2$) and the monolayer $\tilde{n}_x = \tilde{n}_y \, and \, \tilde{n}_z$),

$$\tilde{n}_i = n_i + ik_i \tag{2.21}$$

which is comprised of the real refractive index (*n*) and the extinction coefficient (*k*)

According to the equation presented above, the reflectance at the interface depends on the polarization and the angle of the incoming beam, and also to the refractive index of the system. These parameters have been previously discussed in literature; however, it is key to mention that depending on the angle and polarization of the beam it will affect whether the absorption bands in the IRRAS spectra are positive or negative. For instance, *s*-polarize light, the absorption bands are negative at all angles. Whereas *p*-polarized light band are negative at angles up to θ_B, thus changing to a positive band at angles greater than θ_B.[74,77] For the IRRAS spectra shown here unpolarized light was used and the angle used for all experiments are less than θ_B.

2.5.1 Infrared Reflection–Absorption Spectroscopy Instrument

IRRAS spectra are collected with an FTIR spectrometer (Frontier, Perkin Elmer) with an HgCdTe (MCT) detector. The IRRAS setup is built on a breadboard which is placed into the spectrometer chamber, where two gold mirrors are used to direct the beam to a liquid nitrogen cooled the MCT detector (**Figure 4**). During the experiments, a Langmuir trough or Petri dish are placed inside the FTIR spectrometer. With the help of the first mirror the unpolarized IR beam is directed to the sample surface at a 48° angle of incidence. The reflected beam is then directed to the second gold mirror and finally to the liquid nitrogen-cooled MCT detector. All spectra are collected in a single beam mode over a full spectral range of 4000–450 cm^{-1} and are the result of averaging 400 scans at a 4 cm^{-1} resolution in 0.5 cm^{-1} increments. IRRAS spectra are plotted as reflectance-absorbance (*RA*). The RA is calculated as –log (R/R_0) where *R* is the reflectivity on the monolayer and R_0 in the reflectivity of the subphase.

2.6 Raman Spectroscopy Theory

This section provides a brief overview of Raman classical theory. Although Raman scattering can be used to obtain information about rotational, electronic, and vibrational transitions, this section concerns primarily with its use in vibrational spectroscopy. Raman is a bulk technique that is used to get vibrational molecular information. In Raman spectroscopy, the sample is irradiated by an intense laser beam in the UV-visible region (ν_0), and the scattered light is observed in the direction perpendicular to the incident beam. Such scattered light consists of two types: one refers as Rayleigh scattering which is strong and has the same frequency as the incident beam (ν_0), and the other, called Raman scattering which is very weak and has frequencies $\nu_0 \pm \nu_m$ where ν_m is the vibrational frequency of a molecule. In Raman spectroscopy, one measures the vibrational frequency (ν_m) as a shift from the incident beam frequency.[78] Based on classical theory, Raman scattering can be explained as: the electric field strength (E), of the electromagnetic wave fluctuates with time (t)

$$E = E_m \cos 2\pi \upsilon_0 t \tag{2.23}$$

where E_m is the vibrational amplitude or the amplitude of the wave and ν_0 is the frequency of the laser. When this oscillating field interacts with the polarizable electron clouds of the sample molecules, it induces a dipole moment *P*.[78,79]

$$P = \alpha E = \alpha E_m \cos 2\pi v_0 t \tag{2.24}$$

where P has the units of C m and α is a proportionality constant and is called polarizability in J^{-1} C^2 m^2. The Raman effect results from the interaction of the polarizability with the normal modes of vibration on the molecules. The polarizability differs with the internuclear separation around its equilibrium value α_0 according to

$$\alpha = \alpha_0 + (r - r_e)(\frac{\partial\alpha}{\partial r})_e + \cdots \tag{2.25}$$

where α_0 is the polarizability of the molecule at the equilibrium bond distance r_e and r is the internuclear separation. Here, the subscript e indicates the evaluation at the equilibrium position. Then the change in internuclear distance varies with the frequency of the vibration according v_v according to

$$r - r_e = r_m \cos(2\pi v_v t) \tag{2.26}$$

where r_m is the maximum internuclear separation relative to the equilibrium position. If equation (2.26) is substituted into equation (2.25) then equation 2.27 is obtained.

$$\alpha = \alpha_0 + (\frac{\partial\alpha}{\alpha r})_e r_m \cos(2\pi v_v t) \tag{2.27}$$

Now if equation 2.27 is substituted into equation 2.24 then the following expression for the induced dipole moment is attained

$$P = \alpha E_m \cos 2\pi v_0 t + E_m\, r_m (\frac{\partial\alpha}{\partial r})_e \cos(2\pi v_v t) \cos(2\pi v_0 t) \tag{2.28}$$

If the identity for two products of two cosines is used, cos x·cos y = [cos(x + y) + cos (x – y)]/2 then the equation becomes:

$$P = \alpha E_m \cos 2\pi v_0 t + \frac{E_m}{2} r_m (\frac{\partial\alpha}{\partial r})_e \cos 2\pi(v_0 + v_v)\, t + \frac{E_m}{2} r_m (\frac{\partial\alpha}{\partial r})_e \cos 2\pi(v_0 - v_v)\, t \tag{2.29}$$

In this equation, the first term represents the Rayleigh scattering (frequency v_0), while the second and third terms represents the anti-Stokes and Stokes Raman scattering, respectively.[78,79]

Requirements for Raman Scattering. The selection rules for Raman scattering are determined by the evaluation of the transition moment, leading to the following equation.

$$R = \int \psi_i^* \left[\alpha_0 + (r - r_e)(\frac{\partial \alpha}{\partial r})_e\right] \psi_j \, d\tau \qquad (2.30)$$

which then reduces to

$$R = \int \psi_i^* \left[(r - r_e)(\frac{\partial \alpha}{\partial r})_e\right] \psi_j \, d\tau \qquad (2.31)$$

It is clear, from this equation, that there must be a change in polarizability during the vibration in order for Raman scattering to occur. Thus, the selection rules further predict that Raman lines, corresponding to fundamental modes, occur with $\Delta \nu = \pm 1$. Just as in IR spectroscopy, overtone transitions, which are much weaker, and appear at $\Delta \nu = \pm 2$. Based on this, it can be stated that for Raman spectroscopy, there must be a change in polarizability during the vibration.[79]

2.6.1 Polarized Raman Spectroscopy Instrument

The polarized Raman spectra are collected utilizing a custom-build polarized Raman spectrometer (**Figure 5**) with a 532 nm diode pumped CW laser with a built-in laser line (±0.5) and polarization filters (>100:1 V, Crystalaser). Excitation is coupled with a custom-build fiber optic polarized Raman probe (InPhotonics) allowing 235 mW power to the sample at a range is 90–4200 cm^{-1}. Two outputs of scatter light are sent to two independent FC fiber-optic end ports a parallel polarized (V) and a perpendicular polarized (H) using a 600 lines mm^{-1} grating. The coupling of the two 200 μm core fibers directly to the spectrograph allowed simultaneous collection of the perpendicular (HV) and parallel (VV) polarized spectra. The wavelength is calibrated to He:Ne emission lines (IsoPlane 320, Princeton Instruments) and detection from the liquid nitrogen-cooled CCD detector (Pylon, 1340 × 400 pixel, Princeton Instruments. Spectra are collected by signal averaging 300 spectra each with a 0.5 s integration time. The Raman spectra presented here are the average of at least three individual trials which have been baseline corrected by line function prior to averaging.

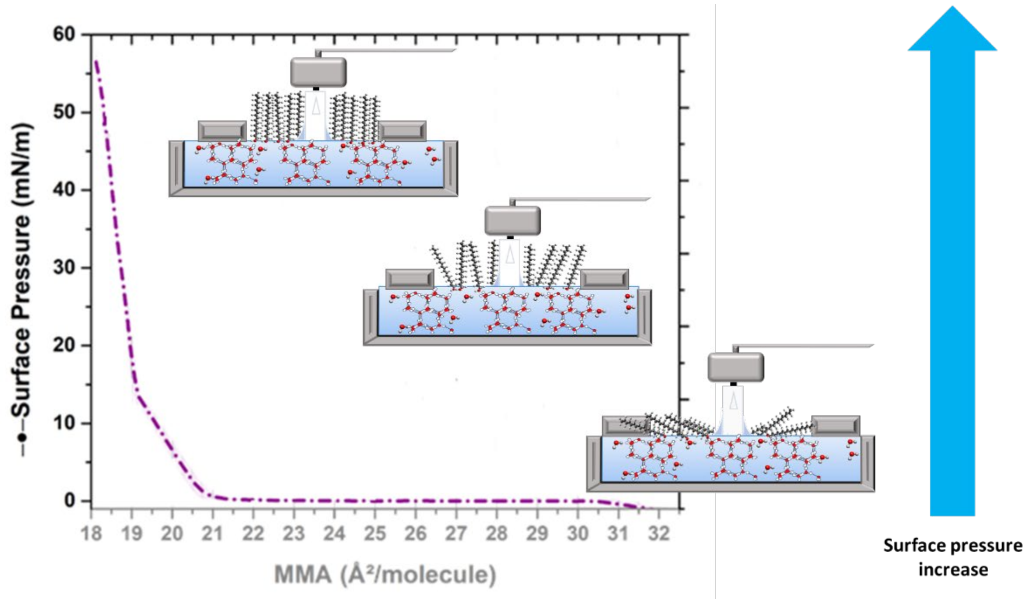

Figure 1. Schematic of pressure–area isotherm as the orientation of the surfactants goes through the different phases

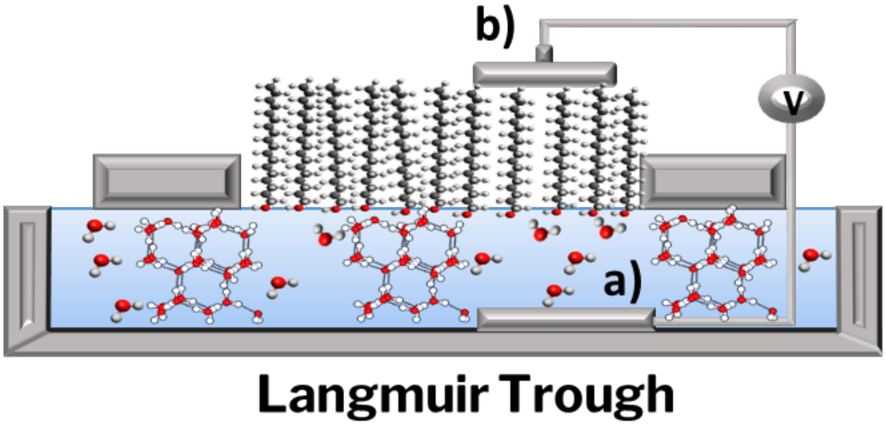

Figure 2. Schematic of the surface potentiometry SPOT based on the vibrating plate method, a) counter electrode and b) vibrating plate serving as the working electrode.

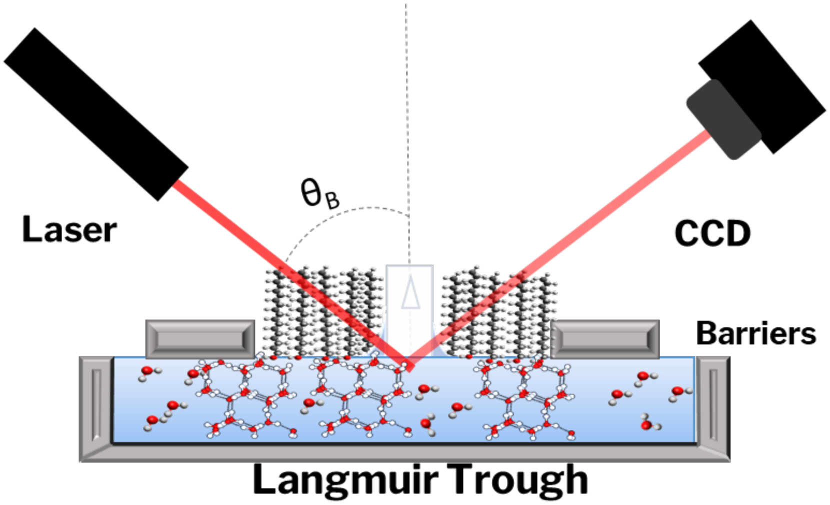

Figure 3. Schematic of a BAM set up with a laser beam directed to the surface and a CCD detector set.at the Brewster angle. The presence of a monolayer changes the condition of the interface and *p*-polarized light is reflected.

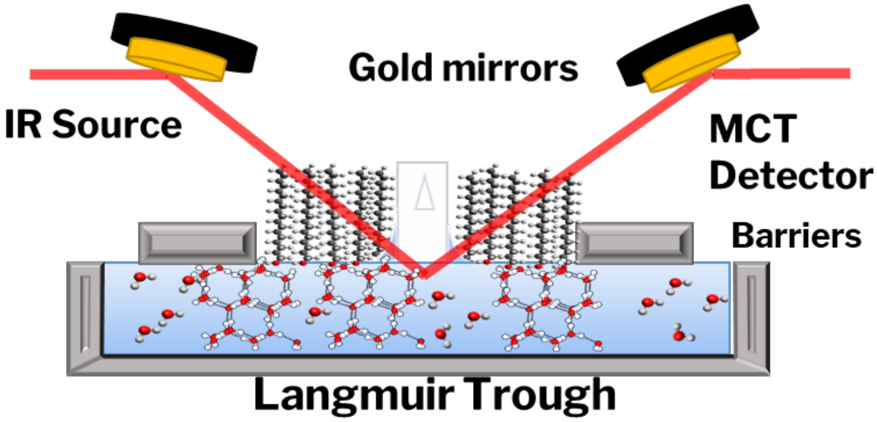

Figure 4. Schematic of the IRRAS setup used in this dissertation. The breadboard containing the gold mirrors is situated in a Frontier Perkin Elmer FTIR spectrometer equipped with an HgCdTe (MCT) detector

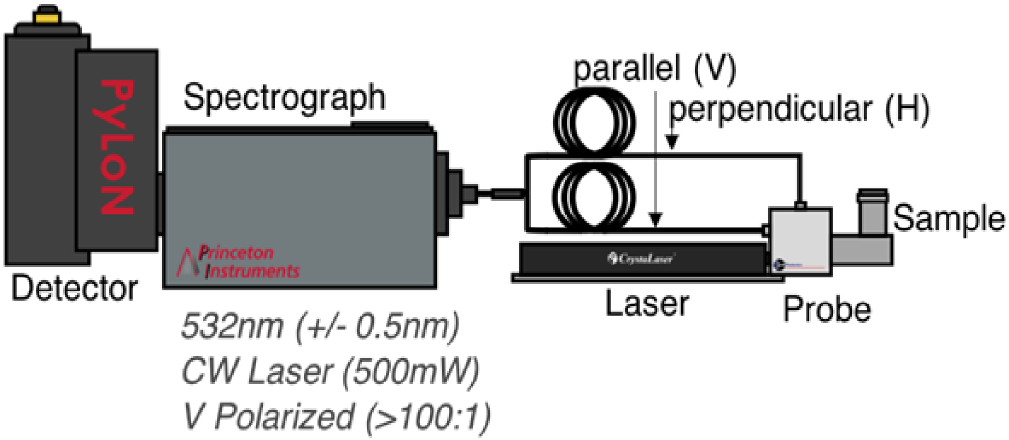

Figure 5. Schematic of the polarized Raman spectrometer with a parallel and perpendicular components equipped with a liquid nitrogen-cooled CCD detector as shown in the scheme.

Chapter 3. Role of Hydrogen in Magnesium versus Calcium Ion Pairing with Carboxylate: Solution and Aqueous Interface

Reproduced in part with permission from Vazquez de Vasquez, M. G.†; Wellen Rudd, B. A.†; Bear, M. D.; Beasley, E. E.; Allen, H. C. "Role of Hydrogen in Magnesium versus Calcium Ion Pairing with Carboxylate: Solution and Aqueous Interface". *J. Phys. Chem. B*, **2021,** *125*, 40, 11308–11319.

3.1 Introduction

Ion–carboxylate coordination geometries as well as mechanisms in aqueous solutions were primarily determined by comparing aqueous spectral responses to those of inorganic solid-state crystal structures of various metal carboxylates.[80–85] The established symmetric and asymmetric stretch frequency data markers are still commonly and widely being used as the predominantly metric for classifying the ion pairing of aqueous ion–carboxylates as ionic, monodentate, bidentate, or bridging with little regard to the vastly different hydration environments on these complexes in aqueous solutions compared to the solid state crystals from which the spectral markers are based.[74,86–94] Critical analysis of this dated interpretation of spectral responses to ion–carboxylate interactions has been recently made through the use of gas phase cluster studies.[95] While this prior study gives insight to ion–carboxylate interactions and the spectroscopic intramolecular mechanism for the observed infrared frequencies, it has limitations in addressing hydration of the ion–carboxylate complex such that the aqueous phase is not fully captured. As infrared and Raman spectroscopy are not completely selective for informing or distinguishing between binding environments, including that of local hydration, a controversy still exists around the designation of the commonly called "ionic interaction" as either contact or solvent-shared ion pairing.

Divalent cation, Ca^{2+} and Mg^{2+}, binding to negatively charged functional groups has significant consequences in the structure and function of many systems of biological[96–102] and atmospheric interest.[21–29] In biology, Ca^{2+} and Mg^{2+} play important roles in ATP synthesis, cell proliferation, and receptor/target information pathways.[97,98,103–106] In addition to biological studies, the role of Ca^{2+} and Mg^{2+} in atmospheric aerosol chemistry is an important area of study. As bubbles burst at the ocean surface, aerosols are released to the atmosphere carrying with them enriched concentrations of surface-active organic molecules and inorganic ions. Despite its lesser concentration in bulk seawater (10 mM compared to 50 mM),[30,31] studies have shown that Ca^{2+} enrichment in sea spray aerosols is much higher than that of Mg^{2+}.[24,25] This likely reveals a favored binding of Ca^{2+} ions to negatively charged surfactant headgroups at the air–sea interface,[32] thus leading to increased transfer of calcium ions to the aerosol phase. The binding of Ca^{2+} and Mg^{2+} to the carboxylate headgroups of marine prevalent fatty acids such as palmitic acid (hexadecanoic acid) and stearic acid (octadecanoic acid) has significant effects on the organization and structure of organic films on sea spray aerosols thus impacting the climate properties of these particles.[22,24,25,29,33,34]

While this paper does not focus on calculating binding constants, prior solution and interfacial studies have been used to determine the binding constants of divalent metal cations to carboxylate groups.[25,107–113] Formerly, reported binding constants of Ca^{2+} and Mg^{2+} to short chain fatty acids in aqueous solutions have been shown to be identical.[114] While, the binding constants provide a numerical value of the number of bound species, it does not necessarily equate to the number of bound species in a particular binding motif. To our knowledge, experimental spectra of both solution and interfacial regimes coupled with calculations have not been used collectively to elucidate the ion pairing details, including that of local hydration, of divalent metal cations interacting with carboxylate groups. In this study, both solution and interfacial spectroscopies are used to obtain a detailed molecular picture of the binding coordinations of Ca^{2+} and Mg^{2+} to carboxylate to inform on contact versus solvent-mediated ion pairing. Prior literature has shown that Raman studies can provide carboxylate binding information about metal cations of different valencies,[115,116] although it is challenging to distinguish differences between metal cations of the same group without a priori information. Studies have shown that surface-sensitive techniques can extract additionally distinguishable spectral signatures of binding events between same-group cations and lipid headgroups. For example, same-group divalent cations have been shown to affect the stabilization of lipid monolayers by altering headgroup hydration despite their similar charge state and properties.[28,29,72,73,95,108,111,117–123] As the selection rules of IR and Raman spectroscopy result in the ability to observe different stretching vibrational modes (COO^- asymmetric in IR and COO^- symmetric in Raman), these two techniques used in surface and solution environments, respectively, provide a more complete picture of the vibrational landscape of our systems of interest.

This study offers structural and energetic insights on the binding motifs of the carboxylate group with the biologically and atmospherically relevant group II metal cations, Ca^{2+} and Mg^{2+}. The spectra of these cations with those of bare acetate and those of the strongly bound Zn^{2+} transition metal are compared;[91,124] zinc's covalent binding structure is established. To evaluate solution and interfacial effects, acetate in the aqueous solution phase and long-chain carboxylic acid monolayers for interfacial studies are investigated. Polarized Raman spectroscopy, coupled with deconvolution methods, to extract the free and ion-perturbed (contact and solvent-shared ion paired) carboxylate spectra are used. Free-energy and spectral calculations describe binding motifs and are compared against the Raman solution and infrared interfacial experiments. Calculations conducted by M. Baer at PNNL, are also used to elucidate the energy barrier for Mg^{2+} relative to Ca^{2+} for the number of first shell coordinated water molecules. Temperature studies track peak areas and frequencies to provide information on the hydration energetics of ion-bound populations. The interfacial infrared aqueous surface spectra, Raman solution spectra, and calculations reveal that Ca^{2+} and Mg^{2+} disclose unique $COO^-:M^{2+}$ spectral signatures, indicating both contact and solvent-shared binding environments for Ca^{2+}, yet dominantly the solvent-shared binding environment for Mg^{2+}.

3.2 Experimental Methods and Materials

3.2.1 Infrared Reflection–Absorption Spectroscopy Measurements

Deuterated palmitic acid (hexadecanoic-d_{31} acid, palmitic-d_{31} acid (C_{15}-COOH) >98%, Cambridge Isotopes Laboratories) was dissolved in chloroform (HPLC grade, Fisher Scientific) at a concentration of ~2mM and was spread dropwise onto the surface of a Petri dish containing 0.3 M solutions of $MgCl_2 \cdot 6H_2O$ (>99%, ACS Certified, Fisher Scientific), $CaCl_2 \cdot 2H_2O$ (>99%, ACS Certified, Fisher Scientific), or $ZnCl_2$ (>98%, Acros Organics) prepared in D_2O (99%, Sigma-Aldrich) at a 20.5 $Å^2$/ molecule mean molecular area. To remove various modes (CH_2 scissoring mode at ~1460–1470 cm^{-1} and the positive H_2O bending mode at ~1650 cm^{-1}) from the spectral region of interest in the infrared reflection–absorption spectroscopy measurements, deuteration of both the lipid chain and the subphase was necessary. The use of D_2O also leads to an increased intensity of the observed bands in the spectra due to changes in subphase optical constants and reflectivities, see **Figure 6**.[87]

A custom-built setup consisting of two planar gold mirrors placed in an FTIR spectrometer (Spectrum 100, PerkinElmer) was used to collect IRRAS spectra. The first gold mirror directs the incoming unpolarized IR beam to the sample surface at a 45° angle of incidence relative to surface normal. The second gold mirror then directs the reflected radiation to a liquid nitrogen cooled MCT detector. Adsorption of atmospheric water vapor to the D_2O surface can lead to HOD interferences in the spectra (**Figure 7**). To minimize such interference, the spectrometer chamber was purged with a constant flow of nitrogen and sealed with plastic during the course of the measurement. Each spectrum was collected over the range 4000–450 cm^{-1}, with 1 cm^{-1} step size, and resulted from co-averaging of 300 scans. The spectra presented here are the average of at least three individual trials which have been baseline corrected by a third-order polynomial prior to averaging. An example of a third-order polynomial fit (Appendix A **Figure 58**) used for baseline-subtraction of the IRRAS spectra is shown in Appendix A. IRRAS spectra are represented in units of reflectance–absorbance ($RA = -\log(R/R_0)$), where the R is the reflectance of the monolayer-covered surface, and the reflectance of the bare surface is R_0.

3.2.2 Raman Spectroscopy Measurements

Sodium acetate (($NaCH_3COO$),Sigma Aldrich) solution was dissolved in nanopure water with a resistivity of 18.2 MΩ•cm (Milli-Q Advantage A10, EMD Millipore, Billerica, MA, USA) at a concentration of 0.5 M. Metal carboxylate solutions were prepared by adding an appropriate mass of sodium acetate (Sigma-Aldrich) and either magnesium chloride ($MgCl_2 \cdot 6H_2O$), calcium chloride ($CaCl_2 \cdot 2H_2O$), or zinc(II) chloride ($ZnCl_2$) (Sigma-Aldrich) to a volumetric flask and completed with nanopure water to make a solution of 0.5 M $NaCH_3COO$:0.25 M $MgCl_2$, $CaCl_2$, or $ZnCl_2$. All solutions were sonicated to for ~5 min to assist dissolution. Both the 0.5 M $NaCH_3COO$:0.25 M $MgCl_2$ and 0.5M $NaCH_3COO$:0.25 M $ZnCl_2$ solutions were passed through a 0.2 μm Whatman syringe filter (Sigma Aldrich). The filter was prewetted with each particular solution to avoid changes in concentration. All salts were used without further purification. The solutions were equilibrated to room temperature.

The polarized Raman spectra were collected using custom-built polarized Raman spectrometer consisting of a 532 nm diode pumped CW laser with a built-in laser line (±0.5) and polarization filters (>100:1 V, Crystalaser). Excitation was directly coupled with a custom-built fiber optic polarized Raman probe (InPhotonics) allowing 235 mW power to the sample at a range of 90–4200 cm^{-1}. Two outputs of scatter light a parallel polarized (V) and a perpendicular polarized (H) were sent to two independent FC fiber-optic end ports. The polarized output ports were fiber coupled to a spectrograph with a 600 lines mm^{-1} grating. The wavelength was calibrated to He:Ne emission lines (IsoPlane 320, Princeton Instruments) and detected using a liquid nitrogen cooled CCD detector (Pylon, 1340 × 400 pixel, Princeton Instruments). The coupling of the two 200 μm core fibers directly to the spectrograph allowed simultaneous collection of the perpendicular (HV) and parallel (VV) polarized spectra. Experiments were performed at the different temperatures, 21, 25, 30, 40, 50, 60, 70, 80, and 85 ºC. Spectra were collected by signal averaging 300 spectra each with a 0.5 s integration time. The Raman spectra presented here are the average of at least three individual trials which have been baseline corrected by fitting two end points to a line prior to averaging.

3.3 Results and Discussion

3.3.1 The Air–Aqueous Interface

At the interface, ion–carboxylate binding events can be studied with surface-sensitive spectroscopy techniques. To this end, infrared reflection–absorption spectroscopy (IRRAS) was used to investigate the binding of Ca^{2+} and Mg^{2+} ions to carboxylic acids at the air–aqueous interface. IRRAS spectra were collected of deuterated C_{16} carboxylic acid (C_{15}-COOH) monolayers spread on the surface of metal chloride ($CaCl_2$, $MgCl_2$, $ZnCl_2$) salt solutions in D_2O. The monolayers were spread to a target mean molecular area (20.5 Å^2/molecule) to ensure full monolayer coverage of the aqueous interface. In this method of monolayer preparation, there are no external perturbations (i.e., continuous compression) acting on the surfactant molecules to create an unstable, elevated surface pressure. These systems represent relaxed surface environments whose molecular organization can be more appropriately compared to their aqueous solution counterparts.

Divalent ions induce the spontaneous deprotonation of long-chain carboxylic acid monolayers at the air–aqueous interface, as has been reported extensively in the literature,[9,29,32,45,72,74,86,92,120]. The COO^- stretching region of the IRRAS spectra is shown in **Figure 8**, demonstrating the ion-induced deprotonation of the C_{15}-COOH monolayers. The predominant feature in these spectra is the asymmetric stretch (ν_{AS}) of the COO^- group between 1500 cm^{-1} and 1625 cm^{-1}.[29,125] The intensity of the COO^- symmetric stretch (ν_S) is weak in infrared measurements but can be seen at ~1425 cm^{-1}. Noise is greater around the ν_S mode due to its proximity to the region in which HOD interference is severe (1500–1200 cm^{-1}).[126]

Analysis of the carboxylate ν_{AS} mode for Ca^{2+} and Mg^{2+} solutions in **Figure 8**, uncovers unique ion-perturbed $COO^-:M^{2+}$ spectral signatures. The various degrees of broadening reveal the presence of multiple binding environments between the metal ions and carboxylate groups. The ν_{AS} mode of the C_{15}-$COO^-:Mg^{2+}$ spectrum is centered at 1557 cm^{-1} and can be described as having asymmetry with greater intensity at higher frequencies. This spectrum is nearly identical to that of the bare carboxylate mode of a spread C_{18} monolayer (C_{17}-COOH, stearic acid, octadecanoic acid) on a basic D_2O subphase previously reported in the literature,[95] thus highly suggestive of a largely hydrated, or solvent-mediated, binding environment.

The spectrum of C_{15}-COO^-:Ca^{2+} displays a broad ν_{AS} mode centered at 1551 cm^{-1}. This ν_{AS} mode extends to lower frequencies and shows a second band with significant intensity at approximately 1526 cm^{-1} that is not strongly present in the C_{15}-COO^-:Mg^{2+} spectrum. The binding of Zn^{2+} ions to carboxylate groups has been well studied and is characterized as a direct, chelating bidentate contact ion pair,[91,127] as such the spectrum of C_{15}-COO^-:Zn^{2+} is employed as a reference for spectral features associated with the more direct contact ion binding motif. Upon comparison of the C_{15}-COO^-:Ca^{2+} spectrum to the corresponding spectrum of C_{15}-COO^-:Zn^{2+}, it can be seen that the lower frequency region of the C_{15}-COO^-:Ca^{2+} complex directly overlays that of the C_{15}-COO^-:Zn^{2+} complex centered at 1529 cm^{-1}. The broadness of the ν_{AS} mode in the C_{15}-COO^-:Ca^{2+} spectrum to frequencies representative of the more direct binding motif similar to that of C_{15}-COO^-:Zn^{2+} provides evidence to the presence of the differences in binding motifs that exist between the Ca^{2+} and Mg^{2+} ions and carboxylate groups at the air–aqueous interface. Based on the spectral responses in these systems, we claim, and later show additional evidence, that some fraction of C_{15}-COO^-:Ca^{2+} ion pairs exist as contact ion pairs in monodentate and/or bidentate geometries in addition to those complexed as solvent-shared ion pairs, whereas C_{15}-COO^-:Mg^{2+} ion pairs are primarily solvent-shared. To gain further insight into the coordination differences between Ca^{2+} and Mg^{2+}, this study turns to investigate these ion-perturbed carboxylate systems in bulk solution with Raman spectroscopy.

3.3.2 Solution Studies of Acetate

Polarized Raman spectroscopy was used to elucidate the binding motifs and local hydration of Ca^{2+} and Mg^{2+} to acetate in aqueous solutions of $CaCl_2$ and $MgCl_2$, respectively. For an individual aqueous metal acetate solution, the raw measured Raman spectrum includes features from both the ion-perturbed and free acetate, as well as the water molecules that are influenced by each of these species (**Figure 9a** and **9b**). In all solutions, the intensities of the ν_S C–C (**Figure 9a**) and ν_S COO^- mode **(Figure 9b**) exhibit differences from that of acetate in pure water. Ben-Amotz and coauthors show that ν_S C–C and ν_S COO^- bands of sodium acetate do not change as a function of concentration and that Na^+ has an insignificant inference on water structure up to 2 M.[114] Thus, sodium acetate was chosen as the bare acetate spectrum due to the lack of frequency shifts and its solvent-separated complexation of $COO^-:Na^+$.[128] Such a lack of frequency shifts does not imply that Na^+ cannot bind to carboxylate, since it has a binding affinity but simply it cannot be spectrally observed. Similarly, to the IRRAS data, the corresponding Zn^{2+} spectrum is obtained as a comparison to the studies of Ca^{2+} and Mg^{2+}. There is no doubt that charge transfer occurs with Zn^{2+} as opposed to Ca^{2+} and Mg^{2+}. The Zn^{2+} spectrum shows the largest intensity change in both the ν_S C–C and ν_S COO^- modes, implying that the Zn^{2+} ion interacts more strongly with acetate, as is expected due to the 4s and 4p orbitals accepting the charge, thus leading to contact ion pairing.[91,109,110,114,129] The presence of Zn^{2+} in solution (**Figure 9a** and **9b**) clearly causes a blue shift in both modes (935.3 to 939.9 cm^{-1} and 1424.7 to 1427.6 cm^{-1}, respectively) and a suppression of the Raman transition moment strength representative of direct-contact ion pairing.

It is clear that Ca^{2+} produces a slightly larger intensity change for the νs C–C and νs COO^- than Mg^{2+} that can be attributed to the differences in binding environments. However, these changes are very small compared to those of Zn^{2+}, thus making ion-pairing assignments a challenge without further analysis of the spectra. Through deconvolution methods the spectrum of the bare acetate was removed from the COO^- :M^{2+}spectra (process described more thoroughly in Ion-perturbed Acetate Spectra section below) and extracted only the ion-perturbed carboxylate spectra associated with each divalent cation as shown **Figure 9c** and **9d**. While the acetate:Zn^{2+} spectrum clearly shows the most dramatic change upon deconvolution due to the large fraction of covalently linked contact ion pairs in solution, the ion-perturbed carboxylate spectra of Ca^{2+} and Mg^{2+} complexes clearly show differences from each other, thus demonstrating variation in binding environments between Mg^{2+} and Ca^{2+} ions with acetate in solution. It is noticed that the νs COO^- mode associated with Ca^{2+} tracks with the acetate:Zn^{2+} spectrum yet shifts to higher frequencies and is broader than that of acetate:Mg^{2+}, indicative of an additional population of contact ion pairs with Ca^{2+}. While the deconvoluted spectra point to differences between Ca^{2+} and Mg^{2+},solution Raman spectra alone may not necessarily be able to identify different ion pair structures. Multiple states contribute to the full spectrum, where some can be subtracted but the remainder constitutes an averaged ensemble in which ion pairs are weighed by their free energy.

Thus, considering the interfacial spectra results as well as computational approaches can aid in identifying most probable ion pair structures.

3.3.3 Ion-Perturbed Acetate Spectra

Extracting the ion-perturbed acetate spectra from COO^{-}:M^{2+} (M^{2+}= Ca^{2+}, and Mg^{2+}) aqueous solution spectra is quite important since little is known about the specific effects derived from ion-perturbation and the resulting band shape differences. Raman spectra of the aqueous solutions were decomposed to obtain a minimum area of non-negative bands in the spectra; these resulting spectra contained only the vibrational features arising from the solute and not from the water molecules that perturbed the solution. All the ion-perturbed Raman spectra, **Figure 9a** and **9d**, and **Figure 10** were normalized to the bare acetate COO^{-} band area. This normalization was performed by calculating a normalization ratio between the bare acetate and the COO^{-}:M^{2+} spectra at the COO^{-} frequency (1423.8 cm^{-1}). Then the bare acetate spectrum was multiplied by this normalization factor. The resulted spectrum was then subtracted from the COO^{-}:M^{2+} spectrum, thereby obtaining a set of spectra as shown in **Figure 10a** and **10b**, where the zero intensity is observed at 1423.8 cm^{-1}. In these series of spectra, both positive and negative peaks were observed, thus, to produce only positive peaks the factors were altered until not negative peaks were shown, **Figure 10c** and **10d**. In other words, the free acetate was removed from the $COO^{-}$$M^{2+}$ solution spectra giving the resultant ion-perturbed spectra. This deconvolution effectively removes any free acetate contributions to the COO^{-}:M^{2+} solution spectra.

3.3.4 Non-Coincidence Effect

To further elucidate hydration effects, polarized versus depolarized Raman spectra were evaluated in terms of the non-coincidence effect. Non-coincidence refers to the difference in frequency between the anisotropic and isotropic parts of the Raman scattering[130–134] and can provide insight into the binding motifs. The non-coincidence effect is a result of resonant transfer of vibrational excitation energy between the molecules coupled by hydrogen bonds, permanent dipole moments, or any other interactions.[133] Prior studies have shown that hydrogen bond formation decreases the non-coincidence effect values where negative values can also be observed.[132,133,135] **Figure 11** shows the convoluted (free + ion-perturbed) and deconvoluted (ion-perturbed) spectra in both polarizations. Here, I_{VV} (incident light and scatter light are at 90°, both polarized vertically) and I_{VH} (incident light is polarized vertically and scattered light is polarized horizontally) were used rather than I_{iso} ($I_{iso} = I_{VV} – (4/3)I_{HV}$) and I_{aniso} ($I_{aniso} = (4/3)I_{HV}$), which affects the intensity of the band and not its spectral position or frequency. The spectra show a larger frequency shift in I_{VH} polarization than in I_{VV} polarization that is observed in both the free + ion-perturbed and ion-perturbed spectra. The frequencies of each cation of the I_{VV} and I_{VH} are plotted in **Figure 12** (spectra shown in **Figure 11**; and difference in **Figure 13**) revealing that Mg^{2+} is the most resistant to changes in frequency, consistent with full hydration. The chemical environment and symmetry of the fully hydrated solvent-shared ion pair give rise to relatively no deviation in frequency between the two polarization conditions, consistent with a steadfast hydrogen bonding environment around the Mg^{2+} ions. Zn^{2+} shows a frequency change because as the carboxylate binds to zinc the water-hydrogen-bonding network changes. Hydrogen bonding is disrupted as the ion sheds some of the solvating water molecules in order to bind with the carboxylate; therefore, an increase in the non-coincidence value is observed. Lastly, a plausible explanation for why the Ca^{2+} frequency differences are the largest is because Ca^{2+} is more labile across two regimes: solvent-shared (fully hydrated) and contact ion paired.

Taking the deconvoluted Raman spectra, the fractions of solvent-shared, monodentate, and bidentate configurations could not be determined; however, the percentage of acetate molecules that are perturbed by an ion–carboxylate interaction in solvent-shared and, more generally, contact ion configurations can be estimated. During the deconvolution process, a normalization factor representing the percentage of the free acetate in the COO^{-}:M^{2+} spectra was calculated between the bare acetate and the COO^{-}:M^{2+} spectra at the COO^{-} frequency (see section 3.3.3). The remaining percent out of 100% represents the percent of acetate species in an ion-perturbed environment, as shown in **Figure 14a**, 12 % for Mg^{2+} and 17% for Ca^{2+}, presenting COO^{-}:Zn^{2+} as a reference for a more directly bound system as previously discussed.

For the surface measurements, as this work is investigating an initially protonated long-chain carboxylic acid monolayer, the full ion-induced deprotonation observed in **Figure 8** would correspond to 100% of carboxylate groups existing in an ion-perturbed environment. As the infrared measurements only show ion-induced deprotonation, 100% of the spectral response is associated with an ion-perturbed system (solvent-shared and contact ion paired) at the interface. A similar analysis can be conducted to the solution phase studies yet instead specifically determine the percent of carboxylate groups in a contact ion paired binding motif. Briefly, the area of the ν_{AS} mode between 1500 and 1625 cm^{-1} in the spectrum of fully deprotonated stearic acid (C_{17}-COOH) on a basic D_2O subphase (**Figure 66**, Appendix A) was used as a reference of the spectral response of a fully solvated carboxylate mode. This area was then subtracted from the area of the ν_{AS} mode associated with the C_{15}-COOH monolayers on Mg^{2+} and Ca^{2+} solutions. Any remaining spectral area is attributed to a contact ion pair spectral response. This area is then normalized to the total area to yield an approximate percent of contact ion paired carboxylate species at the interface. For Mg^{2+}, an estimated 100% of ion-deprotonated carboxylate groups at the interface exist in a solvent-shared environment, whereas in Ca^{2+} solutions, approximately 18% of species exist in a contact ion pairing geometry (**Figure 14b**). For comparison, the result for Zn^{2+} contact ion pairs are also shown for which a similar analysis was conducted between 1500 and 1580 cm^{-1}. While the Raman and IRRAS analyses produce two different insights into ion complexation (ion-perturbed vs contact ion specifically), both the solution and surface measurements agree that carboxylate groups are more so mediated by water with Mg^{2+} compared to Ca^{2+}, thus suggesting a greater fraction of species in a solvent-shared binding motif.

3.3.5 Frequency Calculations

While the previously described Raman and surface IR experiments provide experimentally observed changes in the binding of divalent cations to carboxylic acids and carboxylate ions, an assignment of the complex structure is difficult. Particularly, spectra alone do not provide enough information to distinguish completely between the three different types of metal–carboxylate ion pairs: monodentate, bidentate, or solvent-shared ion pairs. Mono- and bidentate structures are contact ion pairs, whereas solvent-shared ion pairs possess one water molecule that is coordinated to the cation and also hydrogen bonded to the carboxylate. Spectral calculations conducted by M. Baer at PNNL were performed to determine the spectral shift that is induced upon ion binding; ensemble frequencies based on quantum density functional theory (DFT) were computed. Here, spectral signatures were calculated for ensembles of structures corresponding to one of the three different ion pairs based on molecular dynamics simulations (MD). The simulation lengths using DFT MD do not allow for a sampling of transitions between the three ion pairs and estimate of their relative population. The relative population is calculated using umbrella sampling; see Vazquez de Vasquez *et al.*[136]

Frequencies for the acetate in the three binding motifs for Ca^{2+}, Mg^{2+}, Zn^{2+} were calculated for a large number of snapshots extracted from DFT MD (see Vazquez de Vasquez *et al.*[136] for details). The influences on the C–C stretch and the symmetric COO^- stretch as probed by Raman solution spectra have been discussed in detail in the literature following a similar approach.[114] It can be assumed that the observed C–C stretch band deviates from the unperturbed reference (940 cm^{-1}) the closer the cation is to the acetate. In line with this, we see that the frequencies for the solvent-shared ion pairs (for all cations) are not significantly affected yet they are blue-shifted for the contact ion pairs. This shift is more pronounced for Zn^{2+} and Mg^{2+} than Ca^{2+} and is larger for the bidentate than the monodentate ion pairs.

As discussed above, the surface IR spectra show a more pronounced effect for the asymmetric stretch of the deprotonated, ion-complexed carboxylic acid relative to the solution spectra. To elucidate the underpinnings of the spectral differences between Ca^{2+} and Mg^{2+} binding**,** a comparison of the computed and experimental frequencies is shown in Vazquez de Vasquez *et al.*[136] The observed shifts in the asymmetric stretch with Ca^{2+} have been discussed in detail in Denton *et al.*[95] All three binding motifs show distinct spectra, where the solvent-shared pair is blue-shifted, the monodentate is not shifted with respect to the free acetate, and the bidentate is red-shifted. Based on free-energy calculations, we assert that the Ca^{2+} is directly coordinated in mono- and bidentate contact ion pairs as well as solvent-shared pairs. Interestingly, for Mg^{2+}, a red shift for the solvent-shared ion pair with respect to the free acetate and a blue shift for the monodentate is observed. Unlike for Ca^{2+}, the monodentate structure is estimated to be dominant for Mg^{2+},[114] and the bidentate is not significantly populated for the used DFT functional. The resulting spectra for the bidentate is very broad, spanning the range from 1500 to 1550 cm^{-1}. The calculated frequency of the monodentate structure matches the position of the experimental maximum for the Mg^{2+}. The Zn^{2+} bound spectra show a consistent red shift for all three moieties, increasing from the solvent-shared ion pair to the monodentate and largest for the bidentate. Even though the calculated bidentate structure is very broad, the maximum aligns well with the experimental maximum observed. We note that the intensity of ensemble frequencies corresponds to the probability of this frequency to be observed for a given structure. For a direct comparison with experimental intensities, this frequency distribution needs to be weighted by the probability of the structure and the transition dipole moment for IR.

The number of water molecules interacting with ions of size of the solvated complex (ion and first shell water molecules) is shown to correlate with the experimentally determined Jones–Dole B coefficient.[137] The B coefficient is interpreted as the strength of the ion water interaction. In line with the larger barrier calculated for the water exchange for Mg^{2+} compared to Ca^{2+}, the experimental B coefficient for Mg^{2+} is larger than that for Ca^{2+}.[138] Even though both ions are of similar size, an interesting temperature dependence is observed. The B coefficient is changing linearly with increasing temperature for Ca^{2+}, but for Mg^{2+}, a sudden change in slope is observed for temperatures over 30 °C. This might indicate that the barrier for water exchange is temperature dependent.

3.3.6 Temperature-Dependent Acetate Solution Studies

In order to gain more information with respect to the energetics of binding motifs among divalent cations to carboxylate, Raman temperature-dependent measurements were implemented over a large temperature range (20–85 °C). The main goal for these temperature studies was to reveal the energy (temperature) needed for Mg^{2+} to shed one of its hydrating waters and form a direct contact ion pairing with aqueous carboxylate. Changes in frequency and peak area of the deconvoluted ion-perturbed carboxylate spectra were monitored. **Figure 15** shows the changes in frequency of the ion-perturbed ν_S COO^- mode as a function of temperature. Results show a red frequency shift for all solutions as temperature is increased, due to either the disorder induced by the increase in temperature and/or the weakening of ion-water bonds.[139,140] A frequency difference of ~14 cm^{-1} between bare acetate and the ion-perturbed ν_S COO^- mode is clearly observed. The large frequency splitting between the ion-perturbed and the bare acetate spectra is due to the impact of bringing an ion close to the carboxylate. Desolvation also plays a role. As temperature is increased, the enhanced low frequency rattling motion of the ion in and out of proximity to the carboxylate results in a coupling and a frequency lowering of the ν_S COO^- mode. With bare acetate as the temperature is increased, minimal frequency lowering is observed as the coupling of the carboxylate mode to the water rattling motion is far less than that of a doubly charged ion.

Changes or differences in peak area of the ν_S COO^- mode can shed light on the strength of the binding interactions between the divalent ions and carboxylate.[114] **Figure 16** shows the peak area of the ion-perturbed ν_S COO^- mode of acetate in $CaCl_2$ (red) and $MgCl_2$ (blue) solutions. The peak area analysis reveals that at 21 °C both acetate:Ca^{2+} and acetate:Mg^{2+} complexes have the same peak area, suggesting a similar binding environment. However, as the temperature is increased, the peak area of the acetate:Ca^{2+} complex increases more than that of acetate:Mg^{2+}, suggesting possible differences in the amount of carboxylate being perturbed by the metal ion at that particular temperature. The increase in peak area of the ion-perturbed spectra with increasing temperature, which includes information on the fwhm, is correlated to an increase in the bound population. Two slopes for the acetate:Mg^{2+} spectra are also observed. From 10 to 30 °C, no peak area increase is noted; however, after 30 °C a positive slope is observed, indicative of an increase in the number of binding events and correlating with reported changes in the

Jones–Dole B coefficient as described previously, whereas the acetate:Ca^{2+} spectra show only one positive slope, indicating behavior that is not temperature sensitive. For both the Mg^{2+} and Ca^{2+} spectra, the slopes are similar for temperatures above 30 ^{o}C.

3.4 Conclusions

Infrared reflection–absorption spectroscopy, polarized Raman, and theoretical calculations,[136] were used to determine the role of hydration in ion–carboxylate binding in both solution and interfacial aqueous environments. Interfacial studies reveal differentiable spectral responses of the ion–carboxylate complexation. Two bands appear in the infrared reflection spectra strongly suggesting that a significant fraction of C_{15}-COO^{-}:Ca^{2+} bound complexes exist as contact ion pairs in monodentate and/or bidentate geometries in addition to those determined as solvent-shared ion pairs, whereas C_{15}-COO^{-}:Mg^{2+} complexes appear to primarily exist as solvent-shared ion pairs, i.e., C_{15}-COO^{-}: H_2O : Mg^{2+}. To understand more generally the binding motifs, the simpler acetate solution using Raman spectroscopy was further studied. Free and ion-perturbed carboxylate spectra of acetate:M^{2+} solutions were extracted through spectral deconvolution methods. The ion-perturbed carboxylate spectra of acetate:Ca^{2+} and acetate:Mg^{2+} are significantly different, demonstrating variance in binding environment between both ions in acetate aqueous solution, albeit to a lesser extent to the trend observed at the interface. Moreover, analysis of the non-coincidence effect from polarized (and depolarized) Raman spectra revealed hydration differentiation of Mg versus Ca and Zn binding motifs, i.e., solvent-shared versus contact ion pairing, respectively. The invariability of the frequency of the magnesium–acetate system indicates a constant hydrogen bonding environment consistent with solvent sharing. However, large frequency differences between polarization conditions for both calcium and zinc ions demonstrate dehydration, thus indicating contact ion pairing. Importantly, it is noted that the interfacial environment is more efficient at binding both magnesium and calcium ions than in the solution phase environment. Calculations (by M. Baer (PNNL)) highlight the differences in the solvation structure of both ions and its effect on the binding of Ca^{2+} and Mg^{2+} to acetate. According to the potential mean force calculations , the large barrier for water exchange around Mg^{2+} has a large impact on the populations of ion binding motifs. Comparison of calculated spectra for Mg^{2+} and Ca^{2+} with both solution phase Raman and surface infrared reflection spectra leads to the picture in which Mg^{2+} is dominated by solvent-shared ion pairs.

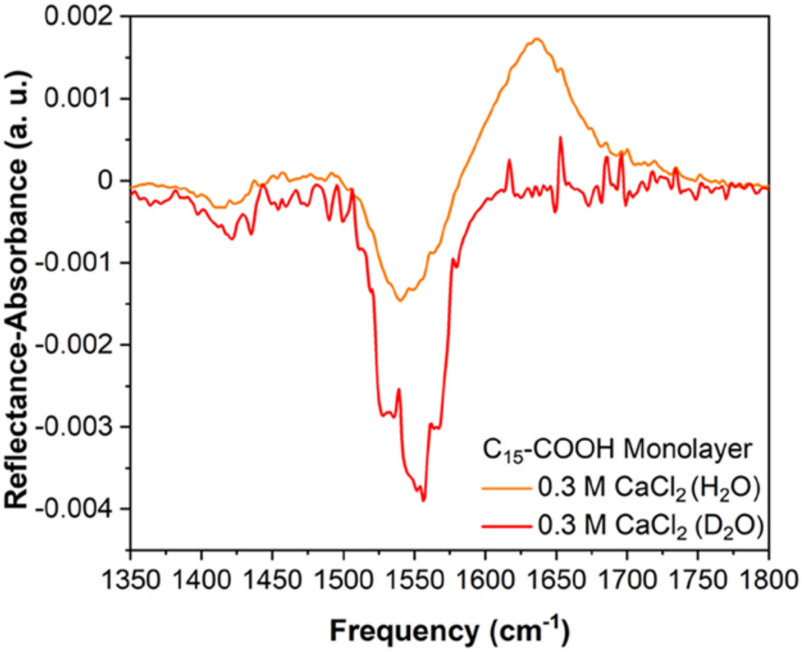

Figure 6. IRRAS spectra of deuterated C_{15}-COOH monolayers on 0.3 M $CaCl_2$ in water (orange) and in D_2O (red). Deuterated of both the lipid chain and the subphase removes various modes (CH_2 scissoring mode at ~1460–1470 cm^{-1} and the positive H_2O bending mode at ~1650 cm^{-1}) from the spectral region in interest in the IRRAS measurements. D_2O leads to an increase in intensity (larger negative response) of the observe bands in the IRRAS spectra due to changes in subphase optical constants and reflectivities data collected by B. Wellen Rudd.

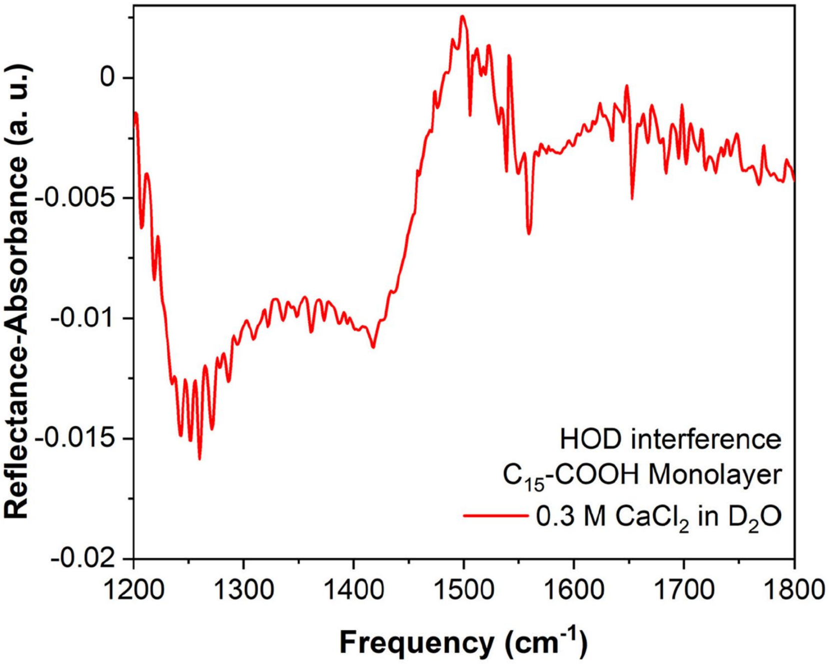

Figure 7. IRRAS spectrum of deuterated C_{15}-COOH monolayer on 0.3 M $CaCl_2$ in D_2O showing that adsorption of atmospheric water vapor to the D_2O surface can lead to HOD interferences in the spectra. Thus, to minimize such interferences the spectrometer chamber must be purged with constant flow of nitrogen and sealed with plastic during the course of the measurement, data collected by B. Wellen Rudd.

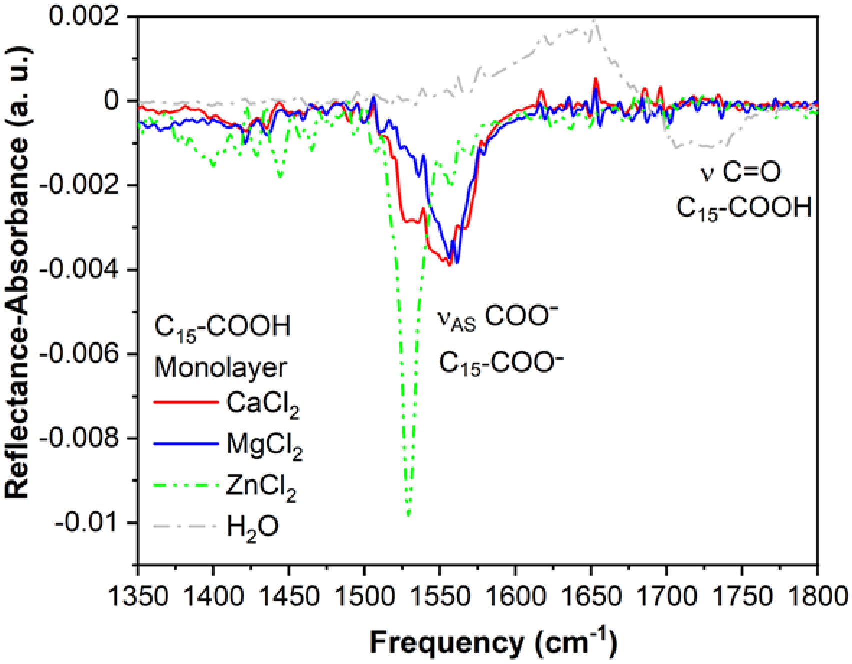

Figure 8. Infrared reflection spectra of deuterated C$_{15}$-COOH monolayers (20.5 Å^2/molecule) on 0.3 M solutions of CaCl$_2$ (red) and MgCl$_2$ (blue) in D$_2$O revealing ion-perturbed spectral responses of the ν$_{AS}$ COO$^-$ mode. The spectrum of the monolayer on a ZnCl$_2$ solution (green, dotted) is also shown for comparison and overlays the significant second band within the ν$_{AS}$ mode in the CaCl$_2$ spectrum. The spectrum of a C$_{15}$-COOH monolayer on pure water (H$_2$O) is shown for comparison to demonstrate the lack of the COO$^-$ mode when the monolayer is protonated. Additionally, the C═O stretch of the protonated carboxylic acid monolayer is not present in the ion-deprotonated spectra. The water bending mode at 1650 cm^{-1} is eliminated with the use of D$_2$O subphases data collected by B. Wellen Rudd.

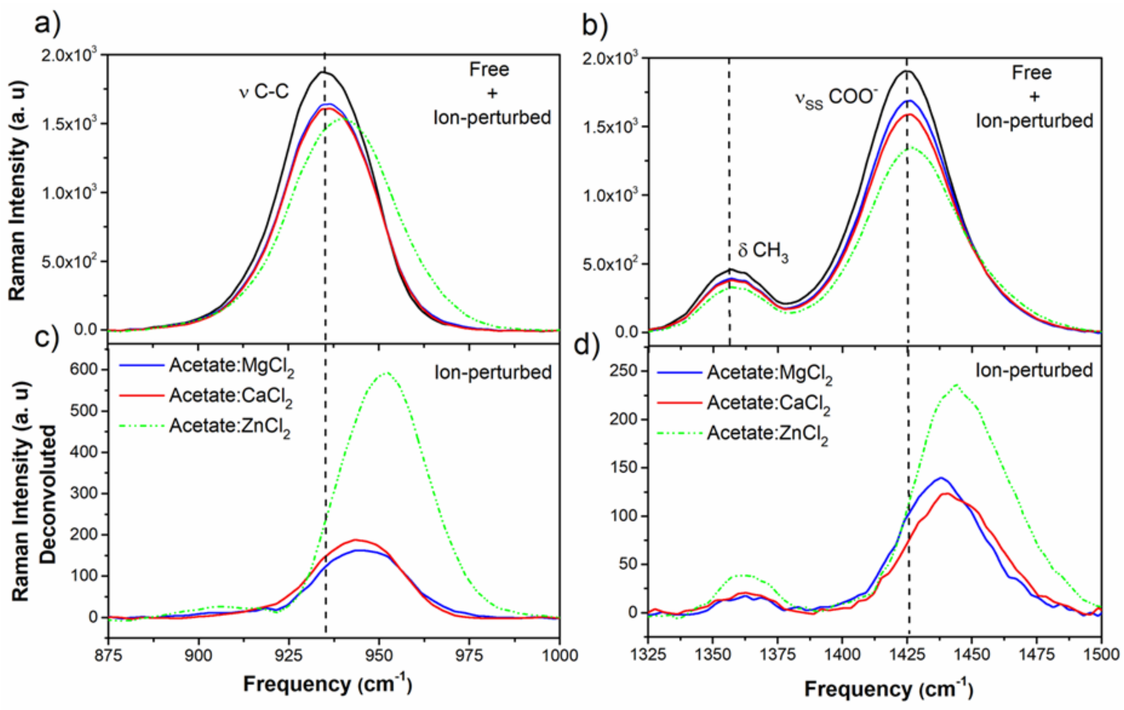

Figure 9. Polarized Raman spectra of the (a) ν_S C–C stretching mode and (b) ν_S COO^- symmetric stretching mode of acetate in 0.25 M solutions of $MgCl_2$ (blue), $CaCl_2$ (red), $ZnCl_2$ (green dotted), and water (black, bare acetate) at 21 ºC. Dashed lines are drawn at the frequency of acetate in pure water for both ν_S C–C and ν_S COO^-. Upon the addition of salt, the intensity of these modes decreases in all solutions. The presence of Zn^{2+} ions in solution causes a significant blue shift of the modes, whereas the frequency of the modes is less affected by Ca^{2+} and Mg^{2+}. The deconvoluted polarized Raman spectra (c) and (d) show the ion-perturbed acetate systems associated with Zn^{2+}, Ca^{2+}, and Mg^{2+} in which frequency and intensity differences are more apparent for all ions.

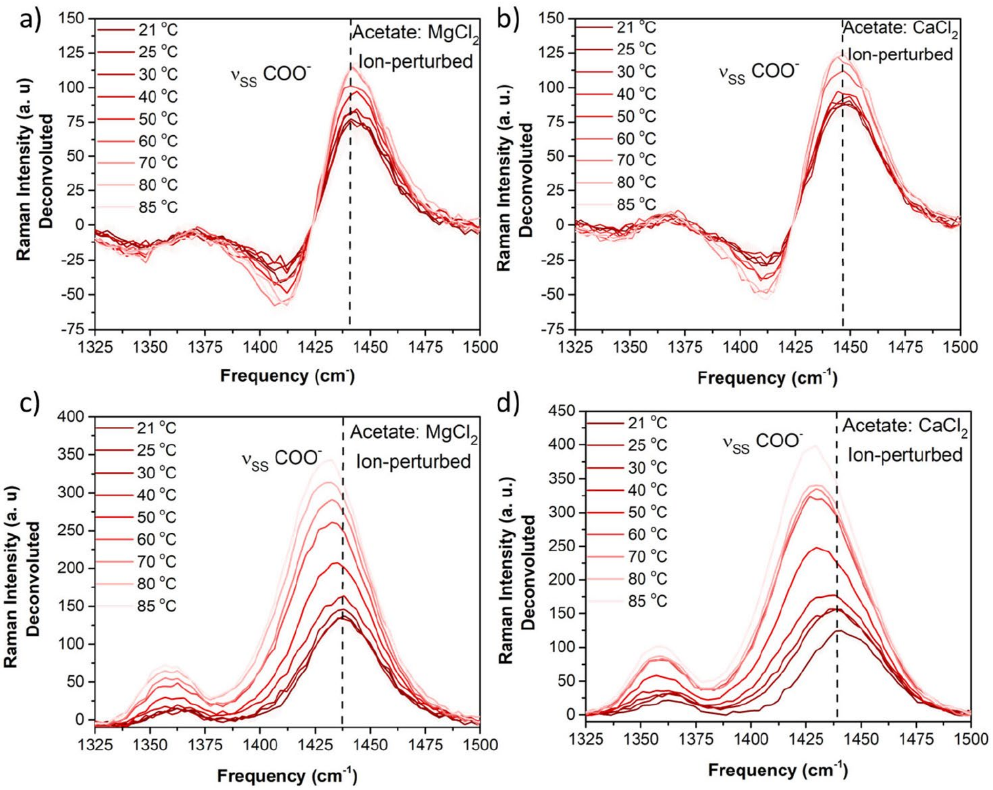

Figure 10. Deconvoluted ion-perturbed acetate spectra of Mg^{2+}, (a) and (c) , and Ca^{2+} (b) and (d), as a function of temperature. The spectra were normalized by performing a curve deconvolution method to the bare acetate. (Curved deconvolutions in this instance refers to producing only positive peaks, so factors were altered until no negative peaks were observed). The ion-perturbed acetate intensity increases and the frequency red shifts as the temperature increases suggesting that as the energy is added to the system more ion-perturbed acetate signal is observed. The frequency of the ion-perturbed acetate is higher in frequency than that of the bare acetate. In addition, the frequency of the ion-perturbed moves to lower frequencies as temperature increases.

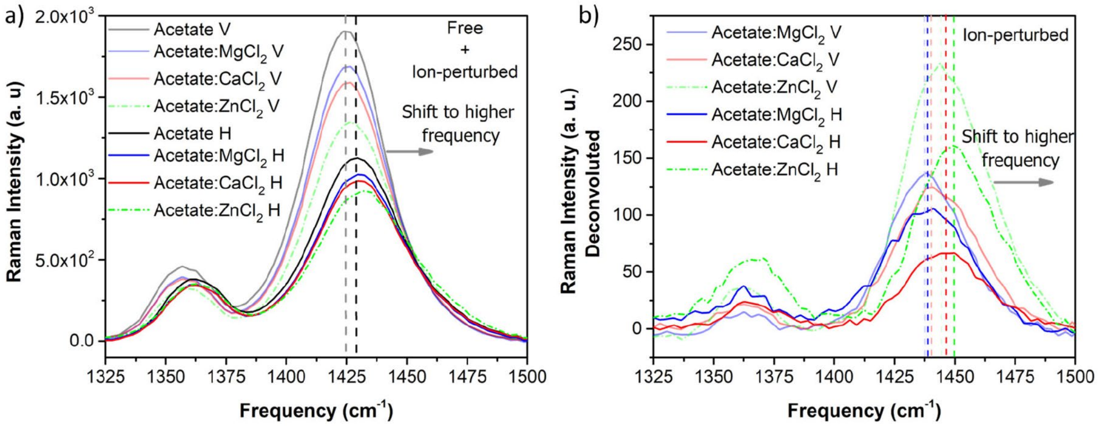

Figure 11. (a) Polarized Raman spectra of acetate COO^- symmetric stretch mode form 0.25 M solutions of $MgCl_2$ (blue), $CaCl_2$ (red), and $ZnCl_2$ (green dotted) at 21 ºC of the I_{VV} (transparent, light shades) and I_{HV} (bold, darked shades). A dashed line is drawn at the frequency of acetate in pure water (black) to guide the eye. The presence of Zn^{2+} ions in solution causes a blue shift of the mode whereas the frequency of ν_S is relatively unaffected in the $MgCl_2$ and $CaCl_2$ solutions. Because of the small changes in frequency and intensity, a deconvolution process of the ion-perturbed acetate to the divalent cation was performed. The deconvoluted spectra (b) show the calculated ion-perturbed acetate for each divalent cation. Here we observe more clearly the differences in frequency among the divalent cations, in particular for Ca^{2+} and Mg^{2+}. These deconvoluted spectra show the I_{VV} ((transparent, light shades) and I_{HV} (bold, darked shades). The Mg^{2+} spectra show the smallest change with frequency between both polarizations whereas Ca^{2+} shows the largest change.

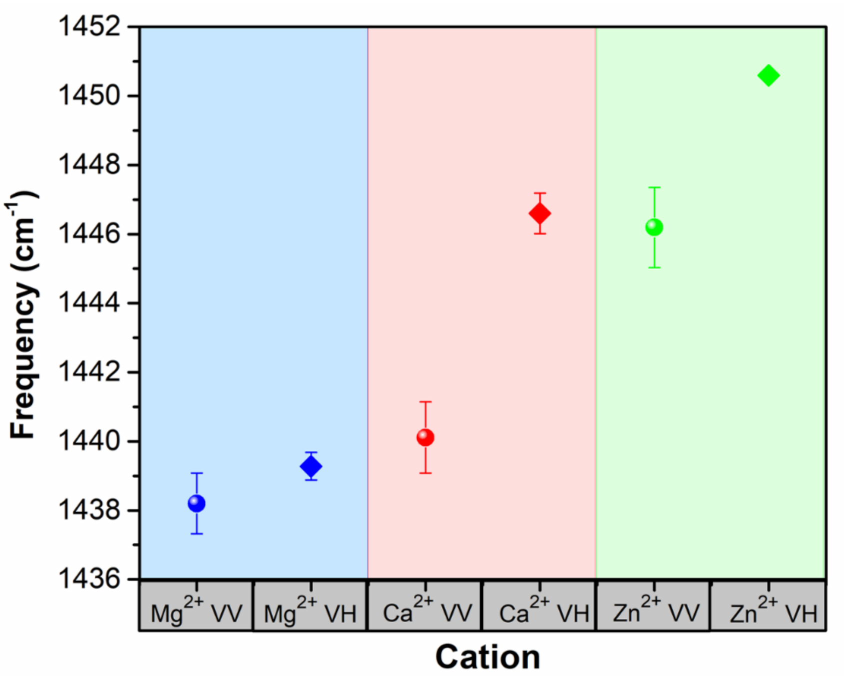

Figure 12. COO$^-$ ion-perturbed frequency of I_{VV} and I_{VH} as a function of the cations in their respective VV/HV polarization. There is a negligible frequency change of ~1 cm^{-1} between I_{VV} and I_{VH} for Mg^{2+},whereas Ca^{2+} shows the largest change in frequency of ~6.5 cm^{-1}. Zn^{2+} is shown as a comparison as a bidentate motif showing a difference of ~4.4 cm^{-1}. Hydrogen bonding perturbations are captured in the frequency differences. Disruption of the H-bonding network is revealed through non-coincidence of the Raman polarized (VV) versus depolarized (VH) frequencies.

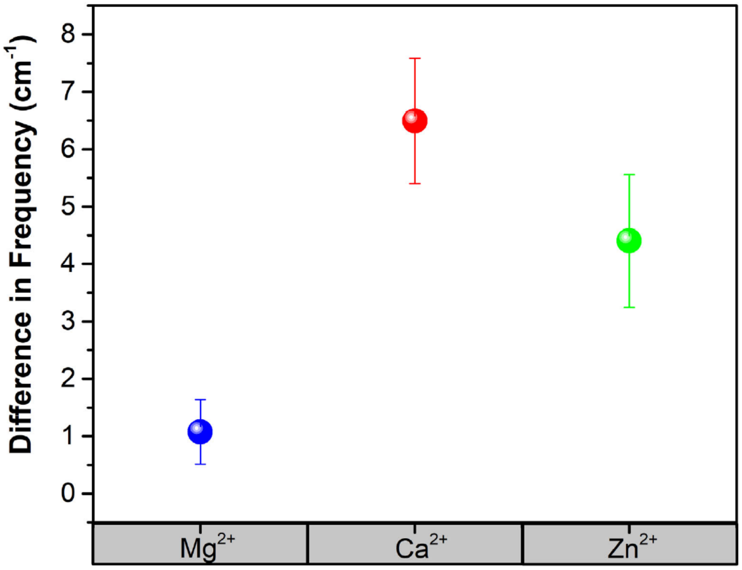

Figure 13. Non-coincidence effect value of the COO$^-$ symmetric peak for the Mg^{2+} (blue), Ca^{2+} (red) and Zn^{2+} (green).

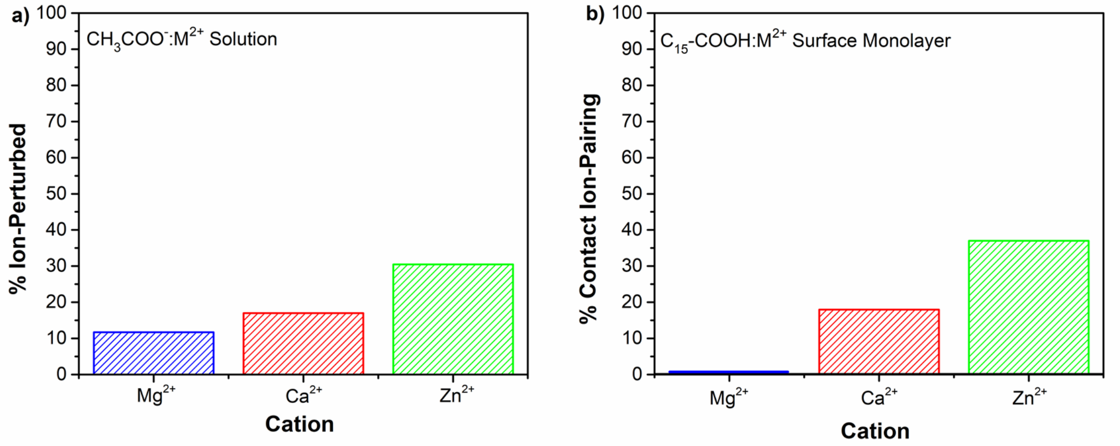

Figure 14. Comparison of a) the percentage of carboxylate species that are ion-perturbed either as solvent-shared or contact ion paired in solution, b) the percentage of carboxylate groups that are specifically contact ion paired at the interface.

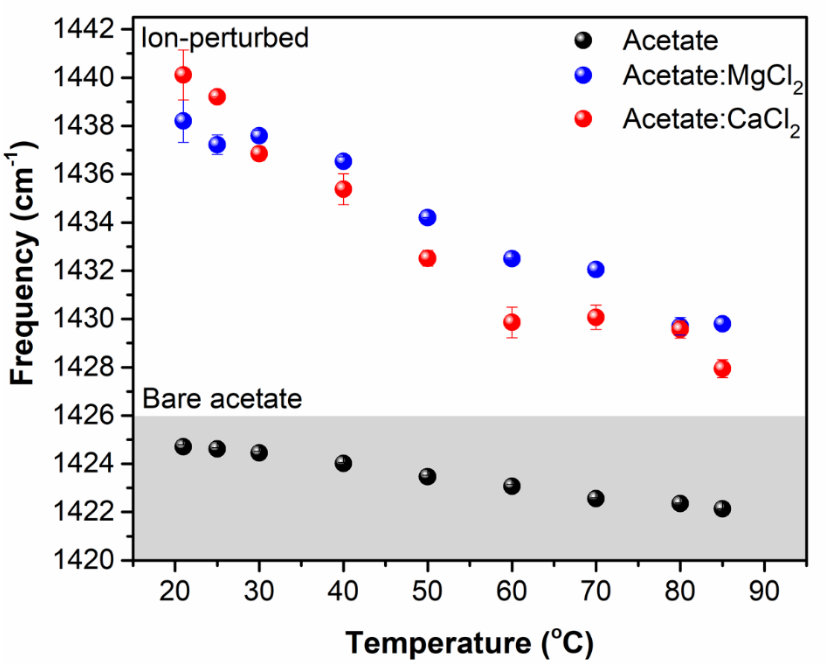

Figure 15. Raman spectral differences in frequency of the bare acetate COO$^-$ symmetric stretching mode (black) versus the ion-perturbed acetate systems of 0.25 M solutions of MgCl$_2$ (blue), and CaCl$_2$ (red) as a function of temperature. The ion-perturbed systems are referred to the deconvoluted spectra which are the result after subtraction of the bare acetate; see section 3.3.3 for details on the deconvolution process. There is a large difference in frequency between the bare acetate and the ion-perturbed spectra due to the influence of bringing an ion close to the carboxylate.

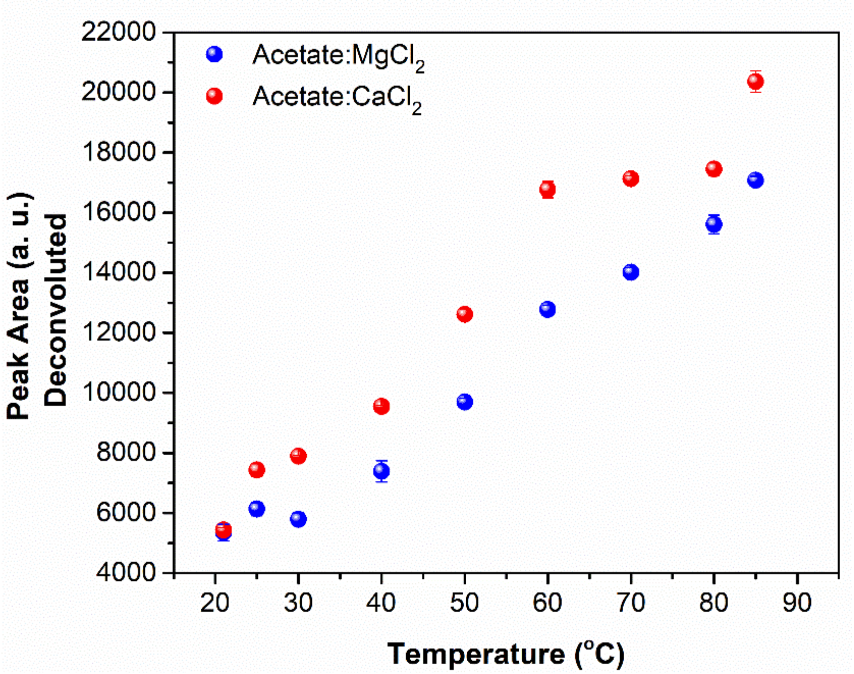

Figure 16. Peak area of the metal acetate after deconvolution of the ion-perturbed acetate as a function of temperature. This peak area increase of the ion-perturbed spectra includes information on the fwhm which can be correlated to an increase in the bound population of the metal ion.

Chapter 4. Hydration and Hydrogen Bond Order of Octadecanoic Acid and Octadecanol Films on Water at 21 °C and 1 °C

Reproduced in part with permission from Vazquez de Vasquez, M. G.†; Carter-Fenk, K. A.†; McCaslin, L. M.; Beasley, E. E.; Clark, J. B.; Allen, H. C. "Hydration and Hydrogen Bond Order of Octadecanoic Acid and Octadecanol Films on Water at 21 ºC and 1 ºC." *J. Phys. Chem. A*, **2021**, *125*, 46, 10065-10078.

4.1 Introduction

Fatty alcohol and fatty acid monolayers are relevant in ocean surface chemistry, aerosols, ice nucleation in clouds, oil recovery, and biomembranes, nevertheless studies of their hydration and surface potential properties at low temperatures are limited. Garrett *et al.* showed that the major organic constituents of the ocean surface are high molecular weight molecules with low water solubility, such as fatty alcohols and acids.[141] Surface activity of these fatty compounds is well established such that they congregate at aqueous surfaces. While the favorable ice nucleation properties of fatty alcohols are well known, recent evidence suggests that at cooler temperatures, long-chain fatty acids from the sea surface microlayer are active in the ice nucleation process.[142,143] It has been shown through molecular simulations and laboratory experiments that ice nucleation efficiency is increased by good structural matching of the hydrogen-bonding structure of water around a fatty alcohol interface to that of bulk ice.[143] This structural matching is well-known as ice templating, where theoretical studies have linked the freezing behavior to the 2D structure at the water interface.[143] Additionally to ice nucleation processes, these fatty compounds are also key components in biomembranes and play a role in chemically enhanced oil recovery.[144] To develop more detailed models for the formation of monolayer and bilayers and their biological functions, Serafin *et al.* showed that phospholipid–fatty alcohol complexes can stably form at the air–water interface.[145]

While research on hydration of fatty acid and alcohols is limited, recent spectroscopic work of the solvation structure of both dilute and concentrated short-and medium chain linear alcohols in solution as a function of temperature is notable.[140,146–149] Davis *et al.*, using Raman scattering measurements, showed that very dilute alcohol solutions at temperatures just above 0 °C promote ordering of the surrounding hydrogen-bond network of water, whereas increasing temperature or alcohol chain length was shown to disrupt the ordering of the hydration shell.[147] These solution Raman studies were later confirmed by Deng *et al.* using IR spectroscopy measurements also revealing changes in the tetrahedral water structure of the hydration shell.[140] In addition to solution-based studies, cluster and molecular simulation approaches provide an important picture on the hydrogen-bonding network in aqueous solutions.[150–155] Previously, it has been shown that three to four water molecules are in direct contact with the OH ion in aqueous solution.[150–152,156] Fujii *et al.* showed that small, protonated methanol clusters undergo a phase change borne out in the hydrogen-bonding structure with temperature elevation.[156] Additionally, a study on freezing behavior of aqueous–alcohol nanodroplets as a function of alcohol concentration showed that nucleation occurs throughout the volume of the nanodroplet (bulk) rather than at or near its surface.[157]

Understanding hydration of monolayers and how differences in microenvironment can affect the hydrogen bond network has been of particular interest for many years.[158–163] In 1993 Alper and coauthors studied the behavior of water hydration in a phospholipid monolayer. Their results revealed rapid water motion yet preferential ordering with three hydration shells about the lipid phosphocholine group with a clathrate-like hydration structure around the choline.[158] Several studies of water in reverse micelles have been used to describe nano confined water and to obtain information regarding perturbations to the hydrogen bond network using a core–shell model. The core–shell model consists of a bulk water component and an interfacial water component for all reverse micelle sizes. This model suggest that the core water molecules would not be substantially affected by the interface.[164,165] Such studies demonstrated that confinement significantly affects the hydrogen bond network evolution of water in small reverse micelles..[159,160] While interfacial and confining environments are not necessarily the same, they both provide important information on the hydrogen-bonding network. The core–shell model of water dynamics were subdivided into two main contributions, a shell region that relates to the water molecules strongly associated with the lipid headgroups and a core region consisting of water molecules away from the headgroup that possess bulk-like properties.[161] Structure and dynamics understanding of liquid water remains an important and challenging problem, in particular, in the interpretation of the OH stretch region since it is extremely sensitive to molecular environments. Studies argue that the intermolecular and intramolecular coupling make the interpretation of this region difficult.[166] Therefore, studies of isotopic dilution focusing on dilute HOD mitigates the effect of intramolecular and intermolecular vibrational coupling to other vibrational modes.[164–169] Moreover, the OD stretch of dilute HOD in H_2O is used to eliminate problems due to vibrational excitation transfer.[164]

This study, first evaluates and quantifies the temperature-dependent hydration effects of two different fatty compound monolayers using interfacial surface pressure (Π) and surface potentiometry (ΔV). Both techniques provide information on the overall monolayer structure and intermolecular interactions. ΔV provides information on dipole moment alignment of the compounds and their hydration shell. To reveal changes in hydration as a function of temperature, infrared reflection–absorption spectroscopy (IRRAS) is utilized to collect surface-sensitive infrared spectra of octadecanol-d_{37} (stearyl-d_{37} alcohol) and octadecanoic-d_{35} acid (stearic-d_{35} acid) monolayers at the air–water interface. IRRAS provides a unique advantage given that it only probes the monolayer and the hydration shell immediately perturbed by the presence of the compounds at the interface. This study spectrally measures the OH stretching modes of the headgroups and their hydration shells as well as the HOH bending modes of the hydrating water molecules. To understand the impacts of vibrational excitation transfer, the OD stretch of dilute HOD in H_2O is also examined. Additionally, to gain insights into the temperature-dependent vibrational structure of the headgroup and water molecules in the first solvation shell around alcohols and carboxylic acids, the IR spectra of the propanol + $6H_2O$ and propionic acid + $10H_2O$ are computed from *ab initio* molecular dynamics (AIMD) calculations were conducted at L. McCaslin group at Sandia National Laboratory. The temperature-dependence of the spectra was then calculated using techniques from fluctuation theory. A spectral decomposition technique was introduced and used to correlate specific OH stretching motions to spectral features. Although, molecular dynamics studies on the changes in hydration structure around the headgroup at the monolayer interface have been previously performed, a study on changes in vibrational structure and transition moments with temperatures have not been conducted. Experimental and theoretical calculations show that strong correlations between OH stretching modes play a significant role in the spectra, as well as coupling between OH stretching and H_2O bending modes. The IRRAS spectra suggest that these highly correlated interactions disrupt the water-water hydrogen-bonding network near freezing temperature. The spectral frequency shifts, however, show a red shift suggesting more ordered water molecules at lower temperatures. The experiments in dilute 10% HOD in H_2O reveal the degree to which vibrational excitation transfer occurs in 100 % H_2O underlining the role of intramolecular coupling.

4.2 Experimental Methods and Materials

4.2.1 Materials

Octadecanoic acid (stearic acid, $CH_3(CH_2)_{16}COOH$, >99%, Sigma Aldrich), octadecanol (stearyl alcohol, $CH_3(CH_2)_{17}OH$, 99%, Sigma Aldrich), deuterated octadecanoic acid (stearic-d_{35} acid, $CD_3(CD_2)_{16}CO_2H$, > 98%, Sigma Aldrich), and deuterated octadecanol (stearyl-d_{37} alcohol, $CD_3(CD_2)_{17}OH$, >98%, Cambridge Isotopes Laboratories) were used as received. The compounds were dissolved in chloroform (HPLC grade, Fisher Scientific) to prepare ~3 mM octadecanoic acid and octadecanol solutions and ~2 mM octadecanoic-d_{35} acid and octadecanol-d_{37} solutions. Control experiments were performed using a cationic surfactant, dimethyldioctadecylammonium (bromo salt, DDBA; > 98% Sigma Aldrich). Nanopure water with a resistivity of 18.2 MΩ·cm (Milli-Q Advantage A10, EMD Millipore) and 5% deuterium oxide (D_2O, 99.9 atom % D, Sigma Aldrich) in nanopure water were used as the aqueous subphases. The ultrapure water had a pH of 5.6 due to atmospheric CO_2 acidification and was equilibrated at room temperature prior to starting experiments.

4.2.2 Surface Pressure and Surface Potential–Area Isotherms

Surface pressure and surface potential–area isotherm (Π-ΔV–A)experiments were conducted in triplicate using a Teflon Langmuir trough with Delrin barriers (KSV NIMA, Biolin Scientific, 549.08 cm^2 in surface area). Prior to a measurement, the trough and barriers were thoroughly cleaned with reagent alcohol (Histological Grade, Fisher Scientific) and ultrapure water. The surface potential (SPOT, KSV NIMA) sensor was placed halfway along the length of the trough and about 1–2 mm above the water surface, leaving enough distance from the trough edges to reduce interference. The counter electrode was submerged in the subphase parallel to the vibrating probe surface. The SPOT sensor was allowed to equilibrate with its surroundings for at least 10 minutes before starting the first experiment. Surface pressure was measured using the Wilhelmy plate method with a filter paper plate (Ashless Grade 41, Whatman, GE Healthcare) that was completely wetted prior to running a compression isotherm experiment. The trough was then filled with ultrapure water; surface cleanliness ($\Pi \leq 0.20$ mN/m) was verified by sweeping the barriers at a compression speed of 270 mm/min/barrier. Π and ΔV were then zeroed, and a microsyringe (Hamilton) was used to spread the surfactant solution dropwise onto the subphase. Ten minutes were allowed for solvent evaporation, followed by symmetrical and constant compression of the monolayer at a rate of 10 mm/minute (5 mm/min/barrier). Surface pressure and surface potential–area isotherms were conducted at 21.0 °C, and 1.0 ± 1.0 °C and a relative humidity of 35 ± 5%.

4.2.3 Infrared Reflection–Absorption Spectroscopy

Interface-sensitive infrared reflection–absorption spectroscopy (IRRAS) was used to spectrally evaluate the interfacial region. A custom-built setup was used and placed in the chamber of a Fourier transform infrared (FTIR) spectrometer (Frontier, PerkinElmer) with a liquid nitrogen-cooled HgCdTe (MCT) detector. A Langmuir trough was set inside the spectrometer on a breadboard containing two gold mirrors. The first mirror directs the incoming unpolarized IR beam to the sample surface at a 48° incident angle relative to the surface normal. As some of the light is reflected off the water surface, it is directed by the second gold mirror toward the MCT detector. Each spectrum was collected as an average of 400 scans using a single-beam mode over the full spectral range of 4000–450 cm^{-1} at a 4 cm^{-1} setting. Data analysis was performed using Origin software (OriginLab 9). The spectra shown here are plotted as an average of at least three individual spectra. The OH stretching region spectra were individually baseline-subtracted using a line function between the end points 3800 and 2900 cm^{-1}, and the HOH bending mode spectra were baseline-subtracted by fitting a fourth order polynomial function along the baseline between 1900 and 1250 cm^{-1}. Spectra were collected at 21.0 °C, and 1.0 ± 1.0 °C and a lab relative humidity of 35 ± 5%.

4.3 Results and Discussion

4.3.1 Impact of Temperature on Fatty Alcohols & Fatty Acid Monolayers Structure

To quantify the temperature-dependent hydration effects on monolayer structure, the organization of the monolayer is first probed via surface pressure–area isotherms in tandem with surface potentiometry, **Figure 17**. Both techniques provide insights on the overall monolayer structure and intermolecular interactions, and surface potentiometry provides semiquantitative information on dipole alignment of the compounds and their hydration shells.[62] Octadecanoic acid ($CH_3(CH_2)_{16}COOH$) and octadecanol ($CH_3(CH_2)_{17}OH$) were chosen to represent model sea spray aerosol films due to their marine-relevance and abundance in laboratory-generated nascent sea spray aerosol.[45] Both compounds have identical chain lengths and are neutrally charged (protonated) at pH 5.6, the pH of ultrapure water used in the experiments. Thus, the headgroup and its hydration structure drive the differences in the surface pressure–area isotherms and surface potential measurements.

All measurements were collected at both room temperature (21.0 ± 0.5 °C) and near freezing (1.0 ± 1.0 C) to represent a realistic range of temperatures experienced by sea spray aerosol in the atmosphere. Π–A isotherms near freezing have not been previously investigated, and prior studies have shown Π data of fatty acids and fatty alcohols[170–172] at temperatures no lower than 5 °C.[170,173] Film studies have also measured the ΔV of both fatty alcohols and fatty acids to obtain organizational information, but not at lower temperatures.[68,171–176] These measurements were carried out to better understand the octadecanol and octadecanoic acid monolayer structural change and altered hydration environments at low temperatures.

At room temperature, our Π–A isotherms closely match isotherms in the literature, **Figure 17a**.[9,45,92,172,177–181] As the barriers compress the octadecanol and octadecanoic acid monolayers to smaller mean molecular area (MMA), the films undergo a 2D phase transition. The first phase transition, known as the lift-off point, starts at the gas-tilted condensed (G-TC) coexistence region in which gaseous regions without aggregated fatty compounds coexist with small circular domains of aggregates in the TC phase. The monolayer transitions to the tilted condensed (TC) phase at 21 Å^2/molecule for octadecanol and 24 Å^2/molecule for octadecanoic acid, where the domains start to fuse together to form a fully condensed monolayer.[9,32,66,182,183] Upon further compression in the TC phase, the monolayers transition into the untilted condensed (UC) phase at 18.6 Å^2/molecule for octadecanol and 19.5 Å^2/molecule for octadecanoic acid. In this phase, the compounds are highly compressed and oriented nearly perpendicular to the water surface, causing the formation of a fully condensed film. Additionally, the octadecanol and octadecanoic acid films reach a maximum Π observed at ~57.5 and ~47 mN/m, respectively. Hence, the octadecanol monolayer is more compressed relative to the octadecanoic acid monolayer across all 2D phases due to the smaller spatial requirement for the alcohol headgroup in comparison to the larger carboxylic acid headgroup.

The Π–A isotherms near freezing (1 °C) shown in **Figure 17a** are remarkably similar in shape to the room temperature isotherms, but there are some clear differences in the isotherm phase transitions. Octadecanol and octadecanoic acid monolayers lift-off at 20 and 23 Å^2/molecule, respectively, decreasing the lift-off points by 1 Å^2/molecule relative to the values at room temperature. The phase transition from the TC to the UC phase occurs at 17.8 Å^2/molecule for octadecanol and at 18.8 Å^2/molecule for octadecanoic acid, 0.8 Å^2/molecule smaller relative to the MMA values for both compounds at room temperature. Moreover, the octadecanol and octadecanoic acid films reach a maximum surface pressure at ~64.4 and ~59.8 mN/m, respectively, approximately 10 mN/m higher than the maximum monolayer Π at room temperature. Thus, low temperature promotes tighter compression of both monolayers. Additionally, the lowered temperature has a nearly identical effect on the magnitude of MMA shifts in the isotherms for octadecanol and octadecanoic acid, suggesting that the magnitude of compression upon lowering the temperature is about the same for both compounds.

Surface-sensitive surface potential measurements were obtained during monolayer compression to gain more insight on monolayer organization and headgroup hydration. ΔV is a technique that measures electrical properties of bare and surfactant-covered aqueous interfaces.[45] In these experiments, ΔV is measured as the difference in voltage from a clean water surface. The hydrophobic tail, polar headgroup, and composition of the underlying aqueous subphase all strongly influence the surface potential measurements.[68,121,171,175,176,184–186] ΔV variation during monolayer compression is often discussed in terms of changes in dipole moment alignment due to tail orientation relative to the water surface; however, increasing molecular density and polar headgroup orientation and dehydration during monolayer compression are also important contributors to the overall surface potential.[187] Quadrupole contributions have also been indicated in some systems.[188] The headgroup hydration shells screen the polar headgroup dipole moments, thereby reducing the surface potential at large MMAs. Monolayer compression to low MMAs dehydrates the polar headgroups, reduces the dipole moment screening, and the increases surface potential.[187]

Figure 17b shows the ΔV response obtained for the three different octadecanol (bottom) and octadecanoic acid (top) monolayer phases (G-TC, TC, and UC). Results show that the ΔV becomes nonzero and increases in magnitude in the G-TC coexistence phase (larger MMA values than the lift-off points in the Π–A isotherms) for both octadecanol and octadecanoic acid at room temperature and near freezing. This suggests that domains are formed throughout compression in the G-TC coexistence phase, resulting in a positive ΔV value even when the Π remains at zero prior to transition into the TC phase. Dehydration of the headgroups is also likely. At room temperature, octadecanoic acid has a ΔV of 157 ± 97 mV in the G-TC phase, and octadecanol has a ΔV of 35 ± 99 mV. One can argue that octadecanoic acid has a higher ΔV than octadecanol in this coexistence region due to a larger number on molecules existing in the TC phase thus less dipole moment screening of hydrating water molecules leading to an increase in dipole moment contribution from the carbonyl headgroup. Also, the octadecanoic acid tail may orient differently in the TC region relative to the alcohol due to its larger headgroup leading to less shielding and thus more exposure of the headgroup dipole moment. Π and ΔV isotherm and exact MMAs used for each surface potential point can be found in **Figure 18** and **Table 1**.

Cooling-induced changes in the G-TC coexistence phase and could play an important role in ice nucleation due to water molecule reorientation within the headgroup region to form ice-like structures.[45,143] It is important to note that the greatest magnitude of surface potential change between room temperature and near freezing occurs for octadecanol in the G-TC phase. At 1.0 °C, the octadecanoic acid ΔV is 296 ± 17 mV, and the octadecanol ΔV is 295 ± 164 mV. Thus, the difference between the 1 and 21 °C surface potential values in the G-TC phase for octadecanoic acid is 140 ± 98 mV, whereas the difference for octadecanol is 260 ± 192 mV. Results suggest that octadecanol undergoes the greatest extent of headgroup hydration reorganization in the G-TC coexistence phase near freezing.

As the monolayer is compressed, the ΔV increases for both compounds until a maximum value is reached in the fully-condensed UC phase. Thus, the rising surface potential shows increasing interfacial molecular density, enhanced ordering, and headgroup dehydration within the monolayer. The maximum ΔV values for octadecanol and octadecanoic acid on water at 21.0 °C are 429 ± 112 and 318 ± 103 mV, respectively, which agree with reported literature values of ~400–338 mV for octadecanol[171,174,175,184] and 280–380 mV for octadecanoic acid.[68,174–176,180,184,189–191] The maximum surface potential response for octadecanol was 111 ± 152 mV greater than the maximum value measured for octadecanoic acid, possibly due to octadecanol's strong C–OH dipole moment alignment at the interface and to the reorganization and structuring of water molecules adjacent to the headgroup. The orientation of the fatty tails affects the orientation of the head group and thus the water molecules at the interface.[68]

Temperature-dependent differences in surface potential are less significant in the UC phase as compared to phases with lower surface coverage, like the G-TC coexistence phase. An octadecanoic acid monolayer at 1 °C in the UC phase has a ΔV of 354 ± 7 mV, and an octadecanol monolayer has a ΔV of 504 ± 36 mV. The difference between the ΔV at 1 and 21 °C is 36 ± 103 mV for octadecanoic acid and 75 ± 109 mV for octadecanol. These fatty compounds have minimal room for rearrangement at high surface coverage due to both van der Waals interactions and dipole repulsion.[187]

4.3.2 Vibrational Spectroscopy Signatures on the Headgroup and Hydration Shells

To elucidate changes in hydration structure as a function of temperature, IRRAS spectroscopy was used to collect surface-sensitive infrared spectra of octadecanol-d_{37} and octadecanoic-d_{35} acid monolayers at the air-aqueous interface. Deuterated fatty compounds were selected to avoid spectral overlap of the carboxylic acid vibrational modes with the CH_2 scissoring modes. IRRAS spectra are plotted as reflectance–absorbance (RA),

$$\mathrm{RA} = -\log\frac{R_\mathrm{f}}{R_0} \tag{4.1}$$

in which R_f corresponds to the reflectance of the film and R_0 corresponds to the reflectance of the bare water surface. Hence, only a reflected signal corresponding to the monolayer and its hydration shell is detected. Both positive and negative peaks are observable in our IRRAS spectra; the reflectance–absorbance values are negative when the film reflectance is greater than the water reflectance ($R_\mathrm{f}/R_0 > 1$), and the reflectance–absorbance values are positive when the reflected signal from water is greater than that of the film ($R_\mathrm{f}/R_0 < 1$). In the IRRAS spectra presented here, the negative peaks correspond to monolayer vibrational modes, and the positive peaks correspond to the hydration shell modes. This observation is consistent with other published IRRAS spectra collected at IR beam angles of incidence less than the Brewster angle of water (~53.1° relative to surface normal).[29,71,72,77,89,95,120,192–196]

Octadecanol-d_{37} and octadecanoic-d_{35} acid IRRAS spectra were collected at a Π of 40 mN/m, which corresponds to the UC phase of the monolayers. To directly compare peak intensities between the spectra of the two compounds, an additional scaling factor is required to account for differences in film surface density at constant Π. The scaling factor is calculated by dividing the MMA of the octadecanoic-d_{35} acid monolayer by the MMA of the octadecanol-d_{37} monolayer at 40 mN/m, and this ratio is then multiplied into the octadecanoic-d_{35} acid spectral peak intensities. As a result, the spectra of both fatty compounds have equivalent surface coverage for direct comparison of peak intensities. The scaling factors are plotted in **Figure 19** and all octadecanoic-d_{35} acid spectra have been scaled.

The influence of the polar headgroup on the hydration shell as a function of temperature is not fully understood, especially at high number densities and at monolayer surfaces. For dilute solutions of water-soluble alcohols, the influence of the alcohol headgroup on the OH stretching region is negligible.[147] The alcohol OH stretch becomes significant at higher concentrations upon alcohol aggregation (greater than ~2.7 M for *tert*-butyl alcohol and *n*-propanol), meaning that the alcohol OH stretch is difficult, if not impossible, to separate from that of the water OH stretching modes. As a result, Deng *et* *al.* instead conducted their analysis on the HOH bending mode to isolate the contribution from water alone, but the water molecules solvating the headgroup versus surrounding the alkyl chain of the soluble alcohol could not be distinguished.[140]

IRRAS offers a unique advantage in that it only probes the monolayer and the hydration shell immediately perturbed by the presence of the fatty compounds at the interface; any signal from water molecules that matches the bare water surface reflectance will be subtracted from the reflectance–absorbance spectrum. Additionally, octadecanoic acid and octadecanol are highly insoluble, so their alkyl tails are directed toward and mostly exist in the air phase while only their polar headgroups are completely solvated within the water surface and subsurface region. Thus, IRRAS was used to spectrally probe the OH stretching (ν (OH), ~3000–3800 cm^{-1}) modes of the headgroups and their hydration shells as well as the HOH bending (δ (HOH), ~1500–1800 cm^{-1}) modes of the hydrating water molecules. The ν (OD) modes of dilute HOD were also probed to remove resonant vibrational excitation transfer, a Förster transfer mechanism mediated by transition dipole moment coupling; the ν (OD) modes thus act as uncoupled local modes for more reliable reporting of water structure.[166,167,197–202] All spectra were collected at 21.0 ± 0.5 and 1.0 ± 1.0 °C. Shifts in the OH and OD stretching region spectra as a function of temperature were quantified by Gaussian peak fitting.

4.3.2.1 Fatty Alcohol Headgroup Hydration as a Function of Temperature

The OH (100% H_2O) and OD (10% HOD) stretching region spectra of octadecanol-d_{37} at 21.0 and 1.0 °C are plotted in **Figure 20a** and **20b**, respectively. For better visualization of the peak intensity changes, the Gaussian spectral deconvolutions at each temperature are plotted in **Figure 21** and **Figure 22**. Numerical values of the Gaussian peak fitted parameters are reported in **Table 3–6**. The ν (OH) and ν (OD) spectra have significantly different shapes. The ν (OH) region of the 100% H_2O subphase exhibits a two-peak structure (**Figure 20a**) and exhibits dramatically different spectral shifts with temperature; higher frequency regions of the ν (OH) spectra increase in peak intensity at low temperature, and the low frequency regions decrease in peak intensity. Thus, the intra- and intermolecular vibrational coupling mechanisms are likely highly sensitive to changes in temperature, resulting in the relative intensity shifts of the two main peaks in the OH stretching spectra. More specifically, changes in temperature alter the transition dipole moment strengths and hydrogen-bonding configurations of the interfacial water molecules, thereby shifting the distribution of resonant vibrational frequencies. Others have shown that an increase in temperature induces a frequency mismatch between the stretch fundamental and the bending overtone of bulk water, leading to a decrease in the Fermi resonance intramolecular coupling at ~3250 cm^{-1}.[203–207] Intramolecular coupling dominates the vibrational relaxation pathways in interfacial water.[201,208–210] Thus, intramolecular coupling is possibly driving the temperature-dependent spectral shifts observed in **Figure 22a**, but the exact mechanisms responsible for these spectral shifts are currently unknown. Vibrational coupling to octadecanol-d_{37} vibrational modes is also possible.[211,212] Additionally, it is nontrivial to distinguish between peak intensity contributions caused by changes in hydration shell number density and structure versus changes in transition dipole moment strength as a function of temperature, further complicating the spectral interpretation. Consequently, calculations were performed that intrinsically include intra- and intermolecular coupling to study the contribution of transition dipole moments changes due to temperature for a single hydrogen-bonding configuration shown in Vazquez de Vasquez *et al*.

In **Figure 20b**, the ν (OD) region of the 10% HOD spectrum contains a single peak. This decoupled spectral signature provides important insight into the hydrogen-bonding character of the hydration shell of the fatty acid and the fatty alcohol. As the temperature decreases to 1.0 °C, the ν (OD) spectrum red-shifts ~10 cm^{-1}, indicating the formation of stronger hydrogen bonds with cooling, consistent with ice templating behavior for both the fatty acid and the fatty alcohol.

4.3.2.2 Ab Initio Molecular Dynamics (AIMD) Calculations and the Fundamental Vibrational Structure of IR Features.

In order to gain insights into the temperature-dependent vibrational structure of the OH stretches of the headgroup and water molecules in the first solvation shell, AIMD calculations were performed on two model systems by L. McCaslin at Sandia National Laboratory: propanol + $6H_2O$ and propionic acid + $10H_2O$. These systems were chosen to have a short, three carbon chain to be sufficiently long that the water remains localized to the headgroup while keeping the system small for computational efficiency. One benefit of using cluster models was the ease with which internal coordinates (i.e. bond stretches, angle bends, and dihedral bends) can be defined for spectral decomposition. This allowed for a detailed analysis of the hydrogen-bonding structure of the water molecules surrounding the headgroups as well as which molecular motions correspond with IR spectral features in the OH stretching region. While molecular dynamics studies have been performed on the changes in hydration structure around headgroups at monolayer interfaces, a study on the changes in vibrational structure and transition moments with temperature had not been conducted. In order to unravel the differences between changes in hydration structure and changes in transition moment, this study turned to AIMD studies of model cluster systems, see Vazquez de Vasquez *et al.*[213] for more details.

Propanol + 6 H_2O Cluster.

The OH stretching region of the IR spectrum in the propanol + 6H_2O cluster was computed from AIMD calculations. It was shown that the alcohol OH forms a donor hydrogen bond to water, which forms a four membered ring (three H_2O and alcohol) that donates a hydrogen bond back to the alcohol. Using the spectral decomposition scheme described in Vazquez de Vazquez *et al.*,[213] L. McCaslin determined that three groupings of OH stretching motions, which were called Regions 1–3, are highly correlated. L. McCaslin showed that Region 1 is made up of three OH stretches: the alcohol OH stretch and two water OH stretches that form a chain coming from the alcohol OH stretch. Region 2 is made up of four water OH stretches in a ring with one stretch donating a hydrogen bond back to the OH of the alcohol. Finally, Region 3 is a single water OH stretch by a water that donates a hydrogen bond to the alcohol OH. The spectral decomposition scheme determines that the IR spectrum can be broken up into four natural sections based on changes in the weights of these regions. The OH stretches in Region 1 contributes the most IR intensity to the spectrum between 3200 and 3674 cm^{-1}. However, the weight of Region 2 is not negligible between 3200 and 3674 cm^{-1} and contributes 40% of the IR intensity (vs 49% from Region 1) between 3496 and 3674 cm^{-1}. Between 3674 and 3757 cm^{-1}, the largest weight comes from Region 3, the OH stretch donating a hydrogen bond to the alcohol OH, though Regions 1 and 2 still contribute 18 and 19%, respectively. These spectral decomposition results highlight a key finding that localized groupings of highly correlated stretching motions underlie regions of large IR intensity in the OH stretching region.

The effects of temperature on transition moment were computed as described in Vazquez de Vasquez *et al.*[213] This allows for an isolated study of the effects of temperature on changes in intensity, allowing for comparison to effects on intensity from changes in hydrogen-bonding structure at the monolayer interface, as described in Qiu *et al.*(2017).[143] It was found that between 3460 and 3730 cm^{-1}, the intensities, on average, increase when the temperature lowers to –3 °C. At 3770 cm^{-1}, a feature corresponding to significant weight from Region 3 appears that does not have significant change in intensity with respect to temperature. The OH stretching motions not highlighted do not have significant transition moments that contribute to the spectrum. In order to make a quantitative comparison between experimental and theoretical spectra, a Gaussian regression analysis was performed on the 27 °C and –3 °C spectra. It is found that the decrease in temperature by 30 °C shifts the Gaussian peak to the red by 17 cm^{-1}, in agreement with the red shift seen in both the experimental H_2O and HOD stretching spectra. The decrease in temperature also increases spectral intensities, as seen in the higher frequency peak of the experimental H_2O stretching spectra corresponding to the first solvation shell. The experimental HOD stretching spectra show a decrease in intensity at lower temperatures. The computed spectra from AIMD inherently include intra- and intermolecular coupling that contributes to the unique spectral signatures of the H_2O–octadecanol interface and their temperature dependence. The red shift and intensity increase of the spectra from the propanol + $6H_2O$ cluster underline the role of intra- and intermolecular coupling in the higher frequency peak in the OH stretching region of the H_2O–octadecanol interface, in contrast to the signatures of the DOH–octadecanol stretching region.

4.3.2.3 Fatty Acid Headgroup Hydration as a Function of Temperature

Changes in the OH (**Figure 23a**) and OD (**Figure 23b**) stretching regions of octadecanoic-d_{35} acid monolayers as a function of temperature resemble the trends observed for octadecanol-d_{37} monolayers in **Figure 20a** and **20b**. Gaussian spectral deconvolutions at each temperature are plotted in **Figure 24** and **Figure 25**, and the numerical values of the fitted peak parameters are reported in **Table 3-6**. Like octadecanol-d_{37}, lowering the temperature from 21.0 °C to 1.0 °C also results in a ~10 cm^{-1} red shift in the ν (OD) spectrum of the octadecanoic-d_{35} acid monolayer. The peak center frequencies are nearly identical for both monolayers held at the same temperature, suggesting that the hydrating water structure is quite similar between the two lipids. For the ν (OH) spectra, an increase in the high frequency region peak intensities near freezing matches the octadecanol-d_{37} spectral trends, although the peak intensity changes are not as large in magnitude for the octadecanoic-d_{35} acid monolayer. Suggesting that the intra- and intermolecular coupling mechanisms for interfacial water hydrating octadecanoic-d_{35} acid are weaker than the coupling mechanisms for water hydrating octadecanol-d_{37}.

Consistent with the surface potential data (**Figure 17**), temperature has a smaller effect on octadecanoic acid monolayer organization and hydration structure.

Propanoic Acid + 10 H_2O Cluster

In comparing the OH stretching regions of the propanol + $6H_2O$ system and the propionic acid + $10H_2O$ system, the additional complexity of the carboxylic acid headgroup results in a more complex vibrational structure, shown in Vazquez de Vasquez *et al.*[213] As found in the propanol + $6H_2O$ cluster, L. McCaslin determined that three groupings of OH stretching motions in the propionic acid + $10H_2O$ cluster, which were called Regions 1–3, are highly correlated. Region 1 is made up of five OH stretches from four water molecules forming a ring with two hydrogen bonds to the carboxylic acid ═O. Region 2 is made up of six water OH stretches in a four-water ring with two stretches donating a hydrogen bond to the OH of the carboxylic acid. Finally, Region 3 consists of the OH stretch of the carboxylic acid and a water OH stretch that donates a hydrogen bond to a water molecule in Region 1. The spectral decomposition scheme determines that the IR spectrum can be broken up into four natural sections based on changes in the weights of these regions, shown in Vazquez de Vasquez *et al.*[213] The OH stretches in Region 1 contribute the most IR intensity to the spectrum in the OH stretching region shown. However, the weight of Region 2 is significant (23–28%) between 3240 and 3715 cm^{-1}. Region 3 contributes significant intensity between 3240 and 3401 cm^{-1}, but quickly decreases in weight for higher frequencies and is not a major contributor (only 5%) to regions of large intensity between 3558 and 3715 cm^{-1}.

The effects of temperature on IR intensities are computed for the propionic acid + 10 H_2O system. It is found that in the OH stretching region, the IR intensities, on average, increase when the temperature lowers to –3ºC. As described for the propanol + 6H_2O cluster, a Gaussian regression analysis was performed on the 27 ºC and –3 ºC spectra, included in Vazquez de Vasquez *et al.*[213] It is found that the decrease in temperature by 30 ºC shifts the Gaussian peak to the red by 25 cm^{-1}, which agrees with the spectral shift found in the H_2O–octadecanoic acid and HOD–octadecanoic acid spectra. The decrease in temperature also increases spectral intensities, with the Gaussian peak increasing by 24%, modeling the behavior of the higher frequency peak in the H_2O–octadecanoic acid OH stretch region, which corresponds to the behavior of the first solvation shell. These findings, alongside the findings from the propanol + 6 H2O cluster spectra, strengthen our understanding of the role of intra- and intermolecular effects on the OH stretching region, which is further clarified via comparisons to the experimental HOD–octadecanoic acid stretching region spectra.

The vibrational structure of the model propanol + 6H_2O and propionic acid + 10H_2O systems provides insight into the effects of temperature on the transition moments. Because changes in IR intensity with temperature can be due to changes in hydrogen-bonding structure as well as changes in transition moment, studying such model systems provides this additional layer of complexity that has not been studied in previous dynamics studies of the changes in hydration at the monolayer surface in ice nucleation processes.[143,214–216] Furthermore, the decomposition of IR features from AIMD calculations provides deep insights into the correlation between individual OH stretches into natural groupings, and their contributions to IR features. In both model systems studied, the vibrations within different structural motifs contribute to markedly different IR features. As experimental tools continue to be developed for detection of markers for ice nucleation, predictions of spectral features and the molecular motions that contribute to them will be key to generating a fundamental picture of the chemical physics at play.

4.3.2.4 Water Bending Mode IRRAS Spectra as a Function of Temperature

The water bending mode in the IRRAS spectra provides a useful spectroscopic handle for selectively probing the headgroup hydration shell structure as a function of temperature.[217,218] Although the water bending mode is not as sensitive to the local molecular environment as the OH stretching region due to the smaller transition dipole moment, the water bending region is sufficiently isolated from the headgroup vibrational modes. Additionally, the HOH bending mode is devoid of intramolecular coupling; and intermolecular coupling of the bend vibration is considerably weaker than the stretch vibration, making the bending mode a reliable reporter of the hydration shell structure.[218–222] **Figure 26** shows this spectroscopic region for the octadecanold$_{37}$ (**Figure 26a**) and octadecanoicd$_{35}$ acid (**Figure 26b**) monolayers at room temperature and near freezing. At 21.0 °C, the water bending region is a positive band centered around ~1665 cm^{-1}. The band red-shifts ~18 cm^{-1} for the octadecanol-d$_{37}$ monolayer and ~21 cm^{-1} for the octadecanoic-d$_{35}$ acid monolayer upon cooling to 1.0 °C. Red shifts in the water bending mode region indicate weakened intermolecular interactions within the hydration shell.[140,218,223] Additionally, the peak width increases with decreasing temperature for both compounds in the low frequency end of the spectrum, suggesting that the hydration shell is sampling a more heterogeneous hydrogen-bonding environment.

The small, albeit significant, temperature-dependent shift in the octadecanoic-d_{35} acid carbonyl stretching mode also provides evidence for the hydration structure (**Figure 26**). Cooling from 21.0 to 1.0 °C red-shifts the carbonyl mode by 4.5 cm^{-1} **(Table 2**), indicating that the intermolecular interactions between the headgroup and its surrounding environment increase near freezing. Consequently, this red-shift provides further spectral evidence that the hydrogen-bonding interactions between the headgroup and its hydration shell increase with decreasing temperature.

4.3.2.5 Evaluating the Spectral Impacts of Hydration Structure and Transition Dipole Moment Strength

The experimental OH stretching region IRRAS spectra of octadecanol-d_{37} and octadecanoic-d_{35} acid comprise a temperature-dependent convolution of hydration structure, differing transition dipole moment strengths, and intra- and intermolecular coupling. The AIMD calculations, by L. McCaslin, provide detailed molecular-level insights on the first hydration shell structure, and the calculations isolate the impacts of temperature on the transition dipole moment strengths. Both the experimental and computational spectra increase in intensity in the high frequency stretching regions at lower temperature, indicating that increasing transition dipole moments significantly enhance the 1.0 °C IRRAS spectral intensities for both fatty compounds. The higher frequency stretching regions are dominated by contributions from the first solvation shell around the fatty compound, allowing for comparisons between experiment and theory in these regions.

4.4 Conclusions

Through experiment and theory, this work examines the temperature-dependent impacts of hydration structure and transition dipole moment strengths on the OH stretching region infrared reflection–absorption spectra of fatty alcohol and acid monolayers at the air–water interface. The decoupled OD of dilute HOD is also probed to isolate the effects vibrational excitation transfer observed in the pure H_2O data. It is observed that temperature has a large impact on the intra- and intermolecular vibrational coupling between the octadecanol and octadecanoic acid headgroups and their hydration shells. It was also found that changes in temperature affect the transition dipole moment strength, thus shifting the resonant vibrational frequency distributions. According to the surface pressure and surface potential–area isotherms results, lowering the temperature promotes tighter packing. Monolayer compression to small surface area per molecule dehydrates the polar headgroups relative to the expanded monolayer at large areas per molecule, yielding a reduction in dipole moment screening between the headgroups. The infrared reflection–absorption ν OH spectra of these two compounds show two main OH stretching bands at 3600 and 3250 cm^{-1}, whereas the ν (OD) region contains a single peak at 2580 cm^{-1}. At low temperature the ν (OD) spectrum red-shifts, indicating the formation of stronger hydrogen bonds with cooling. Contrary, the ν (OH) reveals dramatically different spectral shifts. The higher frequency regions of the ν (OH) spectra increase in peak intensity at low temperature, whereas the low frequency regions decrease in peak intensity. This work argues that intra- and intermolecular coupling dominates the vibrational relaxation pathways in interfacial water, thereby intramolecular coupling is more likely driving the temperature-dependent ν (OH) spectra shifts. Overall, the infrared reflection spectra suggest that temperature has a large impact on the intra- and intermolecular interactions between the headgroups and their hydration shells, and the octadecanol hydration shell. In the 10% HOD spectra, the ν (OD) mode is decoupled from the ν (OH) mode and reveal the behavior of the hydrogen-bonding network. A significant red shift was observed which is correlated to ice templating behavior for both the fatty acid and the fatty alcohol. Moreover, the surface potential data corroborate prior observations of enhanced ice nucleating activity by long chain alcohols at the air–water interface.

Ab initio molecular dynamics (AIMD) simulations of propanol + $6H_2O$ and propionic acid + $10H_2O$, by L. McCaslin, further reveal the effects of intra- and intermolecular coupling on the temperature-dependent transition dipole moment strengths in the OH stretching region spectra. For both the alcohol and the carboxylic acid, the overall calculated infrared spectral intensities increase with decreasing temperature due to enhanced transition dipole moment strengths. Thus, the increasing transition dipole moment strengths likely have a significant contribution to the increase in infrared reflection–absorption spectral peak intensities near freezing in the higher frequency stretching regions that represent the first solvation shell around the fatty compound. The cluster studies reveal the effects of the intra- and intermolecular coupling on the OH stretching region around the fatty compounds and simultaneously untangle the effects of cooling on the transition dipole moment strengths.

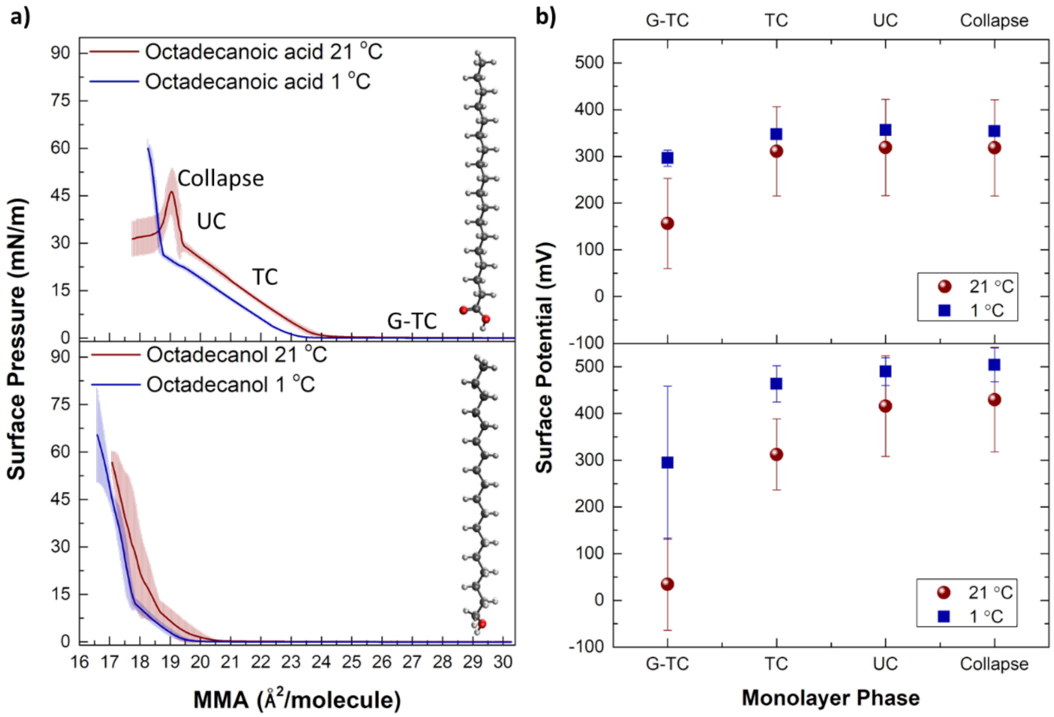

Figure 17. a) Surface pressure isotherm of octadecanoic acid (top) and octadecanol (bottom) at 21.0 °C (red) and 1.0 ± 1.0 °C (blue) indicating the different phase transitions. b) Surface potential changes of octadecanoic acid (top) and octadecanol (bottom) as a function of monolayer density at 21.0 °C (red) and 1.0 ± 1.0 °C (blue).

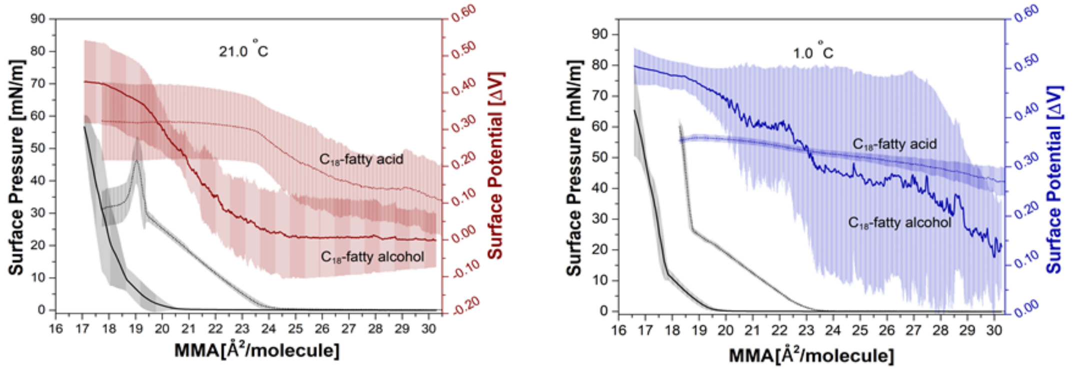

Figure 18. Surface pressure and surface potential isotherms of C_{18}-fatty alcohol (stearyl alcohol) and C_{18}-fatty acid (stearic acid) at 21 (left) and 1 ºC (right). Shaded regions show standard deviation of three trials.

Table 1. MMA range used in the surface potential plot. For example, the MMA range used for the G-TC phase surface potential values for the fatty alcohol at 21 °C was from 33.30–21.00 Å^2/molecule. The surface potential values at this range were then average and the average value was reported in **Figure 19**(b).

Compound	**Phase**	**Temperature (°C)**	**MMA Range (Å^2/Molecule)**
Fatty Alcohol	G-TC	21	33.30-21.00
Fatty Alcohol	TC	21	21.00-18.70
Fatty Alcohol	UC	21	18.70-17.20
Fatty Alcohol	Collapse	21	17.20-17.08
Fatty Acid	G-TC	21	31.65-24.00
Fatty Acid	TC	21	24.00-19.50
Fatty Acid	UC	21	19.50-19.11
Fatty Acid	Collapse	21	19.11-19.04
Fatty Alcohol	G-TC	1	31.30-19.50
Fatty Alcohol	TC	1	19.50-17.85
Fatty Alcohol	UC	1	17.85-16.70
Fatty Alcohol	Collapse	1	16.70-16.60
Fatty Acid	G-TC	1	31.65-23.50
Fatty Acid	TC	1	23.5-18.80
Fatty Acid	UC	1	18.80-18.30
Fatty Acid	Collapse	1	18.30-18.27

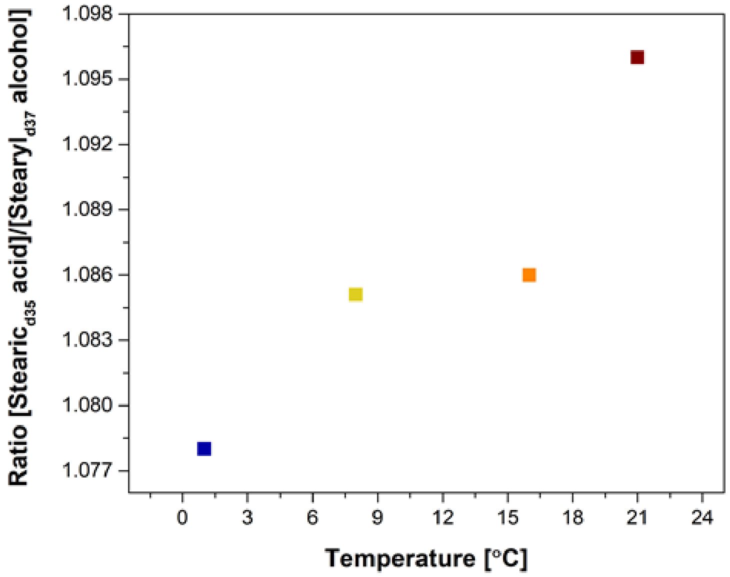

Figure 19. Normalization plot based on the surface pressure isotherms at the respectively MMA of each fatty compound at 40 mN/m at each temperature. Octadecanoic-d_{35} acid was multiplied by the specific ratio.

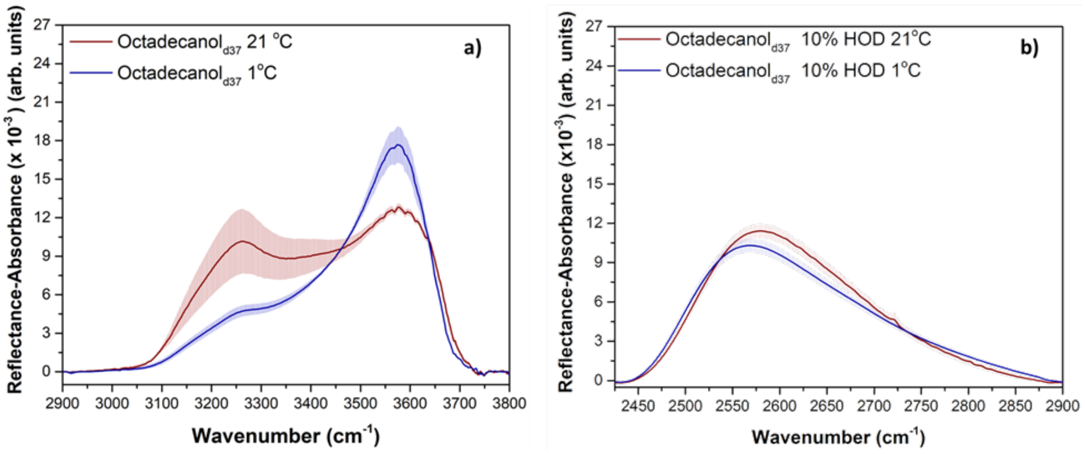

Figure 20. IRRAS spectra of the ν(OH) and ν (OD). a) octadecanol-d_{37} alcohol illustrates the main ν(OH) bands one at 3600 cm^{-1}, typically attributed to the OH stretch of the groups weakly interacting with the neighbors and a 3250 cm^{-1} band due to strong interacting solvent (water) molecules at 21 ºC ± 1 (red) and 1 ºC ± 1 (blue); b) shows the (OD) spectral region of octadecanol-d_{37} in 5% D_2O in water (10% HOD). The ν(OD) is decoupled from the OH oscillators. The ν(OD) change in frequency (~10 cm^{-1} red shift) with temperature can be found **Table 2**.

Table 2. Vibrational OH and OD modes and respective frequencies of IRRAS spectra of both octadecanoic-d_{35} acid and octadecanol-d_{37} at 21 °C and 1° C in 100 % water and in 5 % D_2O (10 % HOD).

Octadecanoic-d_{35} acid	Vibrational Mode	21° C Frequency (cm^{-1})	1° C Frequency (cm^{-1})
	ν (C=O)	1734.08	1729.58
	ν (C-OH)	1275.38	1278.38
	δ (HOH)	1668.77	1649.25
	ν_s (CD_2)	2088.49	2088.49
	ν_{as} (CD_2)	2193.60	2192.89
	δ (CD_2)	1089.52	1090.10
	ν (OD)	2581.00	2569.00
	ν (OH)	3578.38	3574.77
Octadecanol-d_{37}	δ (HOH)	1665.77	1655.26
	ν_s (CD_2)	2089.19	2089.19
	ν_{as} (CD_2)	2193.60	2192.89
	δ (CD_2)	1089.10	1089.52
	ν (OD)	2580.50	2568.50
	ν (OH)	3576.57	3574.77

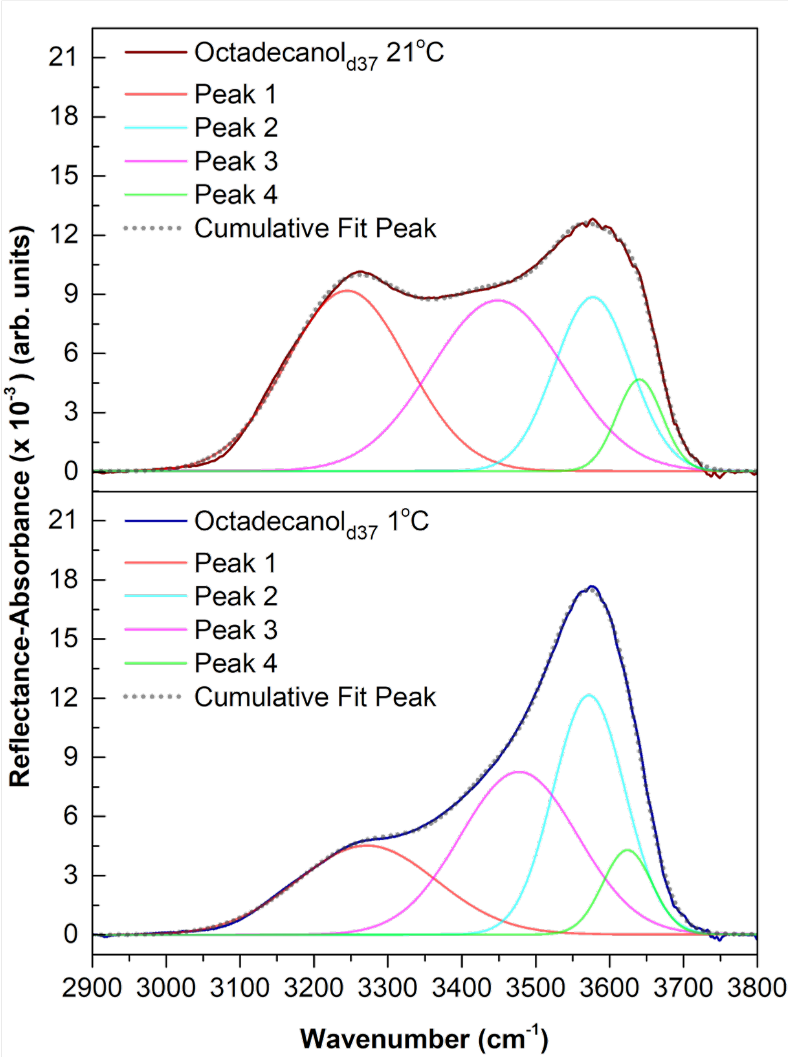

Figure 21. IRRAS spectra with corresponding Gaussian fits of an octadecanol-d$_{37}$ monolayer at 21 ºC (top) and 1 ºC (bottom) of the OH vibrational region at 40 mN/m spread onto a 100% water subphase.

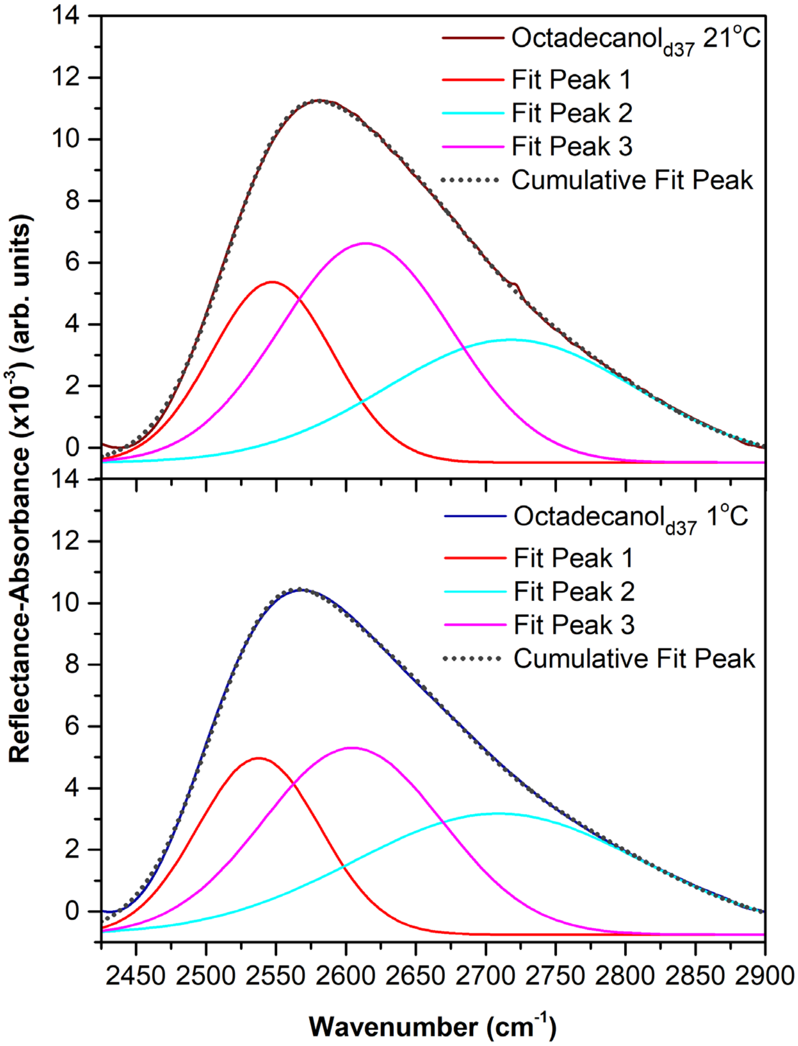

Figure 22. IRRAS spectra with corresponding Gaussian fits of a octadecanol-d$_{37}$ monolayer at 21 ºC (top) and 1 ºC (bottom) of the OD vibrational region at 40 mN/m spread onto a 5 % D_2O (10 % HOD) in water subphase.

Table 3. Center wavelengths (λ, cm^{-1}), reflectance–absorbance intensities (RA Int.), peak area, full width at half max (FWHM, cm^{-1}) values of Gaussian fits of the IRRAS spectra OH vibrational mode region of ocatadecanoic-d$_{35}$ acid monolayer and octadecanol-d$_{37}$ monolayer at 40 mN/m spread onto a 100 % water subphase at pH 5.6 and 21 °C.

ν OH Mode	Octadecanoic-d$_{35}$ acid (Stearic acid-d$_{35}$) 21 °C			
	Center λ	RA Int.	Area	FMHM
Peak 1	3265.6 ±21	6.3 ± 1.3	1477.3 ± 119	223.9 ± 34
Peak 2	3581.5 ± 2.9	8.9 ± 0.62	1152.0 ± 42.1	121.9 ± 6.5
Peak 3	3473.3 ± 18	8.3 ± 0.52	1748.7 ± 231	198.0 ± 17
Peak 4	3639.9 ± 0.59	3.9 ± 0.51	277.7 ± 40.2	67.4 ± 1.4
ν OH Mode	Octadecanol-d$_{37}$ (Stearyl-d$_{37}$ alcohol) 21 °C			
	Center λ	RA Int.	Area	FMHM
Peak 1	3246.7 ± 9.1	9.1 ± 1.9	1877.7 ± 235	196.3 ± 19
Peak 2	3578.3 ± 1.2	8.8 ± 0.20	1147.9 ± 45	122.4 ± 2.5
Peak 3	3450.3 ± 17	8.7 ± 0.91	1968.4 ± 330	211.4 ± 14
Peak 4	3640.8 ± 0.39	4.6 ± 0.10	353.3 ± 12	72.4 ± 1.1

Table 4. Center wavelengths (λ, cm^{-1}), reflectance–absorbance intensities (RA Int.), peak area, full width at half max (FWHM, cm^{-1}) values of Gaussian fits of the IRRAS spectra OH vibrational mode region of octadecanoic-d$_{35}$ acid monolayer and octadecanol-d$_{37}$ monolayer at 40 mN/m spread onto a 100 %water subphase at pH 5.6 and 1 °C.

ν OH Mode	Octadecanoic-d$_{35}$ acid (Stearic acid-d$_{35}$) 1 °C			
	Center λ	RA Int.	Area	FMHM
Peak 1	3322.8 ± 45	3.8 ± 0.24	1055.4 ± 175	263.7 ± 40
Peak 2	3578.5 ± 4.3	13 ± 0.50	1486.1 ± 88.0	110.7 ± 2.8
Peak 3	3497.9 ± 15	8.3 ± 0.27	1556.1 ± 142	176.0 ± 10
Peak 4	3629.4 ± 4.0	3.9 ± 0.72	245.3 ± 75.7	69.8 ± 7.5
ν OH Mode	Octadecanol-d$_{37}$ (Stearyl-d$_{37}$ alcohol) 1 °C			
	Center λ	RA Int.	Area	FMHM
Peak 1	3270.9 ± 5.3	4.5 ± 0.41	1057.3 ± 147	220.4 ± 12
Peak 2	3572.6 ± 2.8	12 ± 0.99	1468.9 ± 113	114.6 ± 0.74
Peak 3	3477.7 ± 5.2	8.3 ± 0.20	1665.1 ± 37.3	189.0 ± 0.36
Peak 4	3624.3 ± 3.5	4.3 ± 0.74	356.3 ± 77.4	78.3 ± 3.6

Table 5. Center wavelengths (λ, cm^{-1}), reflectance—absorbance intensities (RA Int.), peak area, full width at half max (FWHM, cm^{-1}) values of Gaussian fits of the IRRAS spectra OD vibrational mode region of octadecanoic-d$_{35}$ acid monolayer and octadecanol-d$_{37}$ monolayer at 40 mN/m spread onto a 5% D$_2$O (10% HOD) in water subphase at pH 5.6 and 21 °C.

ν OD Mode	Octadecanoic-d$_{35}$ acid (Stearic acid-d$_{35}$) 21 °C			
	Center λ	RA Int.	Area	FMHM
Peak 1	2547.9 ± 0.6	4.4 ± 0.19	487.3 ± 21.7	103.7 ± 0.21
Peak 2	2728.6 ± 3.4	2.8 ± 0.10	605.0 ± 17.1	202.8 ± 3.6
Peak 3	2615.7 ± 0.7	5.6 ± 0.40	884.4 ± 70.0	148.4 ± 1.2
ν OD Mode	Octadecanol-d$_{37}$ (Stearyl-d$_{37}$ alcohol) 21 °C			
	Center λ	RA Int.	Area	FMHM
Peak 1	2547.2 ± 0.6	5.9 ± 0.16	638.3 ± 17.7	102.5 ± 0.33
Peak 2	2719.8 ± 4.2	3.9 ± 0.13	1968.4 ±330	208.3 ± 5.0
Peak 3	2614.2 ± 0.7	7.2 ± 0.51	1114.7 ± 87.5	145.6 ± 6.5

Table 6. Center wavelengths (λ, cm^{-1}), reflectance–absorbance intensities (RA Int.), peak area, full width at half max (FWHM, cm^{-1}) values of Gaussian fits of the IRRAS spectra OD vibrational mode region of octadecanoic-d$_{35}$ acid monolayer and octadecanol-d$_{37}$ monolayer at 40 mN/m spread onto a 5% D$_2$O (10% HOD) in water subphase at pH 5.6 and 1 °C.

ν OD Mode	Octadecanoic-d$_{35}$ acid (Stearic acid-d$_{35}$) 1 °C			
	Center λ	RA Int.	Area	FMHM
Peak 1	2538.0 ± 0.65	4.7 ± 0.43	520.1 ± 43.8	104.6 ± 0.92
Peak 2	2709.7 ± 1.6	3.3 ± 0.38	832.1 ± 95.0	244.6 ± 0.67
Peak 3	2604.3 ± 1.1	4.9 ± 0.52	784.3 ± 78.1	152.2 ± 1.1
ν OD Mode	Octadecanol-d$_{37}$ (Stearyl-d$_{37}$ alcohol) 1 °C			
	Center λ	RA Int.	Area	FMHM
Peak 1	2537.7 ± 0.38	5.7 ± 0.29	624.5 ± 32.0	103.4 ± 0.20
Peak 2	2708.5 ± 0.60	3.9 ± 0.20	978.6 ± 45.7	242.2 ± 2.0
Peak 3	2604.4 ± 0.36	6. 0 ± 0.28	970.5 ± 45.7	121.1 ± 0.40

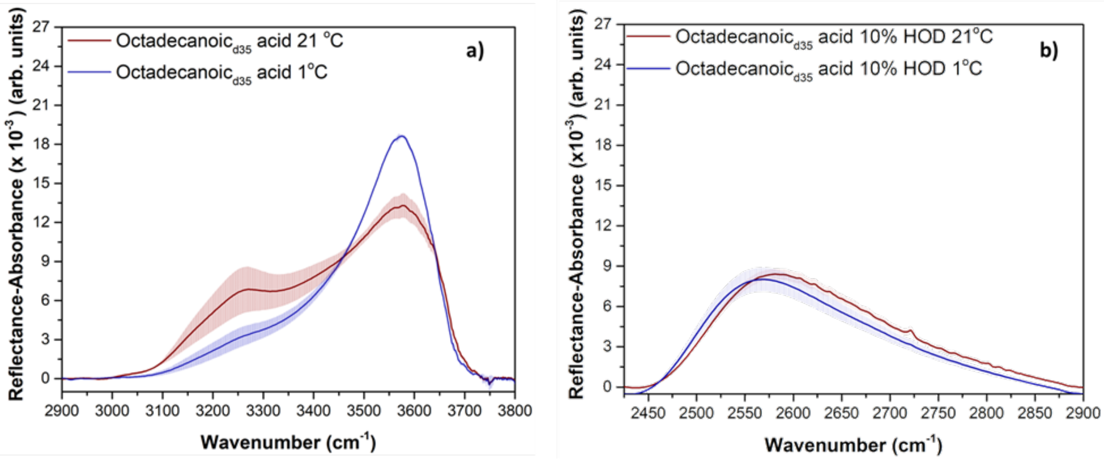

Figure 23. IRRAS spectra of the ν (OH) and ν (OD). a) Octadecanoic-d$_{35}$ acid illustrates the main ν (OH) bands one at 3600 cm^{-1}, typically attributed to the OH stretch of the groups weakly interacting with the neighbors and a 3250 cm^{-1} band due to strong interacting solvent (water) molecules at 21 ºC ± 1 (red) and 1 ºC ± 1(blue). b) shows the ν (OD) spectra region of octadecanoic-d$_{35}$ acid in 5% D_2O in water (10% HOD). (The OD and the OH oscillators are decoupled. The ν (OD) change in frequency as a function of temperature can be found in **Table 2**.

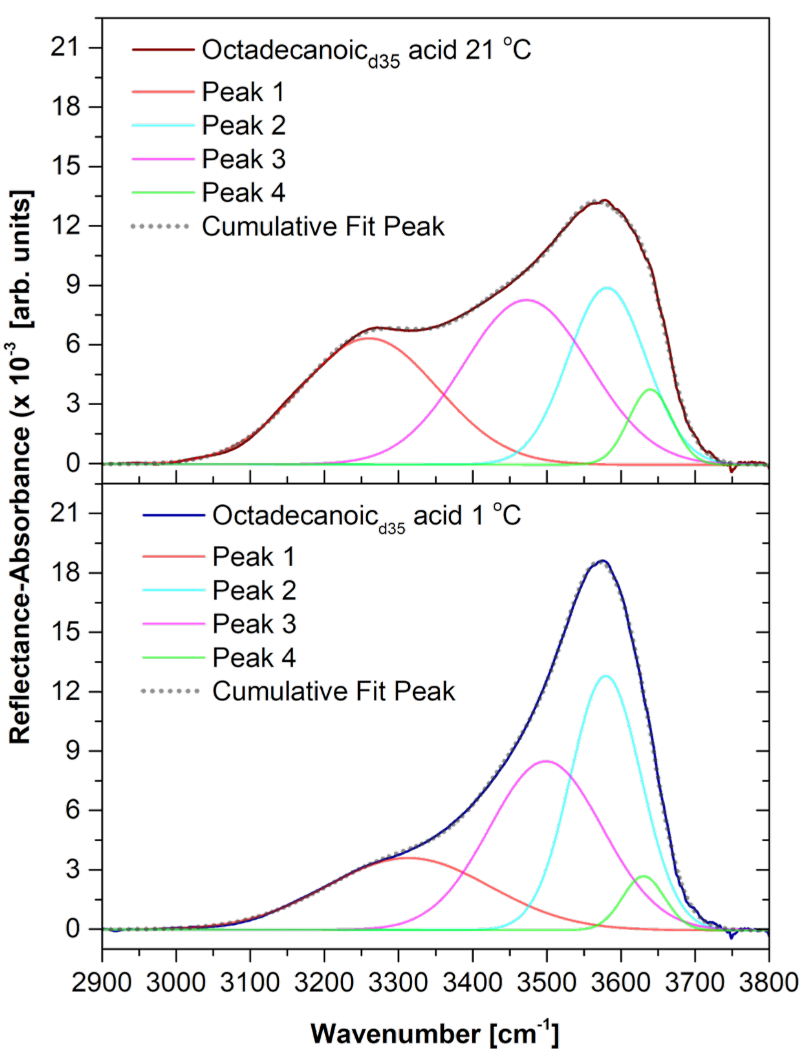

Figure 24. IRRAS spectra with corresponding Gaussian fits of an octadecanoic-d$_{35}$ acid monolayer at 21 ºC (top) and 1 ºC (bottom) of the OH vibrational region at 40 mN/m spread onto a 100 % water subphase.

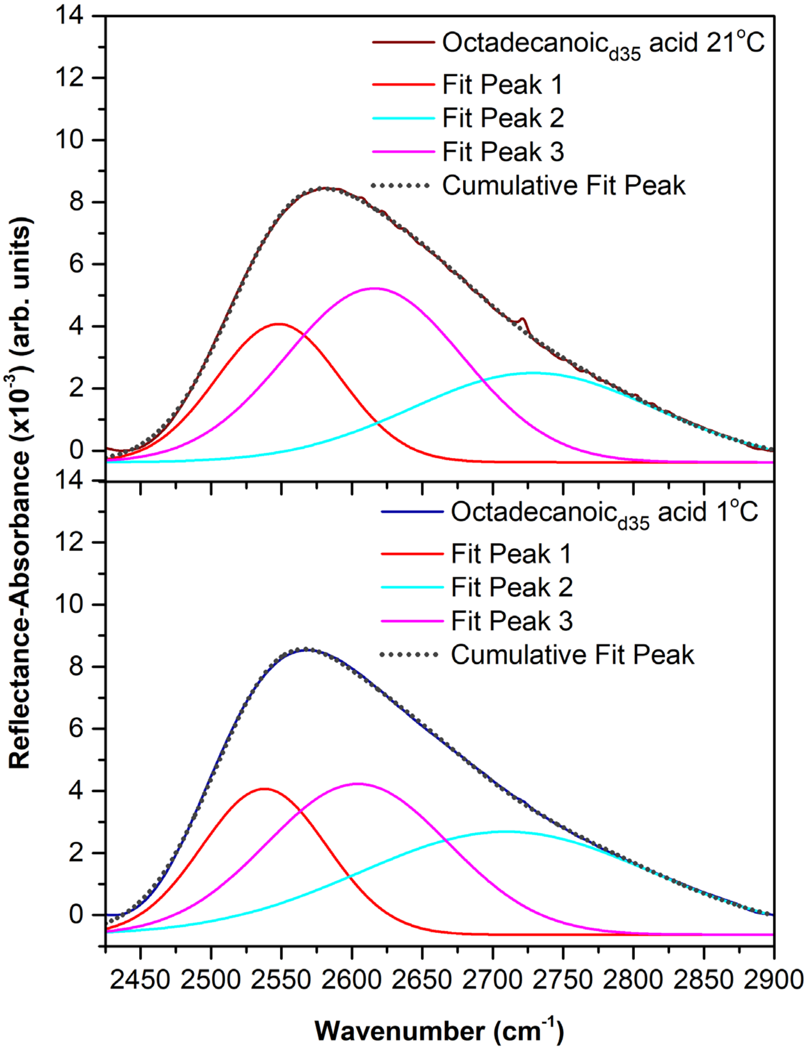

Figure 25. IRRAS spectra with corresponding peak fits of a octadecanoic-d$_{35}$ acid monolayer at 21 ºC (top) and 1 ºC (bottom) of the OD vibrational region at 40 mN/m spread onto a 5 % D$_2$O (10 % HOD) in water subphase

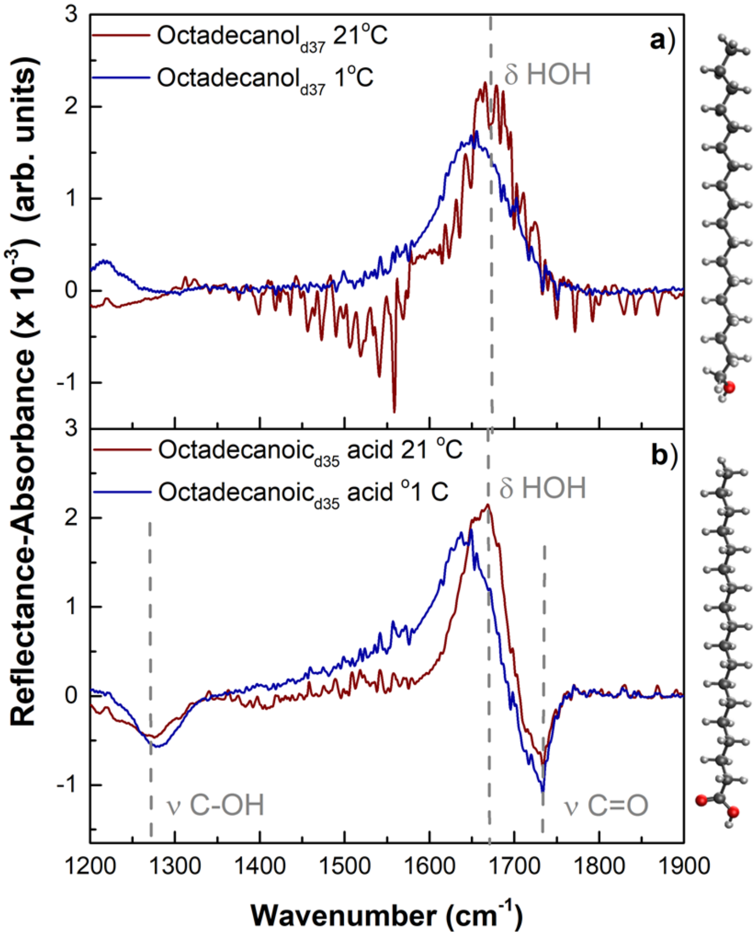

Figure 26. IRRAS spectra of the δ (OH) region of a) Octadecanol-d$_{37}$ (top), as well as b) Octadeconaoic-d$_{35}$ acid (bottom) where we can also observe the ν C═O and ν C–OH regions. Changes in intensity as well as frequency are observed. The changes in frequency can be found in **Table 2**. Both a) and b) at 21 ºC ± 1(red) and 1 ºC ± 1(blue).

Chapter 5. Relating Structure and Ice Nucleation of Mixed Surfactant Systems Relevant to Sea Spray Aerosol

Reproduced in part with permission from Perkins, R. J.; Vazquez de Vasquez, M. G.; Beasley, E. E.; Hill, T. C. J.; Stone, E. A.; Allen, H. C.; DeMott, P. J. "Relating Structure and Ice Nucleation of Mixed Surfactant Systems Relevant to Sea Spray Aerosol. *J. Phys. Chem. A*, **2020**, *124*, 8806-882.

5.1 Introduction

Clouds have important climate and weather effects due to radiative forcing and precipitation. Such effects are controlled by the phase state of cloud droplets. It is well known that pure water does not begin to freeze homogeneously until around –38 ºC. On the other hand, heterogeneous processes are responsible for freezing initiation under most atmospheric conditions.[224] For instance, in cloud droplets, heterogeneous freezing can be initiated by special rare aerosol particles known as ice nucleating particles (INPs). These INPs contain an active site known as the ice nucleating entity (INE) which is typically a small portion of the particle where its composition and structure in usually unknown.[224] Mineral dust is one of the most common and relative efficient INP sources near terrestrial regions.[225–227] INPs from the ocean are release via sea spray aerosol (SSA), and can be important in regions with little terrestrial influence.[228–230] The exact identities of ocean - sourced INEs are not certain, although there are several promising candidates. Cultures of several phytoplankton species have been shown to promote freezing, however the ice nucleation active components are not known.[231] Previous analysis of residual components of frozen particles suggest that 15 to 75% of the INPs that are active at –30 ºC are mainly composed of fatty acid particles, depending on the time period examined.[232] Surfactants such as fatty alcohols and fatty acid are produced biogenetically from the breakdown of cell membranes. Studies have shown that fatty alcohol monolayers are good ice nucleators,[233–236] however, different surfactant headgroups can produce quite different behavior. Previous, experiments on fatty acid freezing behavior have found that such monolayers are; however, poor ice nucleators, even though solid fatty acid particles show more promising INEs.[237]

Fatty alcohols have drawn a great deal of attention because they are one of the few simple surfactants with the ability to nucleate ice, which are also found in the environment. Prior studies have examined the ability of fatty alcohols to template ice an promote freezing.[238] Theoretical studies of this phenomenon have linked the freezing behavior to the surfactant 2D crystal structure at the water interface, with warmer freezing predicted for monolayers that more closely match the hexagonal ice crystal structure.[239] It has been shown that fatty alcohol films have a refreezing effect where such films better nucleate ice if they have been frozen previously.[240] This effect appeared to dissipate if the film was allowed to heat sufficiently between cycles. It was hypothesized that the effect was due to changes in the film structure. Zobrist *et al.* reproduced this effect.[235] Refreezing effects have been observed in dust material and parameterized in terms of modified classical nucleation theory, however the underlying mechanism remains uncertain.[241] Another class of refreezing effects has been attributed to ice preserved in pores,[242] although this requires the temperatures do not rise significantly above 0 °C which was not the case in the above experiments.

In the environment, a great degree of compositional complexity is expected. Although nascent SSA emissions show some selectivity toward surfactants,[58] they contain a variety of organic components and sea salt.[33,34,243] Little work has been done examining the freezing of mixed surfactant films. Previous work by Popovitz-Biro *et. al*.[234] generally showed freezing point depression for mixtures of alcohols of different chain length, and for 30 carbon (C-30) fatty acid-fatty alcohol mixtures. Thus, to better understand the ability of surfactants found in SSA to nucleate ice, this work has studied the composition, structure, and conditional dependence of model surfactant systems.

5.2 Experimental Methods and Material

5.2.1 Materials

5.2.1.1 Spectroscopy, Isotherms, and Imaging Sample Solution Preparation

Here sample solutions for isotherms, imaging, and spectroscopy were prepared with the following chemicals without further purification. Octadecanoic acid (stearic acid $CH_3(CH_2)_{16}COOH$, C_{18} fatty acid, >99%, Sigma-Aldrich) and octadecanol (stearyl $CH_3(CH_2)_{17}OH$, C_{18} fatty alcohol, 99%, Sigma-Aldrich) as well as deuterated octadecanoic acid (octadecanoinc-d_{35} acid (stearic-d_{35} acid, $CD_3(CD_2)_{16}CO_2H$, >98%, Sigma-Aldrich) and deuterated octadecanol (octadecanol-d_{37} (stearyl-d_{37} alcohol, $CD_3(CD_2)_{17}OH$, >98%, Cambridge Isotopes Laboratories) were dissolved in chloroform (HPLC grade, Fisher Scientific) to prepare ~3 mM C_{18} fatty acid and C_{18} fatty alcohol solutions as well as an ~3 mM 50:50 C_{18} fatty alcohol: fatty acid mixture for surface pressure−surface potential measurements and Brewster angle microscopy (BAM) experiments. An ~2 mM octadecanoic-d_{35} acid and octadecanol-d_{37} spreading solutions were prepared for infrared reflection−absorption spectroscopy (IRRAS). All experiments were performed on nanopure water, as a subphase, with a resistivity of 18.2 MΩ/cm (Milli-Q Advantage A10, EMD Millipore) and a pH of 5.6 due to atmospheric CO_2 acidification. The nanopure water was equilibrated at room temperature.

5.2.2 Methods

5.2.2.1 Surface Pressure and Surface Potential Area Isotherms

These measurements were performed in triplicate on Teflon Langmuir trough with Delrin barriers (KSV NIMA, Biolin Scientific, Espoo, Finland, area 549.08 cm^2). The trough and barriers were meticulously cleaned with reagent alcohol (histological grade, Fisher Scientific, Fair Lawn, NJ) and nanopure water and dry with N_2 gas to remove all water droplets . The surface potential (SPOT) sensor was coupled with the Langmuir trough, placing it in the middle of the trough within enough distance from edges. The counter electrode was placed in the trough making sure that the subphase completely covered it. The vibrating working electrode plate was placed about 1−2 mm above the subphase surface directly above the counter electrode. The SPOT sensor head was turned on at least ten minutes before starting the experiment. The surface pressure was measured using the Wilhelmy plate method using a thoroughly wetted filter-paper plate (Ashless Grade 41, Whatman, GE Healthcare, Chicago, IL). The trough was filled with the subphase of interest. Surface cleanliness (≤0.20 mN/m) was verified by sweeping the barriers at a maximum compression speed of 270 mm/min/barrier. A microsyringe (Hamilton, Reno NV) was used to spread the surfactant solution dropwise onto the subphase. Before the surfactant solution was spread, both the surface pressure and surface potential were zeroed. Ten minutes were allowed for solvent evaporation, and then symmetrical compression of the monolayer began at a rate of 10 mm/min (5 mm/min/barrier). These surface pressure−surface potential area isotherms were conducted at the following temperatures: 24, 16, and 2 ± 1.0 °C and a relative humidity of 35 ± 5%

5.2.2.2 Brewster Angle Microscopy (BAM) Imaging

BAM experiments were performed via a custom-built BAM setup, which has been previously described in the literature.[32,67,244] The 1.5 mW He−Ne laser source (Research Electro-Optics, Boulder, CO) emits polarized light at a wavelength of 543 nm with linear polarization. The *p*-polarized light travels through a Glan-laser calcite polarizer for further purification before being reflected off the aqueous surface. The BAM setup is mounted on a goniometer, which permits the adjustment of the angle of incidence to the Brewster angle of the air−water interface at 53.1°. The reflected light is then collected and collimated by a 10 × infinity-corrected superlong working distance objective lens (CFI60 Tu Plan EPI, Nikon Instruments, Melville, NY) and a tube lens (MXA22018, Nikon, Instruments, Melville, NY; focal length 200 mm). Then, the collimated light is collected by a back-illuminated EM-CCD camera (iXon DV887-BV, Andor Technology USA, Concord, MA; 512 × 512 active pixels, 16 µm × 16 µm pixel size). The BAM images were processed using ImageJ software (version 1.52a, National Institutes of Health, Bethesda, MD)[245] and cropped from their original size of 8.2 × 8.2

mm^2 to show the region of highest resolution. The dark regions of the BAM images correspond to the aqueous surface or to the less condensed phases of the surfactant, whereas the bright regions correspond to the surfactant domains. In this work, BAM was used to perform freezing and thawing experiments following the next procedure: (1) The subphase was decanted into the trough, previously cleaned using the procedure mentioned above, maintaining the temperature at 21 ± 1.0 °C. (2) The surface cleanliness was checked by sweeping the barriers at a maximum compression speed of 270 mm/minute/barrier. A surface pressure less than 0.20 mN/m was required before continuing. (3) After zeroing the surface pressure, a microsyringe (Hamilton, Reno NV) was used to spread the surfactant solution dropwise onto the subphase to a surface coverage of 30 Å^2 /molecule MMA, without barrier compression. (4) 200−250 frames were acquired before freezing was initiated. (5) The subphase was cooled to −10 ± 1.0 °C, where freezing began. The subphase was completely frozen after 1−2 h. (6) The subphase was then thawed to 21 ± 1.0 °C for 1−2 h. (7) 200−250 frames were taken after thawing. This process was performed for the pure C_{18} fatty acid and C_{18} fatty alcohol as well as the 50:50 C_{18} fatty alcohol: fatty acid mixture.

5.2.2.3 Infrared Reflection–Absorption Spectroscopy (IRRAS) Experiments

IRRAS is a surface-sensitive technique and has been used to obtain structural information of surfactants at the air–water interface. A custom-built IRRAS set up was utilized in the chamber of a Fourier transform infrared (FTIR) spectrometer (Frontier, Perkin-Elmer), with a liquid nitrogen cooled MCT detector. During the experiments, a Langmuir trough was placed inside the FTIR spectrometer. Two gold mirrors were used to reflect the IR beam off the surface of the water contained in the trough at an incidence angle of 48° from the surface normal. Each spectrum was collected as an average of 400 scans using an unpolarized light single beam mode over the full spectral range of 4000–450 cm^{-1} at a 4 cm^{-1} resolution, with 0.5 cm^{-1}step size. IRRAS spectra were plotted as reflectance-absorbance (*RA*). The *RA* is calculated as $-log (R_m/R_0)$ where R_m is the reflectivity of the monolayer and R_0 is the reflectivity of the subphase, in this case nanopure water. Data analysis was performed by using Origin software (OriginLab 9, Northampton, MA USA). The spectra shown here are plotted as an average of at least three individual spectra using the average function on Origin which has been baseline-subtracted by a 4th order polynomial. In order, to compare the spectra of the pure and the mixture solutions an additional scaling factor is required to account for the surface density of the films. To calculate this, the ratio of the MMA of the film in question to the fatty alcohol film was calculated. In this case all films were held at 40 mN/m, so the MMA used could be taken from the compression isotherms shown in **Figure 34**.

5.3 Results and Discussion

5.3.1 Film and Solid Structure

Ice nucleation depends on its structural characteristics, for this reason it is fundamental to consider the structure of the surfactant films and the variables that affect them. It is well known that composition, temperature, as well as surface pressure control the phase state of insoluble surfactant monolayers. An estimated phase diagram for the system studying here is shown in **Figure 28**. The phases illustrated in the diagram have been referred to by different names, with L_1, L_2, S, and CS being referred to as liquid expanded, liquid condensed, solid, and crystalline solid, respectively. Phases become more oriented and less tilted with increasing surface pressure and more crystalline (increased long-range order) with decreasing temperature. Following the phase changes in the diagram, moving from L_2 to L_2' to L_2'', the long-range order in the film increases. The LS to S to CS series follows a similar trend. The main difference between the two series is in their chain tilt, with the low-pressure series ($L_2/L_2'/L_2''$) having a tilted fatty tail groups and the high-pressure series (LS/S/CS) possessing the untilted ones. A detail discussion of the different phases can be found in Kaganer *et al*.[246] It should be noted that all of the data below 0 °C comes from measurements of longer-chain length (C_{20}−C_{24}) surfactants that have been shifted in temperature based on observed trends and is particularly uncertain.[246] The addition of equal chain fatty alcohol to the monolayer produces an expansion in the L_2' region. By fifty percent fatty alcohol composition, the L_2' phase completely replaced the L_2 phase in the C_{21} fatty acid in the 14–30 ºC temperature range measured.[247,248]

In both the environment and in ice nucleation freezing measurements, surface pressure is not completely controlled and is instead a function of the amount of material present on the surface as well as the temperature. Insoluble surfactants can be characterized based on their equilibrium spreading pressure (ESP), which is refer as the maximum equilibrium surface pressure that a surfactant can achieve after been deposited onto a water surface. Higher surface pressures can be achieved, for example by compressing surface material onto a smaller area, but would eventually relax to the ESP for the material.[29,172,249] It is known that ESPs are temperature-dependent. Previous studies have shown that octadecanoic acid has an ESP of 5–7 mN/m[250,251] and octadecanol an ESP of ~34 mN/m[251] that decrease with decreasing temperature.[252–254] Although measurements have not been made on supercooled water, ESPs less than 1 mN/m are predicted at temperatures where freezing occurs for all surfactant used in this study. Because of this, the relevant phases are the L_1, L_2, L_2', L_2" and the 3D solid. Here, we considered the 3D solid to be either the amorphous crystalline form of the surfactant while not in a monolayered, bilayered, or micellar state. The exact structure on the 3D solid is unclear given the formation mechanism and surfactant mixture. The entirety of the surfactant need not be present solely in one of these phases, there can be coexistence between them under some conditions. If the surface pressure is equal to the ESP, material can exist as the 3D-solid in addition to the 2D phases that exist. In addition, multiple 2D phases can coexist. In the case of fatty acid and alcohols, L_1 and L_2 phases coexist below about 1 mN/m. In addition, to further complicate the matte, at particular temperatures, depending on film composition, transitions between the L_2 phases occur, causing for a brief period for the 2D film exist in both L_2 phases. It is possible that multilayered structures or micelles could coexist with the film and 3D-solid phases, but under the conditions of the measurements they are unlikely to exist.[255,256]

In order to gain more insight into the organization of the film during nucleation, several surface-sensitive techniques were employed for these systems as a function of temperature. One of the first methods employed was compression isotherms and surface potential measurements, shown in **Figure 29**. Surface potential is measured as the difference in voltage from a clean water surface. In the presence of a surfactant, this voltage arises from anisotropic molecular orientations that yield a net dipole moment normal to the water surface. This can have contributions from the aqueous subphase, the surfactant headgroups, and the surfactant tails. In the case of fatty acids and alcohols, it indicates that the dipole of aliphatic tails dominates the changes in the surface potential.[175] Thus, the surface potential of these system can be used as a proxy for molecular orientation of the surfactants, with higher surface potentials indicating that the tails are more perpendicularly oriented to the water surface. For all systems as the films are compressed the surface potential increases and the mean molecular areas decrease.[68] Such result is expected, as the films become more condensed and oriented. However, it should be noted, that the increase in surface potential occurs at larger MMAs than the increase in surface pressure. This is due to a coexistence of L_1, and L_2/L_2' phases in this region, where the more surfactant exists in the L_2/L_2' phases as MMA is decreased. The increase in surface pressure marks the end of the coexistence region, where there is no longer surfactant in the L_1 phase.

Commonly, surface potential increases as temperature decreases for all systems, suggesting an increase in the ordering and orientation of the film, which is known to be beneficial for IN ability.[239] In the case of the fatty alcohol film, this is true for all phases. For the pure fatty acid film, the changes are smaller at the temperatures examined in this study. Yet, there is a large increase in surface potential when the $L_1$and L_2 mixed phases are cooled from 16 to 2 °C. The changes to the L_1 and L_2/L_2' mixed are the most relevant to ice nucleating behavior as the expected state of the film in the freezing experiments. Based on the IRRAS spectra shown in **Figure 30**, films remain hexagonally packed and miscible at 2 ºC. This indicates that the film structure of the mixture is similar to that observed previously for pure fatty acids and fatty alcohols close to room temperature. Destruction of the hexagonal structure would likely indicate a loss of ice nucleating ability, due to the requirement of lattice matching to ice,[239] and the hexagonal structure of ice crystals. Moreover, the compression isotherms also change upon cooling. Phase changes in the fatty acid film are pushed to smaller MMA, indicating more densely packed condensed regions. Furthermore, for the alcohol and acid films, collapse pressures increase with decreasing temperature, indicating more stable condensed films. The more tightly packed film promotes IN processed in these films,[239] however the role of compression stability is uncertain. The mixed film displays the opposite behavior for the pure counterparts: phase transition MMAs increase, and collapse behavior decrease at 2 ºC compared with the warmer films. Thus, while the mixed film gets less densely packed and less stable as it cools, it still becomes more ordered as indicated by the surface potential data. This produces competing effects on IN efficiency of the film, with the increased ordering expected to promote IN activity, while the decrease packing density diminishes it. By comparison, the pure films show increases in both packing density and ordering upon cooling, with both likely to produce more efficient freezing.

As suggested previously, another possible structure that could act as an ice nucleator is the 3D solid surfactant.[237] As the temperature is lowered and the system cools, the solid phase could stabilize over the monolayer phase resulting in the formation of a 3D solid. Such process would be analogous to crystal formation process from films previously studied at constant temperature, where the films are held above the ESP and the surfactant crystallization occurs and a 3D solid is observed.[250,251] These processes can be slow; however, the kinetics are uncertain during colling. To determine if this is possible from an initial staring point of a monolayer, with no 3D solid present, we can examine how the maximum equilibrium MMA changes with temperature. The ESP is essentially the surface pressure is which the surface becomes saturated, and additional material exist only in the 3D bulk phase. The maximin equilibrium MMA can be defined as the MMA at which the film exists for a given ESP and temperature. For fatty alcohol, the compression isotherm varies little while the ESP decreases with decreasing temperatures. The results show an increase in the maximum equilibrium MMA of the film as in cools and has been reported previously for pure fatty acid and fatty alcohol film.[254,257]

The changes in the film state as a function of temperature may provide some details into the mechanism of the refreezing effect. Such changes observed with decreasing in temperature, increasing film density and order, are expected to increase the freezing temperature of the film.[239] As the kinetics of some transitions in monolayer films can be quite slow, particularly at low temperatures, it is possible that the structural changes in the film persist once the film is returned to room temperature. There is also another possibility that a similar change could take place as the subphase freezes, and the polar side of the surfactant interacts with a quite different environment. Although, we do not have direct information regarding film morphology on an ice substrate, it is clearly a form with more favorable ice–surfactant binding or interactions, which are expected to produce warmer freezing temperatures as well.

Previous examinations of alcohol freezing have shown some dependence of freezing temperature on drop surface area. These observations have been interpreted in terms of temperature-dependence rates, through several different classical nucleation theory frameworks. Previous experiment performed by Seeley and Seidler[240] fit their data with two parameters: one proportional to the nucleation energy barrier and another considered attempt frequency. Based on this, they concluded that the majority of the change in freezing temperature was due to the energy barrier terms and suggested that the refreezing effects were due to structural changes in the film. Zobrist *et al.*[235] fit the data using one-parameter model which relates the contact angle between the film and the ice embryo to the effective nucleation energy barrier and letting the contact angle vary with temperature. They concluded that the film becomes a worse ice nucleator at lower temperatures. This contrasts the observed and predicted changes in the film, structure with decreasing temperature. This discrepancy amongst the measurements may indicate that the film is not the ice nucleating entity, but the 3D solid is instead, as discussed above. It could also be that the different theoretical framework may resolve the apparent disagreement.

To examine this further, BAM images were taken of the films before and after freezing and are shown in **Figure 31**. In these images the bright regions of the images reveal the areas where the film is present which correspond to a more condensed phase, whereas dark regions correspond to areas with lower surfactant densities regions.[258] There are several differences observed in the different systems. The fatty acid monolayer appears to have fewer of the smallest (less than ~10 μm) domains compared to the fatty alcohol and has large noncircular domains that are absent for the alcohol. In the case of the 50:50 mixture, it appears to contain only the smaller circular domains of less condensed film prior to freezing. Upon freeze–thaw cycling, the morphology of the pure alcohol and acid films are preserved, but significant differences are observed for the mixed film: large, circular, or oval dark domains become prevalent, and the images become more reminiscent of the alcohol film. Domain shape is determined by the balance between line tension and long-range electrostatic forces in the film.[259–261] While it is difficult to determine exactly what energetic changes have occurred to validate the change in the morphology of the mixed film, it is certainly driven by a change in packing by one or more of the phases present.

Relating the BAM studies to the phase diagram illustrated in **Figure 28**, a possible explanation for the 50:50 mixed film case is that cooling promotes a transition from L_2 to L_2' phase state. This phase state then persists upon thawing due to kinetic trapping: at room temperature, L_2 state is more stable, but reorganization of the film is slow, so the film remains in the L_2' state. This is consistent with the morphological similarity between the freeze–thaw cycled mixed film and the pure alcohol film, which exists in and L_2' phase state at room temperature. The main difference among the L_2 and L_2' states is in long-range order, which is certainly expected to change the controlling factors of the domain shape.[259–261] Kinetic trapping for the film state could explain the refreezing effect in this experiments. The first time the system is frozen, a reorganization happens in the film. Based on the experiments performed, upon thawing the film does not return to its previous state immediately but does gradually. The low-temperature, or ice-bound, film structure is likely to be a better ice nucleator given the higher degree of crystallinity, closer packing, and more energetically favorable ice binding that are expected to occur.[239] While this explanation is consistent and supported by the experiments, it is perhaps not the only possibility. The 3D solid phase can form upon cooling to some extent and very likely to be kinetically trapped and persist upon warming as well. Only small amounts would be required and would not necessarily be observed in the BAM images. The required sizes for crystal to be effective ice nucleator are in the order of the germ or critical ice embryo size.[262] For homogeneous freezing, the ice germ size decreases with decreasing temperature and is ~10 nm diameter at –25 °C.[263] For heterogeneous freezing, discussed here, the size is expected to be approximately the same.[241] Thus, 3D solid surfactant crystals need only be on the order of 10 nm in diameter to be effective ice nucleators. With the two possibilities for refreezing IN active sites, the reconstructed film or the solid, and evidence that both are formed upon cooling, comparisons of freezing studies on the solid surfactant particles can be made to determine which is most likely to occur.

5.4 Conclusions

Mixed films of these two surfactants retain some ice nucleating ability, even in fatty acid-dominated films. Here we have examined in depth the changes to partitioning of surfactant between phases upon cooling. As films cool, they can enter more crystalline states. BAM studies suggest that these film states persist upon warming and could be responsible for the refreezing effect that is observed. Thermodynamic considerations indicate that as the film cools ESP decreases, and the maximum equilibrium MMA increases. This forces a less compact film and material partitions to the 3D solid phase. This partitioning allows for IN processes to occur on the 3D solid in addition to the film, even for initial states of fully spread monolayers. The 3D solid phase is also likely to be kinetically trapped as the system warms. Because these structural changes occur simultaneously, it is difficult to say with certainty whether the film or the solid is the INE in these experiments. There is also evidence in support of both potential sites allowing for IN to take place, and it is possible that the dominant site changes between the solid and film depending on experimental conditions.

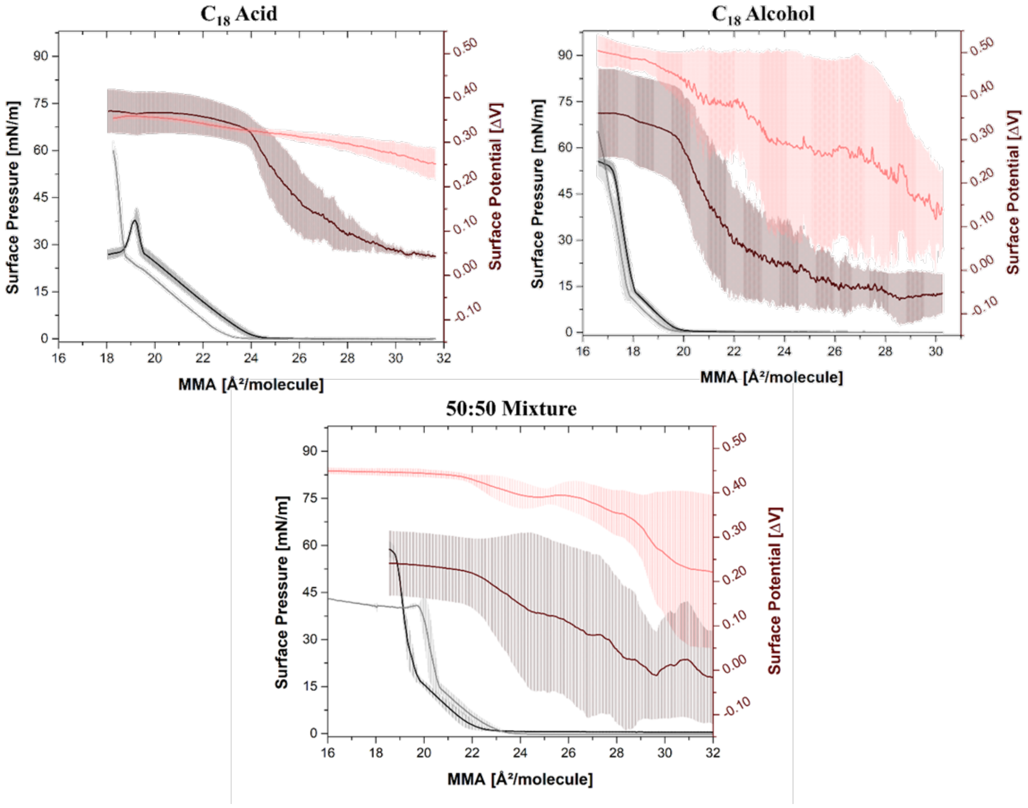

Figure 27. Surface pressure and surface potential during compression isotherms at 24 and 2 °C. Surface potentials are shown in maroon (24 °C) and pink (2 °C). Surface pressures are shown in black (24 °C) and grey (2 °C). Shaded regions show standard deviation of three trials. Films were composed of pure C_{18} fatty alcohol film (top right), pure C_{18} fatty acid film (top left), and 50:50 mixture of the two (bottom middle).

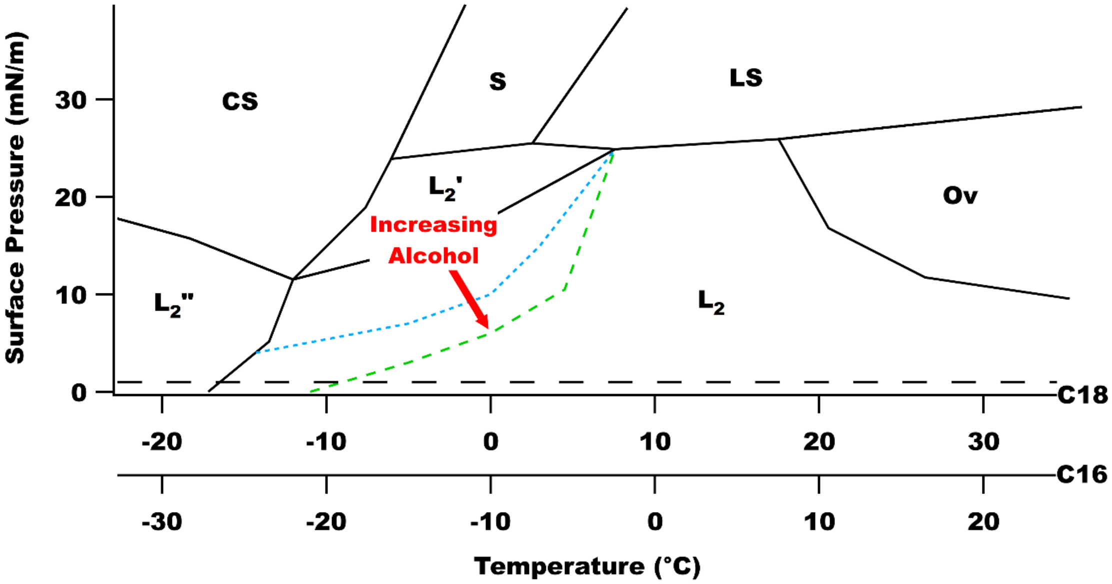

Figure 28. Approximate phase diagram of two dimensional fatty acid films on liquid water (black lines), reproduced from data in Kaganer *et al.*[246] Below the black dashed line, the L_1 phase can coexist with the L_2/L_2'/L_2'' phase. X axes show transition temperatures for 18 and 16 carbon films, following the observed approximate shift of 10 °C with every additional two carbons. Blue and green dashed lines show changes to the L_2'-L_2 phase boundary upon addition of fatty alcohol of the same chain length.[247,248] Phase boundaries for the S and LS phases are relatively unchanged with this addition,[247,248] and insufficient data is available to determine changes in the L_2'' and CS phase boundaries, data from and discuss in Perkins *et al.*[45]

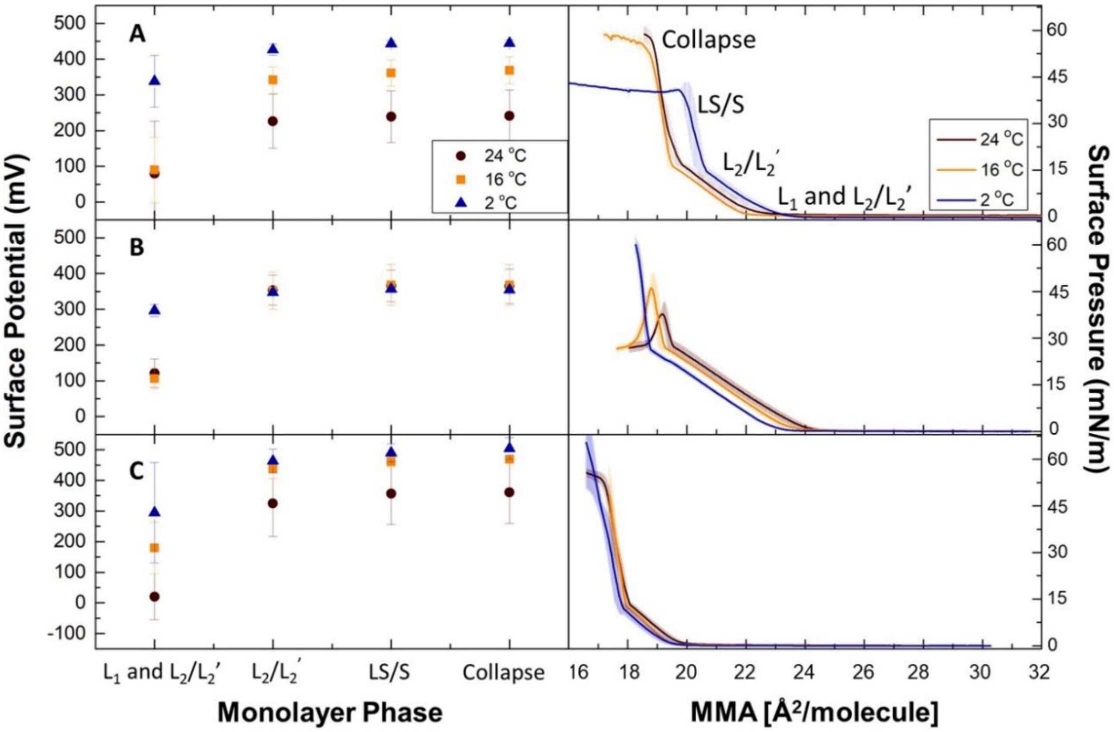

Figure 29. Changes in surface potential of C_{18} monolayers as a function of film density. The left panels show surface potential measurements, and the right panels show surface pressure and film phases, separated by changes in slope, as a function of film mean molecular area. Data for surface pressure and surface potential are collected concurrently on the same film. Graphs **A**, **B**, and **C** correspond to 50:50 mixture, pure fatty acid film, and pure fatty alcohol film, respectively. Exact MMAs used for each surface potential point are chosen to correspond exactly with the associated phase and can be found in **Table 7** and full surface potential scans in **Figure 34**.

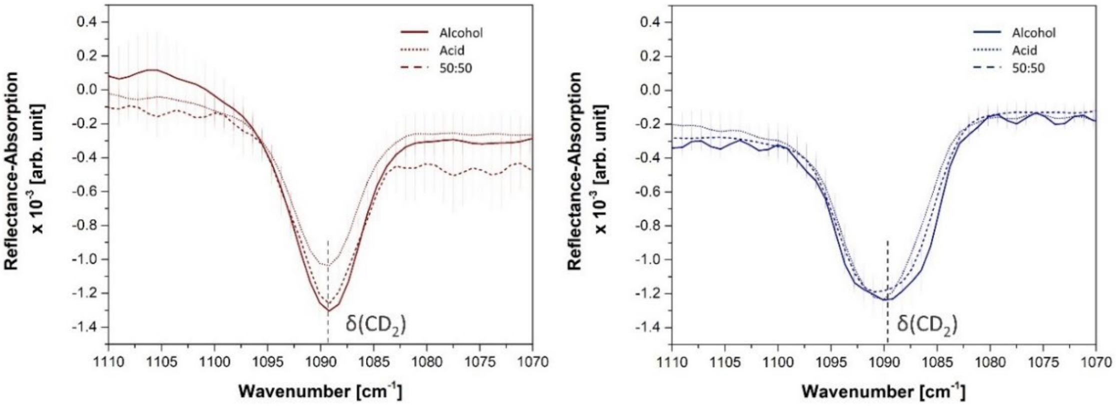

Figure 30. Vibrational modes associated with the CD_2 scissoring mode (δ CD_2) of the alkyl chain of a deuterated C_{18} fatty acid and alcohol monolayers. Spectra on the left were collected at 24 °C and spectra on the right at 2 °C. Monolayers usually can pack in the three different lattice patterns: hexagonal (δCH_2 1468 cm^{-1}, δCD_2 1089 cm^{-1}), triclinic (δCH_2 1471 cm^{-1}, δCD_2 1092cm^{-1}) and orthorhombic (δCH_2 1462/1474 cm^{-1}, δCD_2 1084/1094 cm^{-1} doublet).[29,71,120,264] Due to differences in the interchain vibrational interactions of the surfactant molecules each lattice packing structure results in a unique scissoring mode frequently. At a frequency of 1089 cm^{-1}, it is determined that the C_{18} fatty acid, fatty alcohol and 50:50 mixture comprising the monolayers are packed in hexagonal arrangements at both temperatures. Because of the single peaks at both temperatures, this also supports the idea that the films remain miscible, as splitting of the peak would likely occur with two different hexagonal phases. Changes in shoulder heights are almost certainly due to baselining procedures described in the experimental section, and not changes in the film.

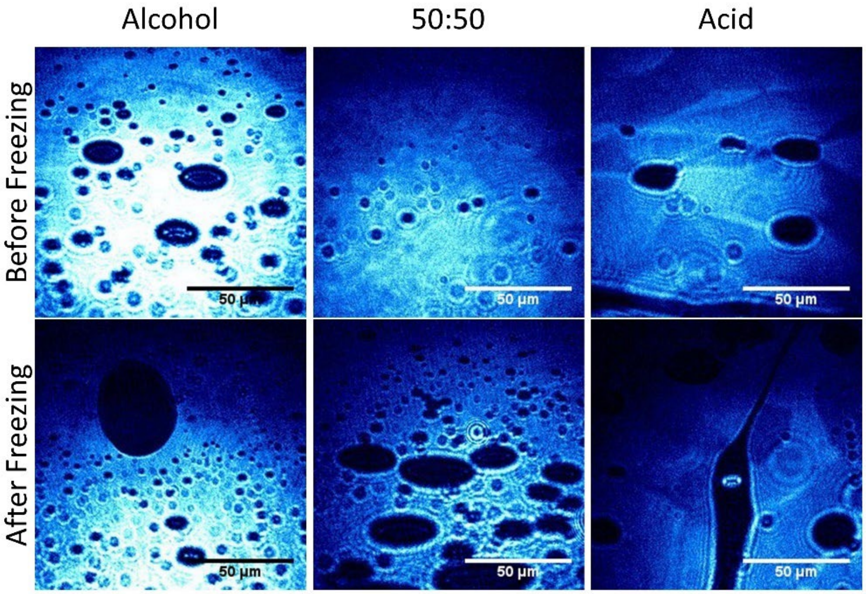

Figure 31. Representative Brewster Angle Microscopy images of pure and mixed fatty acid and fatty alcohol films, before and after freezing of the subphase. Top row shows images before freezing, while bottom row shows images after freezing. From left to right are the alcohol, 50:50 mixture, and the acid. Bright regions depict areas of thicker film, corresponding with more condensed phase, and dark areas with less surfactant density. Images were taken at 21 °C and 30 Å^2/molecule MMA.

Table 7. Exact MMAs used for each surface potential point which correspond exactly to the associated phase

Compound	**Phase**	**Temperature (°C)**	**MMA Range (Å^2/Molecule)**
Fatty Alcohol	L_1-L_2/L_2’	24	31.30-20.00
Fatty Alcohol	L_2/L_2’	24	20.00-18.00
Fatty Alcohol	LS/S	24	18.00-17.20
Fatty Alcohol	Collapse	24	17.20-16.60
Fatty Acid	L_1-L_2/L_2’	24	31.65-24.18
Fatty Acid	L_2/L_2’	24	24.18-19.57
Fatty Acid	LS/S	24	19.57-19.25
Fatty Acid	Collapse	24	19.25-19.18
50:50	L_1-L_2/L_2’	24	31.67-22.51
50:50	L_2/L_2’	24	22.51-19.81
50:50	LS/S	24	19.81-18.66
50:50	Collapse	24	18.66-18.56
Fatty Alcohol	L_1-L_2/L_2’	16	31.30-19.50
Fatty Alcohol	L_2/L_2’	16	19.50-17.96
Fatty Alcohol	LS/S	16	17.96-17.40
Fatty Alcohol	Collapse	16	17.40-17.37

Continued

Table 7. Continued

Fatty Acid	L_1-L_2/L_2’	16	31.65-24.00
Fatty Acid	L_2/L_2’	16	24.00-19.30
Fatty Acid	LS/S	16	19.30-18.86
Fatty Acid	Collapse	16	18.86-19.79
50:50	L_1-L_2/L_2’	16	31.68-22.51
50:50	L_2/L_2’	16	22.51-19.54
50:50	LS/S	16	19.54-18.72
50:50	Collapse	16	18.72-17.20
Fatty Alcohol	L_1-L_2/L_2’	2	31.30-19.50
Fatty Alcohol	L_2/L_2’	2	19.50-17.85
Fatty Alcohol	LS/S	2	17.85-16.70
Fatty Alcohol	Collapse	2	16.70-16.60
Fatty Acid	L_1-L_2/L_2’	2	31.65-23.50
Fatty Acid	L_2/L_2’	2	23.5-18.80
Fatty Acid	LS/S	2	18.80-18.30
Fatty Acid	Collapse	2	18.30-18.27
50:50	L_1-L_2/L_2’	2	31.68-23.51
50:50	L_2/L_2’	2	23.51-20.65
50:50	LS/S	2	20.65-19.81
50:50	Collapse		19.70-19.59

Chapter 6. Zinc-Carboxylate Binding in Mixed Octadecanoic Acid and Octadecanol Monolayers on Proxy Seawater Solution Surfaces

Reproduced in part with permission from Auvil N. C.†;Vazquez de Vasquez, M. G.†; Allen, H. C. "Zinc–Carboxylate Binding in Mixed Octadecanoic Acid and Octadecanol Monolayers on Proxy Seawater Solution Surfaces". *ACS Earth Space and Chem.*, **2021,** 2021, 5, 10, 2947–2956.

6.1 Introduction

The air–water interface houses unique chemical and physical phenomena that can be considerably different than in the aqueous solution phase.[265–275] Surfactants, which are surface active molecules that possess both hydrophobic and hydrophilic characteristics, gather in the interfacial region.[276] The air–water interface gives rise to preferred orientations of these surface active molecules such that the hydrophobic portion stays in the air phase and the hydrophilic portion interacts with the solution phase (i.e. the interfacial or subsurface water), thus minimizing the free energy of the surface.[277] Following this principle, water-soluble organic molecules generally gather at the ocean's surface to form a film called the sea surface microlayer (SSML); these molecules are then transferred from the SSML to sea spray aerosol (SSA) during mechanical wave action and bubble bursting.[278,279]

Two important types of surfactant molecules naturally found in the SSML are fatty acids and fatty alcohols.[280–282] These molecules were recently discovered to exist in a nine to one ratio in oceanic emission samples.[283] Octadecanoic acid (OA, stearic acid, $C_{18}OOH$), a C_{18} saturated fatty acid, is known to be enriched in SSA, and octadecanol (OL, stearyl alcohol, $C_{18}OH$) is its C_{18} saturated fatty alcohol analogue.[284,285] OA is often used as a proxy for the organic film on SSA surfaces because it is the most predominant oceanic fatty acid along with hexadecanoic acid (palmitic acid, $C_{16}OOH$), both of which are derived from biogenic material including marine organisms.[286–288] An aim of this study is to emulate and observe the behavior of mixed monolayers containing OA and OL in ocean relevant ratios to provide insight on how film composition impacts metal–carboxylic acid binding and thus metal cation enrichment at the air–aqueous interface.

With an average concentration of 468 mM, Na^+ is the most concentrated metal ion in the ocean.[289] Zn^{2+} is known to have an average oceanic concentration of 6 nM and a high SSML enrichment factor relative to other oceanic metal ions despite its low concentration.[289,290] The total concentration of multivalent trace metals in the ocean is estimated to be about 164 nM.[289] Trace metal ions like Zn^{2+} have seawater concentrations various orders of magnitude lower than major metal ionic components like Na^+ and Mg^{2+}, yet have been found to be enriched in SSA at significantly higher relative proportions.[289,291] Ion–surfactant interactions are hypothesized to cause this disparity in SSA enrichment. Na^+ partakes in weak ionic interactions with surfactant headgroups.[292] Contrary to monovalent Na^+, multivalent metals have the ability to form strong ionic and, in some cases, covalent bonds with surfactant headgroups. Trace metals such as Zn^{2+} have previously been identified in the SSML at concentrations reaching one hundred times above those found in the subsurface bulk seawater, indicating significant enrichment factors.[290,293] When wave breaking or bubble bursting events occur, surfactant-bound trace metals can be transferred into sea spray aerosol.

Aspects of surfactant film structure including surface molecule orientation and packing can be altered by interactions with ions.[290,294,295] Previous studies have shown considerable ordering effects when divalent cations such as Zn^{2+} interact with a fatty acid film composed of OA, showing strong binding and even metal-induced deprotonation of the –COOH group.[290,296,297] On the other hand, monovalent Na^+ is not expected to interact as strongly with the carboxylate headgroup due to its smaller charge and larger ionic radius.[290,295] When compared to the metal complexation strength of OA, OL's binding affinity is assumed to be negligible due to its hydroxy headgroup.[290]

The main goal of this study is to probe the effect of mixed monolayer composition on trace metal binding with monolayers composed of fatty acid and fatty alcohol molecules, typical components in SSML and SSA. Mixed monolayers of OA and OL are thus systematically evaluated at four different ratios, and each ratio is studied on eight aqueous solutions of differing concentrations of $ZnCl_2$ while maintaining a constant NaCl seawater concentrations.[290] In this study, Zn^{2+} is chosen as the model trace metal due to its previously reported interaction strength with OA and its large enrichment factors in sea spray aerosol.[290,298] Infrared reflection–absorption spectroscopy (IRRAS) is used to probe these surface films and to quantify apparent surface binding constants using the integrated areas of carboxylate asymmetric stretch peaks as reporters.

6.2 Experimental

6.2.1 Materials and Sample Preparation

The materials were purchased and used without further purification unless otherwise noted. Octadecanoic acid (OA, stearic acid, a C_{18} fatty acid, Sigma-Aldrich, $\geq$ 98.5% grade 1) and octadecanol (OL, stearyl alcohol, a C_{18} fatty alcohol, 99%, Sigma-Aldrich) were dissolved in chloroform (HPLC Grade, Fisher Scientific) to make ~3.8 mM OA and OL stock solutions. These solutions were combined in varying proportions to prepare ~3.8 mM mixed solutions at the ratios 100:0, 95:5, 90:10, and 85:15 OA:OL (w/w). Sodium chloride salt (NaCl) (99.999% trace metals basis, Aldrich, and 99.998% trace metals basis, Fisher Scientific) was baked in a furnace at 675 °C for >8 hours to remove possible organic contamination. Zinc chloride salt ($ZnCl_2$) (99.999% trace metals basis, Aldrich) was used as purchased. NaCl and $ZnCl_2$ salt solutions were prepared using ultrapure water with a resistivity of 18.2 MΩ•cm (Milli-Q® Advantage A10, Millipore Sigma, Burlington, MA). The NaCl solution was filtered through Dionex OnGuard II M cartridges (Thermo Fisher Scientific) to remove possible trace metal impurities. NaCl and $ZnCl_2$ solutions are combined in the Langmuir trough to create the solution. The measured pH of the mixed salt solutions was 5.7 ± 0.15.

6.2.2 Surface Pressure–Area Isotherms

Although surface pressure–area (Π–A) isotherms were not directly utilized in determining the Zn^{2+}–carboxylate surface binding constants, they were necessary for maintaining monolayer surface pressure during IRRAS scans and calibrating surfactant solution concentrations. (Π–A) isotherms were performed on a Teflon Langmuir trough with an area of 144.5 cm^2 fitted with movable Delrin barriers (KSV NIMA, Finland). Surface pressure (Π) was measured using custom cut filter paper Wilhelmy plates (ashless grade, Whatman). The trough and barriers were thoroughly rinsed with reagent alcohol (Histological Grade, Fisher Scientific) and nanopure water and dried before each trial. After the aqueous solution is added to the trough, surface is checked for contamination by compressing the barriers and ensuring that the surface pressure does not rise above 0.20 mN/m. The surfactant solutions were spread onto the surface dropwise using a microsyringe (Hamilton). Ten minutes were allowed for chloroform evaporation before compression. The resulting monolayer was compressed at a constant rate of 5 mm/min/barrier until a surface pressure of 35 mN/m was achieved. The barriers then moved back and forth synchronously at a slow rate of 1 mm/minute/barrier to maintain this surface pressure. All experiments were replicated three times to ensure reproducibility. The concentrations of the OA and OL stock solutions were calibrated to 24 and 21 Å^2/molecule, respectively.[299] All trials were run at 21 ± 1 °C and at a relative humidity of 31 ± 9%.

6.2.3 Infrared Reflection–Absorption Spectroscopy

Infrared reflection–absorption spectroscopy (IRRAS) was the main technique utilized to analyze Zn^{2+}–carboxylate binding. All IRRAS spectra were collected with a Fourier transform infrared (FTIR) spectrometer (Frontier, Perkin Elmer) equipped with a cooled liquid -nitrogen HgCdTe (MCT) detector. The Langmuir trough is placed inside the FTIR on a breadboard alongside two planar gold-plated mirrors positioned such that the beam reflects off the monolayer at an incident angle of 48° relative to surface normal

(**Figure 32** and **Figure 33**). The incident unpolarized IR beam is reflected off the input gold mirror and onto the surface, where the beam interacts with the interface and is then reflected to the output mirror and finally to the detector. IRRAS scans were taken at 35 mN/m, a surface pressure at which the monolayer is in the untilted condensed phase. All spectra were collected as soon as reaching the surface pressure of 35 mN/m.

IRRAS provides information about molecules at and near the air–water interface. Even though IRRAS is not explicitly surface-specific because infrared reflected light has a probe depth of a few μm, this technique is selective to probe surface monolayers due to ratioing of the reflectivity of the spread monolayer on the solution (R) to that of the spectral solution reflectivity (R_0).[300–305] The reflectance–absorbance (RA) is found using equation 6.1 and is then plotted versus frequency.

$$RA = -log_{10}\left(\frac{R}{R_0}\right). \qquad (6.1)$$

The analysis of RA data is based on spectral band frequency and intensity. Hydrocarbon chain conformation of the surfactants in the monolayer can be determined by evaluating the CH_2 symmetric and asymmetric stretching vibrational bands.[303] Additionally, the vibrational modes of the surfactant molecules' headgroups provide information about aqueous ion–surfactant binding interactions.[269,275,290,306] Surface binding affinities can be quantified via IRRAS using the techniques presented by Neal *et al*. and by Ariga.[269,275]

Each spectrum is an average of 400 scans in single beam mode with a resolution of 4 cm^{-1} within the range 4000–450 cm^{-1}, with a 0.5 cm^{-1}step size. RA spectral baselines were corrected using a 4th order polynomial in the region of interest in addition to other minor data processing (OriginLab 9, Northampton, MA). All spectra shown here are averaged from at least three spectra using Origin Pro 9's average function. The reported spectral uncertainties are considerable mostly due to spectral noise from insufficient or over subtraction of water vapor absorption. Humidity above the monolayer surface can be an issue, especially in the carboxylate region (**Figure 35**).[307,308] Given these interferences, note that for the 0, 10, and 25 mM Zn spectra in **Figure 36** and **Figure 37**, the water vapor line centered at 1559 cm^{-1} was removed as it obscured the band of interest. In addition, the sharp line centered at 1542 cm^{-1} in the 90:10 and 85:15 spectrum was removed for the same reason (see **Table 8** for values). Complete removal of gas phase water lines due to the high humidity of the lab air during acquisition days is nontrivial. Reported binding affinity errors incorporate both spectral and fitting uncertainties.

To determine the influence of monolayer composition on trace metal surface binding, surfactant headgroup-ion interactions were probed using surface-sensitive IRRAS in conjunction with Π–A isotherms (**Figure 32**). The OA:OL monolayer ratios examined were 100:0, 95:5, 90:10, and 85:15 (**Figure 38**). Each monolayer ratio was analyzed over aqueous solutions consisting of a constant NaCl background of 468 mM with eight varying $ZnCl_2$ concentrations between 0 and 25 mM. When the highest concentration of $ZnCl_2$ is included in the NaCl solution, the ionic strength increases to 543 mM. While the largest difference in molarity across all aqueous solutions is 25 mM, the difference in ionic strength is 75 mM due to the charge of the zinc ion. The molecular interaction of interest is the binding of divalent metal cations, Zn^{2+}, to the carboxylate headgroups within the monolayer. The intensity of the asymmetric carboxylate band at each concentration is normalized and fit to an adsorption curve to calculate the surface binding constant of Zn^{2+} at each ratio of fatty acid to fatty alcohol. This allows for quantitative comparison of binding between the four monolayer compositions.

6.3 Results and Discussion

A pure monolayer is composed of only one type of surfactant at the air–water interface, whereas a mixed monolayer contains a combination of two or more surfactants.[309] Due to the vast diversity in sources from which atmospheric and oceanic organic molecules originate, mixed monolayer films are more suitable for the purpose of representing SSA and the SSML. Experimental techniques and molecular dynamics simulations have both been used to study the interfacial properties of mixed monolayers at the air-water interface.[286,310,311] Surface properties of binary mixtures of fatty acids with other organic molecules such as amines, esters, cholesterols, and alcohols have received significant attention during the past two decades.[310,312,313] These studies have revealed substantial differences between the physical and chemical properties of a pure fatty acid monolayer and a mixed monolayer that contains fatty acid. The inclusion of a secondary surfactant in a fatty acid monolayer has been shown to alter film packing structure[286], thermodynamic behavior[313], and monolayer stability.[310] Despite the considerable impact monolayer composition can have on film structure and stability, single-component monolayer studies dominate the field.[288,290,292,294–296,306,314–318] To the author's knowledge, no previous studies have investigated how monolayer composition impacts trace metal surface enrichment.

While the complexity of mixed monolayers allows for better representation of real-world systems, it also creates experimental challenges. One challenge is the physical design of a mixed monolayer. Immiscibility of two or more surfactants can create two-dimensional domains, which are island-like structures on the water's surface. This is in contrast to a miscible film in which two or more types of surfactants mix to form an ideal homogenous film.[309] In 2015, Lee et al. conducted a study to determine the best method for generating a homogenously mixed multi-component monolayer that contained OA and other surfactants.[319] Lee et al. found that the main factor in monolayer mixing is the spreading method used in preparing the monolayer. When OA and the other surfactant are prepared in separate organic solutions and spread individually onto the aqueous solution, the two surfactants cannot mix well, resulting in distinct domain formation.[319] However, when OA and the other surfactants are pre-mixed in the solvent prior to spreading on the aqueous solution, a well-mixed monolayer is formed.[319]

Monolayers in this study were compressed and held at a surface pressure of 35 mN/m with an approximate mean molecular area of 21.5 Å^2/molecule while IRRAS scans were taken. At this surface pressure, a monolayer of OA on a Zn^{2+}-containing solution exists in the highly ordered untitled condensed phase.[306] While this system is not at equilibrium, the highly ordered metastable state may be more representative of atmospheric and ocean films in nature. Active wave oscillation at the ocean's surface and the shrinking of SSA particles in the atmosphere due to evaporation can cause surface films to expand and condense, resulting in deviation from the equilibrium state. Because these film perturbations are ubiquitous in moving or turbulent water, a non-equilibrium system is suitable for their emulation. Additionally, fatty acid molecules such as OA have been found to form complex 3D aggregates at the air–water interface under certain conditions, disrupting the 2D monolayer structure.[320] The high surface pressure and ionic strength used in this study may play a role in inhibiting the formation of these aggregates, thus stabilizing the monolayer throughout measurement.[315]

IRRAS spectra in the alkyl region of OA:OL mixed monolayers spread on solutions of 25 mM $ZnCl_2$ and 468 mM NaCl are shown in **Figure 34.** The methylene asymmetric stretch ($\nu_{AS}(CH_2)$) is found at 2918 cm^{-1} and the methylene symmetric stretch ($\nu_S(CH_2)$) is found at 2851 cm^{-1}. The positions of these two modes indicate that the monolayer's hydrocarbon tails take an all-trans conformation.[294,303,306,321] These vibrational modes are located at the same wavenumbers for all different aqueous $ZnCl_2$ solution concentrations **(Figure 39**), conveying that the presence of Zn^{2+} does not impact hydrocarbon tail ordering. In addition, the intensities of the modes in **Figure 34** are the same across all four monolayer compositions, indicating mixed monolayers of different OA:OL ratios have equal alkyl chain surface concentrations.

While there is no noticeable variation between the alkyl regions of the four monolayer compositions in **Figure 34,** there are large spectral differences in the carboxylate region when each monolayer composition is analyzed on a range of aqueous $ZnCl_2$ solution concentrations (**Figure 37**). All spectra have had the aqueous solution background spectrum subtracted and therefore contain information specific to the monolayer film. The full set of IRRAS spectra was utilized to study Zn^{2+}–carboxylate surface binding at the air–water interface. **Figure 36** shows a representative set of these spectra. The methylene scissoring band ($\delta(CH_2)$) is located at 1469 cm^{-1}, thus confirms that the hydrocarbon chains are hexagonal packed.[322] The spectra also reveal the carbonyl stretch ($\nu(C{=}O)$) at 1729 cm^{-1}, the carboxylate symmetric stretch ($\nu_S(COO^-)$) at 1404 cm^{-1}, and the carboxylate asymmetric stretch ($\nu_{AS}(COO^-)$) at 1546 cm^{-1}. These values are consistent with previous studies.[296,306] It is seen across all monolayer compositions that the $\nu_{AS}(COO^-)$ mode increases in area and intensity with increasing Zn^{2+} concentration. This pattern is indicative of binding interaction between Zn^{2+} and the carboxylate headgroup of OA. In addition, the disappearance of the $\nu(C{=}O)$ mode with increasing zinc concentration indicates that the Zn^{2+}–carboxylate binding interaction is primarily bidentate. Because the carboxylate stretching mode exhibits sensitivity to binding, it is used as a probe of Zn^{2+}–carboxylate binding interactions across monolayer compositions.[269,296,306,314]

Prior to evaluation of the specific effect of the mixed monolayer on binding and given the large concentrations of NaCl used in these studies as a proxy for ocean SSML and SSA solutions, we tested the effect of NaCl. As shown in **Figure 40**, the spectra without NaCl have $\nu_{AS}(COO^-)$ modes that are larger in intensity, which is indicative of an increase zinc–OA binding interactions. It is believed that the large ionic strength from the oceanic concentrations of NaCl interfere with the binding efficiency of Zn^{2+} due to ionic shielding. All other experiments in this study have an aqueous solution that contains oceanic levels of NaCl, resulting in an accurate simulation of binding conditions at the SSML and in SSA films.

Now that the effect of NaCl is established, we examine the impact of incorporating OL into an OA monolayer film. When an OA monolayer is diluted with OL, the $\nu_{AS}(COO^-)$ mode changes in area which allows for evaluation of Zn^{2+}–carboxylate binding. To compare the $\nu_{AS}(COO^-)$ modes across all monolayer ratios and zinc concentrations, the peak areas were determined via integration and compiled into **Figure 41**. At low $ZnCl_2$ concentrations, it is observed that peak areas do not vary significantly between monolayer compositions. However, they do at higher $ZnCl_2$ concentrations; the $\nu_{AS}(COO^-)$ peak areas decrease with increasing amounts of OL in the monolayer, most significantly in the 90:10 and 85:15 OA:OL monolayers. This pattern can be observed for the highest $ZnCl_2$ concentration spectra in **Figure 42**. Because the $\nu_{AS}(COO^-)$ mode is sensitive to binding interactions, this analysis suggests that (1) there is a general increase in binding with an increase in Zn^{2+} concentration, and (2) there is relatively no change in binding across the OA:OL ratios except with the higher concentrations of Zn^{2+}. This latter point is somewhat surprising given that the concentration of the carboxylate is decreasing with decreasing amount of OA in the monolayer.

To quantify the binding efficiencies of each monolayer and the impact of film heterogeneity, binding affinities were determined based on the asymmetric carboxylate stretch peak area. The peak areas, shown in **Table 9**, were quantified via peak integration, and normalized via min-max normalization, meaning that a value of 0 corresponds to the peak area on a solution of 0 mM $ZnCl_2$ and 468 mM NaCl and a value of 1 corresponds to the peak area on a solution of 25 mM $ZnCl_2$, 468 mM NaCl. The reported errors correspond to one standard deviation that has been propagated through the operations used in the normalization calculation. Since the minimum value is normalized to the peak area of a system containing only the background NaCl and no $ZnCl_2$, the binding indicated by these peak areas is assumed to be solely due to Zn^{2+}–carboxylate interactions.

Results are plotted in **Figure 43** as concentration of Zn^{2+} versus normalized peak area of $\nu_{AS}(COO^-)$, separated by monolayer composition. All four monolayer compositions show positive correlation between peak area and Zn^{2+} concentration. The plots are fit to two different surface adsorption models, Langmuir and Langmuir-Freundlich (equations 6.2, 6.3)

Langmuir $$A = A_{max}\frac{K_a[Zn^{2+}]}{K_a[Zn^{2+}]+1} \qquad (6.2)$$

Langmuir-Freundlich $$A = A_{max}\frac{[K_a[Zn^{2+}]]^n}{[K_a[Zn^{2+}]]^n+1} \qquad (6.3)$$

where A and A_{max} are peak intensity and maximum peak intensity of $\nu_{as}(COO^-)$, $[Zn^{2+}]$ is the solution concentration of zinc, n is an empirical constant, and K_a is the affinity constant for adsorption which is defined as the inverse of the dissociation constant.[269,323–325] For both adsorption models, the binding is assumed to occur at a 1:1 ratio of zinc to OA. Based on R^2 value, the Langmuir-Freundlich model provides the most precise fit for 100:0, while the Langmuir model provides the most precise fit for 90:10 and 85:15. The two adsorption models result in an equally precise fit for 95:5. Across all monolayer compositions, differences in quality of fit between the two models are minimal.

The Langmuir adsorption model is a well-accepted method for quantifying how an adsorbate forms a layer on a given surface based on the equilibrium of ions between the two phases.[326–328] Because of the simplifications in the Langmuir model, modifications have been developed to create more complex models.[325] The Langmuir-Freundlich adsorption model is one such equation. It includes an exponential term and an empirical constant, *n*, which was used by Soares *et al*. to describe surface adsorption on heterogeneous surfaces.[325,328] This feature can be useful for analyzing adsorption on non-uniform surfaces, such as a mixed OA:OL monolayer. The exponential term of the Langmuir-Freundlich model provides an additional parameter in comparison to the Langmuir model, which should result in Langmuir-Freundlich producing a more precise fit. However, the Langmuir-Freundlich model produced a less precise fit for 2/4 of the ratios studied. In addition, the exponential term is supposed to describe surface heterogeneity such that it would equal 1 for 100:0 (a homogeneous system), resulting in no difference between the Langmuir and Langmuir-Freundlich fits. However, the two models do not produce equal curves for this ratio. The additional parameter in the Langmuir-Freundlich model proved to be less than optimal for representing the physical aspect of surface heterogeneity and improving model precision. Because of this, we report and analyze the binding affinity K_a values derived only from the Langmuir adsorption model (**Figure 44)**.

Overall, it is observed that an increase in the concentration of OL decreases the overall binding affinity of the monolayer, that is, of the carboxylic acid headgroup. For example, for the 90:10 and 85:15 compositions, one would expect a 10 and 15% drop in binding affinity given there is a 10 and 15% lower concentration of OA in the monolayer when compared to 100:0. Yet a ~50% reduction in binding affinity is observed, leading to the conclusion that the alcohol headgroup of the OL reduces the ability of the carboxylic acid headgroup to efficiently bind. This can be simply explained such that the OH of the alcohol perturbs the carboxylic acid and carboxylate intermolecular hydrogen bonding.

The Stoichiometry of Complex Formation. As stated previously, all reported binding information assumes 1:1 Zn^{2+}–carboxylate complexation at the air–water interface. However, this may not be an electrostatically preferred system because the Zn^{2+} ion has a divalent positive charge while the carboxylate group has a monovalent negative charge, meaning that the 1:1 complex would carry a 1+ charge. Moreover, a 1:2 Zn^{2+}–carboxylate complex would carry an overall charge of zero. One proposed mechanism for the formation of the 1:2 complex is a ternary single-step reaction in which the aqueous Zn^{2+} ion and two free, adjacent carboxylate headgroups bind together synchronously (equation 6.4).[329]

$$K_{a1}[Zn^{2+}][OA^-]^2 = [Zn(OA)_2] \tag{6.4}$$

$$A = A_{max}\frac{1+8K_{a1}[S][Zn^{2+}]-\sqrt{1+16K_{a1}[S][Zn^{2+}]}}{8K_{a1}[S][Zn^{2+}]} \tag{6.5}$$

The 1:2 complexation single-step adsorption model is given as equation 6.5, where K_{a1}[S] is the binding parameter of the single-step reaction and [S] specifically is the density of surface binding sites. When applied to the IRRAS data, this adsorption model provides a poor fit with low R^2 values. The poor fit may be due to the fact that ternary reactions are not kinetically favorable and are unlikely to occur spontaneously. Therefore, this ternary mechanism of binding will not be considered further.

Another proposed mechanism for the formation of the 1:2 Zn^{2+}–carboxylate complex is a two-step process. In the first step, which is bimolecular, a Zn^{2+} ion binds to a single carboxylate headgroup to form a 1:1 Zn^{2+}–carboxylate complex (equation 6.6). In the second step, an adjacent and free carboxylate headgroup binds to the existing complex to form a Zn^{2+} ion bound by two carboxylate headgroups (equation 6.7).[329]

Step 1: $$K_a[Zn^{2+}][OA^-] = [Zn(OA)]^+ \tag{6.6}$$

Step 2: $$K_b[OA^-][Zn(OA)]^+ = [Zn(OA)_2] \tag{6.7}$$

$$A = A_{max}\frac{1+8K_b[S]K_a[Zn^{2+}]-\left(K_a[Zn^{2+}]\right)^2+\left(K_a[Zn^{2+}]-1\right)\cdot\sqrt{(K_a[Zn^{2+}]+1)^2+16K_b[S]K_a[Zn^{2+}]}}{16K_b[S]K_a[Zn^{2+}]} \tag{6.8}$$

The 1:2 complexation two-step adsorption model is given in equation 6.8, where K_b[S] is the binding parameter of Step 2 and [S] is the density of surface binding sites.[329] Step 1 is equal to the 1:1 binding mechanism assumed for the previously calculated Langmuir adsorption, and therefore K_a here is equal to the K_a found by Langmuir fitting.[329] Since K_a in the two-step equation is equal to the Langmuir binding constant, K_b[S] is a parameter that is indicative of any 1:2 binding above and beyond the binding achieved in Step 1.[329] The two-step adsorption model fits the data much more precisely than the single-step model. For each ratio of OA:OL, the two-step adsorption curve consistently falls between the Langmuir curve and the Langmuir-Freundlich curve, with R^2 values in the same range. Values from the fit are given in **Figure 45**.

The trend in binding parameters reveals that when there is a higher proportion of OA in the monolayer, 1:1 surface complexes are more likely to complete Step 2 of the mechanism to become 1:2 Zn^{2+}–carboxylate complexes. This trend is kinetically viable because as the OA monolayer is diluted with OL, there is a decreased probability that any given molecule adjacent to a 1:1 complex is OA. When there are less adjacent OA molecules available, it may be more energetically taxing for the 1:1 complex to bind another carboxylate headgroup. A schematic of this motif is presented in **Figure 46**. There is a distinct split in binding parameter value between the upper two and the lower two OA:OL ratios: the upper two are positive, while the lower two are negative. This may indicate that at some point between the 95:5 and 90:10, the proportion of OL in the monolayer becomes too high to support significant 1:2 Zn^{2+}–carboxylate complex formation.

6.4 Conclusions

Mixed monolayers, as opposed to single component monolayers, are more representative of real-world atmospheric and oceanic systems, particularly for evaluating metal surface enrichment and binding. In this study, Zn^{2+}–carboxylate surface binding was probed as a function of octadecanoic acid to octadecanol monolayer composition using (Π–A) isotherms and IRRAS. All systems were evaluated at a surface pressure of 35 mN/m, a mean molecular area of approximately 21.5 Å^2/molecule, and an untilted condensed monolayer structure. Surface binding affinities for 1:1 Zn^{2+}–carboxylate surface complexes were found for each of the four ratios of octadecanoic acid to octadecanol studied (100:0, 95:5, 90:10, and 85:15) via Langmuir adsorption model. All 1:1 Zn^{2+}–carboxylate surface binding affinities were found to be on the order of 10^3, which is about 300 times stronger than the analogous bulk binding process, indicating enhanced binding at the interface. Monolayer composition was found to influence trace metal surface binding affinity; the addition of octadecanol in a monolayer of octadecanoic acid disproportionately reduced Zn^{2+}–carboxylate surface binding. This may be because the alcohol headgroup of octadecanol reduced the ability of the carboxylic acid headgroup to efficiently bind. Finally, the potential of each system to form 1:2 Zn^{2+}–carboxylate surface complexes was analyzed using a divalent binding model. It was found that the two highest monolayer ratios, 100:0 and 95:5, can support formation of 1:2 Zn^{2+}–carboxylate surface complexes via a two-step reaction mechanism. Results reveal that ratios similar to those found in the SSML and SSA films of octadecanoic acid and octadecanol impact surface binding affinity of Zn^{2+}, an oceanic trace metal.

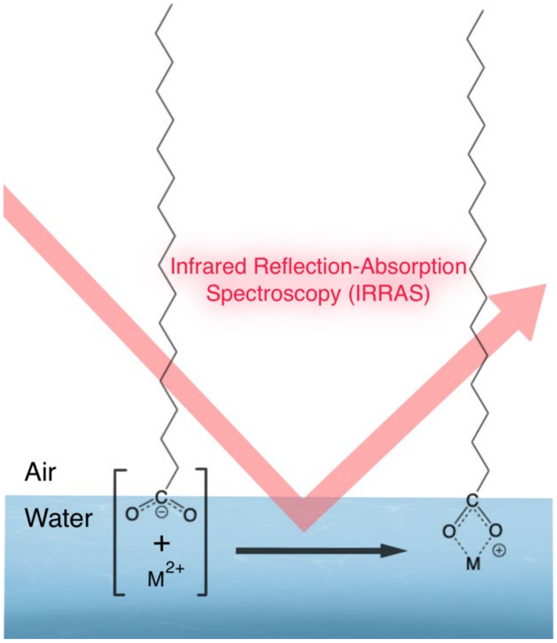

Figure 32. Carboxylate–metal binding at the air–water interface is probed using IRRAS.

Figure 33. Experimental setup featuring Langmuir trough, barriers, Wilhelmy plate, FTIR spectrometer, and mirrors

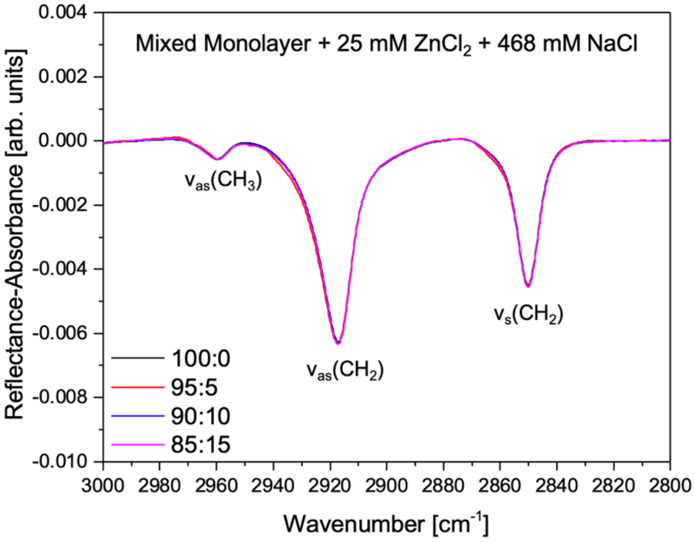

Figure 34. Alkyl region of IRRAS spectra of each monolayer composition (OA:OL) on an aqueous solution of 25 mM ZnCl$_2$ and 468 mM NaCl at a surface pressure of 35 mN/m.

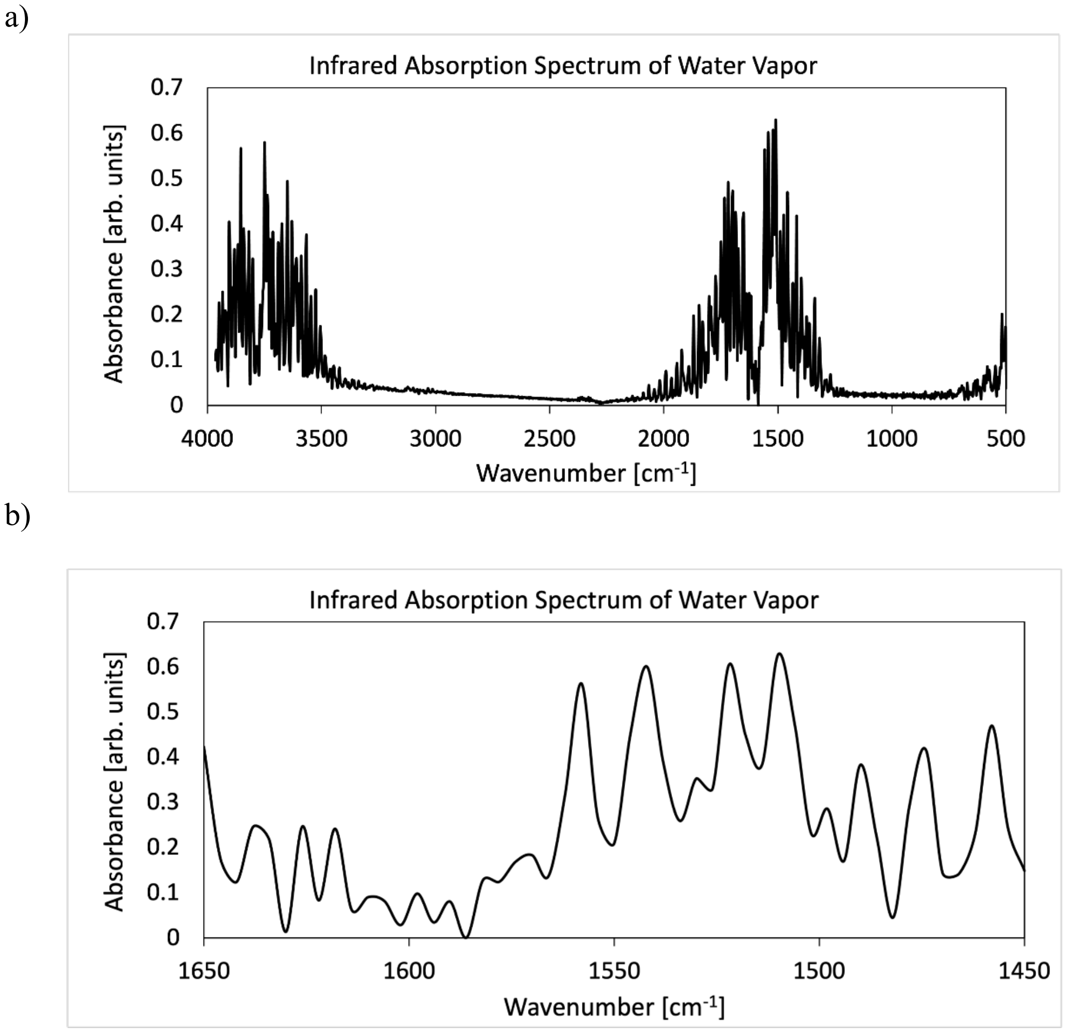

Figure 35. Infrared absorption spectrum of water vapor adapted from data provided by NIST Standard Reference Database 69: *NIST Chemistry WebBook. The spectrum displays considerable noise in the same region where we observe noise in the spectra collected in this study. a) the full spectrum, and b) 1450–1650 cm^{-1}, the region of interest*

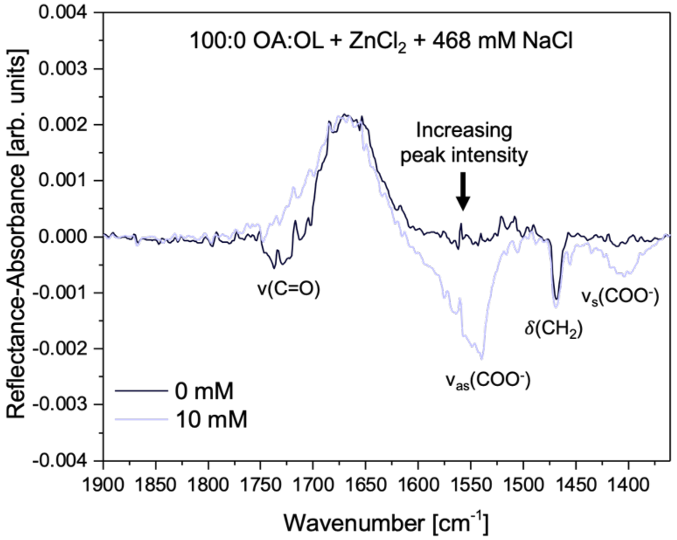

Figure 36. Carboxylate region of IRRAS spectra of the 100:0 OA:OL mixed monolayer on an aqueous solution containing 468 mM NaCl, a variable amount of ZnCl$_2$, and held at a surface pressure of 35 mN/m. Some water vapor lines removed for clarity (**Table 8**).

Table 8. Position and magnitude of each water vapor line removed from **Figure 36** and **Figure 37**.

	ν$_{AS}$(COO$^-$) Water Vapor Line		
OA:OL Ratio	Zn^{2+} Concentration (mM)	Wavenumber (cm^{-1})	Magnitude (arb. units)
100:0	25	1559	-0.00246
95:5	25	1559	-0.00298
90:10	25	1559	-0.00402
	10	1559	-0.00201
	0	1559	-0.00138
	0	1542	-0.00144
85:15	25	1559	-0.00314
	10	1559	-0.00195
	0	1559	-0.00257
	0	1542	-0.00141

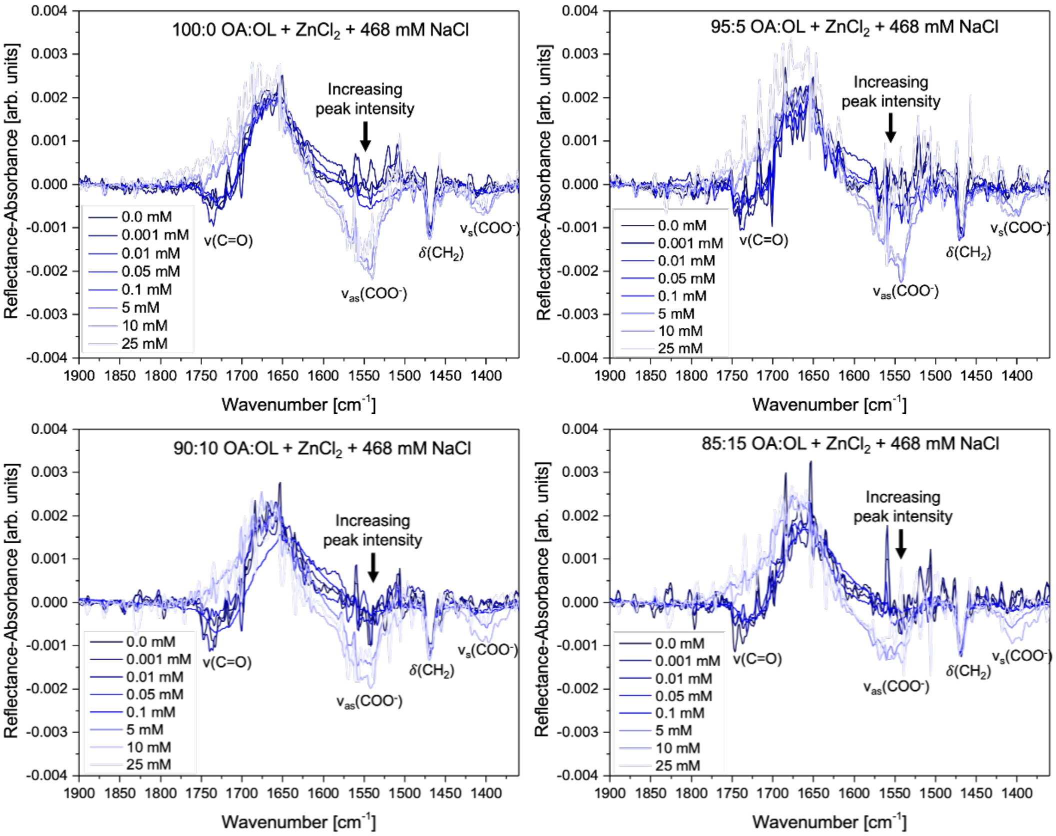

Figure 37. Carboxylate region of IRRAS spectra of OA:OL mixed monolayers in the ratios 100:0 (top left), 95:5 (top right), 90:10 (bottom left), and 85:15 (bottom right). All scans are of a monolayer on an aqueous solution containing 468 mM NaCl, a variable amount of $ZnCl_2$, and a surface pressure of 35 mN/m. Some water vapor lines removed for clarity (see **Table 8**).

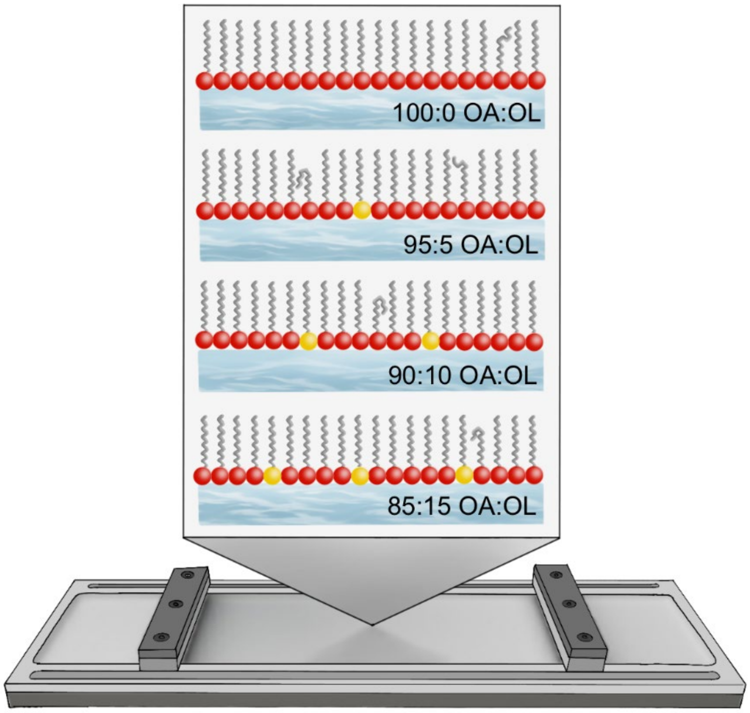

Figure 38. A schematic of the four mixed monolayer ratios used in this study. The molecules with red headgroups represent octadecanoic acid; the molecules with yellow headgroups represent octadecanol. A Langmuir trough is depicted as the vessel.

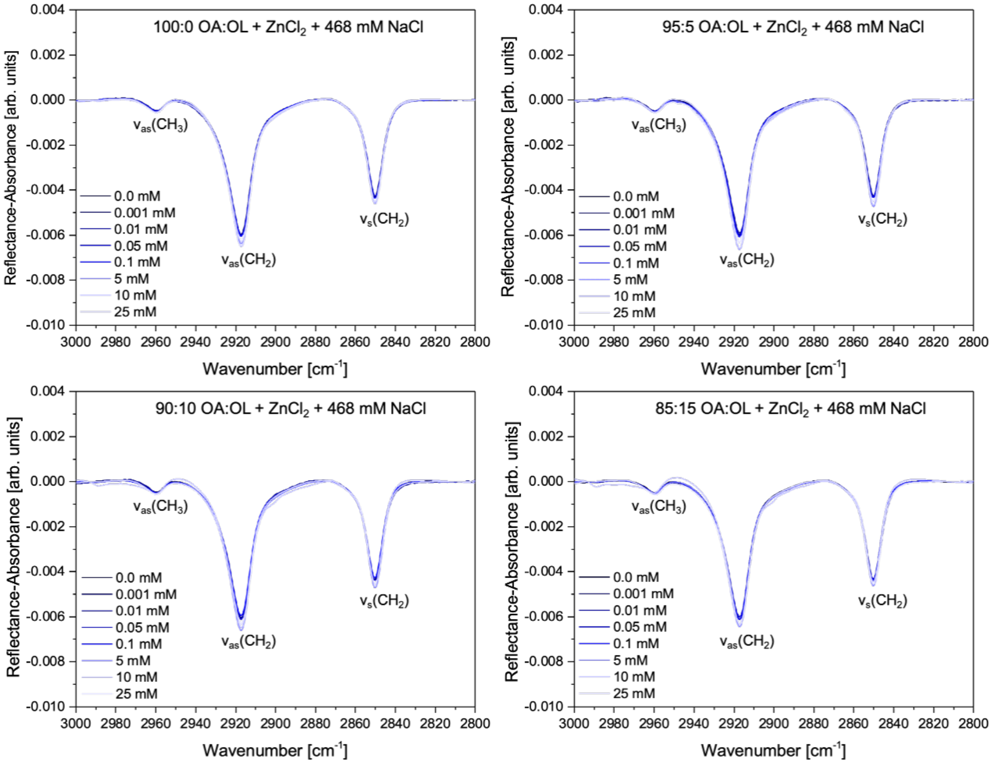

Figure 39. Alkyl region of IRRAS spectra of OA:OL mixed monolayers in the ratios 100:0 (top left), 95:5 (top right), 90:10 (bottom left), and 85:15 (bottom right). All scans are of a monolayer on an aqueous solution containing 468 mM NaCl, a variable amount of $ZnCl_2$, and a surface pressure of 35 mN/m.

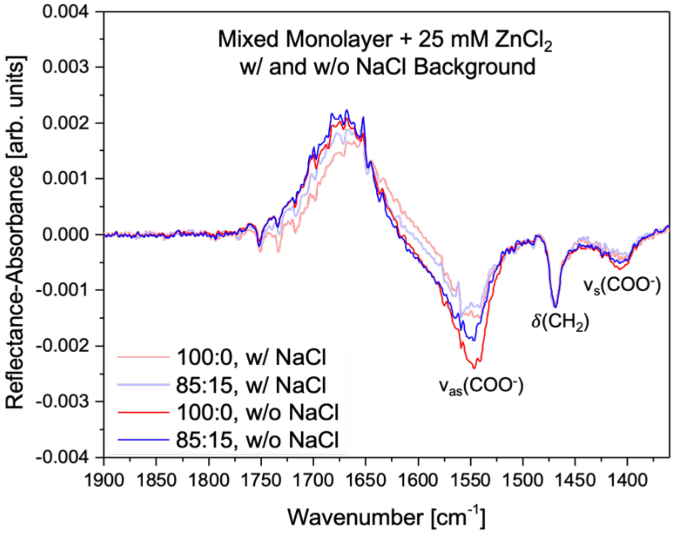

Figure 40. Carboxylate region of IRRAS spectra of the 100:0 and 85:15 OA:OL mixed monolayer compositions on aqueous solutions containing either 0 mM or 468 mM NaCl, 25 mM ZnCl$_2$, and held at a surface pressure of 35 mN/m.

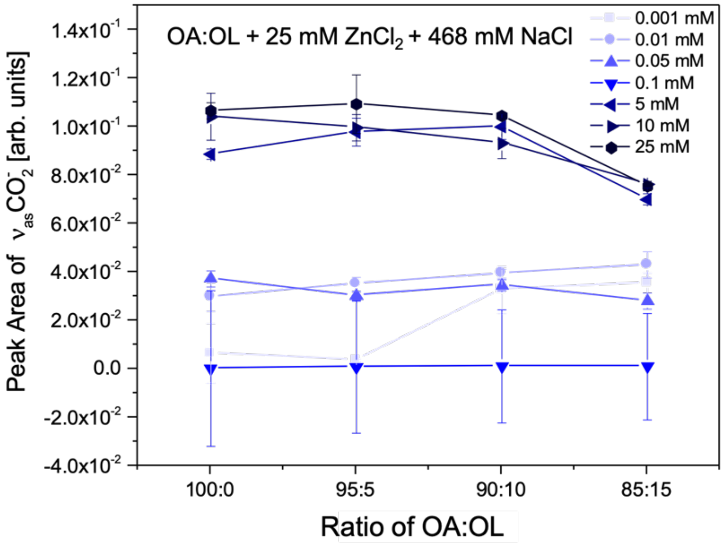

Figure 41. Integrated total peak area of the ν_{AS}(COO$^-$) mode (1490–1610 cm^{-1}) displayed for each aqueous ZnCl$_2$ concentration across all monolayer compositions. Error bars correspond to one standard deviation.

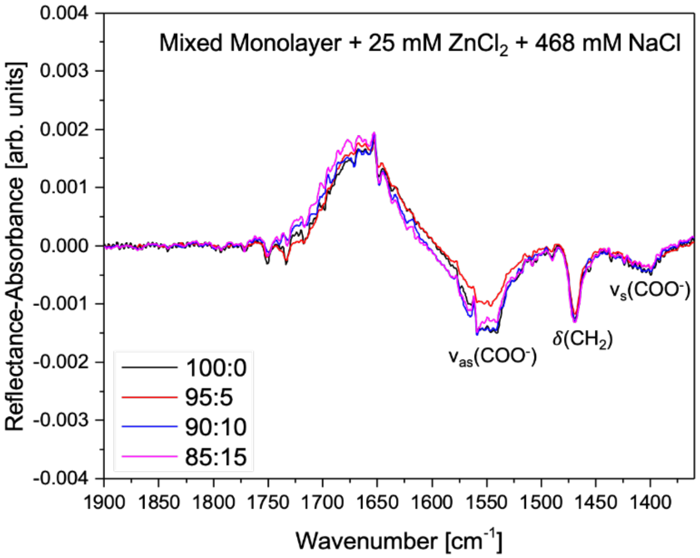

Figure 42. Carboxylate region of IRRAS spectra of OA:OL mixed monolayers in the ratios 100:0, 95:5, 90:10, and 85:15, all on an aqueous solution of 25 mM $ZnCl_2$ and 468 mM NaCl at a surface pressure of 35 mN/m. The ν(C═O) mode at 1729 cm^{-1} is nonexistent at this concentration, indicating full deprotonation of the carboxylate headgroups as well as Zn^{2+}–carboxylate chelation. Most notably, the area of the $\nu_{AS}(COO^-)$ peak varies among monolayer compositions on the same solution.

Table 9. Normalized carboxylate asymmetric peak areas for each zinc concentration and monolayer composition.

Zn^{2+} Concentration (mM)	Normalized $\nu_{AS}(COO^-)$ Peak Area			
	100:0	95:5	90:10	85:15
0	0	0	0	0
0.001	-0.072 ± 0.143	-0.063 ± 0.039	0.118 ± 0.127	0.321 ± 0.074
0.01	0.179 ± 0.085	0.253 ± 0.058	0.201 ± 0.054	0.449 ± 0.093
0.05	0.260 ± 0.069	0.205 ± 0.049	0.141 ± 0.056	0.198 ± 0.059
0.1	0.205 ± 0.063	0.176 ± 0.050	0.002 ± 0.063	0.093 ± 0.033
5	0.808 ± 0.081	0.884 ± 0.132	0.945 ± 0.093	0.907 ± 0.052
10	0.974 ± 0.134	0.902 ± 0.132	0.860 ± 0.099	1.012 ± 0.044
25	1.000 ± 0.094	1.000 ± 0.179	1.000 ± 0.069	1.000 ± 0.051

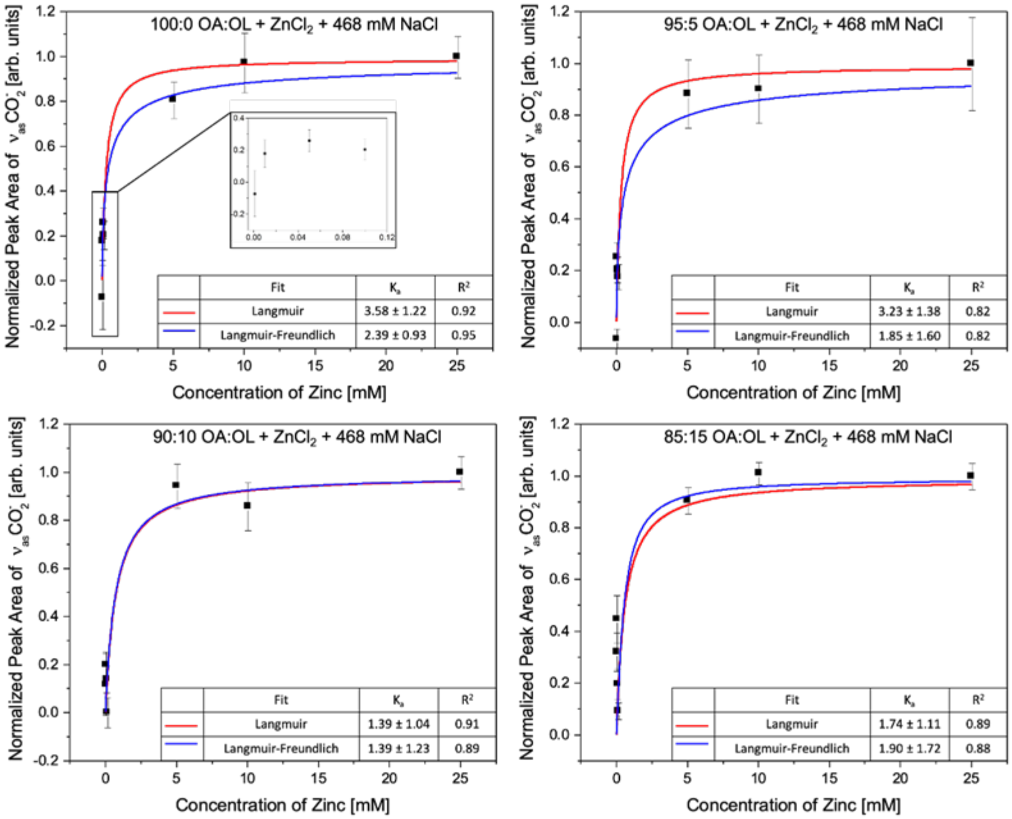

	Fit	K_a	R^2
—	Langmuir	3.58 ± 1.22	0.92
—	Langmuir-Freundlich	2.39 ± 0.93	0.95

	Fit	K_a	R^2
—	Langmuir	3.23 ± 1.38	0.82
—	Langmuir-Freundlich	1.85 ± 1.60	0.82

	Fit	K_a	R^2
—	Langmuir	1.39 ± 1.04	0.91
—	Langmuir-Freundlich	1.39 ± 1.23	0.89

	Fit	K_a	R^2
—	Langmuir	1.74 ± 1.11	0.89
—	Langmuir-Freundlich	1.90 ± 1.72	0.88

Figure 43. Normalized peak area of ν_{AS}(COO$^-$) of OA:OL mixed monolayers in the ratios 100:0 (top left) with inset showing low concentration regime, 95:5 (top right), 90:10 (bottom left), and 85:15 (bottom right). All scans have an aqueous solution containing 468 mM NaCl, a variable amount of $ZnCl_2$, and a surface pressure of 35 mN/m. Surface binding affinities found by each adsorption model are given as mM^{-1}. Error bars correspond to one standard deviation that has been propagated through the operations used in the normalization calculation

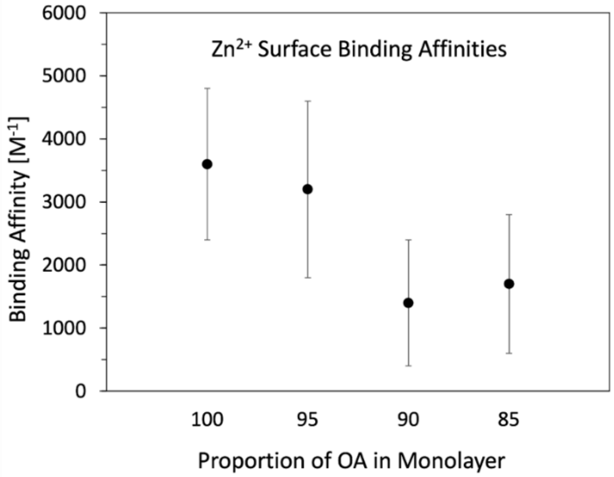

OA:OL Ratio	Binding Affinity (M^{-1})
100:0	3.6 (1.2) × 10^3
95:5	3.2 (1.4) × 10^3
90:10	1.4 (1.0) × 10^3
85:15	1.7 (1.1) × 10^3

Figure 44. Summary of the binding affinities of Zn^{2+} for each of the four reported monolayer compositions. A 1:1 Zn^{2+}–carboxylate binding is assumed. The error values given in parentheses correspond to one standard deviation that has been propagated through the operations used in the normalization calculations.

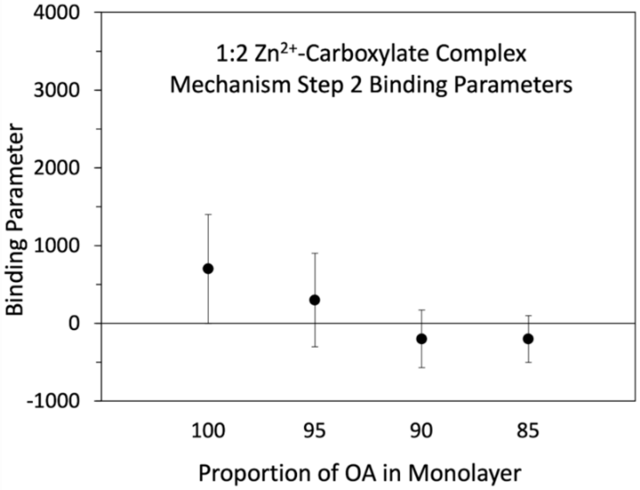

OA:OL Ratio	Binding Parameter
100:0	0.7 (0.7) × 10^3
95:5	0.3 (0.6) × 10^3
90:10	-0.2 (0.4) × 10^3
85:15	-0.2 (0.3) × 10^3

Figure 45. Summary of the binding parameters for Step 2 in the mechanism of 1:2 Zn^{2+}–carboxylate complex formation for each of the four reported monolayer compositions. The error values given in parentheses correspond to one standard deviation that has been propagated through the operations used in the normalization calculations.

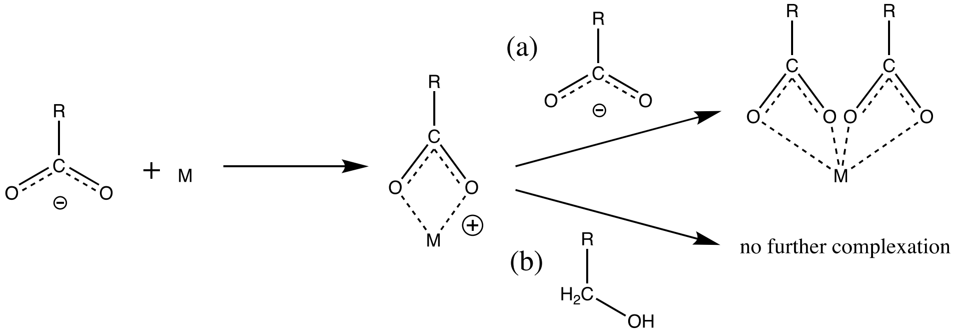

Figure 46. Proposed motif of mechanism Step 2 in the two-step formation of the 1:2 Zn^{2+}–carboxylate complex at the air–water interface. M represents divalent Zn^{2+}. (a) A monolayer environment rich in OA is conducive to successful completion of Step 2, but as the proportion of OL increases (b) the likelihood of Step 2 completion is diminished.

Chapter 7. Discerning Poly- and Monosaccharide Enrichment Mechanisms: Alginate and Glucuronate Co-adsorption to a Stearic Acid Sea Surface Microlayer

Manuscript Submitted: Vazquez de Vasquez, M. G.; Rogers, M. M.; Carter-Fenk, K. A.; Allen, H. C. "Discerning Poly-and Monosaccharide Enrichment Mechanisms: Alginate and Glucuronate Co-adsorption to a Stearic Acid Sea Surface Microlayer". *ACS Earth Space and Chem.,* **2022**

7.1 Introduction

Poly- and monosaccharides comprise a significant fraction of organic carbon in sea spray aerosol (SSA).[35] Estimates have shown that up to 61% of SSA content by mass comes from saccharides with the greatest saccharide enrichment observed in submicron SSA.[24,36,37] Saccharide enrichment in SSA starts with breaking waves entraining air bubbles that become coated in surface-active organic matter, such as saccharides, derived from marine biota.[21,35,36,39,330,331] The adsorbed biogenic organic matter is sprayed into the atmosphere upon bubble bursting.[330,332,333] Yet, the exact transport mechanism of saccharides from bulk seawater to the sea surface microlayer (SSML) remains understudied,[38] causing Earth system models to underestimate saccharide presence in SSA.[21,39,40] Atmospheric processes in the marine boundary layer are dependent upon SSA composition.[41–45,334–336] SSA compounds, especially saccharides, serve as nucleation sites for cold cloud and ice formation.[46–57] Clouds and ice are important regulators of the overall radiative budget on earth, scattering and absorbing solar radiation. Changes in SSA composition alter the abundance of cloud condensation nuclei and ice nucleating particles which ultimately drive climate processes, like temperature and weather, in the marine boundary layer.[24,58–60,337,338] Without accurate measures of saccharide content within SSA, climate models will be based on underestimated inputs, limiting our accurate understanding of global climate trends.

Previous studies have discussed the electrostatic interactions between saccharides and lipid headgroups, calculated the enrichment of saccharides, and measured surface propensity.[339] However, the exact mechanics of such interactions and enrichment had yet to be defined.[38] Recent findings from Hasenecz *et al*. showed a specific enrichment of the polysaccharide alginate in proxy SSA samples that was further enhanced upon the addition of $CaCl_2$ to the subphase.[340] Alginate is a highly abundant oceanic compound produced by *Phaeophyta*, or brown algae.[341] Specifically, alginate is the most abundant polysaccharide produced by brown algae and accounts for 15-60% of its dry weight.[342] Alginate is a linear anionic polysaccharide that provides structural function within the cell walls of brown algae.[343] Some bacteria, such as *Pseudomonas,* can synthesize alginate, as well.[344] However, most marine bacteria depolymerize algal-based alginate via alginate and oligoalginate lyase enzymes.[342,345] Bacteria further degrade the now oligomeric products to their monomeric form. Herein, alginate serves as a vital substrate for bacterial metabolism and source of oligosaccharides and monosaccharides which can also enrich the SSML and SSA environments. Poly-, oligo-, and monosaccharides are all readily available to interact with oceanic salts, such as $CaCl_2$, which have been shown to facilitate bridging to such saccharides, co-adsorbing them to the air–water interface.[346]

Recent work from Carter-Fenk *et al*., measured a cationic bridging mechanism in which alginate co-adsorbs to a deprotonated fatty acid monolayer, providing new insights into the enrichment process of saccharides at the air-water interface.[347] Ca^{2+} facilitates the greatest extent of alginate co-adsorption amongst other oceanic-relevant cations such as Na^+ and Mg^{2+}. This work is foundational in providing empirical parameters to improve the representation of polysaccharides in climate models. While polysaccharide representation and mechanistic transfer to the aerosol environment is becoming better established in the literature, monosaccharides may not maintain the same complexity and mechanics of polysaccharides and require their own systematic studies to quantify their surface propensity. Saccharide content in the SSML and SSA was measured throughout two phytoplankton blooms by Jayarathne *et al*. and found that enrichment factors of monomers hydrolyzed from oligo-/polysaccharides were ~1–16 and ~14–1314 for SSML and submicron SSA, respectively.[24] Studies are therefore needed to understand the mechanistic transfer of monomers to the SSA environment to help explain such enrichment.

This study expands upon the cationic bridging mechanism which drives alginate co-adsorption to deprotonated monolayers by studying glucuronic acid, a commercially available analogue to mannuronic acid and guluronic acid, as it is representative of the monomeric form of alginate. The Langmuir adsorption coefficient and half-saturation concentration was measured of both alginate and glucuronate to stearic-d_{35} acid monolayers using surface-sensitive infrared reflection–absorption spectroscopy (IRRAS). Langmuir surface pressure–area (Π–A) isotherms, in combination with IRRAS, provide structural insights within the stearic-d_{35} acid monolayers. Brewster angle microscopy (BAM) and non-equilibrium relaxation (NER) studies provide the means to calculate monolayer thickness as a function of saccharide concentration. Adsorption of alginate to an insoluble monolayer is observed via cationic bridging and found 11 ±1.9 mg/L to be the minimum concentration of alginate required to observe co-adsorption, and a maximum monolayer thickness of ~5.5 nm. Monomeric studies were performed with glucuronate and found a co-adsorption via intercalation, resulting in an anomalous desorption for the 30 and 40 mg/L concentration studies, which does not persist for other concentrations. It was found that 12 ± 2.3 mg/L is the minimum concentration for glucuronate co-adsorption and a maximum monolayer thickness of 4.2 nm. This suggest that the co-adsorption formation is minimal, and intercalation is the dominating enrichment mechanisms for monosaccharides. The data of poly- and monosaccharide co-adsorption to a deprotonated monolayer suggests that monomer surface propensity is a contributor to saccharide composition but cannot model polysaccharide representation in SSA, all of which help to elucidate important inputs for climate models.

7.2 Experimental Methods

7.2.1 Materials

Stearic acid (octadecanoic acid, $CH_3(CH_2)_{16}COOH$, >99%, Sigma Aldrich), and deuterated octadecanoic acid (stearic-d_{35} acid, $CD_3(CD_2)_{16}CO_2H$, > 98%, Sigma Aldrich) were used as received. The compounds were dissolved in chloroform (HPLC grade, Fisher Scientific) to prepare ~1.5 mM solutions. Calcium chloride dihydrate (Certified ACS, Fisher Chemical) was used as received. Sodium chloride (Certified ACS, Fisher

Chemical) was baked for at least 10 hours in a furnace at 650 ºC to remove residual organic impurities. Alginic acid (sodium salt, ACROS Organics^{TM}, Lot: A0406891) and glucuronic acid (sodium salt monohydrate. 99% ACROS Organics^{TM}, Lot: A0397856) were used as received from the same batch to maximize homogeneity in molecular composition. All aqueous solutions were prepared with nanopure water with a resistivity of 18.2 MΩ·cm (Milli-Q Advantage A10, EMD Millipore) in glassware cleaned with a piranha acid bath. The nanopure water has a pH of 5.6 ± 0.1 due to atmospheric CO_2 acidification. Atmospheric CO_2 also acidifies the proxy aqueous solution, so the solutions were initially pH adjusted to 8.7 ± 0.1 to ensure that the pH will be approximately 8.2 ± 0.1 throughout the experimental measurements. The solution pH was adjusted by adding microliter aliquots of 0.345 M NaOH solution made from sodium hydroxide pellets (98% extra pure, ACROS Organics^{TM}) in nanopure water. The aqueous subphase solution pH was measured before and after experiments.

7.2.2 Langmuir Surface Pressure–Area Isotherms

Langmuir surface pressure–area (Π–A) isotherms were performed on a Teflon Langmuir trough with an area of 148.8 cm^2 fitted with movable Delrin barriers (KSV NIMA, Finland). Surface pressure was measured using a platinum Wilhelmy plate. The Wilhelmy plate, trough, and barriers were thoroughly cleaned with reagent alcohol (Histological grade, Fisher Scientific) and nanopure water and dried before each trial. The Wilhelmy plate was flamed with a Bunsen burner until red hot to remove residual organics. After the aqueous solution was added to the trough, its surface was checked for contamination by compressing the barriers and ensuring that the surface pressure did not rise above 1.0 mN/m. The stearic acid solution was spread dropwise onto the aqueous surface to form a monolayer using a microsyringe (Hamilton, 50 μL). The chloroform solvent was allowed to evaporate for 10 minutes. The barriers were symmetrically compressed at a rate of 5 mm/min/barrier. During the isotherm compression, Brewster angle microscopy images were taken every 4.85 s (see Brewster angle microscopy method section for more details). The microsyringe was cleaned thoroughly between each trial with reagent alcohol, set to dry, and then rinsed 8–10 times with chloroform.

7.2.3 Brewster Angle Microscopy

Brewster angle microscopy (BAM) was performed using a custom-built setup. The BAM setup is mounted on a goniometer which allows for adjusting the angle of incidence to the Brewster angle of the aqueous solution, ~ 53°, from the surface normal for pure water. The 1.5 mW He-Ne laser source (Research Electro-Optics, Boulder, CO) emits polarized light at a wavelength of 543 nm with a linear polarization. The p-polarized light goes through a Glan-laser calcite polarizer for further purification before being reflected off the aqueous surface. The reflected light is then collected and collimated by a 10 × infinity-corrected super-long working distance objective lens (CF160 Tu Plan EPI, Nikon Instruments, Melville, NY USA) and a tube lens (MXA22018, Nikon, instruments, Melville, NY, USA; focal length 200 mm) to collect the collimated beam before going into a back-illuminated EM-CCD camera (iXon DV887-BV, Andor Technology, Concord, MA; 512 × 512 active pixels with 16 μm × 16 μm pixel size). The BAM images were processed using ImageJ software (version 1.52a, National Institute of Health, Bethesda, MD, USA) and cropped from their original size to show the region of highest resolution. The dark regions of the BAM images correspond to the aqueous surface or to the less condensed phases of the surfactant, whereas the bright regions correspond to surfactant-rich areas. In this work, BAM was utilized during the Π–A isotherm and the NER experiments.

7.2.4 Infrared Reflection–Absorption Spectroscopy

Infrared reflection–absorption spectroscopy (IRRAS) measurements were performed using a custom-build optical setup. Two planar gold mirrors at 48° relative to surface normal were placed inside a Fourier transform infrared spectrometer (FTIR) (Frontier, PerkinElmer). The incident unpolarized beam is reflected off the input gold mirror and onto the surface, where the beam interacts with the interface then reflects to the output mirror and finally to the liquid nitrogen-cooled HgCdTe (MCT) detector. Spectra were collected with polarized light as an average of 400 scans in the single-beam mode with a resolution of 4 cm^{-1} within the range of 4000–450 cm^{-1} in 0.5 cm^{-1} increments. Experiments were performed in a petri dish at 20 $Å^2$/molecule to ensure a full monolayer (Untilted Condensed (UC) Phase). Experiments were repeated in at least triplicate, and each spectrum was reported as the average of all trials using the OriginPro 9's average function (OriginLab 9, Northampton, MA). Reflectance–absorbance spectral baseline was corrected using a linear or a fourth-order polynomial in the region of interest. Peak integration was also used. Both processes were performed using OriginPro 9. The OH stretching region was analyzed by fitting a line between 3000 and 3800 cm^{-1} for baseline subtraction, and the area under the curve was integrated between these points. Reported Langmuir adsorption coefficient and half-saturation concentration errors incorporate both spectral and fitting uncertainties.

7.2.5 Monolayer Non-Equilibrium Relaxation at a Constant Surface Pressure

The non-equilibrium relaxation (NER) experiments were also performed using a Teflon Langmuir trough with an area of 148.8 cm^2 fitted with movable Delrin barriers (KSV NIMA, Finland). Surface pressure was measured using a platinum Wilhelmy plate. After the aqueous solution was added to the trough, its surface was checked for contamination as described in the Langmuir surface pressure–area isotherms methods. A monolayer of stearic acid was spread dropwise by a microsyringe (Hamilton, 50 μL) on the solution of interest. The syringe was thoroughly cleaned between each trial with reagent alcohol, set to dry, and then rinsed 8–10 times with chloroform. The monolayer was compressed by symmetric compression of the trough barriers to a target surface pressure of 30 mN/m and was maintained at that surface pressure by continuous motion of the barriers at a maximum rate of forward/backward motion of 1 mm/min/barrier. The change in relative area (A/A_0) was then analyzed as a function of time.

7.3 Results and Discussion

7.3.1 Probing Packing and Morphological Features of Co-adsorbed Poly- and Monosaccharides

Packing and morphological measurements were collected by Π–A isotherms in tandem with Brewster angle microscopy (BAM). **Figure 47** informs on stearic acid monolayer organization while varying the concentration of either alginate or glucuronate in the subphase. Π–A isotherms provide insights into the overall monolayer structure, intermolecular interactions, and the co-adsorption of alginate and glucuronate. BAM imaging provides morphological evidence of monolayer structural changes. Stearic acid was chosen due to its ocean relevance and prevalence in nascent sea spray aerosol.[33,41,348,349] Stearic acid is partially deprotonated at ocean pH (8.2), which is the pH at which these experiments were performed. Thus, the headgroup interaction and its hydration structure drive the differences in the Π–A isotherm measurements.[213]

All measurements were collected at room temperature (23.0 ± 1.0 °C). Each monolayer was analyzed over an aqueous solution of a constant NaCl and $CaCl_2$ background of 467 mM and 10 mM, respectively, with eleven varying alginate or glucuronate concentrations of 0–100 mg/L, as shown in **Figure 47a** and **47b**. Π–A isotherms are consistent with previous high ionic strength studies.[9,350–353]. As the barriers compress the stearic acid monolayer to smaller mean molecular areas (MMAs), the film undergoes a smooth 2D phase transition, from gas-tilted condensed (G-TC) to an untilted condensed (UC) phase. The films reach maximum surface pressure between ~50–60 mN/m for alginate and ~60–65 mN/m for glucuronate. The surface pressure plateau could be due to the slow relaxation kinetics caused by the cohesive forces between the lipids.[9,354] When alginate is added to the proxy aqueous solutions, **Figure 47a**, the stearic acid monolayer expands monotonically as a function of alginate concentration. Thus, the Π–A isotherms suggest that alginate co-adsorbs to the interface, consistent with previous studies revealing that the mechanism for alginate enrichment or co-adsorption is via Ca^{2+} bridging to an insoluble monolayer.[340,347]

In the case of glucuronate, **Figure 47b**, monolayer expansion was also observed relative to the stearic acid monolayer spread in the absence of glucuronate. However, this expansion is not monotonic. The stearic acid monolayers on the 10–20 mg/L glucuronate solutions are the most expanded compared to the other concentrations. This likely indicates intercalation of glucuronate to the interface, therefore altering the monolayer structure. Spectral evidence will be required to clarify if intercalation is occurring. At 50 mg/L glucuronate, directionality in the trend changes and lower MMAs are observed compared to the 10–20 mg/L glucuronate, suggesting monolayer rearrangement. Therefore, monolayer rearrangement is undergoing several potential processes: intercalation of glucuronate, stearic acid monolayer desorption, and cationic bridging. It is evident that the glucuronate mechanism of co-adsorption is very different than that of alginate. This also shows that glucuronate is not a valid proxy system for polysaccharide interactions as it does not exhibit a similar co-adsorption mechanism to an insoluble monolayer.

BAM images were taken simultaneously with the isotherms, showing the changes in between alginate and glucuronate interaction with the monolayer. Increasing saccharide adsorption and monolayer thickness change the interfacial refractive index, thereby increasing the intensity of reflected light from the surface. From the alginate BAM images, **Figure 47c (top)**, distinctive striations are observed in addition to bright overall reflection, which supports the previously suggested divalent cation co-adsorption mechanism. However, stearic acid with glucuronate, **Figure 47c (bottom)**, shows dimmer images overall with intensely bright spots, which are the likely formation of aggregates. The small bright spots, likely due to the formation of aggregates, suggest that the stearic acid monolayer undergoes significant reorganization in the presence of glucuronate, as supported by the pivotal point from expansion to compression in the UC phase as shown in **Figure 47b**. Additionally, the insignificant changes in brightness with increasing glucuronate concentration following 20 mg/L indicates that glucuronate co-adsorbs to the monolayer, which would result in a multilayered interface with increased film thickness, does not occur. Instead, glucuronate intercalation into the monolayer, producing the observed reorganization, is more likely. Based on these studies, one can argue that the co-adsorption mechanism between alginate (polysaccharide) and glucuronate (monosaccharide) are inherently different.

7.3.2 Interfacial Infrared Reflection–Absorption of Alginate and Glucuronate

Studies have shown that polysaccharide enrichment is facilitated by divalent cationic bridging, and Ca^{2+} induces the greatest extent of alginate co-adsorption.[26,35,40,340,347] In this study, alginate and glucuronate co-adsorption to a stearic-d_{35} acid monolayer at constant ionic composition was experimentally investigated as a function of alginate or glucuronate concentration. The ionic composition of the subphase was selected to model seawater. This proxy seawater consisted of 467 mM NaCl and 10 mM $CaCl_2$. Deuterated stearic acid was used to spectrally isolate the CD_2 scissoring mode from the carboxylate stretching region.[95,136,213,347] The protonation state of the carboxylic headgroup of stearic-d_{35} acid was maintained by adjusting the pH value of the subphase solutions from 5.6 to 8.2. A reported *pKa* of stearic acid is ~10.15.[355] The *pKa* values of the alginate monomers guluronic (G) and mannuronic (M) acids are 3.7 and 3.4, respectively.[356] Hence, at seawater pH of 8.2, stearic acid is partially deprotonated and alginate and glucuronate are completely deprotonated. Carboxylic acid deprotonation via salts has been shown at pH values significantly lower than the pKa.[95,125,128,136,213,352,353,357–359]

To measure co-adsorption of alginate and glucuronate to a stearic-d_{35} acid monolayer as function of saccharide concentration infrared reflection–absorption spectroscopy (IRRAS) was used. The IRRAS spectra were collected in a Petri dish, and stearic-d_{35} acid was spread into the condensed phase at an MMA of 20 $Å^2$/molecule. IRRAS spectra were analyzed in the OH stretching region (3000–3800 cm^{-1}), the COOH stretching region (1230–1800 cm^{-1}), and the CD_2 scissoring mode region (1070–1150 cm^{-2}). IRRAS spectra are plotted as reflectance–absorbance (*RA*) using equation 7.1.

$$RA = -\log\left(\frac{R_{monolayer}}{R_{proxy}}\right), \tag{7.1}$$

where $R_{monolayer}$ is defined as the reflectance of the monolayer and R_{proxy} is the reflectance of the bare aqueous solutions surface.[76,87,92,360,361] Thus, only the spectral signal from the interfacial monolayer is captured. In this study, IRRAS spectra, both positive and negative peaks are observed. If the *RA* values are negative, then the reflectance of the monolayer is greater than the reflectance of the proxy aqueous solution ($R_f/R_0 > 1$). If the RA values are positive, then the reflected signal of the proxy aqueous solution is greater than that of the monolayer (($R_f/R_0 > 1$). Alginate and glucuronate were also included in the aqueous solution spectra (R_{proxy}) to isolate the alginate and glucuronate co-adsorbed to the stearic-d$_{35}$ acid monolayer.

7.3.3 Ca^{2+} Alginate Co-Adsorption Coefficient and Half-Saturation Concentration

In this study, the OH stretching region (ν(OH)) was used to quantify changes in interfacial coverage as a function of alginate co-adsorption. **Figure 48a** shows the ν(OH) modes which are positive, indicating the ν(OH) reflectance of the subphase solution decreases upon the co-adsorption of alginate to a fatty acid monolayer. Thus, the co-adsorption of alginate is increasing the surface coverage and enhancing the ν(OH) reflectance-absorbance values.[347] Consequently, increasing the concentration of alginate further intensifies the peak reflectance–absorbance value.

Figure 48a illustrates the changes in the ν(OH) due to the increase in surface coverage via alginate co-adsorption. The spectra show how increasing the alginate concentration increases the reflectance–absorbance value, ultimately increasing its co-adsorption to the stearic-d$_{35}$ acid monolayer. The IRRAS spectrum of the stearic-d$_{35}$ acid monolayer with at least 10 mg/L of alginate closely maintains the shape of the monolayer spectrum on 0 mg/L proxy aqueous solution, where the greatest ν(OH) signal enhancement happens around ~3580 cm^{-1}. This region has been well-defined as the surface water molecules hydrogen bonding to the carboxylic acid headgroup of a fatty acid.[213,359,362–364] As a result, alginate co-adsorption with increasing concentration enhances the signal around 3580 cm^{-1} because of the alginate carboxylate hydration.[213]

To quantify the co-adsorption of alginate to a stearic-d_{35} acid monolayer, the ν(OH) peak area of the film as a function of alginate concentration was fitted to a Langmuir adsorption isotherm. The Langmuir adsorption model is a well-known and accepted method for quantifying how an absorbate forms a layer on a given surface based on equilibration between the two phases.[365,366] The ν(OH) peak areas were quantified via peak area integration and normalized to values between zero and one. A value of 0 corresponds to the peak area of a 0 mg/L alginate solution where the solution only contains the aqueous proxy (467 mM and 10 mM $CaCl_2$); and a value of 1 corresponds to the highest peak area, coming from the 80 mg/L alginate in proxy aqueous solution where alginate co-adsorption to the monolayer is fully saturated. The reported errors correspond to one standard deviation and were propagated through the operations used in the normalization calculation. Because all ν(OH) peak areas are normalized to the peak area of a system containing only the background proxy aqueous solution without alginate, any normalized peak area greater than zero is attributed solely to alginate co-adsorption to the stearic-d_{35} acid carboxylate headgroup.

The spectroscopic results are plotted in **Figure 48b** as alginate concentration versus normalized peak area of ν(OH). All monolayer compositions show a positive correlation between peak area and alginate concentration. The data is fit to a Langmuir model (equation 7.2) such that the Langmuir co-adsorption parameters could be employed in OCEANFILMS-2, a model for SSA composition using a two-layer Langmuir model for surface adsorption layers.[39,40,367]

$$A = A_{max}\frac{K_{sacc}C_{sacc}}{1+K_{sacc}C_{sacc}} = A_{max}\frac{C_{sacc}}{C_{\frac{1}{2},sacc}+C_{sacc}} \tag{7.2}$$

A and A_{max} are peak intensity and maximum peak intensity of ν(OH), C_{sacc} is the concentration of saccharide, K_{sacc} is the affinity coefficient for adsorption, and $C_{1/2sacc}$ is the half-saturation concentration.[39,367] Therefore, the Langmuir adsorption coefficient and half-saturation concentration of alginate to stearic-d_{35} acid monolayer are analyzed and reported. It is found that $K_{alginate} = 0.089 \pm 0.015$ L/mg and $C_{1/2,alginate} = 11 \pm 1.9$ mg/L, as shown in **Figure 48b**. Alginate exhibits a strong adsorption isotherm and reaches saturation at relatively low concentrations.

7.3.4 Glucuronate Co-Adsorption Coefficient and Half-Saturation Concentration

Similar analysis was performed for glucuronate, where the ν(OH) region, shown in **Figure 49a**, indicates that glucuronate is also being adsorbed to the stearic-d_{35} acid monolayer but to a lesser extent and possibly by a different co-adsorption mechanism. IRRAS spectra of the stearic-d_{35} acid monolayer spread on solutions with at least 10 mg/L of glucuronate also closely follow the shape of the monolayer spectrum on just proxy aqueous solution. Based on the ν(OH) mode at ~3580 cm^{-1}, it is evident that monolayer rearrangement is happening at concentrations of 30 and 40 mg/L glucuronate where the reflectance–absorbance values are less than the reflectance–absorbance value of just the monolayer spread on the proxy aqueous solution. Such a decrease in the reflectance–absorbance values could indicate different co-adsorption mechanisms caused by lipid desorption and/or monolayer rearrangement.

The ν(OH) region peak areas were also quantified via peak area integration and normalization between zero and one, as plotted in **Figure 49b**. Based on the normalized data in **Figure 49b**, the 30 and 40 mg/L glucuronate solutions are negative values relative to the 0 mg/L solution, suggesting that monolayer rearrangement and/or desorption occurs at these particular glucuronate concentrations. Thus, the Langmuir and BAM measurements indicate that glucuronate is unreliable as a proxy system for alginate and does not capture the complexity of the monolayer enrichment via co-adsorption of alginate. The Langmuir adsorption coefficient as well as the half-saturation concentration of glucuronate to the stearic-d_{35} acid monolayer were determined using the same model described above, **Figure 49b (inset)**. As the 30 and 40 mg/L glucuronate measurements are negative compared to the other concentrations, the fitting to the Langmuir adsorption model was inaccurate. To statistically remove these two concentrations from the fitting data, a residual analysis was performed, details are shown in **Figure 50** and **Table 10**. By the removal of these two concentrations from the normalized peak data, the fitting shows an R^2 value of 0.93. The $K_{\text{glucuronate}} = 0.081 \pm 0.015$ L/mg and $C_{1/2.\text{glucuronate}} = 12 \pm 2.3$ mg/L are also calculated (**Figure 49b**). As expected, a smaller Langmuir adsorption coefficient and half-saturation concentration were observed for glucuronate. These quantitative adsorption parameters agree with the qualitative observations of weakened glucuronate co-adsorption to stearic acid monolayers via the Π–A isotherms and BAM images. Additionally, the IRRAS spectra corroborate the Π–A isotherm and BAM image evidence of glucuronate-induced film reorganization and possible desorption into the subphase.

7.3.5. Monolayer Thickness of Co-Adsorbed Alginate and Glucuronate at the Air-Water Interface

To temporally assess the co-adsorption of alginate and glucuronate to a stearic-d_{35} acid monolayer, non-equilibrium relaxation (NER) experiments at a constant surface pressure, 30 mN/m, coupled with BAM were used to calculate thickness as a function of alginate or glucuronate concentration. The NER experiments were performed for three hours (details in Methods section). While the NER experiment was running, BAM images were taken every 120 s for a total of 90 images per trial. Each NER experiment was performed in triplicate for 10, 20, 50, and 100 mg/L for each saccharide (**Figure 51a** and **Figure 52a**). In addition, the NER of stearic acid on 40 mg/L glucuronate was measured to understand the anomalous peak area decrease in the IRRAS spectra. The results from the underlying solution with alginate show that the stearic acid monolayer reflectivity enhances as the concentration of alginate is increased (**Figure 51**), suggesting multilayered alginate adsorption under the monolayer. The T_0 images (**Figure 51b** and **Figure 52b**) correlate to the first image taken as the monolayer is compressed to the desired surface pressure. One can see that as the concentration of alginate increases, a fuller monolayer is observed even at relatively high surface areas.

While the formation of a full stearic acid monolayer on varied glucuronate subphases are seen, the changes in reflectivity are not as stark. A slight decay in the brightness was also observed at concentrations between 20 and 50 mg/L glucuronate, **Figure 52b**. Carter-Fenk *et al.* reports molecular dynamic simulations showing the lack of alginate intercalation into the monolayer. The MD simulations reveal the formation of a second layer beneath the fatty acid monolayer and suggest that Ca^{2+} likely serves as a bridge between the two COO$^-$ moieties. Glucuronate opposes this finding where it intercalates into the monolayer and does not form a second co-adsorbed layer.

To further characterize the changes in film morphology, the relative film thickness was calculated using the BAM image data. Using the refractive index of stearic acid (n_m=1.430),[368,369] the relative thickness (d) can be determined from the following equation[370] used to model ultrathin films (<20nm):[371]

$$d = \frac{\lambda\sqrt{R_p}}{\pi \sin{(2\theta_B - 90)}} \frac{n_m^2(n_a^2 - n_s^2)}{\sqrt{n_a^2 + n_s^2}(n_a^2 - n_m^2)(n_s^2 - n_m^2)} \tag{7.3}$$

In this equation, λ is the laser wavelength, R_p is the p-polarized reflectance, n_m is the refractive index of the stearic acid monolayer, and θ_B is the Brewster angle. The refractive indices of air and seawater are n_a=1.00 and n_s=1.35, respectively.[372]

The monolayer thickness, as a function of alginate and glucuronate concentration, in **Figure 53** shows evidence of the co-adsorption of saccharides to the interface. It is clear that the co-adsorption of alginate causes a larger change in the monolayer thickness evidenced by the increase from ~ 4 nm ([alginate] = 0 mg/L) to ~5.5 nm ([alginate] = 100 mg/L). Previous studies have shown that late stages of an algal bloom had an average thickness of ~5 nm.[373] Other studies of relevant saturated long-chain fatty acids and phospholipids report an average thickness of ~1.3 to 3 nm, subject to the chemical composition of the subphase.[374] This study calculated thickness from alginate goes beyond the monolayer regime, indicating the presence of a multilayer film.[374–376] Aqueous solutions containing glucuronate show smaller changes, ranging from ~4 nm to ~4.2 nm, providing further evidence for minimal co-adsorption of glucuronate into a second layer at the interface. By using experimentally collected reflectivity, or albedo values, to calculate thickness, where the only assumption is the consistent maintenance of the interfacial refractive index, this work has calculated values based on minimally assumed parameters that provide highly informative inputs for climate models. These results reveal the important influence of saccharide co-adsorption to the interface, thus suggesting that the role of monosaccharides as a proxy for a more complex system cannot provide a full picture of saccharide co-adsorption.

7.3.6 Impacts of Alginate versus Glucuronate Co-Adsorption on Stearic Acid Interfacial Structure

Fatty acid protonation states have an impact on the co-adsorption of alginate and glucuronate at the interface. A previous study demonstrated that there is less alginate co-adsorption at pH 5.8 than at basic pH (8.2).[347] It has been suggested that glucuronate ions bind to Ca^{2+} through three chelation sites.[377–379] Thus, for alginate and glucuronate co-adsorption to take place, the headgroup of the fatty acid has to be partially deprotonated. In addition to higher solution pH, previous work has shown that Ca^{2+} facilitates fatty acid headgroup deprotonation,[95,125,136,357,380,381] thereby increasing the number of potential Ca^{2+} bridging sites for alginate or glucuronate co-adsorption. Because the carboxylic spectral region (1230–1800 cm^{-1}) displays sensitivity to binding,[91,95,136,196,382] it is used to obtain additional insights into the co-adsorption of alginate,[347] glucuronate,[39,339,383] and the protonation state of the carboxylic headgroup of stearic-d_{35} acid.[95,136,357,358,380] Stearic-d_{35} acid spread onto the proxy aqueous solution without alginate or glucuronate at pH 8.2 is deprotonated, as shown in **Figure 54a** and **Figure 55a** by the presence of the asymmetric (ν_{AS}) (1500–1630 cm^{-1}) and symmetric (ν_S) (~1410 cm^{-1}) carboxylate (COO$^-$) modes and the disappearance of the carboxyl mode (~1720 cm^{-1}). As the alginate or glucuronate concentrations increase, the peak intensities of the ν_{AS}(COO$^-$) and ν_S(COO$^-$) modes increase. According to previous studies, this increase in intensity is due to co-absorption of alginate via divalent cationic bridging and the co-adsorption of glucuronate.[339,347]

Figure 54a shows each of the ν_{AS}(COO$^-$) and ν_S(COO$^-$) modes splitting into higher and lower frequency bands, where the higher frequency COO$^-$ bands have been previously assigned to the alginate carboxylate modes via harmonic vibrational frequency calculations.[347] Analogous peak enhancement and broadening were observed for the phosphate headgroup vibrational modes of 1,2-dipalmitoyl-sn-glycero-3-phosphatidic acid (DPPA) upon arginine and guanidinium binding.[196] Thus, the spectral signatures of fatty acid deprotonation are highly informative about the energetically favorable complexation between the lipid carboxylate headgroup, Ca^{2+}, and alginate. The spectra characterizing only the proxy seawater solution do not exhibit the high frequency ν_{AS}(COO$^-$) mode. Upon the addition of alginate, a high frequency band appears and increases as the concentration of alginate increases, providing direct spectroscopic evidence for alginate co-adsorption to the stearic-d$_{35}$ acid monolayer. A more drastic increase in the alginate ν_{AS}(COO$^-$) mode intensity is observed between 10 mg/L and 30 mg/L, which is within the calculated half-saturation concentration from the Langmuir adsorption model. A blue shift is also observed for the stearic-d$_{35}$ acid ν_{AS}(COO$^-$) mode. While this vibrational shift is not direct evidence of the alginate co-adsorption to the monolayer; it is possible that alginate disturbs the stearic-d_{35} acid headgroup hydration through electrostatic interactions with the headgroup.[352,384]

Interfacial film organization was also probed via the stearic-d_{35} acid δCD_2 mode (**Figure 54b**). All spectra exhibit a δCD_2 mode with a center wavelength of 1089 cm^{-1}, revealing that the hydrocarbon chains are packed in a hexagonal lattice structure.[385,386] The δCD_2 mode intensity also increases when the concentration of alginate is increased within the proxy aqueous solution. Such signal enhancement is most apparent at alginate concentrations above 10 mg/L, and it is particularly evident in the high frequency regime. Through harmonic vibrational frequency calculations, Carter-Fenk *et al*. showed that the signal enhancement can be assigned to alginate ν, δ(C-O-H), ν(C-O-C), and C-H wagging modes.[347] Therefore, the signal enhancement adjacent to the δCD_2 mode is assigned to alginate co-adsorption via Ca^{2+} bridging with the carboxylate headgroup of stearic-d_{35} acid.

Hydrocarbon chain conformation of surfactants in a monolayer can also be determined by evaluating the ν_S, $\nu_{AS}(CD_2)$ center frequencies.[386] The CD_2 stretching region confirmed that the mechanism of alginate interfacial enrichment is by alginate Ca^{2+} bridging and not by intercalation of alginate into the stearic-d_{35} acid monolayer (**Figure 56a**). If alginate intercalated into the stearic-d_{35} acid monolayer, changes in the CD stretching modes would be observed. Such intercalation would disrupt the monolayer, thus reducing the dispersion interactions between the alkyl tails, causing the CD stretching modes to blue shift. No spectral shifts were observed, ruling out intercalation and confirming that alginate is restrained to the surface region.

Furthermore, the size of the alginate polysaccharide would prohibit intercalation between fatty acids within the monolayer.

When glucuronate is added to the proxy aqueous solution instead of alginate, the carboxyl region modes (1230–1800 cm^{-1}) do not increase in intensity (**Figure 55a**). The split of the asymmetric stretch (~1540 cm^{-1}) is not observed, suggesting that glucuronate Ca^{2+} bridging to the stearic-d_{35} acid headgroup is not the primary mechanism of enrichment. The lack of significant spectral changes with increasing glucuronate concentration shows that the interaction between the stearic-d_{35} acid monolayer and glucuronate is particularly different than its interaction with alginate. Studies have postulated that glucuronate enrichment at the interface occurs via co-adsorption.[26,39,339,383] While this is a possibility, this study results suggest that glucuronate co-adsorption is not facilitated by divalent cationic bridging interactions. Thus, using glucuronate as a proxy system for saccharide co-adsorption will not fully capture alginate's mechanistic enrichment.

Because changes were not observed in the carboxyl region, we looked at the δCD_2 mode (**Figure 55b**). The δCD_2 mode centered at 1089 cm^{-1} reveals hexagonal lattice structure. The enhancement observed for alginate is not present for glucuronate, again indicating the differing adsorption mechanisms for these two saccharides. Interestingly, a decrease in the intensity of the δCD_2 mode was observed at concentrations of 30 and 40 mg/L glucuronate, which is consistent with the shift from expansion to compression observed in the Π–A isotherms (**Figure 47b**), further supporting monolayer rearrangement and potential lipid desorption. The δCD_2 peak areas corresponding to 30 and 40 mg/L glucuronate diminish by ~20 % and 30%, respectively (see **Table 11**for peak area information). The CD_2 stretching region was also inspected (**Figure 56b**). While any changes were observed in the center wavelengths of the $\nu_S(CD_2)$ and $\nu_{AS}(CD_2)$ modes, a decrease was observed in the intensity of these two modes at 30 and 40 mg/L glucuronate. The $\nu_S(CD_2)$ and $\nu_{AS}(CD_2)$ modes decrease by 20% for the solution containing 30 mg/L glucuronate and 30% for the solution containing 40 mg/L, **Table 12**, glucuronate, which is consistent with the results of the δCD_2 mode. This reaffirms that monolayer rearrangement is occurring at these specific concentrations, suggesting that the monosaccharide enrichment mechanism requires future study.

7.4 Conclusions

In this work, poly- and monosaccharide co-adsorption interactions at a proxy sea surface microlayer are measured, compared, and quantified using Langmuir adsorption model fitting and film thickness analyses. This study expands upon previous work characterizing the divalent cationic bridging mechanism driving alginate co-adsorption to deprotonated monolayers by studying glucuronic acid co-adsorption, as it is representative of the monomeric form of alginate. The Langmuir adsorption coefficient and half-saturation concentration were measured of both alginate and glucuronate to stearic-d_{35} acid monolayers using surface-sensitive infrared reflection–absorption spectroscopy (IRRAS). Langmuir surface pressure–area (Π–A) isotherms and IRRAS spectra provided insights into both the stearic-d_{35} acid monolayer and co-adsorbed saccharide structural organization at the air–water interface. Additionally, Brewster angle microscopy (BAM) and non-equilibrium relaxation (NER) studies provided further information on film morphology and monolayer thickness as a function of saccharide concentration.

Alginate co-adsorption to an insoluble monolayer via Ca^{2+} bridging is directly observed and found that 11 ± 1.9 mg/L is the alginate half-saturation concentration. This represents the concentration at which half of the maximum of alginate co-absorption is reached. Alginate co-adsorption also increases film thickness, wherein the monolayer thickness increases from ~4.0 nm in the absence of alginate to a maximum thickness of ~5.5 nm at alginate co-adsorption saturation.

The monosaccharide glucuronate exhibits a strikingly different interplay between co-adsorption and intercalation into the stearic-d_{35} acid monolayer, resulting in an anomalous desorption and film reorganization for the 30 and 40 mg/L concentration studies, although this behavior does not persist for other glucuronate concentrations. It was also found that 12 ± 2.3 mg/L is the minimum concentration for glucuronate co-adsorption, indicating weaker glucuronate co-adsorption than that of alginate. The maximum film thickness is 4.2 nm suggests that glucuronate does not form a second layer underneath the lipid monolayer. Rather, the film morphological changes shown in the BAM images point to a glucuronate intercalation mechanism into the monolayer, yielding significant monolayer reorganization.

This detailed study of poly- and monosaccharide co-adsorption to a deprotonated monolayer demonstrates that saccharide size dramatically impacts the co-adsorption mechanism, organization, and morphology within sea surface microlayer proxy films. Therefore, this work has shown that monosaccharides alone are insufficient to accurately model saccharide transport and enrichment in sea spray aerosol. This study provides Langmuir adsorption fitting parameters of both glucuronate and alginate co-adsorption to a stearic acid monolayer for implementation within Earth system models.

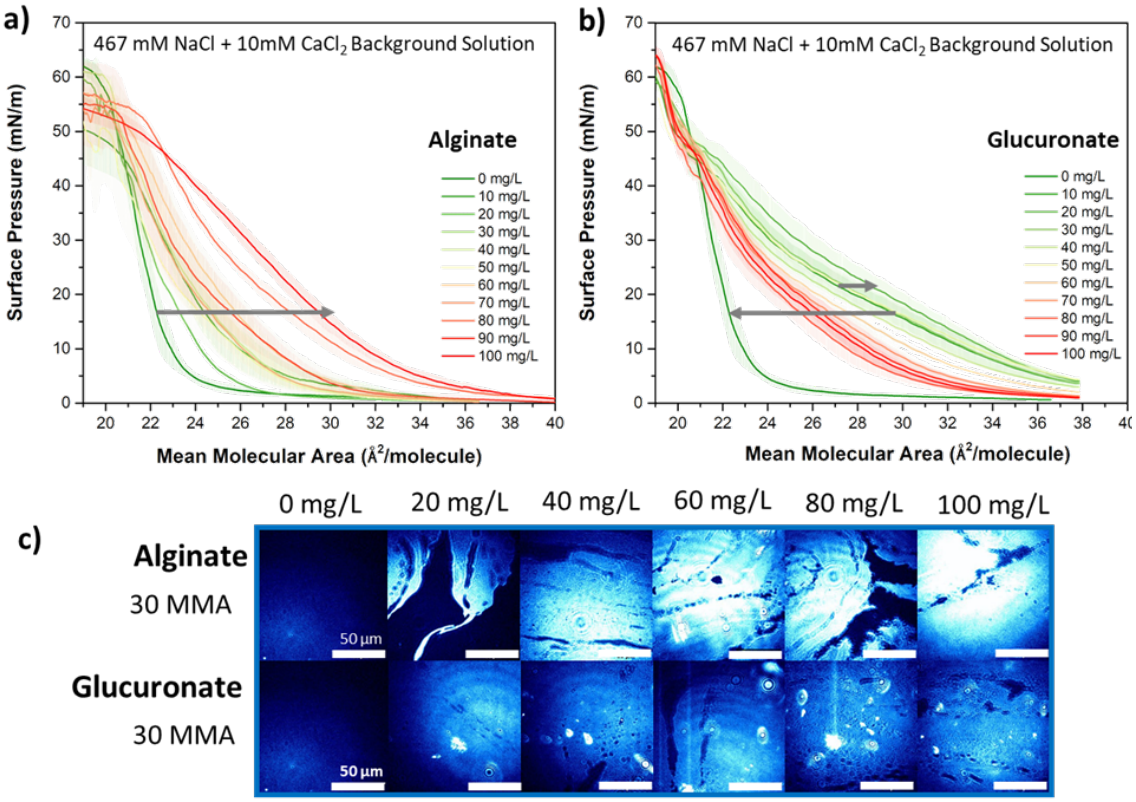

Figure 47. Langmuir Π–A isotherms of (a) alginate co-adsorption to stearic acid monolayer at pH 8.2 at various concentrations. (b) Glucuronate intercalation into the stearic acid monolayer at pH 8.2. (c) BAM images provide evidence of the alginate co-adsorption via Ca^{2+} bridging interactions and of the intercalation of glucuronate to the stearic acid monolayer. Additional BAM images of the full compression isotherms are shown in **Figure 57**. The scale bar in all images is 50 µm.

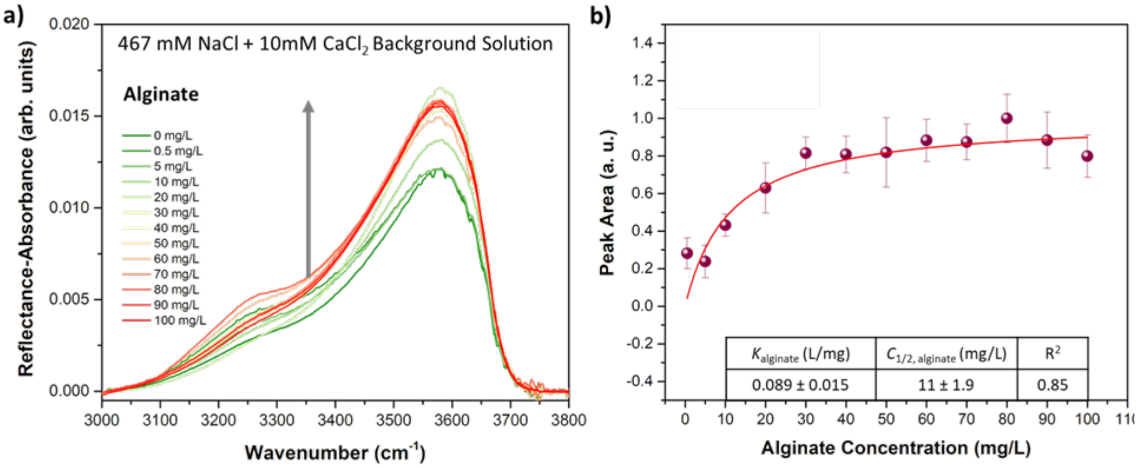

Figure 48. (a) IRRAS spectra of the ν(OH) indicating the significant alginate co-adsorption to stearic-d_{35} acid monolayer at different concentrations. (b) Normalized peak area of the ν(OH) of alginate co-adsorption to stearic-d_{35} acid monolayer. All scans have a constant aqueous solution concentration of 467 mM NaCl and 10 mM $CaCl_2$ with a changing alginate concentration (0–100 mg/L). The Langmuir co-adsorption coefficient, $K_{alginate}$, is given as (L/mg) and the half-saturation concentration, $C_{1/2,alginate}$, as mg/L. Error bars correspond to one standard deviation that has been propagated through the operations used in the normalization calculation

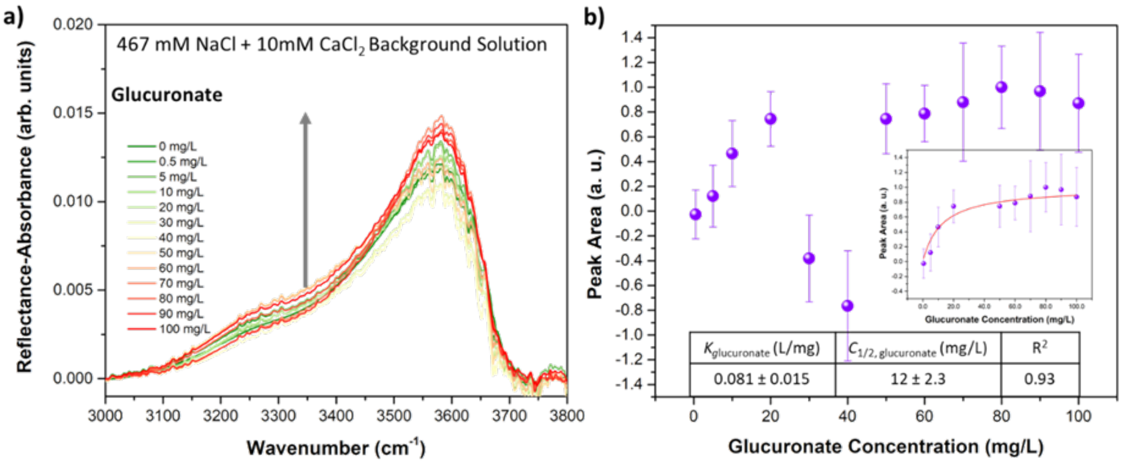

Figure 49. (a) IRRAS spectra of the ν(OH) region indicating glucuronate co-adsorption to a stearic-d35 acid monolayer at different concentrations. (b) Normalized peak area of the ν(OH) region of glucuronate co-adsorption to stearic-d35 acid monolayer. All scans have a constant aqueous solution concentration of 467 mM NaCl and 10 mM $CaCl_2$ with a changing glucuronate concentration (0–100 mg/L). Inset shows the Langmuir fitting of the ν(OH) peak areas following removal of the 30 and 40 mg/L glucuronate data points. The Langmuir co-adsorption coefficient, $K_{glucuronate}$, is given as (L/mg) and the half-saturation concentration, $C_{1/2,glucuronate}$, as mg/L. Error bars correspond to one standard deviation that has been propagated through the operations used in the normalization calculation.

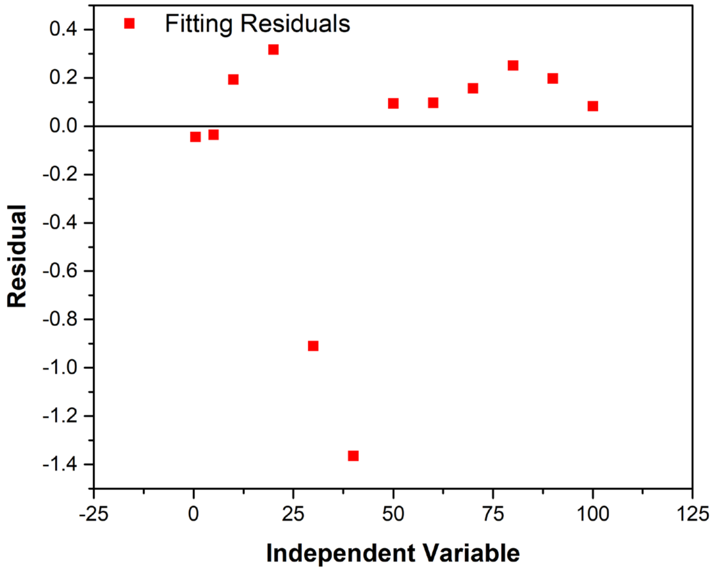

Figure 50. Langmuir adsorption fitting residual showing the 30 mg/L and 40 mg/L glucuronate concentrations as outliers. Data shown in **Table 10**.

Table 10. Peak and normalized peak areas of the OH stretching region of stearic-d_{35} acid monolayer on glucuronate containing solutions. Any residual values that are greater than 1 ± 0. 1 or −1 ± 0.1 are consider outliers.

Glucuronate (mg/L)	Peak Area (a.u)	Normalized Peak Area (a.u)	Residuals
0	3.33551	0	0
0.5	3.32536	-0.02610	-0.04442
5	3.38281	0.12165	-0.0356
10	3.51623	0.46477	0.19302
20	3.62466	0.74364	0.31627
30	3.18733	-0.38109	-0.90928
40	3.03798	-0.76518	-1.364
50	3.62518	0.74499	0.09393
60	3.64185	0.78785	0.09659
70	3.67769	0.88002	0.15686
80	3.72434	1	0.25092
90	3.71176	0.96765	0.19708
100	3.67433	0.87138	0.08272

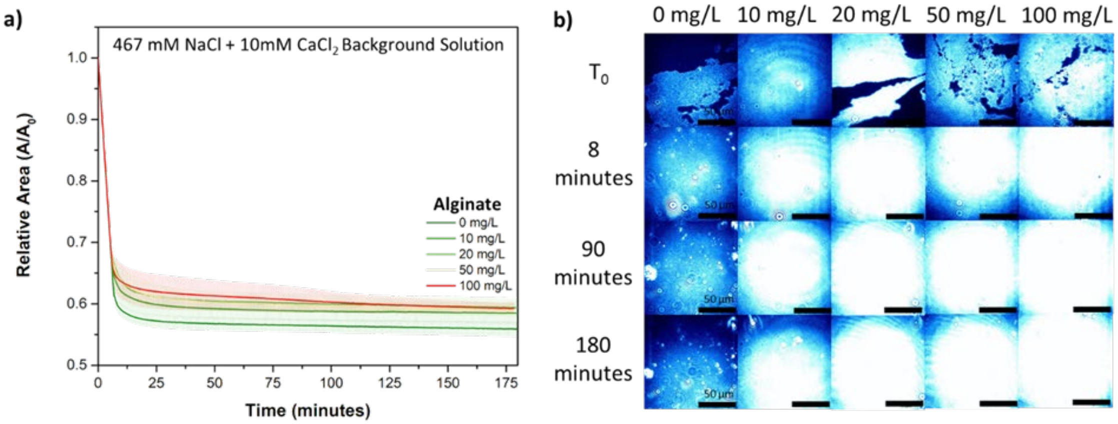

Figure 51. a) Monolayer non-equilibrium relaxation at a constant surface pressure of alginate subphase aqueous solution of 0, 10, 20, 50 and 100 mg/L under a stearic acid monolayer. b) BAM images of each monolayer at various times within the experiment.

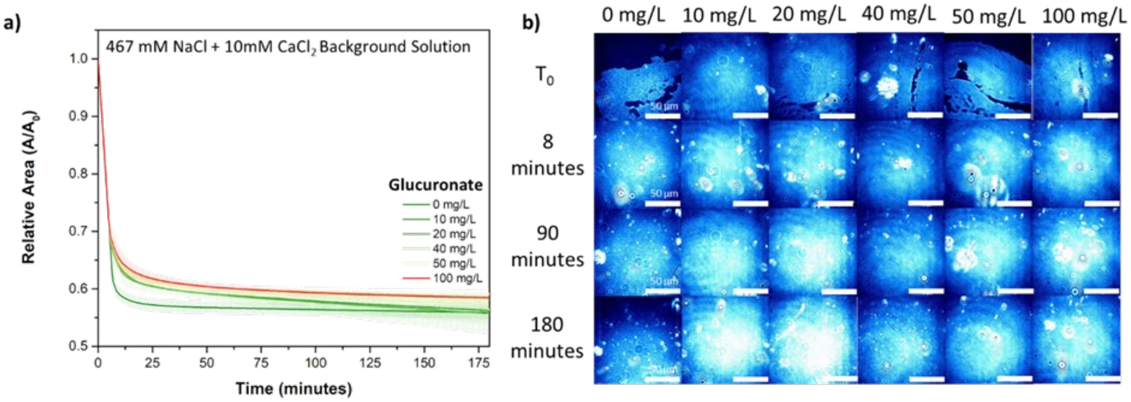

Figure 52. a) Monolayer non-equilibrium relaxation at a constant surface pressure of glucoronate subphase aqueous solution of 0, 10, 20, 40, 50 and 100 mg/L under a stearic acid monolayer. b) BAM images of each monolayer at various times within the experiment

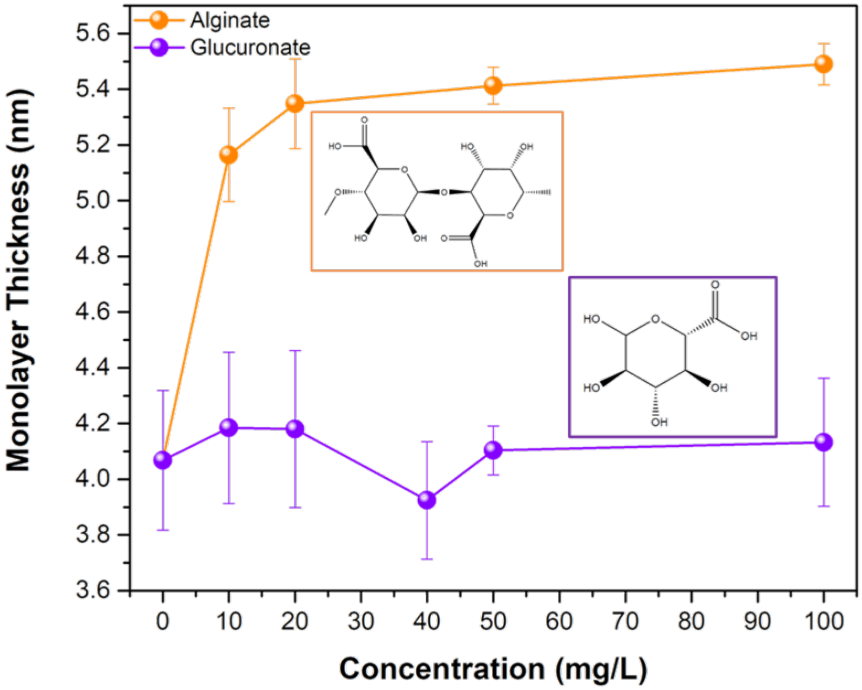

Figure 53. Film thickness of the co-adsorption of alginate (orange) and glucuronate (purple) to a stearic acid monolayer as a function of concentration. (The protonated forms of the molecular structures are shown for reference.)

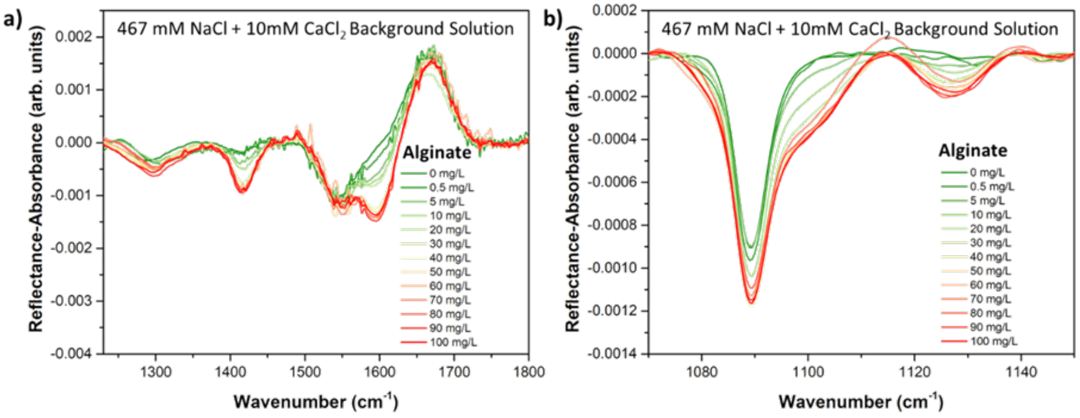

Figure 54. IRRAS spectra of the (a) COOH stretching region provide evidence of the alginate co-adsorption via Ca^{2+} bridging interactions to the stearic-d_{35} acid monolayer at pH 8.2. (b) δCD_2 mode region demonstrates the alginate co-adsorption to the stearic-d_{35} acid monolayer at pH 8.2. The spectra show no stearic-d_{35} acid lattice packing changes upon adsorption.

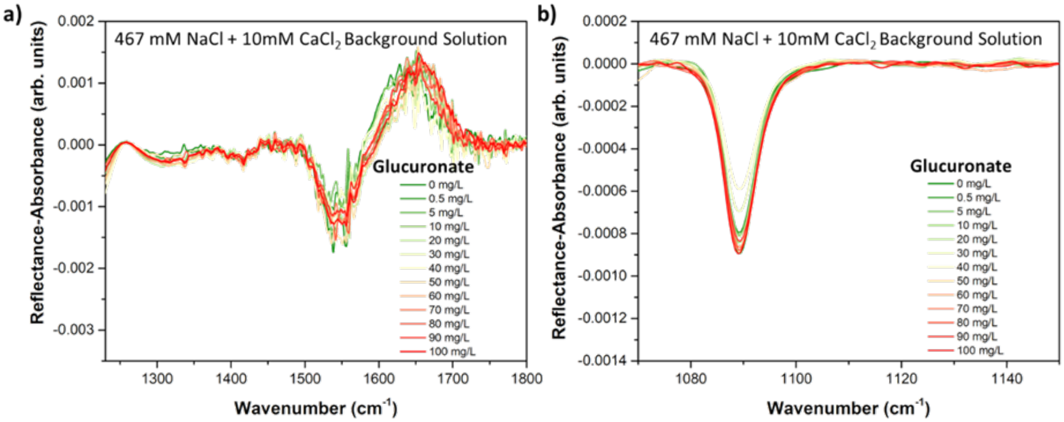

Figure 55. IRRAS spectra of the (a) COOH stretching region of the intercalation interaction of glucuronate to the stearic-d_{35} acid monolayer at pH 8.2. (b) δCD_2 mode region of the intercalation interaction of glucuronate to the stearic-d_{35} acid monolayer at pH 8.2. At 30 and 40 mg/L, a reduction in peak intensity is observed, possibly due to desorption of the stearic-d_{35} acid at these concentrations due to monolayer rearrangement.

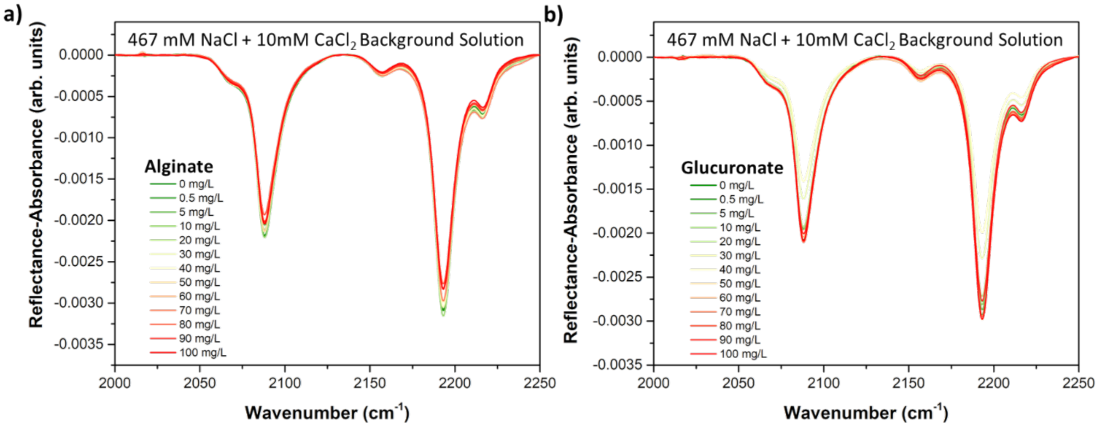

Figure 56. CD2 stretching region spectra of a stearic acid monolayer of the proxy aqueous solution containing a) alginate and b) glucuronate at various concentrations.

Table 11. Peak area of the CD2 scissoring mode at 1089cm^{-1} of stearic-d35 acid monolayer on glucuronate containing aqueous solutions.

Concentration (mg/L)	Peak Area (a.u)
0	0.00705± 0.00113
0.5	0.00606 ± 0.00058
5	0.00640 ± 0.00035
10	0.00659 ± 0.00024
20	0.00674 ± 0.00043
30	0.00542 ± 0.00056
40	0.00479 ± 0.00026
50	0.00698 ± 0.00048
60	0.00719 ± 0.00047
70	0.00664 ± 0.00047
80	0.00708 ± 0.00020
90	0.00672 ± 0.00011
100	0.00726 ± 0.00027

Table 12. Peak area of the ν_S (CD_2) and ν_{AS} (CD_2) modes at 2089cm^{-1} and 2193cm^{-1} of stearic-d_{35} acid monolayer on glucuronate containing aqueous solutions.

Concentration (mg/L)	ν_S (CD_2) Peak Area (a.u)	ν_{AS} (CD_2) Peak Area (a.u)
0	0.03378 ± 0.00229	0.03856 ± 0.00424
0.5	0.03082 ± 0.00274	0.03772 ± 0.00092
5	0.03241 ± 0.00105	0.03825 ± 0.00171
10	0.03243 ± 0.00170	0.03534 ± 0.00172
20	0.03196 ± 0.00253	0.03609 ± 0.00317
30	0.02598 ± 0.00235	0.03054 ± 0.00211
40	0.02280 ± 0.00084	0.02677 ± 0.00099
50	0.03460 ± 0.00090	0.03793 ± 0.00247
60	0.03366 ± 0.00156	0.03800 ± 0.00139
70	0.03417 ± 0.00118	0.03888 ± 0.00083
80	0.03470 ± 0.00187	0.03932 ± 0.00090
90	0.03194 ± 0.00104	0.03752 ± 0.00111
100	0.03400 ± 0.00186	0.03860 ± 0.00199

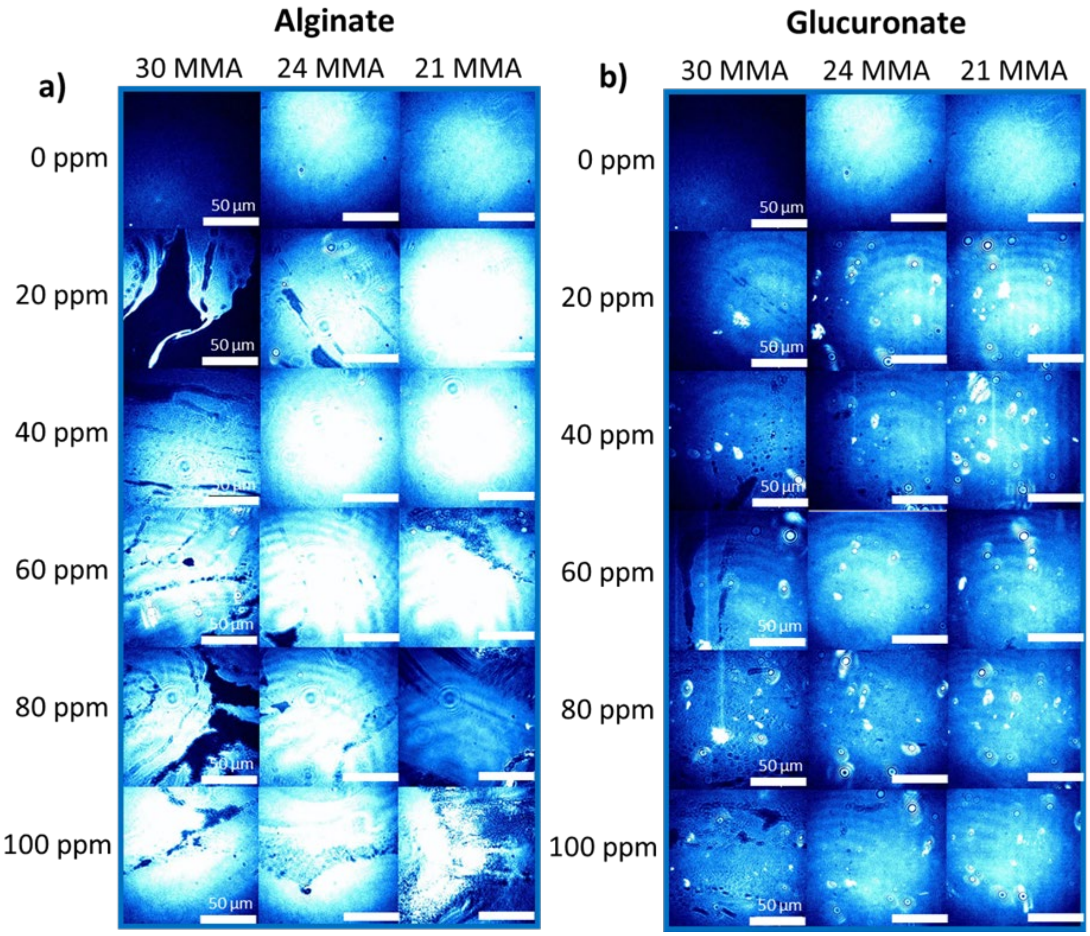

Figure 57. BAM images of alginate and glucuronate co-adsorption to a stearic acid monolayer as a function of concentration taken during Langmuir surface pressure–area isotherms.

References

(1) Finlayson-Pitts, B. J.; Pitts, J. N. *Chemistry of the Upper and Lower Atmosphere: Theory, Experiments, and Applications*; Academic Press, 2000.

(2) Millero, F. J. *Chemical Oceanography, Third Edition*, 3rd ed.; CRC Press, 2005.

(3) Wurl, O.; Ekau, W.; Landing, W. M.; Zappa, C. J. Sea Surface Microlayer in a Changing Ocean – A Perspective. *Elem Sci Anth* **2017**, *5*, 31. https://doi.org/10.1525/elementa.228.

(4) Sieburth, J. McN. Microbiological and Organic-Chemical Processes in the Surface and Mixed Layers. In *Air-Sea Exchange of Gases and Particles*; Liss, P. S., Slinn, W. G. N., Eds.; NATO ASI Series; Springer Netherlands: Dordrecht, 1983; pp 121–172. https://doi.org/10.1007/978-94-009-7169-1_3.

(5) Zafiriou, O. C. Photochemistry and the Sea-Surface Microlayer: Natural Processes and Potential as a Technique. In *Dynamic Processes in the Chemistry of the Upper Ocean*; Burton, J. D., Brewer, P. G., Chesselet, R., Eds.; NATO Conference Series; Springer US: Boston, MA, 1986; pp 129–135. https://doi.org/10.1007/978-1-4684-5215-0_11.

(6) Carlson, D. J. The Early Diagenesis of Organic Matter: Reaction at the Air-Sea Interface. In *Organic Geochemistry: Principles and Applications*; Engel, M. H., Macko, S. A., Eds.; Topics in Geobiology; Springer US: Boston, MA, 1993; pp 255–268. https://doi.org/10.1007/978-1-4615-2890-6_12.

(7) Wang, X.; Deane, G. B.; Moore, K. A.; Ryder, O. S.; Stokes, M. D.; Beall, C. M.; Collins, D. B.; Santander, M. V.; Burrows, S. M.; Sultana, C. M.; Prather, K. A. The Role of Jet and Film Drops in Controlling the Mixing State of Submicron Sea Spray Aerosol Particles. *Proc Natl Acad Sci USA* **2017**, *114*, 6978–6983. https://doi.org/10.1073/pnas.1702420114.

(8) De Leeuw, G.; Andreas, E. L.; Anguelova, M. D.; Fairall, C. W.; Lewis, E. R.; O'Dowd, C.; Schulz, M.; Schwartz, S. E. Production Flux of Sea Spray Aerosol. *Rev Geophys* **2011**, *49*. https://doi.org/10.1029/2010RG000349.

(9) Carter-Fenk, K. A.; Allen, H. C. Collapse Mechanisms of Nascent and Aged Sea Spray Aerosol Proxy Films. *Atmosphere* **2018**, *9*, 503. https://doi.org/10.3390/atmos9120503.

(10) DeMott, P. J.; Hill, T. C. J.; McCluskey, C. S.; Prather, K. A.; Collins, D. B.; Sullivan, R. C.; Ruppel, M. J.; Mason, R. H.; Irish, V. E.; Lee, T.; Hwang, C. Y.; Rhee, T. S.; Snider, J. R.; McMeeking, G. R.; Dhaniyala, S.; Lewis, E. R.; Wentzell, J. J. B.; Abbatt, J.; Lee, C.; Sultana, C. M.; Ault, A. P.; Axson, J. L.; Martinez, M. D.; Venero, I.; Santos-Figueroa, G.; Stokes, M. D.; Deane, G. B.;

Mayol-Bracero, O. L.; Grassian, V. H.; Bertram, T. H.; Bertram, A. K.; Moffett, B. F.; Franc, G. D. Sea Spray Aerosol as a Unique Source of Ice Nucleating Particles. *Proc. Natl. Acad. Sci.* **2016**, *113* (21), 5797–5803. https://doi.org/10.1073/pnas.1514034112.

(11) McCluskey, C. S.; Hill, T. C. J.; Malfatti, F.; Sultana, C. M.; Lee, C.; Santander, M. V.; Beall, C. M.; Moore, K. A.; Cornwell, G. C.; Collins, D. B.; Prather, K. A.; Jayarathne, T.; Stone, E. A.; Azam, F.; Kreidenweis, S. M.; DeMott, P. J. A Dynamic Link between Ice Nucleating Particles Released in Nascent Sea Spray Aerosol and Oceanic Biological Activity during Two Mesocosm Experiments. *J. Atmospheric Sci.* **2016**, *74* (1), 151–166. https://doi.org/10.1175/JAS-D-16-0087.1.

(12) McCluskey, C. S.; Ovadnevaite, J.; Rinaldi, M.; Atkinson, J.; Belosi, F.; Ceburnis, D.; Marullo, S.; Hill, T. C. J.; Lohmann, U.; Kanji, Z. A.; O'Dowd, C.; Kreidenweis, S. M.; DeMott, P. J. Marine and Terrestrial Organic Ice-Nucleating Particles in Pristine Marine to Continentally Influenced Northeast Atlantic Air Masses. *J. Geophys. Res. Atmospheres* **2018**, *123* (11), 6196–6212. https://doi.org/10.1029/2017JD028033.

(13) Alpert, P. A.; Aller, J. Y.; Knopf, D. A. Initiation of the Ice Phase by Marine Biogenic Surfaces in Supersaturated Gas and Supercooled Aqueous Phases. *Phys. Chem. Chem. Phys.* **2011**, *13* (44), 19882–19894. https://doi.org/10.1039/C1CP21844A.

(14) McCluskey, C. S.; Hill, T. C. J.; Sultana, C. M.; Laskina, O.; Trueblood, J.; Santander, M. V.; Beall, C. M.; Michaud, J. M.; Kreidenweis, S. M.; Prather, K. A.; Grassian, V.; DeMott, P. J. A Mesocosm Double Feature: Insights into the Chemical Makeup of Marine Ice Nucleating Particles. *J. Atmospheric Sci.* **2018**, *75* (7), 2405–2423. https://doi.org/10.1175/JAS-D-17-0155.1.

(15) Gavish, M.; Popovitz-Biro, R.; Lahav, M.; Leiserowitz, L. Ice Nucleation by Alcohols Arranged in Monolayers at the Surface of Water Drops. *Science* **1990**, *250* (4983), 973–975. https://doi.org/10.1126/science.250.4983.973.

(16) Popovitz-Biro, R.; Wang, J. L.; Majewski, J.; Shavit, E.; Leiserowitz, L.; Lahav, M. Induced Freezing of Supercooled Water into Ice by Self-Assembled Crystalline Monolayers of Amphiphilic Alcohols at the Air-Water Interface. *J. Am. Chem. Soc.* **1994**, *116* (4), 1179–1191. https://doi.org/10.1021/ja00083a003.

(17) Zobrist, B.; Koop, T.; Luo, B. P.; Marcolli, C.; Peter, T. Heterogeneous Ice Nucleation Rate Coefficient of Water Droplets Coated by a Nonadecanol Monolayer. *J. Phys. Chem. C* **2007**, *111* (5), 2149–2155. https://doi.org/10.1021/jp066080w.

(18) Knopf, D. A.; Forrester, S. M. Freezing of Water and Aqueous NaCl Droplets Coated by Organic Monolayers as a Function of Surfactant Properties and Water Activity. *J. Phys. Chem. A* **2011**, *115* (22), 5579–5591. https://doi.org/10.1021/jp2014644.

(19) DeMott, P. J.; Mason, R. H.; McCluskey, C. S.; Hill, T. C. J.; Perkins, R. J.; Desyaterik, Y.; Bertram, A. K.; Trueblood, J. V.; Grassian, V. H.; Qiu, Y.;

Molinero, V.; Tobo, Y.; Sultana, C. M.; Lee, C.; Prather, K. A. Ice Nucleation by Particles Containing Long-Chain Fatty Acids of Relevance to Freezing by Sea Spray Aerosols. *Environ. Sci. Process. Impacts* **2018**. https://doi.org/10.1039/C8EM00386F.

(20) Ochshorn, E.; Cantrell, W. Towards Understanding Ice Nucleation by Long Chain Alcohols. *J. Chem. Phys.* **2006**, *124* (5), 054714. https://doi.org/10.1063/1.2166368.

(21) Cravigan, L. T.; Mallet, M. D.; Vaattovaara, P.; Harvey, M. J.; Law, C. S.; Modini, R. L.; Russell, L. M.; Stelcer, E.; Cohen, D. D.; Olsen, G.; Safi, K.; Burrell, T. J.; Ristovski, Z. Sea Spray Aerosol Organic Enrichment, Water Uptake and Surface Tension Effects. *Atmospheric Chem. Phys.* **2020**, *20* (13), 7955–7977. https://doi.org/10.5194/acp-20-7955-2020.

(22) Glass, S. J.; Matteson, M. J. Ion Enrichment in Aerosols Dispersed from Bursting Bubbles in Aqueous Salt Solutions. *Tellus* **1973**, *25* (3), 272–280. https://doi.org/10.1111/j.2153-3490.1973.tb00611.x.

(23) Guasco, T. L.; Cuadra-Rodriguez, L. A.; Pedler, B. E.; Ault, A. P.; Collins, D. B.; Zhao, D.; Kim, M. J.; Ruppel, M. J.; Wilson, S. C.; Pomeroy, R. S.; Grassian, V. H.; Azam, F.; Bertram, T. H.; Prather, K. A. Transition Metal Associations with Primary Biological Particles in Sea Spray Aerosol Generated in a Wave Channel. *Environ. Sci. Technol.* **2014**, *48* (2), 1324–1333. https://doi.org/10.1021/es403203d.

(24) Jayarathne, T.; Sultana, C. M.; Lee, C.; Malfatti, F.; Cox, J. L.; Pendergraft, M. A.; Moore, K. A.; Azam, F.; Tivanski, A. V.; Cappa, C. D.; Bertram, T. H.; Grassian, V. H.; Prather, K. A.; Stone, E. A. Enrichment of Saccharides and Divalent Cations in Sea Spray Aerosol During Two Phytoplankton Blooms. *Env. Sci Technol* **2016**, *50*, 11511–11520. https://doi.org/10.1021/acs.est.6b02988.

(25) Salter, M. E.; Hamacher-Barth, E.; Leck, C.; Werner, J.; Johnson, C. M.; Riipinen, I.; Nilsson, E. D.; Zieger, P. Calcium Enrichment in Sea Spray Aerosol Particles: Calcium Enrichment in Sea Spray Aerosol. *Geophys Res Lett* **2016**, *43*, 8277–8285. https://doi.org/10.1002/2016GL070275.

(26) Schill, S. R.; Burrows, S. M.; Hasenecz, E. S.; Stone, E. A.; Bertram, T. H. The Impact of Divalent Cations on the Enrichment of Soluble Saccharides in Primary Sea Spray Aerosol. *Atmosphere* **2018**, *9* (12), 476. https://doi.org/10.3390/atmos9120476.

(27) Xu, G.; Gao, Y. Atmospheric Trace Elements in Aerosols Observed over the Southern Ocean and Coastal East Antarctica. *Polar Res.* **2014**, *33* (1), 23973. https://doi.org/10.3402/polar.v33.23973.

(28) Zhang, T.; Fiamingo, M.; Allen, H. C. Trace Metal Enrichment Driven by Phosphate Functional Group Binding Selectivity. *J. Geophys. Res. Oceans* **2018**, *123* (8), 5286–5297. https://doi.org/10.1029/2018JC013926.

(29) Wellen Rudd, B. A.; Vidalis, A. S.; Allen, H. C. Thermodynamic versus Non-Equilibrium Stability of Palmitic Acid Monolayers in Calcium-Enriched Sea

Spray Aerosol Proxy Systems. *Phys. Chem. Chem. Phys.* **2018**, *20*, 16320–16332. https://doi.org/10.1039/C8CP01188E.

(30) Bruland, K. W. Trace Elements in Sea-Water. In *Chemical Oceanography*; Riley, J. P., Chester, R., Eds.; Academic Press, London, 1983; Vol. Vol. 8, pp 157–220. https://doi.org/10.1016/B978-0-12-588608-6.50009-2.

(31) Bruland, K. W.; Lohan, M. C. 6.02 - Controls of Trace Metals in Seawater. In *Treatise on Geochemistry*; Holland, H. D., Turekian, K. K., Eds.; Pergamon: Oxford, 2003; pp 23–47. https://doi.org/10.1016/B0-08-043751-6/06105-3.

(32) Adams, E. M.; Allen, H. C. Palmitic Acid on Salt Subphases and in Mixed Monolayers of Cerebrosides: Application to Atmospheric Aerosol Chemistry. *Atmosphere* **2013**, *4*, 315–336. https://doi.org/10.3390/atmos4040315.

(33) Cochran, R. E.; Laskina, O.; Jayarathne, T.; Laskin, A.; Laskin, J.; Lin, P.; Sultana, C.; Lee, C.; Moore, K. A.; Cappa, C. D.; Bertram, T. H.; Prather, K. A.; Grassian, V. H.; Stone, E. A. Analysis of Organic Anionic Surfactants in Fine and Coarse Fractions of Freshly Emitted Sea Spray Aerosol. *Environ. Sci. Technol.* **2016**, *50* (5), 2477–2486. https://doi.org/10.1021/acs.est.5b04053.

(34) Cochran, R. E.; Laskina, O.; Trueblood, J. V.; Estillore, A. D.; Morris, H. S.; Jayarathne, T.; Sultana, C. M.; Lee, C.; Lin, P.; Laskin, J.; Laskin, A.; Dowling, J. A.; Qin, Z.; Cappa, C. D.; Bertram, T. H.; Tivanski, A. V.; Stone, E. A.; Prather, K. A.; Grassian, V. H. Molecular Diversity of Sea Spray Aerosol Particles: Impact of Ocean Biology on Particle Composition and Hygroscopicity. *Chem* **2017**, *2* (5), 655–667. https://doi.org/10.1016/j.chempr.2017.03.007.

(35) Hasenecz, E. S.; Jayarathne, T.; Pendergraft, M. A.; Santander, M. V.; Mayer, K. J.; Sauer, J.; Lee, C.; Gibson, W. S.; Kruse, S. M.; Malfatti, F.; Prather, K. A.; Stone, E. A. Marine Bacteria Affect Saccharide Enrichment in Sea Spray Aerosol during a Phytoplankton Bloom. *ACS Earth Space Chem.* **2020**, *4* (9), 1638–1649. https://doi.org/10.1021/acsearthspacechem.0c00167.

(36) Russell, L. M.; Hawkins, L. N.; Frossard, A. A.; Quinn, P. K.; Bates, T. S. Carbohydrate-like Composition of Submicron Atmospheric Particles and Their Production from Ocean Bubble Bursting. *Proc. Natl. Acad. Sci.* **2010**, *107* (15), 6652–6657. https://doi.org/10.1073/pnas.0908905107.

(37) Rastelli, E.; Corinaldesi, C.; Dell'Anno, A.; Lo Martire, M.; Greco, S.; Cristina Facchini, M.; Rinaldi, M.; O'Dowd, C.; Ceburnis, D.; Danovaro, R. Transfer of Labile Organic Matter and Microbes from the Ocean Surface to the Marine Aerosol: An Experimental Approach. *Sci. Rep.* **2017**, *7* (1), 11475. https://doi.org/10.1038/s41598-017-10563-z.

(38) Elliott, S.; Burrows, S. M.; Deal, C.; Liu, X.; Long, M.; Ogunro, O.; Russell, L. M.; Wingenter, O. Prospects for Simulating Macromolecular Surfactant Chemistry at the Ocean–Atmosphere Boundary. *Environ. Res. Lett.* **2014**, *9* (6), 064012. https://doi.org/10.1088/1748-9326/9/6/064012.

(39) Burrows, S. M.; Gobrogge, E.; Fu, L.; Link, K.; Elliott, S. M.; Wang, H.; Walker, R. OCEANFILMS-2: Representing Coadsorption of Saccharides in Marine Films

and Potential Impacts on Modeled Marine Aerosol Chemistry. *Geophys. Res. Lett.* **2016**, *43* (15), 8306–8313. https://doi.org/10.1002/2016GL069070.

(40) Burrows, S. M.; Ogunro, O.; Frossard, A. A.; Russell, L. M.; Rasch, P. J.; Elliott, S. M. A Physically Based Framework for Modeling the Organic Fractionation of Sea Spray Aerosol from Bubble Film Langmuir Equilibria. *Atmospheric Chem. Phys.* **2014**, *14* (24), 13601–13629. https://doi.org/10.5194/acp-14-13601-2014.

(41) Mochida, M.; Kitamori, Y.; Kawamura, K.; Nojiri, Y.; Suzuki, K. Fatty Acids in the Marine Atmosphere: Factors Governing Their Concentrations and Evaluation of Organic Films on Sea-Salt Particles. *J. Geophys. Res. Atmospheres* **2002**, *107* (D17), AAC 1-1-AAC 1-10. https://doi.org/10.1029/2001JD001278.

(42) Hoffman, E. J.; Duce, R. A. Factors Influencing the Organic Carbon Content of Marine Aerosols: A Laboratory Study. *J. Geophys. Res. 1896-1977* **1976**, *81* (21), 3667–3670. https://doi.org/10.1029/JC081i021p03667.

(43) Collins, D. B.; Bertram, T. H.; Sultana, C. M.; Lee, C.; Axson, J. L.; Prather, K. A. Phytoplankton Blooms Weakly Influence the Cloud Forming Ability of Sea Spray Aerosol. *Geophys Res Lett* **2016**, *43*, 9975–9983. https://doi.org/10.1002/2016GL069922.

(44) Forestieri, S. D.; Cornwell, G. C.; Helgestad, T. M.; Moore, K. A.; Lee, C.; Novak, G. A.; Sultana, C. M.; Wang, X.; Bertram, T. H.; Prather, K. A.; Cappa, C. D. Linking Variations in Sea Spray Aerosol Particle Hygroscopicity to Composition during Two Microcosm Experiments. *Atmospheric Chem. Phys.* **2016**, *16* (14), 9003–9018. https://doi.org/10.5194/acp-16-9003-2016.

(45) Perkins, R. J.; Vazquez de Vasquez, M. G.; Beasley, E. E.; Hill, T. C. J.; Stone, E. A.; Allen, H. C.; DeMott, P. J. Relating Structure and Ice Nucleation of Mixed Surfactant Systems Relevant to Sea Spray Aerosol. *J. Phys. Chem. A* **2020**, *124*, 8806–8821. https://doi.org/10.1021/acs.jpca.0c05849.

(46) Zeppenfeld, S.; van Pinxteren, M.; Hartmann, M.; Bracher, A.; Stratmann, F.; Herrmann, H. Glucose as a Potential Chemical Marker for Ice Nucleating Activity in Arctic Seawater and Melt Pond Samples. *Environ. Sci. Technol.* **2019**, *53* (15), 8747–8756. https://doi.org/10.1021/acs.est.9b01469.

(47) Wolf, M. J.; Coe, A.; Dove, L. A.; Zawadowicz, M. A.; Dooley, K.; Biller, S. J.; Zhang, Y.; Chisholm, S. W.; Cziczo, D. J. Investigating the Heterogeneous Ice Nucleation of Sea Spray Aerosols Using Prochlorococcus as a Model Source of Marine Organic Matter. *Environ. Sci. Technol.* **2019**, *53* (3), 1139–1149. https://doi.org/10.1021/acs.est.8b05150.

(48) Hiranuma, N.; Augustin-Bauditz, S.; Bingemer, H.; Budke, C.; Curtius, J.; Danielczok, A.; Diehl, K.; Dreischmeier, K.; Ebert, M.; Frank, F.; Hoffmann, N.; Kandler, K.; Kiselev, A.; Koop, T.; Leisner, T.; Möhler, O.; Nillius, B.; Peckhaus, A.; Rose, D.; Weinbruch, S.; Wex, H.; Boose, Y.; DeMott, P. J.; Hader, J. D.; Hill, T. C. J.; Kanji, Z. A.; Kulkarni, G.; Levin, E. J. T.; McCluskey, C. S.; Murakami, M.; Murray, B. J.; Niedermeier, D.; Petters, M. D.; O&apos;Sullivan, D.; Saito, A.; Schill, G. P.; Tajiri, T.; Tolbert, M. A.; Welti, A.; Whale, T. F.; Wright, T. P.; Yamashita, K. A Comprehensive

Laboratory Study on the Immersion Freezing Behavior of Illite NX Particles: A Comparison of 17 Ice Nucleation Measurement Techniques. *Atmospheric Chem. Phys.* **2015**, *15* (5), 2489–2518. https://doi.org/10.5194/acp-15-2489-2015.

(49) Dreischmeier, K.; Budke, C.; Wiehemeier, L.; Kottke, T.; Koop, T. Boreal Pollen Contain Ice-Nucleating as Well as Ice-Binding 'Antifreeze' Polysaccharides. *Sci. Rep.* **2017**, *7* (1), 41890. https://doi.org/10.1038/srep41890.

(50) Wilson, T. W.; Ladino, L. A.; Alpert, P. A.; Breckels, M. N.; Brooks, I. M.; Browse, J.; Burrows, S. M.; Carslaw, K. S.; Huffman, J. A.; Judd, C.; Kilthau, W. P.; Mason, R. H.; McFiggans, G.; Miller, L. A.; Najera, J. J.; Polishchuk, E.; Rae, S.; Schiller, C. L.; Si, M.; Temprado, J. V.; Whale, T. F.; Wong, J. P. S.; Wurl, O.; Yakobi-Hancock, J. D.; Abbatt, J. P. D.; Aller, J. Y.; Bertram, A. K.; Knopf, D. A.; Murray, B. J. A Marine Biogenic Source of Atmospheric Ice-Nucleating Particles. *Nature* **2015**, No. 7568, 234.

(51) Pummer, B. G. Ice Nucleation by Water-Soluble Macromolecules. *Atmospheric chemistry and physics*. 2015, p 4077.

(52) Hiranuma, N.; Möhler, O.; Yamashita, K.; Tajiri, T.; Saito, A.; Kiselev, A.; Hoffmann, N.; Hoose, C.; Jantsch, E.; Koop, T.; Murakami, M. Ice Nucleation by Cellulose and Its Potential Contribution to Ice Formation in Clouds. *Nat. Geosci.* **2015**, *8* (4), 273–277. https://doi.org/10.1038/ngeo2374.

(53) Pummer, B. G.; Bauer, H.; Bernardi, J.; Bleicher, S.; Grothe, H. Suspendable Macromolecules Are Responsible for Ice Nucleation Activity of Birch and Conifer Pollen. *Atmospheric Chem. Phys.* **2012**, *12* (5), 2541–2550. https://doi.org/10.5194/acp-12-2541-2012.

(54) Leck, C.; Bigg, E. K. Biogenic Particles in the Surface Microlayer and Overlaying Atmosphere in the Central Arctic Ocean during Summer. *Tellus B Chem. Phys. Meteorol.* **2005**, *57* (4), 305–316. https://doi.org/10.3402/tellusb.v57i4.16546.

(55) Orellana, M. V.; Matrai, P. A.; Leck, C.; Rauschenberg, C. D.; Lee, A. M.; Coz, E. Marine Microgels as a Source of Cloud Condensation Nuclei in the High Arctic. *Proc. Natl. Acad. Sci.* **2011**, *108* (33), 13612–13617. https://doi.org/10.1073/pnas.1102457108.

(56) Leck, C.; Gao, Q.; Mashayekhy Rad, F.; Nilsson, U. Size-Resolved Atmospheric Particulate Polysaccharides in the High Summer Arctic. *Atmospheric Chem. Phys.* **2013**, *13* (24), 12573–12588. https://doi.org/10.5194/acp-13-12573-2013.

(57) Leck, C.; Svensson, E. Importance of Aerosol Composition and Mixing State for Cloud Droplet Activation over the Arctic Pack Ice in Summer. *Atmospheric Chem. Phys.* **2015**, *15* (5), 2545–2568. https://doi.org/10.5194/acp-15-2545-2015.

(58) Cochran, R. E.; Jayarathne, T.; Stone, E. A.; Grassian, V. H. Selectivity Across the Interface: A Test of Surface Activity in the Composition of Organic-Enriched Aerosols from Bubble Bursting. *J. Phys. Chem. Lett.* **2016**, *7* (9), 1692–1696. https://doi.org/10.1021/acs.jpclett.6b00489.

(59) O'Dowd, C. D.; de Leeuw, G. Marine Aerosol Production: A Review of the Current Knowledge. *Philos. Trans. R. Soc. Math. Phys. Eng. Sci.* **2007**, *365* (1856), 1753–1774. https://doi.org/10.1098/rsta.2007.2043.

(60) Quinn, P. K.; Bates, T. S.; Schulz, K. S.; Coffman, D. J.; Frossard, A. A.; Russell, L. M.; Keene, W. C.; Kieber, D. J. Contribution of Sea Surface Carbon Pool to Organic Matter Enrichment in Sea Spray Aerosol. *Nat. Geosci.* **2014**, *7* (3), 228–232. https://doi.org/10.1038/ngeo2092.

(61) Marchand, A.; Weijs, J. H.; Snoeijer, J. H.; Andreotti, B. Why Is Surface Tension a Force Parallel to the Interface? *Am. J. Phys.* **2011**, *79* (10), 999–1008. https://doi.org/10.1119/1.3619866.

(62) Butt, H.-J.; Graf, K.; Kappl, M. *Physics and Chemistry of Interfaces*; John Wiley & Sons, 2013.

(63) Barnes, G.; Gentle, I. *Interfacial Science: An Introduction*, Second Edition.; Oxford University Press: Oxford, New York, 2011.

(64) Holmberg, K. Handbook of Applied Surface and Colloid Chemistry, 2 Volume Set | Wiley https://www.wiley.com/en-us/Handbook+of+Applied+Surface+and+Colloid+Chemistry%2C+2+Volume+Set-p-9780471490838 (accessed 2021 -01 -20).

(65) Petty, M. C. *Langmuir-Blodgett Films: An Introduction*; Cambridge University Press, 1996.

(66) Gaines, G. L. *Insoluble Monolayers at Liquid-Gas Interfaces*; Interscience Publishers: New York, NY, USA, 1966.

(67) Casper, C. B.; Verreault, D.; Adams, E. M.; Hua, W.; Allen, H. C. Surface Potential of DPPC Monolayers on Concentrated Aqueous Salt Solutions. *J. Phys. Chem. B* **2016**, *120* (8), 2043–2052. https://doi.org/10.1021/acs.jpcb.5b10483.

(68) Oliveira, O. N.; Taylor, D. M.; Morgan, H. Modelling the Surface Potential-Area Dependence of a Stearic Acid Monolayer. *Thin Solid Films* **1992**, *210–211*, 76–78. https://doi.org/10.1016/0040-6090(92)90172-8.

(69) Demchak, R. J.; Fort, T. Surface Dipole Moments of Close-Packed Un-Ionized Monolayers at the Air-Water Interface. *J Colloid Interface Sci* **1974**, *46*, 191–202. https://doi.org/10.1016/0021-9797(74)90002-2.

(70) Bordo, V. G. Linear Optical Techniques at Surfaces and Interfaces. In *Optics and Spectroscopy at Surfaces and Interfaces*; John Wiley & Sons, Ltd, 2005; pp 111–138. https://doi.org/10.1002/9783527618699.ch5.

(71) Mendelsohn, R.; Brauner, J. W.; Gericke, A. External ν Reflection Absorption Spectrometry of Monolayer Films at the Air-Water Interface. *Annu. Rev. Phys. Chem.* **1995**, *46*, 305–334. https://doi.org/10.1146/annurev.pc.46.100195.001513.

(72) Adams, E. M.; Casper, C. B.; Allen, H. C. Effect of Cation Enrichment on Dipalmitoylphosphatidylcholine (DPPC) Monolayers at the Air-Water Interface. *J. Colloid Interface Sci.* **2016**, *478*, 353–364. https://doi.org/10.1016/j.jcis.2016.06.016.

(73) Adams, E. M.; Verreault, D.; Jayarathne, T.; Cochran, R. E.; Stone, E. A.; Allen, H. C. Surface Organization of a DPPC Monolayer on Concentrated $SrCl_2$ and

ZnCl $_2$ Solutions. *Phys. Chem. Chem. Phys.* **2016**, *18* (47), 32345–32357. https://doi.org/10.1039/C6CP06887A.

(74) Gericke, A.; Michailov, A. V.; Hühnerfuss, H. Polarized External Infrared Reflection-Absorption Spectrometry at the Air/Water Interface: Comparison of Experimental and Theoretical Results for Different Angles of Incidence. *Vib. Spectrosc.* **1993**, *4*, 335–348. https://doi.org/10.1016/0924-2031(93)80007-3.

(75) Gericke, A.; Mendelsohn, R. Partial Chain Deuteration as an IRRAS Probe of Conformational Order of Different Regions in Hexadecanoic Acid Monolayers at the Air/Water Interface. *Langmuir* **1996**, *12*, 758–762. https://doi.org/10.1021/la950608z.

(76) Mendelsohn, R.; Flach, C. R. Infrared Reflection – Absorption Spectrometry of Monolayer Films at the Air – Water Interface. In *Handbook of Vibrational Spectroscopy*; American Cancer Society, 2006. https://doi.org/10.1002/0470027320.s2205.

(77) Mendelsohn, R.; Mao, G.; Flach, C. R. Infrared Reflection-Absorption Spectroscopy: Principles and Applications to Lipid-Protein Interaction in Langmuir Films. *Biochim Biophys Acta* **2010**, *1798*, 788–800. https://doi.org/10.1016/j.bbamem.2009.11.024.

(78) Ferraro, J. R.; Nakamoto, K.; Brown, C. W. Chapter 1 - Basic Theory. In *Introductory Raman Spectroscopy (Second Edition)*; Ferraro, J. R., Nakamoto, K., Brown, C. W., Eds.; Academic Press: San Diego, 2003; pp 1–94. https://doi.org/10.1016/B978-012254105-6/50004-4.

(79) Ingle, J.; Crouch, S. R. *Spectrochemical Analysis*, 1st ed.; Prentice-Hall, Inc.: Englewood, Cliffs, New Jersey, 1988.

(80) Tackett, J. E. FT-IR Characterization of Metal Acetates in Aqueous Solution. *Appl. Spectrosc.* **1989**, *43* (3), 483–489. https://doi.org/10.1366/0003702894202931.

(81) Nakamoto, K.; Fujita, J.; Tanaka, S.; Kobayashi, M. Infrared Spectra of Metallic Complexes. IV. Comparison of the Infrared Spectra of Unidentate and Bidentate Metallic Complexes. *J. Am. Chem. Soc.* **1957**, *79* (18), 4904–4908. https://doi.org/10.1021/ja01575a020.

(82) Fujita, J.; Nakamoto, K.; Kobayashi, M. Infrared Spectra of Metallic Complexes. III. The Infrared Spectra of Metallic Oxalates. *J. Phys. Chem.* **1957**, *61* (7), 1014–1015. https://doi.org/10.1021/j150553a045.

(83) Nakamoto, K.; Morimoto, Y.; Martell, A. E. Infrared Spectra of Aqueous Solutions. I. Metal Chelate Compounds of Amino Acids [1]. *J. Am. Chem. Soc.* **1961**, *83* (22), 4528–4532. https://doi.org/10.1021/ja01483a009.

(84) Kishida, S.; Nakamoto, K. Normal Coordinate Analyses of Hydrogen-Bonded Compounds. II. Dimeric Formic Acid and Acetic Acid. *J. Chem. Phys.* **1964**, *41* (6), 1558–1563. https://doi.org/10.1063/1.1726122.

(85) Nakamoto, K.; Kishida, S. Normal Coordinate Analyses of Hydrogen-Bonded Compounds. I. Monomeric Formic Acid and Acetic Acid. *J. Chem. Phys.* **1964**, *41* (6), 1554–1558. https://doi.org/10.1063/1.1726121.

(86) Brauner, J. W.; Flach, C. R.; Xu, Z.; Bi, X.; Lewis, R. N. A. H.; McElhaney, R. N.; Gericke, A.; Mendelsohn, R. Quantitative Functional Group Orientation in Langmuir Films by Infrared Reflection−Absorption Spectroscopy: CO Groups in Behenic Acid Methyl Ester and Sn2-13C-DSPC. *J. Phys. Chem. B* **2003**, *107* (29), 7202–7211. https://doi.org/10.1021/jp030066r.

(87) Flach, C. R.; Gericke, A.; Mendelsohn, R. Quantitative Determination of Molecular Chain Tilt Angles in Monolayer Films at the Air/Water Interface: Infrared Reflection/Absorption Spectroscopy of Behenic Acid Methyl Ester. *J. Phys. Chem. B* **1997**, *101*, 58–65. https://doi.org/10.1021/jp962288d.

(88) Gericke, A.; Flach, C. R.; Mendelsohn, R. Structure and Orientation of Lung Surfactant SP-C and L-Alpha-Dipalmitoylphosphatidylcholine in Aqueous Monolayers. *Biophys. J.* **1997**, *73*, 492–499. https://doi.org/10.1016/S0006-3495(97)78087-1.

(89) Gericke, A.; Mendelsohn, R. Partial Chain Deuteration as an IRRAS Probe of Conformational Order of Different Regions in Hexadecanoic Acid Monolayers at the Air/Water Interface. *Langmuir* **1996**, *12*, 758–762. https://doi.org/10.1021/la950608z.

(90) Gericke, A.; Moore, D. J.; Erukulla, R. K.; Bittman, R.; Mendelsohn, R. Partially Deuterated Phospholipids as IR Structure Probes of Conformational Order in Bulk and Monolayer Phases. *J. Mol. Struct.* **1996**, *379*, 227–239. https://doi.org/10.1016/0022-2860(95)09201-3.

(91) Simon-Kutscher, J.; Gericke, A.; Hühnerfuss, H. Effect of Bivalent Ba, Cu, Ni, and Zn Cations on the Structure of Octadecanoic Acid Monolayers at the Air−Water Interface As Determined by External Infrared Reflection−Absorption Spectroscopy. *Langmuir* **1996**, *12* (4), 1027–1034. https://doi.org/10.1021/la950731q.

(92) Gericke, A.; Huehnerfuss, H. In Situ Investigation of Saturated Long-Chain Fatty Acids at the Air/Water Interface by External Infrared Reflection-Absorption Spectrometry. *J. Phys. Chem.* **1993**, *97*, 12899–12908. https://doi.org/10.1021/j100151a044.

(93) Robertson, E. J.; Beaman, D. K.; Richmond, G. L. Designated Drivers: The Differing Roles of Divalent Metal Ions in Surfactant Adsorption at the Oil–Water Interface. *Langmuir* **2013**, *29* (50), 15511–15520. https://doi.org/10.1021/la403665n.

(94) Nara, M.; Torii, H.; Tasumi, M. Correlation between the Vibrational Frequencies of the Carboxylate Group and the Types of Its Coordination to a Metal Ion: An Ab Initio Molecular Orbital Study. *J. Phys. Chem.* **1996**, *100* (51), 19812–19817. https://doi.org/10.1021/jp9615924.

(95) Denton, J. K.; Kelleher, P. J.; Johnson, M. A.; Baer, M. D.; Kathmann, S. M.; Mundy, C. J.; Wellen Rudd, B. A.; Allen, H. C.; Choi, T. H.; Jordan, K. D. Molecular-Level Origin of the Carboxylate Head Group Response to Divalent Metal Ion Complexation at the Air–Water Interface. *Proc. Natl. Acad. Sci.* **2019**, *116*, 14874–14880. https://doi.org/10.1073/pnas.1818600116.

(96) Clapham, D. E. Calcium Signaling. *Cell* **2007**, *131* (6), 1047–1058. https://doi.org/10.1016/j.cell.2007.11.028.

(97) Brini, M.; Calì, T.; Ottolini, D.; Carafoli, E. Intracellular Calcium Homeostasis and Signaling. In *Metallomics and the Cell*; Banci, L., Ed.; Metal Ions in Life Sciences; Springer Netherlands: Dordrecht, 2013; pp 119–168. https://doi.org/10.1007/978-94-007-5561-1_5.

(98) de Baaij, J. H. F.; Hoenderop, J. G. J.; Bindels, R. J. M. Magnesium in Man: Implications for Health and Disease. *Physiol. Rev.* **2015**, *95* (1), 1–46. https://doi.org/10.1152/physrev.00012.2014.

(99) Gifford, J. L.; Walsh, M. P.; Vogel, H. J. Structures and Metal-Ion-Binding Properties of the Ca2+-Binding Helix–Loop–Helix EF-Hand Motifs. *Biochem. J.* **2007**, *405* (2), 199–221. https://doi.org/10.1042/BJ20070255.

(100) Hsiao, C.; Williams, L. D. A Recurrent Magnesium-Binding Motif Provides a Framework for the Ribosomal Peptidyl Transferase Center. *Nucleic Acids Res.* **2009**, *37* (10), 3134–3142. https://doi.org/10.1093/nar/gkp119.

(101) Gresh, N.; Garmer, D. R. Comparative Binding Energetics of Mg2+, Ca2+, Zn2+, and Cd2+ to Biologically Relevant Ligands: Combined Ab Initio SCF Supermolecule and Molecular Mechanics Investigation. *J. Comput. Chem.* **1996**, *17* (12), 1481–1495. https://doi.org/10.1002/(SICI)1096-987X(199609)17:12<1481::AID-JCC7>3.0.CO;2-G.

(102) Project, E.; Nachliel, E.; Gutman, M. The Dynamics of Ca2+ Ions within the Solvation Shell of Calbindin D9k. *PLoS ONE* **2011**, *6* (2). https://doi.org/10.1371/journal.pone.0014718.

(103) Jahnen-Dechent, W.; Ketteler, M. Magnesium Basics. *Clin. Kidney J.* **2012**, *5* (Suppl 1), i3–i14. https://doi.org/10.1093/ndtplus/sfr163.

(104) Yamanaka, R.; Shindo, Y.; Oka, K. Magnesium Is a Key Player in Neuronal Maturation and Neuropathology. *Int. J. Mol. Sci.* **2019**, *20* (14). https://doi.org/10.3390/ijms20143439.

(105) Neuhaus, G.; Bowler, C.; Kern, R.; Chua, N.-H. Calcium/Calmodulin-Dependent and -Independent Phytochrome Signal Transduction Pathways. *Cell* **1993**, *73* (5), 937–952. https://doi.org/10.1016/0092-8674(93)90272-R.

(106) Eldik, L. V.; Eldik, L. J. V.; Watterson, D. M. *Calmodulin and Signal Transduction*; Gulf Professional Publishing, 1998.

(107) Martinek, T.; Duboué-Dijon, E.; Timr, Š.; Mason, P. E.; Baxová, K.; Fischer, H. E.; Schmidt, B.; Pluhařová, E.; Jungwirth, P. Calcium Ions in Aqueous Solutions: Accurate Force Field Description Aided by Ab Initio Molecular Dynamics and Neutron Scattering. *J. Chem. Phys.* **2018**, *148* (22), 222813. https://doi.org/10.1063/1.5006779.

(108) Duboué-Dijon, E.; Mason, P. E.; Fischer, H. E.; Jungwirth, P. Hydration and Ion Pairing in Aqueous Mg2+ and Zn2+ Solutions: Force-Field Description Aided by Neutron Scattering Experiments and Ab Initio Molecular Dynamics Simulations. *J. Phys. Chem. B* **2018**, *122* (13), 3296–3306. https://doi.org/10.1021/acs.jpcb.7b09612.

(109) Smith, R. M.; Martell, A. E. Inorganic Ligands. In *Critical Stability Constants: Inorganic Complexes*; Smith, R. M., Martell, A. E., Eds.; Springer US: Boston, MA, 1976; pp 1–129. https://doi.org/10.1007/978-1-4757-5506-0_1.

(110) Bunting, J. W.; Thong, K. M. Stability Constants for Some 1:1 Metal–Carboxylate Complexes. *Can. J. Chem.* **1970**, *48* (11), 1654–1656. https://doi.org/10.1139/v70-273.

(111) Stumpff, F.; McGuigan, J. A. S. Measuring Ca2+ Binding to Short Chain Fatty Acids and Gluconate with a Ca2+ Electrode: Role of the Reference Electrode. *Anal. Biochem.* **2014**, *459*, 46–52. https://doi.org/10.1016/j.ab.2014.05.001.

(112) Edwards, D. A.; Hayward, R. N. Transition Metal Acetates. *Can. J. Chem.* **1968**, *46* (22), 3443–3446. https://doi.org/10.1139/v68-572.

(113) Dudev, T.; Lim, C. Principles Governing Mg, Ca, and Zn Binding and Selectivity in Proteins. *Chem. Rev.* **2003**, *103* (3), 773–788. https://doi.org/10.1021/cr020467n.

(114) Oliveira, D. M. de; Zukowski, S. R.; Palivec, V.; Hénin, J.; Martinez-Seara, H.; Ben-Amotz, D.; Jungwirth, P.; Duboué-Dijon, E. Binding of Divalent Cations to Acetate: Molecular Simulations Guided by Raman Spectroscopy. *Phys. Chem. Chem. Phys.* **2020**, *22* (41), 24014–24027. https://doi.org/10.1039/D0CP02987D.

(115) Otero, V.; Sanches, D.; Montagner, C.; Vilarigues, M.; Carlyle, L.; Lopes, J. A.; Melo, M. J. Characterisation of Metal Carboxylates by Raman and Infrared Spectroscopy in Works of Art. *J. Raman Spectrosc.* **2014**, *45* (11–12), 1197–1206. https://doi.org/10.1002/jrs.4520.

(116) Deacon, G. B.; Phillips, R. J. Relationships between the Carbon-Oxygen Stretching Frequencies of Carboxylato Complexes and the Type of Carboxylate Coordination. *Coord. Chem. Rev.* **1980**, *33* (3), 227–250. https://doi.org/10.1016/S0010-8545(00)80455-5.

(117) Adrian-Scotto, M.; Mallet, G.; Vasilescu, D. Hydration of Mg++: A Quantum DFT and Ab Initio HF Study. *J. Mol. Struct. THEOCHEM* **2005**, *728* (1), 231–242. https://doi.org/10.1016/j.theochem.2005.02.006.

(118) DePalma, J. W.; Kelleher, P. J.; Tavares, L. C.; Johnson, M. A. Coordination-Dependent Spectroscopic Signatures of Divalent Metal Ion Binding to Carboxylate Head Groups: H_2 - and He-Tagged Vibrational Spectra of $M^{2+} \cdot RCO_2^{-}$ (M = Mg and Ca, R = $-CD_3$, $-CD_2CD_3$) Complexes. *J. Phys. Chem. Lett.* **2017**, *8* (2), 484–488. https://doi.org/10.1021/acs.jpclett.6b02964.

(119) II, D. W. D.; Pedersen, L. G. The First Solvation Shell of Magnesium and Calcium Ions in a Model Nucleic Acid Environment: An Ab Initio Study. *J. Biomol. Struct. Dyn.* **1995**, *13* (1), 167–180. https://doi.org/10.1080/07391102.1995.10508828.

(120) Adams, E. M.; Wellen, B. A.; Thiraux, R.; Reddy, S. K.; Vidalis, A. S.; Paesani, F.; Allen, H. C. Sodium–Carboxylate Contact Ion Pair Formation Induces Stabilization of Palmitic Acid Monolayers at High PH. *Phys Chem Chem Phys* **2017**, *19*, 10481–10490. https://doi.org/10.1039/C7CP00167C.

(121) Casper, C. B.; Verreault, D.; Adams, E. M.; Hua, W.; Allen, H. C. Surface Potential of DPPC Monolayers on Concentrated Aqueous Salt Solutions. *J Phys Chem B* **2016**, *120*, 2043–2052. https://doi.org/10.1021/acs.jpcb.5b10483.

(122) Zhang, T.; Cathcart, M. G.; Vidalis, A. S.; Allen, H. C. Cation Effects on Phosphatidic Acid Monolayers at Various PH Conditions. *Chem Phys Lipids* **2016**, *200*, 24–31. https://doi.org/10.1016/j.chemphyslip.2016.06.001.

(123) Zhang, X.; Kumar, R.; Kuroda, D. G. Acetate Ion and Its Interesting Solvation Shell Structure and Dynamics. *J. Chem. Phys.* **2018**, *148* (9), 094506. https://doi.org/10.1063/1.5019363.

(124) Grigor'ev, A. I. Infrared Absorption Spectra of Acetated of Elements in Groups I and II of the Periodic System. *Russ. J. Inorg. Chem.* **1963**, *8* (4), 409–414.

(125) Tang, C. Y.; Huang, Z.; Allen, H. C. Binding of Mg2+ and Ca2+ to Palmitic Acid and Deprotonation of the COOH Headgroup Studied by Vibrational Sum Frequency Generation Spectroscopy. *J. Phys. Chem. B* **2010**, *114* (51), 17068–17076. https://doi.org/10.1021/jp105472e.

(126) Desmeules, P.; Penney, S.-É.; Desbat, B.; Salesse, C. Determination of the Contribution of the Myristoyl Group and Hydrophobic Amino Acids of Recoverin on Its Dynamics of Binding to Lipid Monolayers. *Biophys. J.* **2007**, *93* (6), 2069–2082. https://doi.org/10.1529/biophysj.106.103481.

(127) Poyton, M. F.; Pullanchery, S.; Sun, S.; Yang, T.; Cremer, P. S. Zn2+ Binds to Phosphatidylserine and Induces Membrane Blebbing. *J. Am. Chem. Soc.* **2020**, *142* (43), 18679–18686. https://doi.org/10.1021/jacs.0c09103.

(128) Tang, C. Y.; Allen, H. C. Ionic Binding of Na+ versus K+ to the Carboxylic Acid Headgroup of Palmitic Acid Monolayers Studied by Vibrational Sum Frequency Generation Spectroscopy. *J. Phys. Chem. A* **2009**, *113*, 7383–7393. https://doi.org/10.1021/jp9000434.

(129) He, H.-T.; Xing, L.-C.; Zhang, J.-S.; Tang, M. Binding Characteristics of Cd2+, Zn2+, Cu2+, and Li+ with Humic Substances: Implication to Trace Element Enrichment in Low-Rank Coals. *Energy Explor. Exploit.* **2016**, *34* (5), 735–745. https://doi.org/10.1177/0144598716656067.

(130) Fini, G.; Mirone, P.; Fortunato, B. Evidence for Short-Range Orientation Effects in Dipolar Aprotic Liquids from Vibrational Spectroscopy. Part 1. - Ethylene and Propylene Carbonates. *J. Chem. Soc. Faraday Trans. 2 Mol. Chem. Phys.* **1973**, *69*, 1243–1248. https://doi.org/10.1039/F29736901243.

(131) Mirone, P.; Fini, G. Local Order and Vibrational Coupling in Solutions of Polar Molecules. *J. Chem. Phys.* **1979**, *71* (5), 2241–2243. https://doi.org/10.1063/1.438557.

(132) Bhattacharjee, D.; Ghosh (Purkayastha), A.; Misra, T. N.; Nandy, S. K. The Non-Coincidence Effect in Polar Liquids. *Spectrochim. Acta. A. Mol. Biomol. Spectrosc.* **1995**, *51* (14), 2539–2543. https://doi.org/10.1016/0584-8539(95)01518-3.

(133) Kecki, Z.; Sokołowska, A. Crossing of Anisotropic and Isotropic Raman Components in the Intermolecular Resonance Coupling of Vibrations. IV—

Methanol Solutions in Acetone. *J. Raman Spectrosc.* **1996**, *27* (5), 429–432. https://doi.org/10.1002/(SICI)1097-4555(199605)27:5<429::AID-JRS981>3.0.CO;2-O.

(134) Sokołowska, A. Raman Study of the Influence of KCl and KI on Polarization Contours of OH Stretching Band of Water. *J. Raman Spectrosc.* **1996**, *27* (8), 621–624. https://doi.org/10.1002/(SICI)1097-4555(199608)27:8<621::AID-JRS4>3.0.CO;2-J.

(135) Thomas, H. D.; Jonas, J. Hydrogen Bonding and the Raman Noncoincidence Effect. *J. Chem. Phys.* **1989**, *90* (8), 4632–4633. https://doi.org/10.1063/1.456605.

(136) Vazquez de Vasquez, M. G.; Wellen Rudd, B. A.; Baer, M. D.; Beasley, E. E.; Allen, H. C. Role of Hydration in Magnesium versus Calcium Ion Pairing with Carboxylate: Solution and the Aqueous Interface. *J. Phys. Chem. B* **2021**, *125* (40), 11308–11319. https://doi.org/10.1021/acs.jpcb.1c06108.

(137) Baer, M. D.; Mundy, C. J. An Ab Initio Approach to Understanding the Specific Ion Effect. *Faraday Discuss.* **2013**, *160* (0), 89–101. https://doi.org/10.1039/C2FD20113E.

(138) Jenkins, H. D. B.; Marcus, Y. Viscosity B-Coefficients of Ions in Solution. *Chem. Rev.* **1995**, *95* (8), 2695–2724. https://doi.org/10.1021/cr00040a004.

(139) Bulmer, J. T.; Irish, D. E.; Ödberg, L. The Temperature Dependence of Raman Band Parameters for Aquated Mg(II) and Zn(II). *Can. J. Chem.* **1975**, *53* (24), 3806–3811. https://doi.org/10.1139/v75-550.

(140) Deng, G.-H.; Shen, Y.; Chen, H.; Chen, Y.; Jiang, B.; Wu, G.; Yang, X.; Yuan, K.; Zheng, J. Ordered-to-Disordered Transformation of Enhanced Water Structure on Hydrophobic Surfaces in Concentrated Alcohol–Water Solutions. *J. Phys. Chem. Lett.* **2019**, *10*, 7922–7928. https://doi.org/10.1021/acs.jpclett.9b03429.

(141) Garrett, W. D. The Organic Chemical Composition of the Ocean Surface. *Deep Sea Res. Oceanogr. Abstr.* **1967**, *14*, 221–227. https://doi.org/10.1016/0011-7471(67)90007-1.

(142) DeMott, P. J.; Mason, R. H.; McCluskey, C. S.; Hill, T. C. J.; Perkins, R. J.; Desyaterik, Y.; Bertram, A. K.; Trueblood, J. V.; Grassian, V. H.; Qiu, Y.; et al. Ice Nucleation by Particles Containing Long-Chain Fatty Acids of Relevance to Freezing by Sea Spray Aerosols. *Env. Sci Process. Impacts* **2018**, *20*, 1559–1569. https://doi.org/10.1039/C8EM00386F.

(143) Qiu, Y.; Odendahl, N.; Hudait, A.; Mason, R.; Bertram, A. K.; Paesani, F.; DeMott, P. J.; Molinero, V. Ice Nucleation Efficiency of Hydroxylated Organic Surfaces Is Controlled by Their Structural Fluctuations and Mismatch to Ice. *J Am Chem Soc* **2017**, *139*, 3052–3064. https://doi.org/10.1021/jacs.6b12210.

(144) Sharma, G.; Mohanty, K. K. Wettability Alteration in High-Temperature and High-Salinity Carbonate Reservoirs. *SPE J.* **2013**, 646–655. https://doi.org/doi.org/10.2118/147306-PA.

(145) Serafin, A.; Figaszewski, Z. A.; Petelska, A. D. Phosphatidylcholine-Fatty Alcohols Equilibria in Monolayers at the Air/Water Interface. *J. Membr. Biol.* **2015**, *248*, 767–773. https://doi.org/10.1007/s00232-015-9793-x.

(146) Tong, H.-J.; Yu, J.-Y.; Zhang, Y.-H.; Reid, J. P. Observation of Conformational Changes in 1-Propanol−Water Complexes by FTIR Spectroscopy. *J. Phys. Chem. A* **2010**, *114* (25), 6795–6802. https://doi.org/10.1021/jp912180d.

(147) Davis, J. G.; Gierszal, K. P.; Wang, P.; Ben-Amotz, D. Water Structural Transformation at Molecular Hydrophobic Interfaces. *Nature* **2012**, *491*, 582–585. https://doi.org/10.1038/nature11570.

(148) Matvejev, V.; Zizi, M.; Stiens, J. Hydration Shell Parameters of Aqueous Alcohols: THz Excess Absorption and Packing Density. *J. Phys. Chem. B* **2012**, *116*, 14071–14077. https://doi.org/10.1021/jp305356d.

(149) Wu, X.; Lu, W.; Streacker, L. M.; Ashbaugh, H. S.; Ben-Amotz, D. Temperature-Dependent Hydrophobic Crossover Length Scale and Water Tetrahedral Order. *J. Phys. Chem. Lett.* **2018**, *9*, 1012–1017. https://doi.org/10.1021/acs.jpclett.7b03431.

(150) Tuckerman, M. E.; Marx, D.; Parrinello, M. The Nature and Transport Mechanism of Hydrated Hydroxide Ions in Aqueous Solution. *Nature* **2002**, *417*, 925–929. https://doi.org/10.1038/nature00797.

(151) Tuckerman, M.; Laasonen, K.; Sprik, M.; Parrinello, M. Ab Initio Molecular Dynamics Simulation of the Solvation and Transport of H3O+ and OH- Ions in Water. *J. Phys. Chem.* **1995**, *99*, 5749–5752. https://doi.org/10.1021/j100016a003.

(152) Robertson, W. H.; Diken, E. G.; Price, E. A.; Shin, J.-W.; Johnson, M. A. Spectroscopic Determination of the OH− Solvation Shell in the OH−·(H2O)n Clusters. *Science* **2003**, *299*, 1367–1372. https://doi.org/10.1126/science.1080695.

(153) Robertson, W. H.; Johnson, M. A. Molecular Aspects of Halide Ion Hydration: The Cluster Approach. *Annu. Rev. Phys. Chem.* **2003**, *54*, 173–213. https://doi.org/10.1146/annurev.physchem.54.011002.103801.

(154) Buch *, V.; Sigurd, B.; Devlin, J. P.; Buck, U.; Kazimirski, J. K. Solid Water Clusters in the Size Range of Tens–Thousands of H2O: A Combined Computational/Spectroscopic Outlook. *Int. Rev. Phys. Chem.* **2004**, *23*, 375–433. https://doi.org/10.1080/01442350412331316124.

(155) Buck, U.; Pradzynski, C. C.; Zeuch, T.; Dieterich, J. M.; Hartke, B. A Size Resolved Investigation of Large Water Clusters. *Phys. Chem. Chem. Phys.* **2014**, *16*, 6859–6871. https://doi.org/10.1039/C3CP55185G.

(156) Fujii, A.; Sugawara, N.; Hsu, P.-J.; Shimamori, T.; Li, Y.-C.; Hamashima, T.; Kuo, J.-L. Hydrogen Bond Network Structures of Protonated Short-Chain Alcohol Clusters. *Phys. Chem. Chem. Phys.* **2018**, *20*, 14971–14991. https://doi.org/10.1039/C7CP08072G.

(157) Sun, T.; Ben-Amotz, D.; Wyslouzil, B. E. The Freezing Behavior of Aqueous N-Alcohol Nanodroplets. *Phys. Chem. Chem. Phys.* **2021**, *23*, 9991–100005. https://doi.org/DOI: 10.1039/d0cp06131j.

(158) Alper, H. E.; Bassolino-Klimas, D.; Stouch, T. R. The Limiting Behavior of Water Hydrating a Phospholipid Monolayer: A Computer Simulation Study. *J. Chem. Phys.* **1993**, *99*, 5547–5559. https://doi.org/10.1063/1.465947.

(159) Tan, H.-S.; Piletic, I. R.; Riter, R. E.; Levinger, N. E.; Fayer, M. D. Dynamics of Water Confined on a Nanometer Length Scale in Reverse Micelles: Ultrafast Infrared Vibrational Echo Spectroscopy. *Phys. Rev. Lett.* **2005**, *94*, 057405. https://doi.org/10.1103/PhysRevLett.94.057405.

(160) Piletic, I. R.; Moilanen, D. E.; Spry, D. B.; Levinger, N. E.; Fayer, M. D. Testing the Core/Shell Model of Nanoconfined Water in Reverse Micelles Using Linear and Nonlinear IR Spectroscopy. *J. Phys. Chem. A* **2006**, *110*, 4985–4999. https://doi.org/10.1021/jp061065c.

(161) Zhao, W.; Moilanen, D. E.; Fenn, E. E.; Fayer, M. D. Water at the Surfaces of Aligned Phospholipid Multibilayer Model Membranes Probed with Ultrafast Vibrational Spectroscopy. *J. Am. Chem. Soc.* **2008**, *130*, 13927–13937. https://doi.org/10.1021/ja803252y.

(162) Berkowitz, M. L.; Vácha, R. Aqueous Solutions at the Interface with Phospholipid Bilayers. *Acc. Chem. Res.* **2012**, *45*, 74–82. https://doi.org/10.1021/ar200079x.

(163) Berkowitz, M. L.; Bostick, D. L.; Pandit, S. Aqueous Solutions next to Phospholipid Membrane Surfaces: Insights from Simulations. *Chem. Rev.* **2006**, *106*, 1527–1539. https://doi.org/10.1021/cr0403638.

(164) Moilanen, D. E.; Fenn, E. E.; Wong, D.; Fayer, M. D. Water Dynamics in Large and Small Reverse Micelles: From Two Ensembles to Collective Behavior. *J. Chem. Phys.* **2009**, *131*, 014704. https://doi.org/10.1063/1.3159779.

(165) Moilanen, D. E.; Fenn, E. E.; Wong, D.; Fayer, M. D. Geometry and Nanolength Scales versus Interface Interactions: Water Dynamics in AOT Lamellar Structures and Reverse Micelles. *J. Am. Chem. Soc.* **2009**, *131*, 8318–8328. https://doi.org/10.1021/ja901950b.

(166) Auer, B. M.; Skinner, J. L. IR and Raman Spectra of Liquid Water: Theory and Interpretation. *J. Chem. Phys.* **2008**, *128*, 224511. https://doi.org/10.1063/1.2925258.

(167) Auer, B.; Kumar, R.; Schmidt, J. R.; Skinner, J. L. Hydrogen Bonding and Raman, IR, and 2D-IR Spectroscopy of Dilute HOD in Liquid D2O. *Proc. Natl. Acad. Sci.* **2007**, *104*, 14215–14220. https://doi.org/10.1073/pnas.0701482104.

(168) Hare, D. E.; Sorensen, C. M. Raman Spectroscopic Study of Dilute HOD in Liquid H $_2$ O in the Temperature Range − 31.5 to 160 °C. *J. Chem. Phys.* **1990**, *93*, 6954–6961. https://doi.org/10.1063/1.459472.

(169) Hare, D. E.; Sorensen, C. M. Interoscillator Coupling Effects on the OH Stretching Band of Liquid Water. *J. Chem. Phys.* **1992**, *96*, 13–22. https://doi.org/10.1063/1.462852.

(170) Valdes-,Covarrubias, M. A.; Cadena-Nava, R. D.; Vasquez-Martinez, E.; Valdez-Perez, D.; Ruiz-Garcia, J. Crystallite Structure Formation at the Collapse Pressure of Fatty Acid Langmuir Films - IOPscience. *J Phys Condens Matter* **2004**, *16*, S2097–S2107. https://doi.org/10.1088/0953-8984/16/22/008.

(171) Oliveira,Jr., O. N.; Bonardi, C. The Surface Potential of Langmuir Monolayers Revisited. *Langmuir* **1997**, *13*, 5920–5924. https://doi.org/10.1021/la970272o.

(172) Bois, A. G.; Ivanova, M. G.; Panaiotov, I. I. Marangoni Effect and Relaxations of Surface Potential in Pentadecanoic Acid and Octadecanol Monolayers. *Langmuir* **1987**, *3*, 215–217. https://doi.org/10.1021/la00074a012.

(173) Kang, Y. S.; Lee, D. K.; Kim, Y. S. A Study on Temperature Dependency and in Situ Observation of Domain Structure in Langmuir Layers of Stearic Acid/γ-Fe2O3 Nanoparticle Complex at the Air/Water Interface. *Synth. Met.* **2001**, *117*, 165–167. https://doi.org/10.1016/S0379-6779(00)00489-6.

(174) Taylor, D. M.; Bayes, G. F. Calculating the Surface Potential of Unionized Monolayers. *Phys. Rev. E* **1994**, *49*, 1439–1449. https://doi.org/10.1103/PhysRevE.49.1439.

(175) Oliveira, O. N.; Taylor, D. M.; Lewis, T. J.; Salvagno, S.; Stirling, C. J. M. Estimation of Group Dipole Moments from Surface Potential Measurements on Langmuir Monolayers. *J. Chem. Soc. Faraday Trans. 1 Phys. Chem. Condens. Phases* **1989**, *85*, 1009. https://doi.org/10.1039/f19898501009.

(176) Taylor, D. M.; De Oliveira, O. N.; Morgan, H. Models for Interpreting Surface Potential Measurements and Their Application to Phospholipid Monolayers. *J. Colloid Interface Sci.* **1990**, *139*, 508–518. https://doi.org/10.1016/0021-9797(90)90123-6.

(177) Boyd, G. E. Energy Relations in Monolayer Formation: The Spreading of Long-Chain Fatty Acids on Aqueous Surfaces. *J Phys Chem* **1958**, *62*, 536–541. https://doi.org/10.1021/j150563a006.

(178) Bernett, M. K.; Jarvis, N. L.; Zisman, W. A. Properties of Monolayers of -Monohalogenated Fatty Acids and Alcohols Adsorbed on Water. *J. Phys. Chem.* **1964**, *68*, 10.

(179) Lo Nostro, P.; Gabrielli, G. Temperature and Subphase Effects on Aliphatic Alcohol Films at the Air-Water Interface. *Langmuir* **1993**, *9*, 3132–3137. https://doi.org/10.1021/la00035a063.

(180) Linden, D. J. M.; Peltonen, J. P. K.; Rosenholm, J. B. Adsorption of Some Multivalent Transition-Metal Ions to a Stearic Acid Monolayer. *Langmuir* **1994**, *10*, 1592–1595. https://doi.org/10.1021/la00017a044.

(181) Can, S. Z.; Mago, D. D.; Walker, R. A. Structure and Organization of Hexadecanol Isomers Adsorbed to the Air/Water Interface. *Langmuir* **2006**, *22*, 8043–8049. https://doi.org/10.1021/la060816z.

(182) Nutting, G. C.; Harkins, W. D. Pressure--Area Relations of Fatty Acid and Alcohol Monolayers. *J. Am. Chem. Soc.* **1939**, *61*, 1180–1187. https://doi.org/10.1021/ja01874a050.

(183) Fischer, A.; Sackmann, E. Electron Microscopy and Electron Diffraction Study of Coexisting Phases of Pure and Mixed Monolayers Transferred onto Solid Substrates. *J. Colloid Interface Sci.* **1986**, *112*, 1–14. https://doi.org/10.1016/0021-9797(86)90064-0.

(184) Vogel, V.; Möbius, D. Local Surface Potentials and Electric Dipole Moments of Lipid Monolayers: Contributions of the Water/Lipid and the Lipid/Air Interfaces. *J. Colloid Interface Sci.* **1988**, *126*, 408–420. https://doi.org/10.1016/0021-9797(88)90140-3.

(185) Brockman, H. Dipole Potential of Lipid Membranes. *Chem Phys Lipids* **1994**, *73*, 57–79. https://doi.org/10.1016/0009-3084(94)90174-0.

(186) Nakahara, H.; Nakamura, S.; Nakamura, K.; Inagaki, M.; Aso, M.; Higuchi, R.; Shibata, O. Cerebroside Langmuir Monolayers Originated from the Echinoderms: I. Binary Systems of Cerebrosides and Phospholipids. *Colloids Surf. B Biointerfaces* **2005**, *42*, 157–174. https://doi.org/10.1016/j.colsurfb.2005.01.012.

(187) Shimoaka, T.; Tanaka, Y.; Shioya, N.; Morita, K.; Sonoyama, M.; Amii, H.; Takagi, T.; Kanamori, T.; Hasegawa, T. Surface Properties of a Single Perfluoroalkyl Group on Water Surfaces Studied by Surface Potential Measurements. *J. Colloid Interface Sci.* **2016**, *483*, 353–359. https://doi.org/10.1016/j.jcis.2016.08.055.

(188) Adel, T.; Ng, K. C.; Vazquez de Vasquez, M. G.; Velez-Alvarez, J.; Allen, H. C. Insight into the Ionizing Surface Potential Method and Aqueous Sodium Halide Surfaces. *Langmuir* **2021**, *37*, 7863–7874. https://doi.org/10.1021/acs.langmuir.1c00465.

(189) Vleet, E. S. V.; Williams, P. M. Surface Potential and Film Pressure Measurements in Seawater Systems. *Limnol. Oceanogr.* **1983**, *28*, 401–414. https://doi.org/10.4319/lo.1983.28.3.0401.

(190) Yazdanian, M.; Yu, H.; Zografi, G.; Kim, M. W. Divalent Cation-Stearic Acid Monolayer Interactions at the Air/Water Interface. *Langmuir* **1992**, *8*, 630–636. https://doi.org/10.1021/la00038a055.

(191) Porter, E. F. Monomolecular Films of α-Aminostearic Acid, Stearic Acid, and Heptadecylamine. *J. Am. Chem. Soc.* **1937**, *59*, 1883–1888. https://doi.org/10.1021/ja01289a026.

(192) Gericke, A.; Huehnerfuss, H.; Michailov, A. V. Infrared Absorption-Reflection Spectroscopy of Long Chain Alcohols at the Air-Water Interface. In *Proc. SPIE.*; Int. Soc. Opt. Eng., 1992; Vol. 1575, pp 554–556. https://doi.org/10.1117/12.56440.

(193) Flach, C. R.; Gericke, A.; Mendelsohn, R. Quantitative Determination of Molecular Chain Tilt Angles in Monolayer Films at the Air/Water Interface: Infrared Reflection/Absorption Spectroscopy of Behenic Acid Methyl Ester. *J. Phys. Chem. B* **1997**, *101*, 58–65. https://doi.org/10.1021/jp962288d.

(194) Flach, C. R.; Mendelsohn, R.; Rerek, M. E.; Moore, D. J. Biophysical Studies of Model Stratum Corneum Lipid Monolayers by Infrared Reflection−Absorption

Spectroscopy and Brewster Angle Microscopy. *J. Phys. Chem. B* **2000**, *104*, 2159–2165. https://doi.org/10.1021/jp9936805.

(195) Dote, J. L.; Mowery, R. L. Infrared Reflectance-Absorption Spectra of Langmuir-Blodgett Stearic Acid Monolayers on Gold and Aluminum: Influence of Substrate. *J. Phys. Chem.* **1988**, *92*, 1571–1575. https://doi.org/10.1021/j100317a040.

(196) Neal, J. F.; Zhao, W.; Grooms, A. J.; Flood, A. H.; Allen, H. C. Arginine–Phosphate Recognition Enhanced in Phospholipid Monolayers at Aqueous Interfaces. *J. Phys. Chem. C* **2018**, *122*, 26362–26371. https://doi.org/10.1021/acs.jpcc.8b03531.

(197) Gaffney, K. J.; Piletic, I. R.; Fayer, M. D. Orientational Relaxation and Vibrational Excitation Transfer in Methanol–Carbon Tetrachloride Solutions. *J. Chem. Phys.* **2003**, *118* (5), 2270–2278. https://doi.org/10.1063/1.1534580.

(198) Corcelli, S. A.; Skinner, J. L. Infrared and Raman Line Shapes of Dilute HOD in Liquid H2O and D2O from 10 to 90 °C. *J. Phys. Chem. A* **2005**, *109* (28), 6154–6165. https://doi.org/10.1021/jp0506540.

(199) Yang, M.; Skinner, J. L. Signatures of Coherent Vibrational Energy Transfer in IR and Raman Line Shapes for Liquid Water. *Phys. Chem. Chem. Phys.* **2010**, *12* (4), 982–991. https://doi.org/10.1039/B918314K.

(200) Yang, M.; Li, F.; Skinner, J. L. Vibrational Energy Transfer and Anisotropy Decay in Liquid Water: Is the Förster Model Valid? *J. Chem. Phys.* **2011**, *135* (16), 164505. https://doi.org/10.1063/1.3655894.

(201) Zheng, R.; Wei, W.; Sun, Y.; Song, K.; Shi, Q. Theoretical Study of Vibrational Energy Transfer of Free OH Groups at the Water-Air Interface. *J. Chem. Phys.* **2016**, *144* (14), 144701. https://doi.org/10.1063/1.4945424.

(202) Woutersen, S.; Bakker, H. J. Resonant Intermolecular Transfer of Vibrational Energy in Liquid Water. *Nature* **1999**, *402* (6761), 507–509. https://doi.org/10.1038/990058.

(203) Lock, A. J.; Bakker, H. J. Temperature Dependence of Vibrational Relaxation in Liquid H2O. *J. Chem. Phys.* **2002**, *117* (4), 1708–1713. https://doi.org/10.1063/1.1485966.

(204) Kraemer, D.; Cowan, M. L.; Paarmann, A.; Huse, N.; Nibbering, E. T. J.; Elsaesser, T.; Miller, R. J. D. Temperature Dependence of the Two-Dimensional Infrared Spectrum of Liquid H2O. *Proc. Natl. Acad. Sci.* **2008**, *105* (2), 437–442. https://doi.org/10.1073/pnas.0705792105.

(205) Ramasesha, K.; De Marco, L.; Mandal, A.; Tokmakoff, A. Water Vibrations Have Strongly Mixed Intra- and Intermolecular Character. *Nat. Chem.* **2013**, *5* (11), 935–940. https://doi.org/10.1038/nchem.1757.

(206) Hunter, K. M.; Shakib, F. A.; Paesani, F. Disentangling Coupling Effects in the Infrared Spectra of Liquid Water. *J. Phys. Chem. B* **2018**, *122* (47), 10754–10761. https://doi.org/10.1021/acs.jpcb.8b09910.

(207) Kananenka, A. A.; Skinner, J. L. Fermi Resonance in OH-Stretch Vibrational Spectroscopy of Liquid Water and the Water Hexamer. *J. Chem. Phys.* **2018**, *148* (24), 244107. https://doi.org/10.1063/1.5037113.

(208) Sovago, M.; Campen, R. K.; Wurpel, G. W. H.; Müller, M.; Bakker, H. J.; Bonn, M. Vibrational Response of Hydrogen-Bonded Interfacial Water Is Dominated by Intramolecular Coupling. *Phys. Rev. Lett.* **2008**, *100* (17), 173901. https://doi.org/10.1103/PhysRevLett.100.173901.

(209) Ishiyama, T. Energy Relaxation Path of Excited Free OH Vibration at an Air/Water Interface Revealed by Nonequilibrium Ab Initio Molecular Dynamics Simulation. *J. Chem. Phys.* **2021**, *154* (10), 104708. https://doi.org/10.1063/5.0038709.

(210) Ishiyama, T. Energy Relaxation Dynamics of Hydrogen-Bonded OH Vibration Conjugated with Free OH Bond at an Air/Water Interface. *J. Chem. Phys.* **2021**. https://doi.org/10.1063/5.0069618.

(211) Fischer, T. L.; Wagner, T.; Gottschalk, H. C.; Nejad, A.; Suhm, M. A. A Rather Universal Vibrational Resonance in 1:1 Hydrates of Carbonyl Compounds. *J. Phys. Chem. Lett.* **2021**, *12* (1), 138–144. https://doi.org/10.1021/acs.jpclett.0c03197.

(212) Jiang, S.; Su, M.; Yang, S.; Wang, C.; Huang, Q.-R.; Li, G.; Xie, H.; Yang, J.; Wu, G.; Zhang, W.; Zhang, Z.; Kuo, J.-L.; Liu, Z.-F.; Zhang, D. H.; Yang, X.; Jiang, L. Vibrational Signature of Dynamic Coupling of a Strong Hydrogen Bond. *J. Phys. Chem. Lett.* **2021**, *12* (9), 2259–2265. https://doi.org/10.1021/acs.jpclett.1c00168.

(213) Vazquez de Vasquez, M. G.; Carter-Fenk, K. A.; McCaslin, L. M.; Beasley, E. E.; Clark, J. B.; Allen, H. C. Hydration and Hydrogen Bond Order of Octadecanoic Acid and Octadecanol Films on Water at 21 and 1 °C. *J. Phys. Chem. A* **2021**, *125* (46), 10065–10078. https://doi.org/10.1021/acs.jpca.1c06101.

(214) Hudait, A.; Moberg, D. R.; Qiu, Y.; Odendahl, N.; Paesani, F.; Molinero, V. Preordering of Water Is Not Needed for Ice Recognition by Hyperactive Antifreeze Proteins. *Proc. Natl. Acad. Sci.* **2018**, *115*, 8266–8271. https://doi.org/10.1073/pnas.1806996115.

(215) Lupi, L.; Hanscam, R.; Qiu, Y.; Molinero, V. Reaction Coordinate for Ice Crystallization on a Soft Surface. *J. Phys. Chem. Lett.* **2017**, *8*, 4201–4205. https://doi.org/10.1021/acs.jpclett.7b01855.

(216) Lupi, L.; Peters, B.; Molinero, V. Pre-Ordering of Interfacial Water in the Pathway of Heterogeneous Ice Nucleation Does Not Lead to a Two-Step Crystallization Mechanism. *J. Chem. Phys.* **2016**, *145*, 211910. https://doi.org/10.1063/1.4961652.

(217) Seki, T.; Sun, S.; Zhong, K.; Yu, C.-C.; Machel, K.; Dreier, L. B.; Backus, E. H. G.; Bonn, M.; Nagata, Y. Unveiling Heterogeneity of Interfacial Water through the Water Bending Mode. *J. Phys. Chem. Lett.* **2019**, *10*, 6936–6941. https://doi.org/10.1021/acs.jpclett.9b02748.

(218) Seki, T.; Chiang, K.-Y.; Yu, C.-C.; Yu, X.; Okuno, M.; Hunger, J.; Nagata, Y.; Bonn, M. The Bending Mode of Water: A Powerful Probe for Hydrogen Bond Structure of Aqueous Systems. *J. Phys. Chem. Lett.* **2020**, *11*, 8459–8469. https://doi.org/10.1021/acs.jpclett.0c01259.

(219) Bakker, H. J.; Skinner, J. L. Vibrational Spectroscopy as a Probe of Structure and Dynamics in Liquid Water. *Chem. Rev.* **2010**, *110*, 1498–1517. https://doi.org/10.1021/cr9001879.

(220) Ni, Y.; Skinner, J. L. IR and SFG Vibrational Spectroscopy of the Water Bend in the Bulk Liquid and at the Liquid-Vapor Interface, Respectively. *J. Chem. Phys.* **2015**, *143*, 014502. https://doi.org/10.1063/1.4923462.

(221) Dutta, C.; Benderskii, A. V. On the Assignment of the Vibrational Spectrum of the Water Bend at the Air/Water Interface. *J. Phys. Chem. Lett.* **2017**, *8*, 801–804. https://doi.org/10.1021/acs.jpclett.6b02678.

(222) Yu, C.-C.; Chiang, K.-Y.; Okuno, M.; Seki, T.; Ohto, T.; Yu, X.; Korepanov, V.; Hamaguchi, H.; Bonn, M.; Hunger, J.; Nagata, Y. Vibrational Couplings and Energy Transfer Pathways of Water's Bending Mode. *Nat. Commun.* **2020**, *11* (1), 5977. https://doi.org/10.1038/s41467-020-19759-w.

(223) Zelent, B.; Nucci, N. V.; Vanderkooi, J. M. Liquid and Ice Water and Glycerol/Water Glasses Compared by Infrared Spectroscopy from 295 to 12 K. *J. Phys. Chem. A* **2004**, *108*, 11141–11150. https://doi.org/10.1021/jp0475584.

(224) Hoose, C.; Möhler, O. Heterogeneous Ice Nucleation on Atmospheric Aerosols: A Review of Results from Laboratory Experiments. *Atmospheric Chem. Phys.* **2012**, *12* (20), 9817–9854. https://doi.org/10.5194/acp-12-9817-2012.

(225) DeMott, P. J.; Sassen, K.; Poellot, M. R.; Baumgardner, D.; Rogers, D. C.; Brooks, S. D.; Prenni, A. J.; Kreidenweis, S. M. African Dust Aerosols as Atmospheric Ice Nuclei. *Geophys. Res. Lett.* **2003**, *30* (14). https://doi.org/10.1029/2003GL017410.

(226) Kanji, Z. A.; Ladino, L. A.; Wex, H.; Boose, Y.; Burkert-Kohn, M.; Cziczo, D. J.; Krämer, M. Overview of Ice Nucleating Particles. *Meteorol Monogr* **2017**, *58*, 1.1-1.33. https://doi.org/10.1175/AMSMONOGRAPHS-D-16-0006.1.

(227) Price, H. C.; Baustian, K. J.; McQuaid, J. B.; Blyth, A.; Bower, K. N.; Choularton, T.; Cotton, R. J.; Cui, Z.; Field, P. R.; Gallagher, M.; Hawker, R.; Merrington, A.; Miltenberger, A.; Iii, R. R. N.; Parker, S. T.; Rosenberg, P. D.; Taylor, J. W.; Trembath, J.; Vergara-Temprado, J.; Whale, T. F.; Wilson, T. W.; Young, G.; Murray, B. J. Atmospheric Ice-Nucleating Particles in the Dusty Tropical Atlantic. *J. Geophys. Res. Atmospheres* **2018**, *123* (4), 2175–2193. https://doi.org/10.1002/2017JD027560.

(228) DeMott, P. J.; Hill, T. C. J.; McCluskey, C. S.; Prather, K. A.; Collins, D. B.; Sullivan, R. C.; Ruppel, M. J.; Mason, R. H.; Irish, V. E.; Lee, T.; Hwang, C. Y.; Rhee, T. S.; Snider, J. R.; McMeeking, G. R.; Dhaniyala, S.; Lewis, E. R.; Wentzell, J. J. B.; Abbatt, J.; Lee, C.; Sultana, C. M.; Ault, A. P.; Axson, J. L.; Martinez, M. D.; Venero, I.; Santos-Figueroa, G.; Stokes, M. D.; Deane, G. B.; Mayol-Bracero, O. L.; Grassian, V. H.; Bertram, T. H.; Bertram, A. K.; Moffett,

B. F.; Franc, G. D. Sea Spray Aerosol as a Unique Source of Ice Nucleating Particles. *Proc Natl Acad Sci* **2016**, *113*, 5797–5803. https://doi.org/10.1073/pnas.1514034112.

(229) McCluskey, C. S.; Hill, T. C. J.; Malfatti, F.; Sultana, C. M.; Lee, C.; Santander, M. V.; Beall, C. M.; Moore, K. A.; Cornwell, G. C.; Collins, D. B.; Prather, K. A.; Jayarathne, T.; Stone, E. A.; Azam, F.; Kreidenweis, S. M.; DeMott, P. J. A Dynamic Link between Ice Nucleating Particles Released in Nascent Sea Spray Aerosol and Oceanic Biological Activity during Two Mesocosm Experiments. *J Atmos Sci* **2016**, *74*, 151–166. https://doi.org/10.1175/JAS-D-16-0087.1.

(230) McCluskey, C. S.; Ovadnevaite, J.; Rinaldi, M.; Atkinson, J.; Belosi, F.; Ceburnis, D.; Marullo, S.; Hill, T. C. J.; Lohmann, U.; Kanji, Z. A.; O'Dowd, C.; Kreidenweis, S. M.; DeMott, P. J. Marine and Terrestrial Organic Ice-Nucleating Particles in Pristine Marine to Continentally Influenced Northeast Atlantic Air Masses. *J. Geophys. Res. Atmospheres* **2018**, *123* (11), 6196–6212. https://doi.org/10.1029/2017JD028033.

(231) Alpert, P. A.; Aller, J. Y.; Knopf, D. A. Initiation of the Ice Phase by Marine Biogenic Surfaces in Supersaturated Gas and Supercooled Aqueous Phases. *Phys. Chem. Chem. Phys.* **2011**, *13* (44), 19882–19894. https://doi.org/10.1039/C1CP21844A.

(232) McCluskey, C. S.; Hill, T. C. J.; Sultana, C. M.; Laskina, O.; Trueblood, J.; Santander, M. V.; Beall, C. M.; Michaud, J. M.; Kreidenweis, S. M.; Prather, K. A.; Grassian, V.; DeMott, P. J. A Mesocosm Double Feature: Insights into the Chemical Makeup of Marine Ice Nucleating Particles. *J Atmos Sci* **2018**, *75*, 2405–2423. https://doi.org/10.1175/JAS-D-17-0155.1.

(233) Gavish, M.; Popovitz-Biro, R.; Lahav, M.; Leiserowitz, L. Ice Nucleation by Alcohols Arranged in Monolayers at the Surface of Water Drops. *Science* **1990**, *250*, 973–975.

(234) Popovitz-Biro, R.; Wang, J. L.; Majewski, J.; Shavit, E.; Leiserowitz, L.; Lahav, M. Induced Freezing of Supercooled Water into Ice by Self-Assembled Crystalline Monolayers of Amphiphilic Alcohols at the Air-Water Interface. *J Am Chem Soc* **1994**, *116*, 1179–1191. https://doi.org/10.1021/ja00083a003.

(235) Zobrist, B.; Koop, T.; Luo, B. P.; Marcolli, C.; Peter, T. Heterogeneous Ice Nucleation Rate Coefficient of Water Droplets Coated by a Nonadecanol Monolayer. *J. Phys. Chem. C* **2007**, *111* (5), 2149–2155. https://doi.org/10.1021/jp066080w.

(236) Knopf, D. A.; Forrester, S. M. Freezing of Water and Aqueous NaCl Droplets Coated by Organic Monolayers as a Function of Surfactant Properties and Water Activity. *J Phys Chem A* **2011**, *115*, 5579–5591. https://doi.org/10.1021/jp2014644.

(237) DeMott, P. J.; Mason, R. H.; McCluskey, C. S.; Hill, T. C. J.; Perkins, R. J.; Desyaterik, Y.; Bertram, A. K.; Trueblood, J. V.; Grassian, V. H.; Qiu, Y.; et al. Ice Nucleation by Particles Containing Long-Chain Fatty Acids of Relevance to

Freezing by Sea Spray Aerosols. *Environ. Sci. Process. Impacts* **2018**, *20*, 1559–1569. https://doi.org/10.1039/C8EM00386F.

(238) Ochshorn, E.; Cantrell, W. Towards Understanding Ice Nucleation by Long Chain Alcohols. *J. Chem. Phys.* **2006**, *124* (5), 054714. https://doi.org/10.1063/1.2166368.

(239) Qiu, Y.; Odendahl, N.; Hudait, A.; Mason, R.; Bertram, A. K.; Paesani, F.; DeMott, P. J.; Molinero, V. Ice Nucleation Efficiency of Hydroxylated Organic Surfaces Is Controlled by Their Structural Fluctuations and Mismatch to Ice. *J. Am. Chem. Soc.* **2017**, *139* (8), 3052–3064. https://doi.org/10.1021/jacs.6b12210.

(240) Seeley, L. H.; Seidler, G. T. Preactivation in the Nucleation of Ice by Langmuir Films of Aliphatic Alcohols. *J. Chem. Phys.* **2001**, *114* (23), 10464–10470. https://doi.org/10.1063/1.1375151.

(241) Kaufmann, L.; Marcolli, C.; Luo, B.; Peter, T. Refreeze Experiments with Water Droplets Containing Different Types of Ice Nuclei Interpreted by Classical Nucleation Theory. *Atmospheric Chem. Phys.* **2017**, *17* (5), 3525–3552. https://doi.org/10.5194/acp-17-3525-2017.

(242) Marcolli, C. Pre-Activation of Aerosol Particles by Ice Preserved in Pores. *Atmospheric Chem. Phys.* **2017**, *17* (3), 1595–1622. https://doi.org/10.5194/acp-17-1595-2017.

(243) Bertram, T. H.; Cochran, R. E.; Grassian, V. H.; Stone, E. A. Sea Spray Aerosol Chemical Composition: Elemental and Molecular Mimics for Laboratory Studies of Heterogeneous and Multiphase Reactions. *Chem. Soc. Rev.* **2018**, *47* (7), 2374–2400. https://doi.org/10.1039/C7CS00008A.

(244) Griffith, E. C.; Perkins, R. J.; Telesford, D.-M.; Adams, E. M.; Cwiklik, L.; Allen, H. C.; Roeselová, M.; Vaida, V. Interaction of L-Phenylalanine with a Phospholipid Monolayer at the Water-Air Interface. *J. Phys. Chem. B* **2015**, *119* (29), 9038–9048. https://doi.org/10.1021/jp508473w.

(245) Schneider, C. A.; Rasband, W. S.; Eliceiri, K. W. NIH Image to ImageJ: 25 Years of Image Analysis. *Nat. Methods* **2012**, *9* (7), 671–675.

(246) Kaganer, V. M.; Möhwald, H.; Dutta, P. Structure and Phase Transitions in Langmuir Monolayers. *Rev Mod Phys* **1999**, *71*, 779–819. https://doi.org/10.1103/RevModPhys.71.779.

(247) Shih, M. C.; Durbin, M. K.; Malik, A.; Zschack, P.; Dutta, P. Lattice Structures and Molecular Tilts in Langmuir Monolayers of Saturated Fatty Acid–Alcohol Mixtures. *J. Chem. Phys.* **1994**, *101* (10), 9132–9136. https://doi.org/10.1063/1.468042.

(248) Fischer, B.; Teer, E.; Knobler, C. M. Optical Measurements of the Phase Diagram of Langmuir Monolayers of Fatty Acid–Alcohol Mixtures. *J. Chem. Phys.* **1995**, *103*, 2365–2368. https://doi.org/10.1063/1.469659.

(249) Kajiyama, T.; Oishi, Y.; Uchida, M.; Morotomi, N.; Ishikawa, J.; Tanimoto, Y. Evaluation of Melting and Crystalline Relaxation Temperatures of Fatty Acid Monolayers on the Water Surface and Their Importances for Molecular

Aggregation States in Monolayers. *Bull. Chem. Soc. Jpn.* **1992**, *65* (3), 864–870. https://doi.org/10.1246/bcsj.65.864.

(250) Weis, M. Kinetics of Slow Collapse Process: Thermodynamic Description of Rate Constants. *Appl. Surf. Sci.* **2006**, *253*. https://doi.org/10.1016/j.apsusc.2006.02.029.

(251) De Keyser, P.; Joos, P. Kinetics of Monolayer Collapse as a Nucleation Process. *J. Phys. Chem.* **1984**, *88* (2), 274–280. https://doi.org/10.1021/j150646a022.

(252) Tsuji, M.; Nakahara, H.; Moroi, Y.; Shibata, O. Water Evaporation Rates across Hydrophobic Acid Monolayers at Equilibrium Spreading Pressure. *J. Colloid Interface Sci.* **2008**, *318* (2), 322–330. https://doi.org/10.1016/j.jcis.2007.10.047.

(253) Deo, A. V.; Kulkarni, S. B.; Gharpurey, M. K.; Biswas, A. B. Equilibrium Film Pressure of the Monolayers on Water of N-Long-Chain Alcohols and n-Long-Chain Alkoxy-Ethanols. *J. Colloid Sci.* **1964**, *19* (9), 813–819. https://doi.org/10.1016/0095-8522(64)90057-1.

(254) Jalal, I. M.; Zografi, G.; Rakshit, A. K.; Gunstone, F. D. Monolayer Properties of Fatty Acids. I. Thermodynamics of Spreading. *J. Colloid Interface Sci.* **1980**, *76* (1), 146–156. https://doi.org/10.1016/0021-9797(80)90280-5.

(255) Hargreaves, W. R.; Deamer, D. W. Liposomes from Ionic, Single-Chain Amphiphiles. *Biochemistry* **1978**, *17* (18), 3759–3768. https://doi.org/10.1021/bi00611a014.

(256) Tzocheva, S. S.; Kralchevsky, P. A.; Danov, K. D.; Georgieva, G. S.; Post, A. J.; Ananthapadmanabhan, K. P. Solubility Limits and Phase Diagrams for Fatty Acids in Anionic (SLES) and Zwitterionic (CAPB) Micellar Surfactant Solutions. *J. Colloid Interface Sci.* **2012**, *369* (1), 274–286. https://doi.org/10.1016/j.jcis.2011.12.036.

(257) Jalal, I. M. Thermodynamics of Insoluble Fatty Acid Monolayers., University of Wisconsin, Madison, Wisconsin, 1978.

(258) Daear, W.; Mahadeo, M.; Prenner, E. J. Applications of Brewster Angle Microscopy from Biological Materials to Biological Systems. *Biochim. Biophys. Acta BBA - Biomembr.* **2017**, *1859* (10), 1749–1766. https://doi.org/10.1016/j.bbamem.2017.06.016.

(259) Lee, K. Y. C.; McConnell, H. M. Quantized Symmetry of Liquid Monolayer Domains. *J. Phys. Chem.* **1993**, *97* (37), 9532–9539. https://doi.org/10.1021/j100139a044.

(260) Rivière, S.; Hénon, S.; Meunier, J.; Albrecht, G.; Boissonnade, M. M.; Baszkin, A. Electrostatic Pressure and Line Tension in a Langmuir Monolayer. *Phys. Rev. Lett.* **1995**, *75* (13), 2506–2509. https://doi.org/10.1103/PhysRevLett.75.2506.

(261) Wurlitzer, S.; Steffen, P.; Wurlitzer, M.; Khattari, Z.; Fischer, Th. M. Line Tension in Langmuir Monolayers Probed by Point Forces. *J. Chem. Phys.* **2000**, *113* (9), 3822–3828. https://doi.org/10.1063/1.1287907.

(262) Pummer, B. G.; Budke, C.; Augustin-Bauditz, S.; Niedermeier, D.; Felgitsch, L.; Kampf, C. J.; Huber, R. G.; Liedl, K. R.; Loerting, T.; Moschen, T.; Schauperl, M.; Tollinger, M.; Morris, C. E.; Wex, H.; Grothe, H.; Pöschl, U.; Koop, T.;

Fröhlich-Nowoisky, J. Ice Nucleation by Water-Soluble Macromolecules. *Atmos Chem Phys* **2015**, *15*, 4077–4091. https://doi.org/10.5194/acp-15-4077-2015.

(263) Ickes, L.; Welti, A.; Hoose, C.; Lohmann, U. Classical Nucleation Theory of Homogeneous Freezing of Water: Thermodynamic and Kinetic Parameters. *Phys. Chem. Chem. Phys.* **2015**, *17* (8), 5514–5537. https://doi.org/10.1039/C4CP04184D.

(264) Small, D. M. Lateral Chain Packing in Lipids and Membranes. *J. Lipid Res.* **1984**, *25* (13), 1490–1500.

(265) Murdachaew, G.; Varner, M. E.; Phillips, L. F.; Finlayson-Pitts, B. J.; Gerber, R. B. Nitrogen Dioxide at the Air–Water Interface: Trapping, Absorption, and Solvation in the Bulk and at the Surface. *Phys. Chem. Chem. Phys.* **2012**, *15* (1), 204–212. https://doi.org/10.1039/C2CP42810E.

(266) Tinel, L.; Rossignol, S.; Bianco, A.; Passananti, M.; Perrier, S.; Wang, X.; Brigante, M.; Donaldson, D. J.; George, C. Mechanistic Insights on the Photosensitized Chemistry of a Fatty Acid at the Air/Water Interface. *Environ. Sci. Technol.* **2016**, *50* (20), 11041–11048. https://doi.org/10.1021/acs.est.6b03165.

(267) Nissenson, P.; Dabdub, D.; Das, R.; Maurino, V.; Minero, C.; Vione, D. Evidence of the Water-Cage Effect on the Photolysis of NO3− and FeOH2+. Implications of This Effect and of H2O2 Surface Accumulation on Photochemistry at the Air–Water Interface of Atmospheric Droplets. *Atmos. Environ.* **2010**, *44* (38), 4859–4866. https://doi.org/10.1016/j.atmosenv.2010.08.035.

(268) Kusaka, R.; Nihonyanagi, S.; Tahara, T. The Photochemical Reaction of Phenol Becomes Ultrafast at the Air–Water Interface. *Nat. Chem.* **2021**, *13* (4), 306–311. https://doi.org/10.1038/s41557-020-00619-5.

(269) Neal, J. F.; Zhao, W.; Grooms, A. J.; Flood, A. H.; Allen, H. C. Arginine–Phosphate Recognition Enhanced in Phospholipid Monolayers at Aqueous Interfaces. *J. Phys. Chem. C* **2018**, *122* (46), 26362–26371. https://doi.org/10.1021/acs.jpcc.8b03531.

(270) Rogers, M. M.; Neal, J. F.; Saha, A.; Algarni, A. S.; Hill, T. C. J.; Allen, H. C. The Ocean's Elevator: Evolution of the Air–Seawater Interface during a Small-Scale Algal Bloom. *ACS Earth Space Chem.* **2020**, *4* (12), 2347–2357. https://doi.org/10.1021/acsearthspacechem.0c00239.

(271) Van Loon, L. L.; Allen, H. C. Uptake and Surface Reaction of Methanol by Sulfuric Acid Solutions Investigated by Vibrational Sum Frequency Generation and Raman Spectroscopies. *J. Phys. Chem. A* **2008**, *112* (34), 7873–7880. https://doi.org/10.1021/jp712134s.

(272) Finlayson-Pitts, B. J. Reactions at Surfaces in the Atmosphere: Integration of Experiments and Theory as Necessary (but Not Necessarily Sufficient) for Predicting the Physical Chemistry of Aerosols. *Phys. Chem. Chem. Phys.* **2009**, *11* (36), 7760–7779. https://doi.org/10.1039/B906540G.

(273) Sakurai, M.; Tamagawa, H.; Inoue, Y.; Ariga, K.; Kunitake, T. Theoretical Study of Intermolecular Interaction at the Lipid−Water Interface. 1. Quantum Chemical

Analysis Using a Reaction Field Theory. *J. Phys. Chem. B* **1997**, *101* (24), 4810–4816. https://doi.org/10.1021/jp9700591.

(274) Tamagawa, H.; Sakurai, M.; Inoue, Y.; Ariga, K.; Kunitake, T. Theoretical Study of Intermolecular Interaction at the Lipid−Water Interface. 2. Analysis Based on the Poisson−Boltzmann Equation. *J. Phys. Chem. B* **1997**, *101* (24), 4817–4825. https://doi.org/10.1021/jp9700600.

(275) Ariga, K. Molecular Recognition at the Air–Water Interface: Nanoarchitectonic Design and Physicochemical Understanding. *Phys. Chem. Chem. Phys.* **2020**, *22* (43), 24856–24869. https://doi.org/10.1039/D0CP04174B.

(276) Characteristic Features of Surfactants. In *Surfactants and Interfacial Phenomena*; John Wiley & Sons, Ltd, 2012; pp 1–38. https://doi.org/10.1002/9781118228920.ch1.

(277) Donaldson, D. J.; Vaida, V. The Influence of Organic Films at the Air−Aqueous Boundary on Atmospheric Processes. *Chem. Rev.* **2006**, *106* (4), 1445–1461. https://doi.org/10.1021/cr040367c.

(278) Cochran, R. E.; Jayarathne, T.; Stone, E. A.; Grassian, V. H. Selectivity Across the Interface: A Test of Surface Activity in the Composition of Organic-Enriched Aerosols from Bubble Bursting. *J. Phys. Chem. Lett.* **2016**, *7* (9), 1692–1696. https://doi.org/10.1021/acs.jpclett.6b00489.

(279) Resch, F.; Afeti, G. Film Drop Distributions from Bubbles Bursting in Seawater. *J. Geophys. Res. Oceans* **1991**, *96* (C6), 10681–10688. https://doi.org/10.1029/91JC00433.

(280) Alpert, P. A.; Ciuraru, R.; Rossignol, S.; Passananti, M.; Tinel, L.; Perrier, S.; Dupart, Y.; Steimer, S. S.; Ammann, M.; Donaldson, D. J.; George, C. Fatty Acid Surfactant Photochemistry Results in New Particle Formation. *Sci. Rep.* **2017**, *7* (1), 12693. https://doi.org/10.1038/s41598-017-12601-2.

(281) Cochran, R. E.; Laskina, O.; Jayarathne, T.; Laskin, A.; Laskin, J.; Lin, P.; Sultana, C.; Lee, C.; Moore, K. A.; Cappa, C. D.; Bertram, T. H.; Prather, K. A.; Grassian, V. H.; Stone, E. A. Analysis of Organic Anionic Surfactants in Fine and Coarse Fractions of Freshly Emitted Sea Spray Aerosol. *Environ. Sci. Technol.* **2016**, *50* (5), 2477–2486. https://doi.org/10.1021/acs.est.5b04053.

(282) Lin, J.; Dai, Q.; Zhao, H.; Cao, H.; Wang, T.; Wang, G.; Chen, C. Photoinduced Release of Volatile Organic Compounds from Fatty Alcohols at the Air–Water Interface: The Role of Singlet Oxygen Photosensitized by a Carbonyl Group. *Environ. Sci. Technol.* **2021**, *55* (13), 8683–8690. https://doi.org/10.1021/acs.est.1c00313.

(283) Perkins, R. J.; Vazquez de Vasquez, M. G.; Beasley, E. E.; Hill, T. C. J.; Stone, E. A.; Allen, H. C.; DeMott, P. J. Relating Structure and Ice Nucleation of Mixed Surfactant Systems Relevant to Sea Spray Aerosol. *J. Phys. Chem. A* **2020**, *124* (42), 8806–8821. https://doi.org/10.1021/acs.jpca.0c05849.

(284) Ellison, G. B.; Tuck, A. F.; Vaida, V. Atmospheric Processing of Organic Aerosols. *J. Geophys. Res. Atmospheres* **1999**, *104* (D9), 11633–11641. https://doi.org/10.1029/1999JD900073.

(285) Rouvière, A.; Ammann, M. The Effect of Fatty Acid Surfactants on the Uptake of Ozone to Aqueous Halogenide Particles. *Atmospheric Chem. Phys.* **2010**, *10* (23), 11489–11500. https://doi.org/10.5194/acp-10-11489-2010.

(286) Griffith, E. C.; Adams, E. M.; Allen, H. C.; Vaida, V. Hydrophobic Collapse of a Stearic Acid Film by Adsorbed L-Phenylalanine at the Air–Water Interface. *J. Phys. Chem. B* **2012**, *116* (27), 7849–7857. https://doi.org/10.1021/jp303913e.

(287) Cheng, S.; Li, S.; Tsona, N. T.; George, C.; Du, L. Insights into the Headgroup and Chain Length Dependence of Surface Characteristics of Organic-Coated Sea Spray Aerosols. *ACS Earth Space Chem.* **2019**, *3* (4), 571–580. https://doi.org/10.1021/acsearthspacechem.8b00212.

(288) Li, S.; Du, L.; Wei, Z.; Wang, W. Aqueous-Phase Aerosols on the Air-Water Interface: Response of Fatty Acid Langmuir Monolayers to Atmospheric Inorganic Ions. *Sci. Total Environ.* **2017**, *580*, 1155–1161. https://doi.org/10.1016/j.scitotenv.2016.12.072.

(289) Bruland, K. W.; Lohan, M. C. 6.02 Controls of Trace Metals in Seawater. 25.

(290) Zhang, T.; Fiamingo, M.; Allen, H. C. Trace Metal Enrichment Driven by Phosphate Functional Group Binding Selectivity. *J. Geophys. Res. Oceans* **2018**, *123* (8), 5286–5297. https://doi.org/10.1029/2018JC013926.

(291) Barker, D. R.; Zeitlin, H. Metal-Ion Concentrations in Sea-Surface Microlayer and Size-Separated Atmospheric Aerosol Samples in Hawaii. *J. Geophys. Res. 1896-1977* **1972**, *77* (27), 5076–5086. https://doi.org/10.1029/JC077i027p05076.

(292) Adams, E. M.; Wellen, B. A.; Thiraux, R.; Reddy, S. K.; Vidalis, A. S.; Paesani, F.; Allen, H. C. Sodium–Carboxylate Contact Ion Pair Formation Induces Stabilization of Palmitic Acid Monolayers at High PH. *Phys. Chem. Chem. Phys.* **2017**, *19* (16), 10481–10490. https://doi.org/10.1039/C7CP00167C.

(293) Zhang, Z.; Liu, L.; Liu, C.; Cai, W. Studies on the Sea Surface Microlayer: II. The Layer of Sudden Change of Physical and Chemical Properties. *J. Colloid Interface Sci.* **2003**, *264* (1), 148–159. https://doi.org/10.1016/S0021-9797(03)00390-4.

(294) Adams, E. M.; Verreault, D.; Jayarathne, T.; Cochran, R. E.; Stone, E. A.; Allen, H. C. Surface Organization of a DPPC Monolayer on Concentrated $SrCl_2$ and $ZnCl_2$ Solutions. *Phys. Chem. Chem. Phys.* **2016**, *18* (47), 32345–32357. https://doi.org/10.1039/C6CP06887A.

(295) Li, S.; Du, L.; Tsona, N. T.; Wang, W. The Interaction of Trace Heavy Metal with Lipid Monolayer in the Sea Surface Microlayer. *Chemosphere* **2018**, *196*, 323–330. https://doi.org/10.1016/j.chemosphere.2017.12.157.

(296) Simon-Kutscher, J.; Gericke, A.; Hühnerfuss, H. Effect of Bivalent Ba, Cu, Ni, and Zn Cations on the Structure of Octadecanoic Acid Monolayers at the Air−Water Interface As Determined by External Infrared Reflection−Absorption Spectroscopy. *Langmuir* **1996**, *12* (4), 1027–1034. https://doi.org/10.1021/la950731q.

(297) Kumar, N.; Wang, L.; Siretanu, I.; Duits, M.; Mugele, F. Salt Dependent Stability of Stearic Acid Langmuir–Blodgett Films Exposed to Aqueous Electrolytes. *Langmuir* **2013**, *29* (17), 5150–5159. https://doi.org/10.1021/la400615j.

(298) Ebling, A. M.; Landing, W. M. Sampling and Analysis of the Sea Surface Microlayer for Dissolved and Particulate Trace Elements. *Mar. Chem.* **2015**, *177*, 134–142. https://doi.org/10.1016/j.marchem.2015.03.012.

(299) Gaines, G. L. *Insoluble Monolayers at Liquid-Gas Interfaces*; Interscience Publishers: New York, 1966.

(300) T. Buffeteau; B. Desbat; D. Eyquem. Attenuated Total Reflection Fourier Transform Infrared Microspectroscopy: Theory and Application to Polymer Samples. *Vib. Spectrosc.* **1996**, *11* (1), 29–36. https://doi.org/10.1016/0924-2031(95)00054-2.

(301) Flach, C. R.; Gericke, A.; Mendelsohn, R. Quantitative Determination of Molecular Chain Tilt Angles in Monolayer Films at the Air/Water Interface: Infrared Reflection/Absorption Spectroscopy of Behenic Acid Methyl Ester. *J. Phys. Chem. B* **1997**, *101* (1), 58–65. https://doi.org/10.1021/jp962288d.

(302) Gericke, A.; Huehnerfuss, H. In Situ Investigation of Saturated Long-Chain Fatty Acids at the Air/Water Interface by External Infrared Reflection-Absorption Spectrometry. *J. Phys. Chem.* **1993**, *97* (49), 12899–12908. https://doi.org/10.1021/j100151a044.

(303) Mendelsohn, R.; Brauner, J. W.; Gericke, A. External Infrared Reflection Absorption Spectrometry of Monolayer Films at the Air-Water Interface. *Annu. Rev. Phys. Chem.* **1995**, *46* (1), 305–334. https://doi.org/10.1146/annurev.pc.46.100195.001513.

(304) Mendelsohn, R.; Mao, G.; Flach, C. R. Infrared Reflection–Absorption Spectroscopy: Principles and Applications to Lipid–Protein Interaction in Langmuir Films. *Biochim. Biophys. Acta BBA - Biomembr.* **2010**, *1798* (4), 788–800. https://doi.org/10.1016/j.bbamem.2009.11.024.

(305) Shanmukh, S.; Biswas, N.; Waring, A. J.; Walther, F. J.; Wang, Z.; Chang, Y.; Notter, R. H.; Dluhy, R. A. Structure and Properties of Phospholipid–Peptide Monolayers Containing Monomeric SP-B1–25: II. Peptide Conformation by Infrared Spectroscopy. *Biophys. Chem.* **2005**, *113* (3), 233–244. https://doi.org/10.1016/j.bpc.2004.09.009.

(306) Wang, Y.; Du, X.; Guo, L.; Liu, H. Chain Orientation and Headgroup Structure in Langmuir Monolayers of Stearic Acid and Metal Stearate (Ag, Co, Zn, and Pb) Studied by Infrared Reflection-Absorption Spectroscopy. *J. Chem. Phys.* **2006**, *124* (13), 134706. https://doi.org/10.1063/1.2185629.

(307) Blume, A.; Kerth, A. Peptide and Protein Binding to Lipid Monolayers Studied by FT-IRRA Spectroscopy. *Biochim. Biophys. Acta BBA - Biomembr.* **2013**, *1828* (10), 2294–2305. https://doi.org/10.1016/j.bbamem.2013.04.014.

(308) William E. Wallace. Water. In *NIST Standard Reference Database Number 69*; NIST Chemistry WebBook; National Institute of Standards and Technology: Gaithersburg MD.

(309) Chattoraj, D. K.; Birdi, K. S. Spread Monolayer. In *Adsorption and the Gibbs Surface Excess*; Chattoraj, D. K., Birdi, K. S., Eds.; Springer US: Boston, MA, 1984; pp 179–232. https://doi.org/10.1007/978-1-4615-8333-2_6.

(310) Li, S.; Du, L.; Zhang, Q.; Wang, W. Stabilizing Mixed Fatty Acid and Phthalate Ester Monolayer on Artificial Seawater. *Environ. Pollut. Barking Essex 1987* **2018**, *242* (Pt A), 626–633. https://doi.org/10.1016/j.envpol.2018.07.043.

(311) Kartashynska, E. S.; Vysotsky, Y. B.; Vollhardt, D.; Fainerman, V. B.; Zakharov, A. Yu. Theoretical Description of Mixed Film Formation at the Air/Water Interface: Carboxylic Acids–Alcohols. *ACS Omega* **2018**, *3* (12), 16693–16705. https://doi.org/10.1021/acsomega.8b02583.

(312) Panda, A. K.; Nag, K.; Harbottle, R. R.; Possmayer, F.; Petersen, N. O. Thermodynamic Studies on Mixed Molecular Langmuir Films: Part 2. Mutual Mixing of DPPC and Bovine Lung Surfactant Extract with Long-Chain Fatty Acids. *Colloids Surf. Physicochem. Eng. Asp.* **2004**, *247* (1), 9–17. https://doi.org/10.1016/j.colsurfa.2004.07.008.

(313) Seoane, R.; Miñones, J.; Conde, O.; Miñones, J.; Casas, M.; Iribarnegaray, E. Thermodynamic and Brewster Angle Microscopy Studies of Fatty Acid/Cholesterol Mixtures at the Air/Water Interface. *J. Phys. Chem. B* **2000**, *104* (32), 7735–7744. https://doi.org/10.1021/jp001133+.

(314) Denton, J. K.; Kelleher, P. J.; Johnson, M. A.; Baer, M. D.; Kathmann, S. M.; Mundy, C. J.; Rudd, B. A. W.; Allen, H. C.; Choi, T. H.; Jordan, K. D. Molecular-Level Origin of the Carboxylate Head Group Response to Divalent Metal Ion Complexation at the Air–Water Interface. *Proc. Natl. Acad. Sci.* **2019**, *116* (30), 14874–14880. https://doi.org/10.1073/pnas.1818600116.

(315) Rudd, B. A. W.; Vidalis, A. S.; Allen, H. C. Thermodynamic versus Non-Equilibrium Stability of Palmitic Acid Monolayers in Calcium-Enriched Sea Spray Aerosol Proxy Systems. *Phys. Chem. Chem. Phys.* **2018**, *20* (24), 16320–16332. https://doi.org/10.1039/C8CP01188E.

(316) Zhang, T.; Brantley, S. L.; Verreault, D.; Dhankani, R.; Corcelli, S. A.; Allen, H. C. Effect of PH and Salt on Surface PKa of Phosphatidic Acid Monolayers. *Langmuir* **2018**, *34* (1), 530–539. https://doi.org/10.1021/acs.langmuir.7b03579.

(317) Adams, E. M.; Casper, C. B.; Allen, H. C. Effect of Cation Enrichment on Dipalmitoylphosphatidylcholine (DPPC) Monolayers at the Air-Water Interface. *J. Colloid Interface Sci.* **2016**, *478*, 353–364. https://doi.org/10.1016/j.jcis.2016.06.016.

(318) Wolstenholme, G. A.; Schulman, J. H. Metal-Monolayer Interactions in Aqueous Systems. Part I.—The Interaction of Monolayers of Long-Chain Polar Compounds with Metal Ions in the Underlying Solution. *Trans. Faraday Soc.* **1950**, *46* (0), 475–487. https://doi.org/10.1039/TF9504600475.

(319) Lee, Y.-L.; Yang, Y.-C.; Shen, Y.-J. Monolayer Characteristics of Mixed Octadecylamine and Stearic Acid at the Air/Water Interface. *J. Phys. Chem. B* **2005**, *109* (10), 4662–4667. https://doi.org/10.1021/jp045251z.

(320) Pfrang, C.; Rastogi, K.; Cabrera-Martinez, E. R.; Seddon, A. M.; Dicko, C.; Labrador, A.; Plivelic, T. S.; Cowieson, N.; Squires, A. M. Complex Three-Dimensional Self-Assembly in Proxies for Atmospheric Aerosols. *Nat. Commun.* **2017**, *8*. https://doi.org/10.1038/s41467-017-01918-1.

(321) Neumann, V.; Gericke, A.; Huehnerfuss, H. Comparison of Enantiomeric and Racemic Monolayers of 2-Hydroxyhexadecanoic Acid by External Infrared Reflection-Absorption Spectroscopy. *Langmuir* **1995**, *11* (6), 2206–2212. https://doi.org/10.1021/la00006a058.

(322) Cameron, D. G.; Casal, H. L.; Gudgin, E. F.; Mantsch, H. H. The Gel Phase of Dipalmitoyl Phosphatidylcholine. An Infrared Characterization of the Acyl Chain Packing. *Biochim. Biophys. Acta BBA - Biomembr.* **1980**, *596* (3), 463–467. https://doi.org/10.1016/0005-2736(80)90135-2.

(323) Schaefer, C. E.; Culina, V.; Nguyen, D.; Field, J. Uptake of Poly- and Perfluoroalkyl Substances at the Air–Water Interface. *Environ. Sci. Technol.* **2019**, *53* (21), 12442–12448. https://doi.org/10.1021/acs.est.9b04008.

(324) Khayyun, T. S.; Mseer, A. H. Comparison of the Experimental Results with the Langmuir and Freundlich Models for Copper Removal on Limestone Adsorbent. *Appl. Water Sci.* **2019**, *9* (8), 170. https://doi.org/10.1007/s13201-019-1061-2.

(325) Soares, J. C.; Soares, A. C.; Pereira, P. A. R.; Rodrigues, V. da C.; Shimizu, F. M.; Melendez, M. E.; Neto, C. S.; Carvalho, A. L.; Leite, F. L.; Machado, S. A. S.; Oliveira, O. N. Adsorption According to the Langmuir–Freundlich Model Is the Detection Mechanism of the Antigen P53 for Early Diagnosis of Cancer. *Phys. Chem. Chem. Phys.* **2016**, *18* (12), 8412–8418. https://doi.org/10.1039/C5CP07121F.

(326) Langmuir, I. The Adsorption of Gases on Plane Surfaces of Glass, Mica, and Platinum. *J. Am. Chem. Soc.* **1918**, *40* (9), 1361–1403. https://doi.org/10.1021/ja02242a004.

(327) Henry, D. C. LX. *A Kinetic Theory of Adsorption*. *Lond. Edinb. Dublin Philos. Mag. J. Sci.* **1922**, *44* (262), 689–705. https://doi.org/10.1080/14786441108634035.

(328) Jeppu, G. P.; Clement, T. P. A Modified Langmuir-Freundlich Isotherm Model for Simulating PH-Dependent Adsorption Effects. *J. Contam. Hydrol.* **2012**, *129–130*, 46–53. https://doi.org/10.1016/j.jconhyd.2011.12.001.

(329) Pisarchick, M.L.; Thompson, N.L. Binding of a Monoclonal Antibody and Its Fab Fragment to Supported Phospholipid Monolayers Measured by Total Internal Reflection Fluorescence Microscopy. *Biophys. J.* **1990**, *58* (5), 1235–1249. https://doi.org/10.1016/S0006-3495(90)82464-4.

(330) Mopper, K.; zhou, J.; Sri Ramana, K.; passow, U.; dam, H. G.; Drapeau, D. T. The Role of Surface-Active Carbohydrates in the Flocculation of a Diatom Bloom in a Mesocosm. *Deep Sea Res. Part II Top. Stud. Oceanogr.* **1995**, *42* (1), 47–73. https://doi.org/10.1016/0967-0645(95)00004-A.

(331) Frossard, A. A.; Russell, L. M.; Burrows, S. M.; Elliott, S. M.; Bates, T. S.; Quinn, P. K. Sources and Composition of Submicron Organic Mass in Marine

Aerosol Particles. *J. Geophys. Res. Atmospheres* **2014**, *119* (22), 12,977-13,003. https://doi.org/10.1002/2014JD021913.

(332) Gao, Q.; Leck, C.; Rauschenberg, C.; Matrai, P. A. On the Chemical Dynamics of Extracellular Polysaccharides in the High Arctic Surface Microlayer. *Ocean Sci.* **2012**, *8* (4), 401–418. https://doi.org/10.5194/os-8-401-2012.

(333) Zhou, J.; Mopper, K.; Passow, U. The Role of Surface-Active Carbohydrates in the Formation of Transparent Exopolymer Particles by Bubble Adsorption of Seawater. *Limnol. Oceanogr.* **1998**, *43* (8), 1860–1871. https://doi.org/10.4319/lo.1998.43.8.1860.

(334) Collins, D. B.; Zhao, D. F.; Ruppel, M. J.; Laskina, O.; Grandquist, J. R.; Modini, R. L.; Stokes, M. D.; Russell, L. M.; Bertram, T. H.; Grassian, V. H.; Deane, G. B.; Prather, K. A. Direct Aerosol Chemical Composition Measurements to Evaluate the Physicochemical Differences between Controlled Sea Spray Aerosol Generation Schemes. *Atmospheric Meas. Tech.* **2014**, *7* (11), 3667–3683. https://doi.org/10.5194/amt-7-3667-2014.

(335) Modini, R. L.; Russell, L. M.; Deane, G. B.; Stokes, M. D. Effect of Soluble Surfactant on Bubble Persistence and Bubble-Produced Aerosol Particles. *J. Geophys. Res. Atmospheres* **2013**, *118* (3), 1388–1400. https://doi.org/10.1002/jgrd.50186.

(336) Wonaschütz, A.; Coggon, M.; Sorooshian, A.; Modini, R.; Frossard, A. A.; Ahlm, L.; Mülmenstädt, J.; Roberts, G. C.; Russell, L. M.; Dey, S.; Brechtel, F. J.; Seinfeld, J. H. Hygroscopic Properties of Smoke-Generated Organic Aerosol Particles Emitted in the Marine Atmosphere. *Atmospheric Chem. Phys.* **2013**, *13* (19), 9819–9835. https://doi.org/10.5194/acp-13-9819-2013.

(337) Sanchez, K. J.; Russell, L. M.; Modini, R. L.; Frossard, A. A.; Ahlm, L.; Corrigan, C. E.; Roberts, G. C.; Hawkins, L. N.; Schroder, J. C.; Bertram, A. K.; Zhao, R.; Lee, A. K. Y.; Lin, J. J.; Nenes, A.; Wang, Z.; Wonaschütz, A.; Sorooshian, A.; Noone, K. J.; Jonsson, H.; Toom, D.; Macdonald, A. M.; Leaitch, W. R.; Seinfeld, J. H. Meteorological and Aerosol Effects on Marine Cloud Microphysical Properties. *J. Geophys. Res. Atmospheres* **2016**, *121* (8), 4142–4161. https://doi.org/10.1002/2015JD024595.

(338) Modini, R. L.; Frossard, A. A.; Ahlm, L.; Russell, L. M.; Corrigan, C. E.; Roberts, G. C.; Hawkins, L. N.; Schroder, J. C.; Bertram, A. K.; Zhao, R.; Lee, A. K. Y.; Abbatt, J. P. D.; Lin, J.; Nenes, A.; Wang, Z.; Wonaschütz, A.; Sorooshian, A.; Noone, K. J.; Jonsson, H.; Seinfeld, J. H.; Toom-Sauntry, D.; Macdonald, A. M.; Leaitch, W. R. Primary Marine Aerosol-cloud Interactions off the Coast of California. *J Geophys Res Atmos* **2015**, *120*, 4282–4303. https://doi.org/10.1002/2014JD022963.

(339) Link, K. A.; Spurzem, G. N.; Tuladhar, A.; Chase, Z.; Wang, Z.; Wang, H.; Walker, R. A. Organic Enrichment at Aqueous Interfaces: Cooperative Adsorption of Glucuronic Acid to DPPC Monolayers Studied with Vibrational Sum Frequency Generation. *J. Phys. Chem. A* **2019**, *123* (26), 5621–5632. https://doi.org/10.1021/acs.jpca.9b02255.

(340) Hasenecz, E. S.; Kaluarachchi, C. P.; Lee, H. D.; Tivanski, A. V.; Stone, E. A. Saccharide Transfer to Sea Spray Aerosol Enhanced by Surface Activity, Calcium, and Protein Interactions. *ACS Earth Space Chem.* **2019**, *3* (11), 2539–2548. https://doi.org/10.1021/acsearthspacechem.9b00197.

(341) de Moura, M. R.; Ahmad Aouada, F.; Favaro, S. L.; Radovanovic, E.; Forti Rubira, A.; Muniz, E. C. Release of BSA from Porous Matrices Constituted of Alginate–Ca2+ and PNIPAAm-Interpenetrated Networks. *Mater. Sci. Eng. C* **2009**, *29* (8), 2319–2325. https://doi.org/10.1016/j.msec.2009.05.022.

(342) Lin, J. D.; Lemay, M. A.; Parfrey, L. W. Diverse Bacteria Utilize Alginate Within the Microbiome of the Giant Kelp Macrocystis Pyrifera. *Front. Microbiol.* **2018**, *9*.

(343) Zhang, L.; Li, X.; Zhang, X.; Li, Y.; Wang, L. Bacterial Alginate Metabolism: An Important Pathway for Bioconversion of Brown Algae. *Biotechnol. Biofuels* **2021**, *14* (1), 158. https://doi.org/10.1186/s13068-021-02007-8.

(344) Jain, S.; Ohman, D. E. Role of an Alginate Lyase for Alginate Transport in Mucoid Pseudomonas Aeruginosa. *Infect. Immun.* **2005**. https://doi.org/10.1128/IAI.73.10.6429-6436.2005.

(345) Thomas, F.; Barbeyron, T.; Tonon, T.; Génicot, S.; Czjzek, M.; Michel, G. Characterization of the First Alginolytic Operons in a Marine Bacterium: From Their Emergence in Marine Flavobacteriia to Their Independent Transfers to Marine Proteobacteria and Human Gut Bacteroides. *Environ. Microbiol.* **2012**, *14* (9), 2379–2394. https://doi.org/10.1111/j.1462-2920.2012.02751.x.

(346) Hassler, C. S.; Schoemann, V.; Nichols, C. M.; Butler, E. C. V.; Boyd, P. W. Saccharides Enhance Iron Bioavailability to Southern Ocean Phytoplankton. *Proc. Natl. Acad. Sci.* **2011**, *108* (3), 1076–1081. https://doi.org/10.1073/pnas.1010963108.

(347) Carter-Fenk, K. A.; Dommer, A. C.; Fiamingo, M. E.; Kim, J.; Amaro, R. E.; Allen, H. C. Calcium Bridging Drives Polysaccharide Co-Adsorption to a Proxy Sea Surface Microlayer. *Phys. Chem. Chem. Phys.* **2021**, *23* (30), 16401–16416. https://doi.org/10.1039/D1CP01407B.

(348) Mandalakis, M.; Stephanou, E. G. Study of Atmospheric PCB Concentrations over the Eastern Mediterranean Sea. *J. Geophys. Res. Atmospheres* **2002**, *107* (D23), ACH 18-1-ACH 18-14. https://doi.org/10.1029/2001JD001566.

(349) Mashayekhy Rad, F.; Leck, C.; Ilag, L. L.; Nilsson, U. Investigation of Ultrahigh-Performance Liquid Chromatography/Travelling-Wave Ion Mobility/Time-of-Flight Mass Spectrometry for Fast Profiling of Fatty Acids in the High Arctic Sea Surface Microlayer. *Rapid Commun. Mass Spectrom.* **2018**, *32* (12), 942–950. https://doi.org/10.1002/rcm.8109.

(350) Patil, G. S.; Matthews, R. H.; Cornwell, D. G. Effect of Ionization and Cation Selectivity on the Expansion of Stearic Acid Monolayers. *J. Lipid Res.* **1972**, *13* (5), 574–579.

(351) Sears, D. F.; Schulman, J. H. Influence of Water Structures on the Surface Pressure, Surface Potential, and Area of Soap Monolayers of Lithium, Sodium,

Potassium, and Calcium. *J. Phys. Chem.* **1964**, *68* (12), 3529–3534. https://doi.org/10.1021/j100794a015.

(352) Neal, J. F.; Rogers, M. M.; Smeltzer, M. A.; Carter-Fenk, K. A.; Grooms, A. J.; Zerkle, M. M.; Allen, H. C. Sodium Drives Interfacial Equilibria for Semi-Soluble Phosphoric and Phosphonic Acids of Model Sea Spray Aerosol Surfaces. *ACS Earth Space Chem.* **2020**, *4* (9), 1549–1557. https://doi.org/10.1021/acsearthspacechem.0c00132.

(353) Auvil, N. C.; Vazquez de Vasquez, M. G.; Allen, H. C. Zinc–Carboxylate Binding in Mixed Octadecanoic Acid and Octadecanol Monolayers on Proxy Seawater Solution Surfaces. *ACS Earth Space Chem.* **2021**, *5* (10), 2947–2956. https://doi.org/10.1021/acsearthspacechem.1c00272.

(354) Angelova, A.; Vollhardt, D.; Ionov, R. 2D−3D Transformations of Amphiphilic Monolayers Influenced by Intermolecular Interactions: A Brewster Angle Microscopy Study. *J. Phys. Chem.* **1996**, *100* (25), 10710–10720. https://doi.org/10.1021/jp960417k.

(355) Kanicky, J. R.; Shah, D. O. Effect of Degree, Type, and Position of Unsaturation on the PKa of Long-Chain Fatty Acids. *J. Colloid Interface Sci.* **2002**, *256* (1), 201–207. https://doi.org/10.1006/jcis.2001.8009.

(356) Bu, H.; Kjøniksen, A.-L.; Elgsaeter, A.; Nyström, B. Interaction of Unmodified and Hydrophobically Modified Alginate with Sodium Dodecyl Sulfate in Dilute Aqueous Solution: Calorimetric, Rheological, and Turbidity Studies. *Colloids Surf. Physicochem. Eng. Asp.* **2006**, *278* (1), 166–174. https://doi.org/10.1016/j.colsurfa.2005.12.016.

(357) Rudd, B. A. W.; Vidalis, A. S.; Allen, H. C. Thermodynamic versus Non-Equilibrium Stability of Palmitic Acid Monolayers in Calcium-Enriched Sea Spray Aerosol Proxy Systems. *Phys. Chem. Chem. Phys.* **2018**, *20* (24), 16320–16332. https://doi.org/10.1039/C8CP01188E.

(358) Luo, M.; Wauer, N. A.; Angle, K. J.; Dommer, A. C.; Song, M.; Nowak, C. M.; Amaro, R. E.; Grassian, V. H. Insights into the Behavior of Nonanoic Acid and Its Conjugate Base at the Air/Water Interface through a Combined Experimental and Theoretical Approach. *Chem. Sci.* **2020**, *11* (39), 10647–10656. https://doi.org/10.1039/D0SC02354J.

(359) Tang, C. Y.; Huang, Z.; Allen, H. C. Interfacial Water Structure and Effects of Mg2+ and Ca2+ Binding to the COOH Headgroup of a Palmitic Acid Monolayer Studied by Sum Frequency Spectroscopy. *J. Phys. Chem. B* **2011**, *115* (1), 34–40. https://doi.org/10.1021/jp1062447.

(360) Buffeteau, T.; Desbat, B.; Eyquem, D. Attenuated Total Reflection Fourier Transform Infrared Microspectroscopy: Theory and Application to Polymer Samples. *Vib. Spectrosc.* **1996**, *11* (1), 29–36. https://doi.org/10.1016/0924-2031(95)00054-2.

(361) Shanmukh, S.; Biswas, N.; Waring, A. J.; Walther, F. J.; Wang, Z.; Chang, Y.; Notter, R. H.; Dluhy, R. A. Structure and Properties of Phospholipid–Peptide Monolayers Containing Monomeric SP-B1–25: II. Peptide Conformation by

Infrared Spectroscopy. *Biophys. Chem.* **2005**, *113* (3), 233–244. https://doi.org/10.1016/j.bpc.2004.09.009.

(362) Miranda, P. B.; Du, Q.; Shen, Y. R. Interaction of Water with a Fatty Acid Langmuir Film. *Chem. Phys. Lett.* **1998**, *286*, 1–8. https://doi.org/10.1016/S0009-2614(97)01476-0.

(363) Tang, F.; Ohto, T.; Sun, S.; Rouxel, J. R.; Imoto, S.; Backus, E. H. G.; Mukamel, S.; Bonn, M.; Nagata, Y. Molecular Structure and Modeling of Water–Air and Ice–Air Interfaces Monitored by Sum-Frequency Generation. *Chem. Rev.* **2020**, *120* (8), 3633–3667. https://doi.org/10.1021/acs.chemrev.9b00512.

(364) Balzerowski, P.; Meister, K.; Versluis, J.; Bakker, H. J. Heterodyne-Detected Sum Frequency Generation Spectroscopy of Polyacrylic Acid at the Air/Water-Interface. *Phys. Chem. Chem. Phys.* **2016**, *18* (4), 2481–2487. https://doi.org/10.1039/C5CP06177F.

(365) Langmuir, I. THE ADSORPTION OF GASES ON PLANE SURFACES OF GLASS, MICA AND PLATINUM. *J. Am. Chem. Soc.* **1918**, *40* (9), 1361–1403. https://doi.org/10.1021/ja02242a004.

(366) Henry, D. C. LX. A Kinetic Theory of Adsorption. *Lond. Edinb. Dublin Philos. Mag. J. Sci.* **1922**, *44* (262), 689–705. https://doi.org/10.1080/14786441108634035.

(367) Chen, H.; Gan, W.; Lu, R.; Guo, Y.; Wang, H. Determination of Structure and Energetics for Gibbs Surface Adsorption Layers of Binary Liquid Mixture 2. Methanol + Water. *J. Phys. Chem. B* **2005**, *109* (16), 8064–8075. https://doi.org/10.1021/jp0501906.

(368) Ayoub, G. T.; Bashara, N. M. Characterization of a Very Thin Uniaxial Film on a Nonabsorbing Substrate by Multiple Wavelength Ellipsometry: Palmitic Acid on Water*. *JOSA* **1978**, *68* (7), 978–983. https://doi.org/10.1364/JOSA.68.000978.

(369) Craig, B. M. Refractive Indices of Some Saturated and Monoethenoid Fatty Acids and Methyl Esters. *Can. J. Chem.* **1953**, *31* (5), 499–504. https://doi.org/10.1139/v53-068.

(370) Pusterla, J. M.; Malfatti-Gasperini, A. A.; Puentes-Martinez, X. E.; Cavalcanti, L. P.; Oliveira, R. G. Refractive Index and Thickness Determination in Langmuir Monolayers of Myelin Lipids. *Biochim. Biophys. Acta BBA - Biomembr.* **2017**, *1859* (5), 924–930. https://doi.org/10.1016/j.bbamem.2017.02.005.

(371) Winsel, K.; Hönig, D.; Lunkenheimer, K.; Geggel, K.; Witt, C. Quantitative Brewster Angle Microscopy of the Surface Film of Human Broncho-Alveolar Lavage Fluid. *Eur. Biophys. J.* **2003**, *32* (6), 544–552. https://doi.org/10.1007/s00249-003-0290-2.

(372) Austin, R. W.; Halikas, G. *The Index of Refraction of Seawater:*; Defense Technical Information Center: Fort Belvoir, VA, 1976. https://doi.org/10.21236/ADA024800.

(373) Rogers, M. M.; Neal, J. F.; Saha, A.; Algarni, A. S.; Hill, T. C. J.; Allen, H. C. The Ocean's Elevator: Evolution of the Air–Seawater Interface during a Small-

Scale Algal Bloom. *ACS Earth Space Chem.* **2020**, *4* (12), 2347–2357. https://doi.org/10.1021/acsearthspacechem.0c00239.

(374) Adams, E. M.; Verreault, D.; Jayarathne, T.; Cochran, R. E.; Stone, E. A.; Allen, H. C. Surface Organization of a DPPC Monolayer on Concentrated SrCl2 and ZnCl2 Solutions. *Phys. Chem. Chem. Phys.* **2016**, *18* (47), 32345–32357. https://doi.org/10.1039/C6CP06887A.

(375) Kienle, D. F.; de Souza, J. V.; Watkins, E. B.; Kuhl, T. L. Thickness and Refractive Index of DPPC and DPPE Monolayers by Multiple-Beam Interferometry. *Anal. Bioanal. Chem.* **2014**, *406* (19), 4725–4733. https://doi.org/10.1007/s00216-014-7866-9.

(376) Reynolds, P. A.; McGillivray, D. J.; Gilbert, E. P.; Holt, S. A.; Henderson, M. J.; White, J. W. Neutron and X-Ray Reflectivity from Polyisobutylene-Based Amphiphiles at the Air−Water Interface. *Langmuir* **2003**, *19* (3), 752–761. https://doi.org/10.1021/la0206920.

(377) DeLucas, L.; Bugg, C. E.; Terzis, A.; Rivest, R. Calcium Binding to D-Glucuronate Residues: Crystal Structure of a Hydrated Calcium Bromide Salt of D-Glucuronic Acid. *Carbohydr. Res.* **1975**, *41* (1), 19–29. https://doi.org/10.1016/S0008-6215(00)87003-2.

(378) Ferrari, E.; Grandi, R.; Lazzari, S.; Saladini, M. Hg(II)-Coordination by Sugar-Acids: Role of the Hydroxy Groups. *J. Inorg. Biochem.* **2005**, *99* (12), 2381–2386. https://doi.org/10.1016/j.jinorgbio.2005.09.005.

(379) Whitfield, D. M.; Stojkovski, S.; Sarkar, B. Metal Coordination to Carbohydrates. Structures and Function. *Coord. Chem. Rev.* **1993**, *122* (1), 171–225. https://doi.org/10.1016/0010-8545(93)80045-7.

(380) Kundu, S.; Langevin, D. Fatty Acid Monolayer Dissociation and Collapse: Effect of PH and Cations. *Colloids Surf. Physicochem. Eng. Asp.* **2008**, *325* (1), 81–85. https://doi.org/10.1016/j.colsurfa.2008.04.037.

(381) Le Calvez, E.; Blaudez, D.; Buffeteau, T.; Desbat, B. Effect of Cations on the Dissociation of Arachidic Acid Monolayers on Water Studied by Polarization-Modulated Infrared Reflection−Absorption Spectroscopy. *Langmuir* **2001**, *17* (3), 670–674. https://doi.org/10.1021/la000224v.

(382) Wang, Y.; Du, X.; Guo, L.; Liu, H. Chain Orientation and Headgroup Structure in Langmuir Monolayers of Stearic Acid and Metal Stearate (Ag, Co, Zn, and Pb) Studied by Infrared Reflection-Absorption Spectroscopy. *J. Chem. Phys.* **2006**, *124* (13), 134706. https://doi.org/10.1063/1.2185629.

(383) Link, K. A.; Hsieh, C.-Y.; Tuladhar, A.; Chase, Z.; Wang, Z.; Wang, H.; Walker, R. A. Vibrational Studies of Saccharide-Induced Lipid Film Reorganization at Aqueous/Air Interfaces. *Chem. Phys.* **2018**, *512*, 104–110. https://doi.org/10.1016/j.chemphys.2018.02.011.

(384) Neal, J. F.; Zhao, W.; Grooms, A. J.; Smeltzer, M. A.; Shook, B. M.; Flood, A. H.; Allen, H. C. Interfacial Supramolecular Structures of Amphiphilic Receptors Drive Aqueous Phosphate Recognition. *J. Am. Chem. Soc.* **2019**, *141* (19), 7876–7886. https://doi.org/10.1021/jacs.9b02148.

(385) Cameron, D. G.; Casal, H. L.; Gudgin, E. F.; Mantsch, H. H. The Gel Phase of Dipalmitoyl Phosphatidylcholine. An Infrared Characterization of the Acyl Chain Packing. *Biochim. Biophys. Acta BBA - Biomembr.* **1980**, *596* (3), 463–467. https://doi.org/10.1016/0005-2736(80)90135-2.

(386) Mendelsohn, R.; Brauner, J. W.; Gericke, A. External Infrared Reflection Absorption Spectrometry of Monolayer Films at the Air-Water Interface. *Annu. Rev. Phys. Chem.* **1995**, *46*, 305–334. https://doi.org/10.1146/annurev.pc.46.100195.001513.

Appendix A. Supporting Information

A.1 Chapter 3 Supporting Information

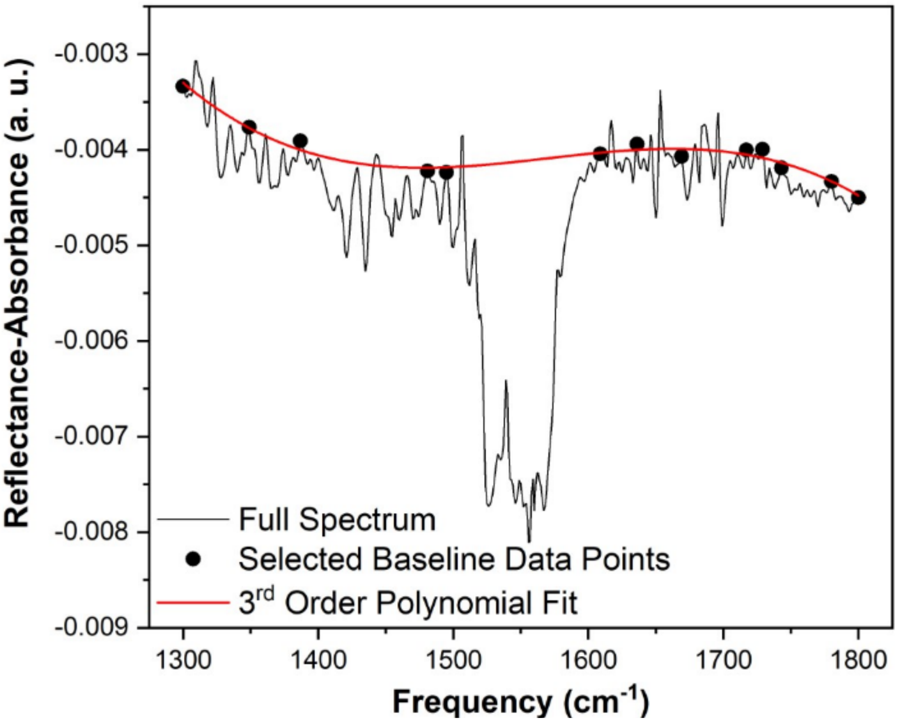

Figure 58. Example of the third-order polynomial fit used to baseline-subtract the IRRAS spectra. Each spectrum is fitted individually between 1300 and 1800 cm^{-1}, and the baseline-subtracted spectra are averaged to produce the spectra shown in **Figure 8**. Data points are selected from the raw spectrum to use as a partial baseline. A third-order polynomial is then fit to these data points. The baseline function is then subtracted from the raw spectrum, data collected by B. Wellen Rudd.

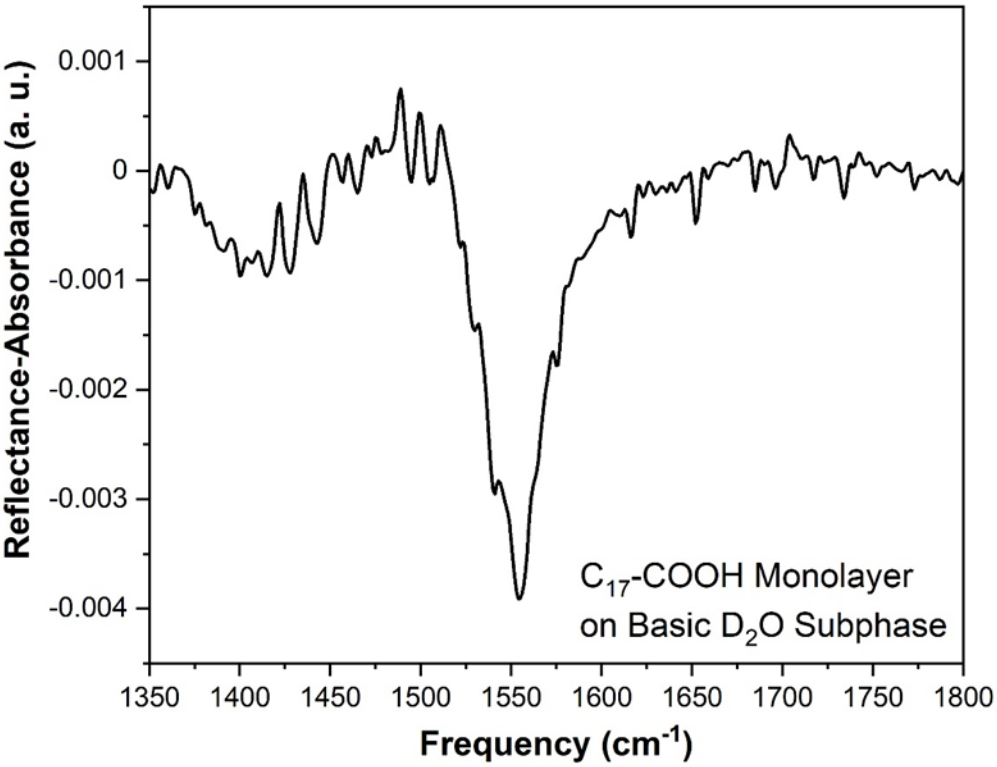

Figure 59. IRRAS spectrum of deuterated C_{17}-COOH monolayer on a basic D_2O subphase. A longer chain fatty acid is necessary on basic subphases in order to for the monolayer to remain at the interface, data collected by B Wellen Rudd.

Appendix B. BAM Optics Cleaning Procedure and BAM SOP

B.1 BAM Optics Cleaning

Cleaning the lens and/or optics can be intimidating, so the best way to avoid having to clean any lenses or optics is to use them carefully and keep them covered when not in use. If a lens gets dirty follow the procedure on how to clean it below.

First locate the dust, if you see a spot on the lens that does not move, it appears at the same location, and you also see it at all powers, it is probably on the outside. If the dust is on the inside, then you would need to have it clean professionally.

If the dust is on the outside, use a squeeze dust blower bulb to remove the dust from the lens. If you need a stronger flow, then you can also use a compressed air can which are used to clean a computer keyboard. You need to be very careful with it since it can damage the lens if not use properly. I highly recommend using a squeeze dust blower bulb rather than a compressed air can.

If using a squeeze dust blower bulb did not remove all the dust, you can also use a lens cleansing tissue. First, you need to fold the tissue together using Kelly forceps for the tissue to be used as a brush. The tissue must be use as one-time brush. If a grime is still there, you will need to use a solvent. Spectral grade methanol is one of the solvents that is generally recommended. Add a drop or two on the folded lens cleaning tissue then hold it against the lens for few seconds to dissolve the crust. Then lightly wipe it free.

Use another lens cleansing tissue if the process needs to be repeated. **Figure 60** shows images of two 10 × objective lenses and **Figure 61** shows the supplies needed for cleaning. **Figure 62** shows the Brewster angle microscopy set up in the Allen's laboratory.

10x Lens
BAM
Nikon 10x cf plan 0.21 epi slwd

10x Lens
106
Microscope

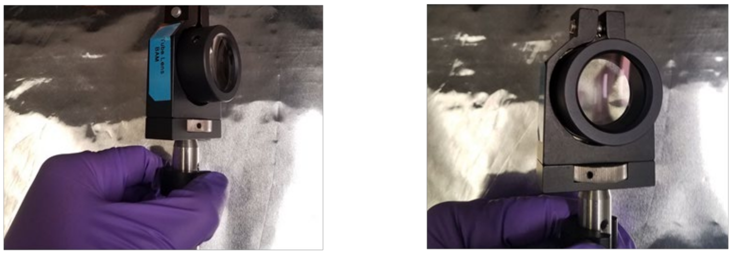

Tube Lens

Figure 60. Image showing two different 10 × lens left side 10x lens BAM (Nikon 10 × cf plan 0.21 epi slwd), right a 10 × lens microscope (NW 106 lab space). Bottom two image is the tube lens.

Figure 61. Supplies needed for lens cleaning in the BAM.

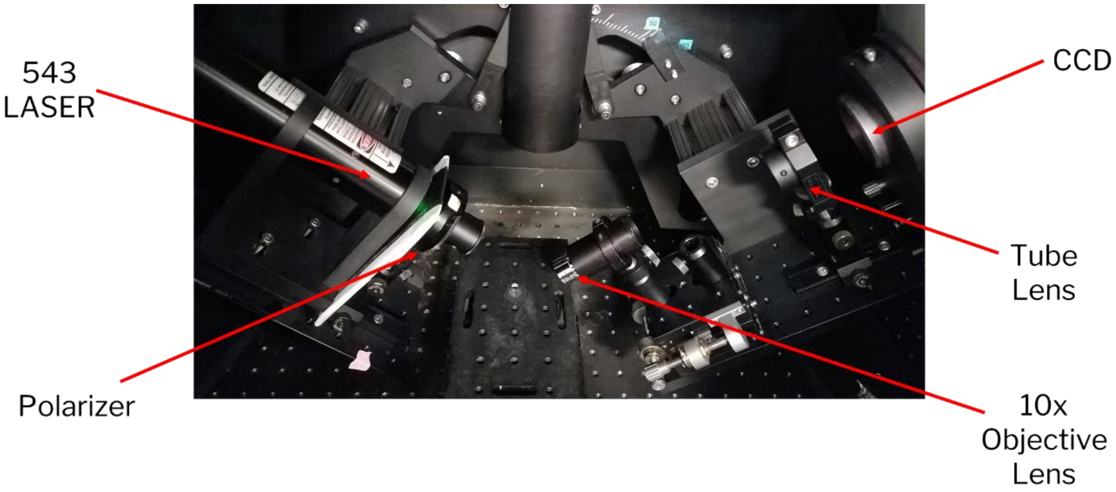

Figure 62. Brewster angle microscopy custom build set-up at the Allen's laboratory.

B.2 BAM and Isotherms Experiments SOP

1) Raise the BAM apparatus (i.e., the optics NOT the sample stage) using the knob in the far back in order to remove the trough without disturbing other components.

2) Place the trough apparatus aside on the right and remove the Teflon trough. Place the Teflon wedge and density filter in the trough and clean all component with reagent alcohol (Histological grade, Fisher Scientific) and nanopure water in the wet. lab.

3) Replace the trough apparatus on the sample stage. The density filter should be on top of the Teflon wedge with the taller part of the wedge facing the incoming beam. These pieces should be directly in line and below the focal lens. The trough can be filled with nanopure water.

4) Turn in the LASER using the key on top of the BAM enclosure. Make sure the blocker is in place.

5) Open Andor Solis Program on PC. Under Hardware, select Shutter Control. Select the following options: External Sutter: Fully Auto, TTL Level: TTL High, Time to open/close: 10/10. Then select OK.

6) Under Hardware, go to Temperature control and turn cooler ON. Set the temperature to -55 °C and click OK.

7) Under Acquisition, go to Setup Data Type. Select Counts (bg corrected) and click OK.

8) Under Acquisition, go to Setup Acquisition. Under Acquisition Mode Single, set the exposure time to 0.011 s. Now select Kinetic under Acquisition Mode. The exposure time should be the same (0.011 s). Set the Kinetic Cycle Time to 4.85 s and Kinetic Series Length to 200 and select OK.

9) Wait for the temperature to lock at –55 °C. The temperature reading will go from red to blue in the lower left-hand corner of the screen.

10) With the blocker in place, lamp of and doors close, go to Acquisition, select Take a Background. The data points should be around 1000 points.

11) Go to Display and select Rescale Data Mode. Select Custom. Set the High Value to 100 and click OK.

12) For aligning the reflected beam into the CCD, go to Display and select Rescale Data Mode. Select Min/Max then select OK.

13) Adjust the polarizer such that the reflected beam is seen going to the CCD. Using a card, center the beam vertically onto the CCD or you can also use the knob in the far back of the set up.

14) Dim the reflected beam by adjusting the polarized so it will not saturate the CCD.

15) Set the Acquisition Mode to Single.

16) Press the Camera Button.

17) Adjust the height of the image with the far back knob until it lies in the center of the image. Left/Right adjustments can be made if necessary, using the small knob bellow the focal lens (small knob coming towards you).

18) When the image is center, dim the polarizer until you cannot see the beam on the card before the CCD.

19) Go to Display and select Data Mode. Select Custom.

20) Take an image by pressing the camera button, with the doors close, if the counts are above 20, dim the polarizer more to diminish the reflected beam. If the light does not seem to be diminished, the angle of the beam may be off. The angle can be adjusted with the knob in the front of the far back knob.

21) Block the beam.

22) Spread 20 μL of stearic or palmitic acid onto the water subphase (volume of trough is 135 mL) using a microliter syringe.

23) Unblock the beam. With the Acquisition Mode in Single click the camera button.

24) Use the knob with the ridges attached to the focal lens. This knob is parallel to the collection arm of the goniometer or facing the laser.

25) Once the image is focus. Block the beam.

26) Rise the trough 4 × with nanopure water.

Ready For Experiment.

27) Turn the KSV Module (the box on the side of the BAM enclosure) with the ON/OFF switch.

28) Open the Layer Builder icon on the desktop. When the KSV widow opens, select the icon on the upper left corner as well.

29) Attach the hook to the hanging part of the trough apparatus. Make sure the density filter and wedge are directly below the focal lens. Fill the trough with water or solution of interest.

30) Add the barriers that have been washed with reagent alcohol and dry to the trough apparatus. The wider side should be sitting on the subphase.

31) Add a paper pate that has been prewetted in nanopure water to the hanging hook using a pair of tweezers.

32) Select the Manual Control tab. On the Manual Control Panel, Zero Balance when reading is relative stable.

33) In the Barrier Tab, close the barriers until you reach a position of 55. If the surface pressure reading goes above 0.20 mN/m, you need to re-clean. Open barriers.

34) Once re-clean and the apparatus is re-set , zero the balance and check for cleanness again.

35) You may need to make sure the beam is centered on the CCD. Adjust the far back knob to center the reflected beam to the CCD. You may need to adjust the polarization in order to see the beam.

36) Set the Display to Min/Max option.

37) Adjust the back knob until the image is centered.

38) Used the polarizer to diminish the reflected beam.

39) Change the Display Mode to Custom and take an image. If the counts exceed 20, adjust the polarizer accordingly. Set the Acquisition Mode to Kinetic.

40) On the LB Control Software. Click the "Iso" button.

41) Fill the necessary information (i.e., Title, name, sample, etc.). You want the volume spread to initially place you at about 20 Å2/molecule higher than the liftoff.

For example, the liftoff for palmitic acid is 26 Å^2/molecule. Spreading 40 µL of 1 mM sample should put you at about 20 Å^2/molecule higher.

42) Spread your sample. If any changes were made in the volume, correct that information. Now press Start.

43) Now the Trough Controls panel has appeared. Select Constant Rate Compression and the Go to Target Option. Set the target as the barrier position and set that to be 64

mm with a Rate of 5.0 mm/min (this is mm/min/barrier). Also set the Wait Time Before Go to 10 minutes. Press Go.

44) Make sure that your Acquisition Mode is Kinetic.

45) Once the Wait Time countdown hits 1s, press the camera button on the PC for BAM.

46) When the experiment if no longer "Running" stop the camera with the stop button. Block the beam.

47) Save the BAM image as a .sif file. on a personal folder in the BAM PC (THIS IS A VERY IMPORTANT STEP since data is not automatically saved).

48) Frames can be individually saved as .jpg files and movies can be saved with .m1v or .avi files.

49) After each experiment, rise the trough 4 × with nanopure water. A new experiment can be started by repeating instruction from step 29.

Appendix C. Cleaning Solutions and Filters and Cartridges

C.1 ACS Grade Salts Treatment and Filtration: Removal of Organics

Sodium chloride solution are baked at 650 ºC for 10 hours in a muffle furnace (Isotemp, 150–14, Fisher Scientific). Salt solutions are prepared by dissolving ACS grade salts in nanopure water and then filtering them three times using activated carbon filters (Whatman Carbon Cap 75, Fisher Scientific) to remove any organic impurities. Their concentrations are standardized by a Mohr titration. If $CaCl_2$ of $MgCl_2$ solutions are prepared, then these solutions are only filter using the activated carbon filters. Please note that the activated carbon filters have to be rise at least 10 minutes before and after filtration. Additionally, it is important to note that bacteria can grow in these filters so noting the date of first use is very important.

C.2 ACS and Trace Metal Grade Salt Filtration: Removal of Trace Heavy Metals

A Dionex OnGard II M Cartridges (Thermo Scientific, P/N 088356) can be used for the removal of trace heavy metal in sodium chloride solutions, **Figure 63**. These cartridges are generally used to remove any transition metal from the solution or matrix under study. The functional group in these cartridges is an iminodiacetate which is a tridentate ligand. This tridentate ligand forms a metal complex which consists of two fused five member chelate rings. These cartridges are designed for concentrating or removing transition metal at pH > 4, while allowing alkali and alkaline-earth metal to pass through. The transition meal can be eluted using 0.5 M nitic acid. It is important to mention that all water, reagents, and equipment must be metal free. Vials and other containers should be acid clean for at least an hour. Samples containing particulates should be filtered through a 0.45 of 0.2 μm polypropylene filters. The cartridge has to be flush with 10 mL of 2 M ammonium acetate pH 5.5, then the solution or sample of interest is filtered, discarding the first 6 mL of solution.

Figure 63. Dionex OnGard II M Cartridges (Product No. 088356, ThermoScientific) for the removal of trace heavy metals in solutions

C.3 Other Dionex OnGard II Cartridges

The Dionex OnGard II Cartridges line of sample pretreatment: These cartridges are suitable for matrix elimination and for some analyte solid phase extraction methods. This matrix elimination is a sample preparation that removes interfering matrix species via binding, leaving the analyte ready for the analysis. **Table 13** shows some of the Dionex OnGard Cartridges available as well as their applications.

Table 13. Various Dionex OnGard Cartridges available showing its functional group, usage, and application.

Cartridge Type	Functional Group	Mode of Use	Example Applications
On Gard II RP	Divinylbenzene	Adsorption	Removal of hydrophobic species
On Gard II H	Sulfonic Acid	Ion Exchange	Removal of cations, pH adjustment
On Gard II A	HCO^{-3} from quaternary amine	Ion Exchange	Removal of highly retained anions, pH adjustment
On Gard II M	Iminodiacetate Ammonium-Form	Chelation	Removal/ concentration of transition metals
On Gard II P	Poly-vinylpyrrolidone	H-bonding complexation	Removes phenols, Azo dyes, and humic acids
On Gard II Na	Cation Exchange Sodium form	Ion Exchange	Removes alkaline earth and cationic transitions metals without a pH change
On Gard II Ag	Ag^+-form sulfonate	Precipitation Ion Exchange	Removal of halides
On Gard II Ba	Ba^{2+}-form sulfonate	Precipitation Ion Exchange	Removal of sulfate
On Gard II Ba/Ag/H	Ba^{2+}-form sulfonate Ag^+-form sulfonate Sulfonic acid	Precipitation Ion Exchange Precipitation Ion Exchange Ion Exchange	Removal of sulfate Removal of halides plus excess of Ag^+
On Gard II Ag/H	Ag^+-form sulfonate Sulfonic acid	Precipitation Ion Exchange Ion Exchange	Removal of halides plus excess of Ag^+

Appendix D. KSV NIMA Surface Potentiometry (SPOT)

D.1 About the Instrument

The KSV surface potentiometry (SPOT) is a small computer control stand-alone surface potential measuring instrument. SPOT is based on the non-contact and non-destructive vibrating plate capacitor method. Such method is mainly designed for monolayer measurements, but due to its stand-alone property it is also stable for surface potential measurements over a range of solids and solutions. The method enables the user to complement surface pressure data by providing extra information about a monolayer such as composition, dissociation degree, orientation, interaction, and adsorption.

The instrument consists of the following parts, KSV SPOT measuring head, a counter electrode made of stainless steel, the stand for SPOT, a cable for connecting the measuring head and the counter electrode (crocodile clip-RCA cable), a15-pin device cable for connecting the SPOT measuring head to LayerBuilder (LB) unit, and a CD-ROM disk for installing the SpotMonitor software (for stand-alone usage). If the KSV SPOT is intended to be used in combination with KSV's monolayer trough the software for controlling the KSV SPOT will be integrated within the LB software.

The KSV SPOT measuring head is connected to the LayerBuilder unit with the 15-pin cable. Then the counter electrode is connected to the SPOT measuring head with the crocodile clip-RCA cable. **Figure 64** shows how the counter electrode, and the measuring head should be connected using the crocodile clip-RCA. It is important to note that the KSV is factory calibrated and there should be no need for re-calibrating, however the calibration procedure is noted below in section D2.

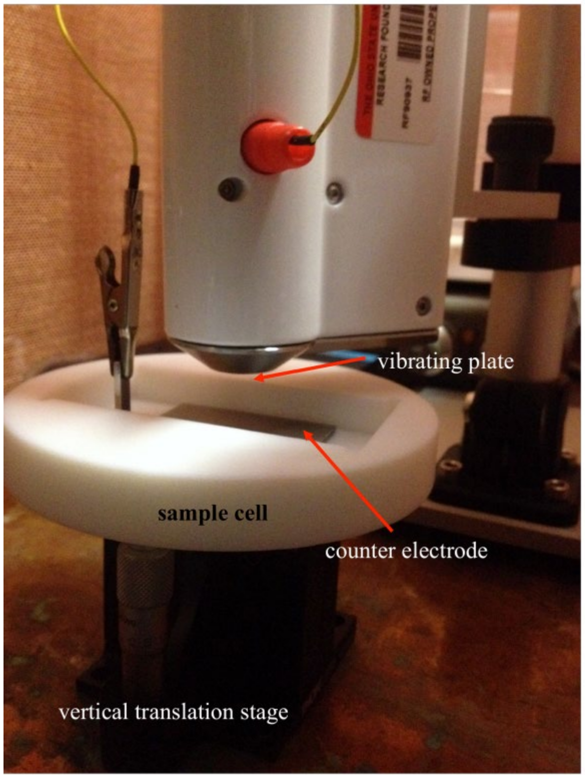

Figure 64. Picture of surface potential measuring head connected to the counter electrode vis crocodile clip-RCA.

D.2 Calibration of the KSV SPOT

A DC-power supply is connected between the counter electrode and the RCA connector on SPOT measuring head front panel. The positive voltage should be connected to the counter electrode and ground to RCA connector. The voltage should be between 2.0 and 3.5 Vdc. Start the KSV WinLB software. To calibrate the devices, enter the system diagnostics and calibration software by choosing **Experiment→System**

Diagnostics and Calibration or pressed the **System Diagnostics and Calibration** in the main menu window. A window should appear, scroll down the system diagnostics devices list to select **Spm()** and press calibrate. Measure the connected voltage with digital voltage meter, showing at least 3 decimal places, and enter the value to **the Fist Potential (V)** field. It is important to make sure that the reading in the **First Value** has stabilized before pressing next. Now change the DC- power supply connection to vice versa, the ground should be connected to the counter electrode and the positive voltage to the RCA connector. The complement negative value is then entered to the **Second Potential (V)** field, let the value to stabilized and press next. After this the calibration is done and new calibration factor is saved into the SPOT memory.

D.3 KSV Surface Potentiometry couple with KSV trough

When using the KSV SPOT tandem with a Langmuir trough, one can utilize any of the available experiments in the KSV WinLB software. Although, a few steps need to be taken before the surface potential can be used simultaneously. Fist the KSV WinLB software needs to be started, from the **KSV Control Software** window open the **Edit** drop down menu and chose **Device Parameter** an **Instrument Parameter** widow appears, here unchecked the **Sound card Spm connected** box in the lower right corner and press **OK** and close all the windows and the KSV WinLB software. Now, everything is set for surface potential measurements.

To continue with the experiments of surface potential and surface pressure measurements. The KSV SPOT measuring head is place in the middle of the trough with sufficient distance from the trough edges. Hereafter, the counter electrode is place in the subphase and the vibrating pate a few mm from the subphase surface. If the vibrating plate touches the subphase accidentally and get wet, it does not do any harm to the measuring head. The plate should just let to dry out before a new experiment. Start the measuring head by switching the toggle switch to up position. The complete system should be powered on at least one hour before starting and experiment and the SPOT head should be turned on at least 10 minutes before starting an experiment. Clean the trough meticulously with reagent alcohol and nanopure water, filled the trough with water or subphase solution. Confirm the cleanness of the trough by compressing the barriers at maximum speed, the surface pressure should not go beyond 0.20mN/m, since the surface potential is more sensitive to impurities than the surface pressure.

Always zero the measuring head before spreading any substance on the surface. The measuring head can be zeroed by choosing the **Zero SPM** from the **Control** drop dawn menu in the **KSV LB Control Software** window. After spreading the substance let the solvent ($CHCl_3$) to evaporate for 10 minutes before compressing. The surface potential often increases faster before the surface pressure starts to increase, so it is important to spread a small amount of the substance on the subphase. The ideal shape for the trough used for surface potential measurement should be long and reasonably narrow. Please note that the barriers should not be compressed closer than 1 cm to the measuring head, since this can induce variations in the results due to static disturbances from the material of the barriers. Lastly, surface potential values can be shown in the screen while the experiment is running by selecting **SP(V)** as the other y-axis for the drop-down menu in the **Graph**. A full image of the set up can be found in **Figure 65**.

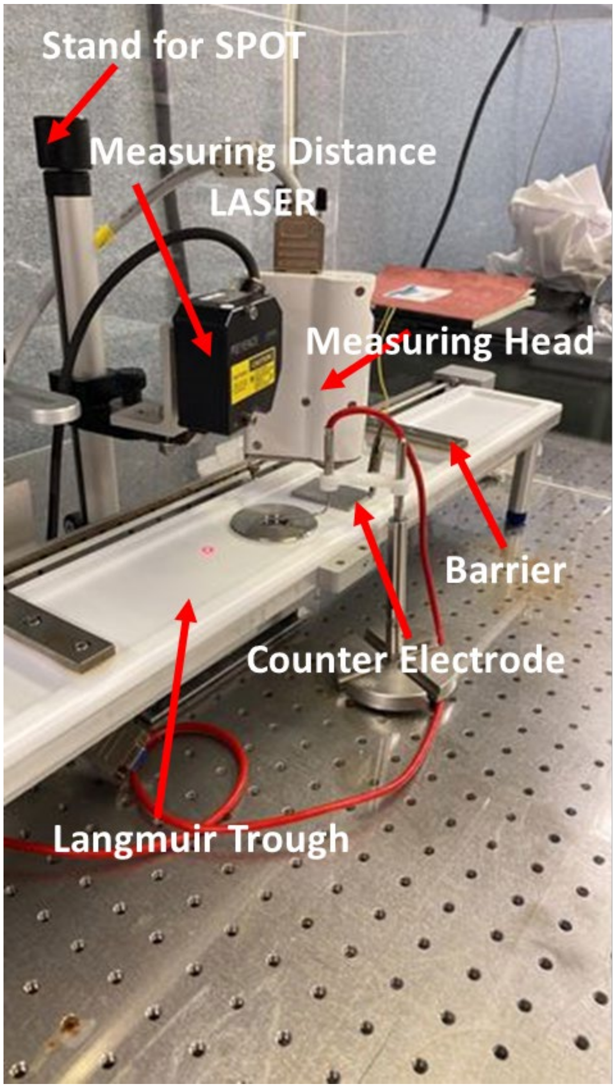

Figure 65. Surface pressure and surface potential area isotherm setup, consisting of long Langmuir trough with compression barriers, measuring head, counter electrode, and measuring distance laser.

The measuring distance (MDS) laser is used to be consistent with the distance between the measuring head (vibrating plate) and the surface within trials. The MDS laser controller is connected to a power outlet, and it will turn on automatically the screen will show –FFFFFF as shown in **Figure 66**. Once you start lowering the measuring head by using the top knob on the stand for the SPOT, (see **Figure 65**), you will start to see numbers on the screen, stop when the number is between 0.0010 and –0.0005. The vibrating plate should be at ~2 mm above the water or aqueous surface. Please do not zero the MS laser controller since this will required a new laser heigh calibration.

Figure 66. Measuring distance laser controller.